Technische Universität Dresden

Investigation of Low Optical-Gap Donor and Acceptor Materials for Organic Solar Cells

M. Sc.
Rishi Ramdas Shivhare

der Fakultät Elektrotechnik und Informationstechnik
der Technischen Universität Dresden
zur Erlangung des akademischen Grades

Doktoringenieur

(Dr.-Ing.)

genehmigte Dissertation

Vorsitzender:	Prof. Dr. Johann W. Bartha	Tag der Einreichung: 19.08.2019
Gutachter:	Prof. Dr. Stefan C. B. Mannsfeld 1	Tag der Verteidigung: 11.10.2019
Gutachterin:	Prof. Dr. Natalie Banerji 2	

1. Gutachter : Prof. Dr. Stefan C. B. Mannsfeld
2. Gutachterin: Prof. Dr. Natalie Banerji

Abstract

Development of efficient and clean energy sources to meet the ever-increasing demand of humankind is one of the greatest challenges of the 21st century. There is a dire need to decarbonise the power sector, and the focus needs to shift to renewable resources such as wind and solar energy. In this regard, organic solar cells are a promising and novel technology owing to its low carbon footprint, innovative applications, and possible integration into the current infrastructure. Due to its unique advantages, a considerable research effort has been put into its development in the last decades. As a result, the power conversion efficiency (PCE) of the organic photovoltaics has steadily risen from as low as 0.5% to around 17 % at the current stage. This improvement primarily originates from the better understanding of the underlying physical processes and as a result of extensive material development.

In the most general case, organic solar cells consist of a binary blend of an electron donating and an electron accepting organic semiconductor forming the so-called 'bulk-heterojunction' (BHJ) morphology. Thermodynamics places an upper limit on the power conversion efficiency (PCE) of binary blend BHJ devices and for further enhancement in efficiency novel device concepts like the use of ternary blends and tandem device architectures is being investigated. In relation to these approaches, the development of low optical-gap ($E_{opt} \leq 1.5$ eV) organic semiconductors has gained importance as these materials provide for the complementary absorption with respect to the other components and better harvesting of the solar spectrum.

This work mainly deals with the investigation of low optical gap donor and acceptor materials for organic solar cells. We investigate the effect of the molecular structure on the device performance and the photophysical processes in the binary and ternary blend configuration. In the first part of the thesis, we study a family of low optical-gap diketopyrrolopyrrole (DPP) based polymers while varying the conjugated core and the branching position and length of the solubilizing alkyl side chains. The branching position of the side chains is found to have a significant influence on the polymers ability to crystallize, which in turn influences the mobility of free charge carriers. The branching position also affects the solubility of the polymer, which in turn influences the morphology of the bulk-heterojunction (BHJ) and ultimately the yield of photogenerated charge carriers.

To investigate the electron transfer and charge separation dynamics in the blends consisting of DPP polymers and fullerene, we employed ultrafast pump-probe spectroscopic techniques. In the spectroscopy data, we observe signatures suggesting an ultrafast electron transfer process and an efficient charge separation process due to the high mobility of the free charge carriers shortly after separation (∼10-100 ps).

Lastly, we investigated indacenodithiophene (IDT) based non-fullerene acceptor (NFA) molecules. In particular, we studied the effect of fluorination on the device performance when these acceptors are blended with PTB7-Th and P3HT donor polymers. The kinetics of the photophysical processes in the binary and ternary blends are characterized using ultrafast spectroscopy and related to the morphology of the blend and the molecular structure of the acceptors.

Overall, we investigated the structural variations in the DPP polymers and fluorinated non-fullerene acceptor (NFA) molecules and suggest design rules for the synthesis of optimal DPP polymers and non-fullerene acceptors to achieve superior device performance. Additionally, we also shed light on the phenomenological processes happening on an ultrafast time scale (0.2-1000 ps) in the binary and the ternary blends with the aim of developing a better understanding of the photophysical processes in these promising material systems.

Publications

Articles

A1 Riccardo Di Pietro, Tim Erdmann, Joshua H Carpenter, Naixiang Wang, Rishi Ramdas Shivhare, Petr Formanek, Cornelia Heintze, Brigitte Voit, Dieter Neher, Harald Ade, Anton Kiriy: "On the synthesis of high crystallinity DPP polymers with balanced electron and hole mobility." *Chemistry of Materials*, **2017**, 29, 10220-10232.

A2 Rishi Shivhare, Tim Erdmann, Ulrich Hörmann, Elisa Collado-Fregoso, Stefan Zeiske, Johannes Benduhn, Sascha Ullbrich, Rene Hübner, Mike Hambsch, Anton Kiriy, Brigitte Voit, Dieter Neher, Koen Vandewal, Stefan CB Mannsfeld :"Alkyl Branching Position in Diketopyrrolopyrrole Polymers: Interplay between Fibrillar Morphology and Crystallinity and Their Effect on Photogeneration and Recombination in Bulk-Heterojunction Solar Cells." *Chemistry of Materials*, **2018**, 30, 6801-6809.

A3 Tian-yi Li, Johannes Benduhn, Zhi Qiao, Yuan Liu, Yue Li, Rishi Shivhare, Frank Jaiser, Pei Wang, Jie Ma, Olaf Zeika, Dieter Neher, Stefan C. B. Mannsfeld, Zaifei Ma, Koen Vandewal and Karl Leo: "Effect of H- and J-Aggregation on the Photophysical and Voltage Loss of Boron Dipyrromethene Small Molecules in Vacuum Deposited Organic Solar Cells." *Journal of Physical Chemistry Letters*, **2019**, 10, 2684-2691.

A4 Kejun Liu, Haoyuan Qi, Renhao Dong, Rishi Shivhare, Matthew Addicoat, Tao Zhang, Hafeesudeen Sahabudeen, Thomas Heine, Stefan Mannsfeld, Ute Kaiser, Zhikun Zheng, Xinliang Feng: "On-water surface synthesis of crystalline two-dimensional polymers assisted by surfactant monolayers." *Nature Chemistry (Accepted)*

A5 Cecilia Teixeira da Rocha, Ge Qu, Xuegeng Yang, Rishi Shivhare, Mike Hambsch, Ying Diao, Stefan Mannsfeld: "Mitigating Meniscus Instability through Piezoshearing for Uniform Coating of Organic Field-Effect Transistors."*ACS Applied Materials and Interfaces (Accepted)*

Conference Contribution

- Rishi Shivhare, Tim Erdmann, Petr Formanek, Mike Hambsch, Anton Kiriy, Koen Vandewal, Takuya Tsuda, Stefan Mannsfeld: "Diketopyrrolopyrrole based polymer solar cells: effect of alkyl branching point on device performance (**Conference Presentation**)." *SPIE Photonics Europe, **2018**, Strasbourg, France.*

Contents

Chapter 1

Introduction

> *"I'd put my money on the sun and solar energy. What a source of power! I hope we don't have to wait until oil and coal run out before we tackle that."*
> -Thomas Edison, American inventor

1.1 Fossil fuel based energy ecosystem: Resource Depletion and Global Warming

The global energy needs are steadily rising, and at present, humankind consumes over 14,000 million tonnes (Mtoe) of oil equivalent energy per year [1] (Figure 1.1). The present energy demands are predicted to grow by over 25% by the year 2040 [2]. Thus looking for alternative and clean energy sources is a primary challenge of the 21st century. Most of the energy utilized today is derived from crude oil and coal. It has been estimated that at present, 35 billion barrels of oil are consumed in a year, and around 40 % of the oil reserves have been already utilized. At the current level of extraction, the oil reserves are predicted to last for a mere 53 years, and the coal reserves are estimated to last just over 100 years [3, 4].

Moreover, the use of fossil fuels has resulted in a drastic rise in the emission of greenhouse gases which has had a devastating effect on earth's climate, the phenomenon collectively referred to as 'Global Warming.' The common effects of global warming include the increase in the earth's surface temperature, melting of the glaciers, and the concomitant rise in the sea levels, which has endangered many tropical habitats. As a matter of fact, the past 18 years since 2001 have been the warmest years in earth's history with 2016 being the warmest year ever recorded [5]. Warming climate can be mainly ascribed to the alarming rise in earth's CO_2 content with a present concentration around 411 ppm (parts per million), which is the highest recorded value in the last 800,000 years [6].

1.2 Renewable energy sources and the role of photovoltaics (PVs)

The unprecedented damage to the earth's climate and ever-vanishing fossil fuel resources call for a significant shift in how we manage earth's energy production and usage. Renewable energy sources are required, and they need to replace the existing fossil fuel based industrial sector. In recent years, bioenergy has emerged as

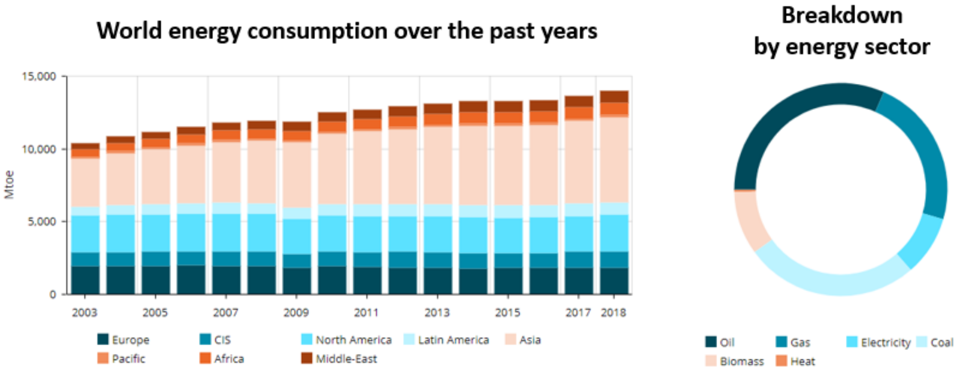

Figure 1.1: Graphical representation of world energy consumption in the period 2003-2018. Individual contribution from the various continental regions of the globe are also stated (left). Breakdown of energy consumption based on the source of origin (right). Republished from [1]

a promising source of renewable energy, primarily contributing to the heating and the transport sector. Whereas the power sector is dominated by hydropower followed by wind and solar photovoltaic (PV) technology as far as the renewables are concerned. In the past few years, world-wide solar installations have reached 400 gigawatt (GW) PV capacity producing around 460 TWh of electricity, which constitutes approximately 2% of the total global power output [7]. The International Energy Agency's (IEC) road-map envisions the global power output from solar PV to rise to 16% by 2050. This would involve the increase in the PV capacity to 4600 GW, which could prevent 4 billion tonnes of CO_2 emissions. At present, crystalline silicon (c-Si) modules dominate the PV sector, which make up 90 % of the market share. The average power conversion efficiency of the commercial modules ranges from 21-23 %. Other major technologies includes the thin-film PVs, which mainly consists of Cadmium Telluride (CdTe) based PVs with the best efficiency around 19% for commercial modules. Copper-indium-gallium-selenide (CIGS) based PV is the other thin film technology with relatively lower efficiency values around 12-14 % for commercial modules. Amorphous silicon (a-Si) based cells have not undergone large scale deployment because of their low efficiency and unstable device performance. Multi-junction solar cells involving the tandem approach where two or more cells are stacked together have also been developed, and efficiencies as high as 38.8% have been achieved under 1-sun exposure [7]. Despite their success, the usage of multi-junction devices has been restricted to space applications and unmanned aerial vehicles due to the use of costly materials.

The market share of c-Si modules is predicted to increase as the prices have reduced drastically over the years. The reduced cost of c-Si modules have also encouraged manufacturers to use the tandem approach, and many novel technologies have been incorporated. For instance, Oxford PV, a company based in the UK, has combined c-Si cell with emerging perovskite solar cells and a record efficiency of around 28 % has been reported for the tandem device [8]. It is worth mentioning that the improved device performance is still only achieved for small area devices and the challenges with upscaling of the technology needs to be tackled in the future. If replicated on the large scale, the improved efficiency of c-Si modules with a low cost can reform the economics of silicon-based solar cells.

1.3 Organic solar cells: an emerging technology

Apart from the silicon and thin film PV technology, there are many other promising PV technologies in their nascent stage. These mainly include dye-sensitized solar cells, perovskite solar cells, and organic photovoltaics (OPV) (see Figure 1.2). Organic solar cells, in particular, are very promising as they provide an avenue for unique applications because of being flexible, lightweight, and in many cases, semi-transparent. But arguably the most important feature of OPV's has to be their solution processability which allows for the possibility of high throughput fabrication using roll-to-roll printing. As the solar cells can be solution processed at a high yield, the commercial modules can be produced at a meager cost with a short energy payback time. In the last couple of decades, intense research effort has been put into the improvement of organic solar cells. As a result, the power conversion efficiency (PCE) values have increased from a few percent to as high as 16% in single junction devices as was reported recently [9]. Other novel approaches such as tandem device architecture and ternary blend devices where more than two semiconductors are blended and cast as thin films, has been adopted. A record efficiency value as high as 17.3 % [10] has been achieved for tandem devices, whereas for ternary blend devices, the highest efficiency value is close to around 14 % [11]. Both the tandem and ternary device approach require complementary absorption between the components so that a wider part of the solar spectrum can be harvested. In the recent past, an extensive repository of wide optical-gap donor polymers and acceptors (mainly fullerenes) have been developed [12, 13] and there is a need for novel low optical-gap donor polymers and acceptors to be used in tandem and ternary devices. The work in this thesis addresses this issue where we investigated the low optical gap polymers and non-fullerene acceptors for their suitability for use in solar cells.

Despite very promising results, there are still certain challenges that need to be addressed before the OPV technology can be successfully commercialized. One of the main obstacles for the 'lab-to-fab' transition is the development of high-performance devices using printing techniques. To date, the majority of the record efficiency devices are fabricated using the spin-coating process, which is not scalable. Another major challenge is the stability of the devices. For commercial viability, the device needs to perform well over a prolonged duration. It is estimated that if an OPV device with an efficiency of 15 % can run over 20 years, it would produce electricity at a cost as low as 7 cents per kilowatt-hour (kWh) [17]. The average cost of electricity in the developed economies at the present date is around 12 cents per kilowatt-hour (kWh). If the issues with stability and scalable processing can be addressed, there is no reason why OPV technology would not flourish in the near future.

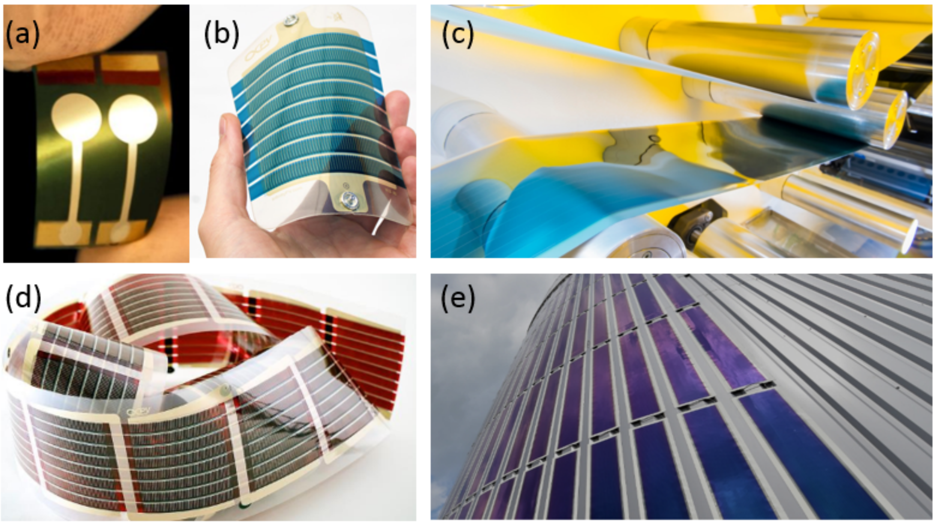

Figure 1.2: (a) Lab scale, small area OPV device fabricated on a flexible substrate [14] (b) Large area series connected OPV device (c) Roll-to-roll processing of OPV in a commercial line [15] (d) Figure showing the commercial OPV modules [16] (e) Integration of OPV modules onto the outer wall of a commercial building [15].

1.4 Outline of the thesis

In Chapter 2, we introduce the fundamentals of organic semiconductors and discuss the working principle of organic solar cells. The main parameters which determine the efficiency of the device are illustrated, and their dependence on various factors is discussed. Chapter 3 lays out all the experimental techniques, a summary of the device fabrication protocol is provided, and the basic theory of techniques, spectroscopic or otherwise is explained in brief. In chapter 4, we investigate a series of diketopyrrolopyrrole (DPP) based low optical gap donor polymers for their use in solar cells. DPP polymers are blended with the fullerene derivative PC[70]BM and the solar cells are fabricated under similar processing conditions. Primary factors which lead to the variations in the device performance are thoroughly investigated. The DPP:PCBM system is identified as a zero driving force system for the electron transfer process, and in Chapter 5 we examine the electron transfer and charge separation dynamics in DPP:fullerene systems and try to elucidate some of the fundamental questions of the OPV technology. In chapter 6, we introduce a new series of materials: fluorinated non-fullerene acceptors (NFA), which also possess a low optical gap. The materials are blended with well-known wide gap donor polymers: P3HT and PBT7-Th, and the device performance is tested for binary and ternary blends. Moreover, the photophysics in binary and ternary blend devices is investigated using ultrafast pump-probe spectroscopy.

Chapter 2

Fundamentals of Organic Semiconductors and Organic Photovoltaic Devices

This chapter introduces the basic concepts of organic semiconductors and outlines the working principle of organic photovoltaic (OPV) devices. In section 2.1, we discuss the electronic structure of organic semiconductors and introduce the 'orbital' and the 'state' picture of the electronic configuration. Section 2.2 expands on the possible optical transitions and discusses the various contributors to the molecular wavefunction. Types of non-radiative transitions are also discussed briefly.

Section 2.3 discusses the effects of polarization in molecular solids and the origin of the broadened density of states (DOS). In section 2.4, we classify the various types of excitons depending on the extent of their localization. Section 2.5 is concerned with the transport properties in organic semiconductors, both excitonic and charge transport theories are introduced.

Section 2.6 elucidates the fundamental mechanism involved in charge generation and charge extraction in organic solar cells. In section 2.7, we invoke the concept of a charge transfer (CT) state and discuss the formalism of the open-circuit potential (V_{OC}). Section 2.8 introduces the key concepts of charge carrier recombination, and the latest models and theories which explain the reduced Langevin behavior are discussed.

2.1 Electronic structure of organic semiconductors

The term 'organic' in organic semiconductors refers to the molecules being mainly constituted of carbon atoms, and their semiconducting behavior arises due to the delocalized nature of the electron density which results from the conjugation of bonds [18, 19]. Since organic semiconductors are mainly composed of carbon atoms, it is worthwhile to look into the electronic structure of carbon to understand the physical properties of organic semiconducting molecules. Carbon in its elemental form consists of 6 electrons. With 2 electrons in the 1s orbital, another 2 electrons in the 2s orbital and the remaining electrons occupy the two of the three p orbitals. The electronic configuration is generally denoted as $1s^2 2s^2 (2p_x)^1 (2p_y)^1 (2p_z)^2$. It is found that an electron from the 2s orbital is almost always promoted to the $2p_z$ orbital in case of bonding with other atoms as the binding energy gained from the bonding process compensates for the energy needed for the transfer of the electron [20]. Thus carbon is capable of making four covalent bonds from the unpaired electrons in the 2s and 2p orbitals.

As the binding partners approach the carbon atom, the 2s and 2p orbitals become degenerate and hybridize to form hybrid atomic orbitals. Depending on the number of 2p orbitals involved in the hybridization process three cases are possible: (i) four $2sp^3$ hybrid orbitals are formed when the 2s orbital 'mixes' with three p orbitals, (ii) three $2sp^2$ orbitals are formed upon mixing of the 2s and two 2p orbitals (iii) two 2sp orbitals are formed upon the mixing of 2s and one 2p orbital. The four $2sp^3$ orbitals are at an angle of 109.5°to each other and assume the shape of a tetrahedron. The three $2sp^2$ orbitals are planar and assume an angle of 120°between each other and the two 2sp orbitals are 180°apart and lie along the internuclear axis of the bonding atoms.

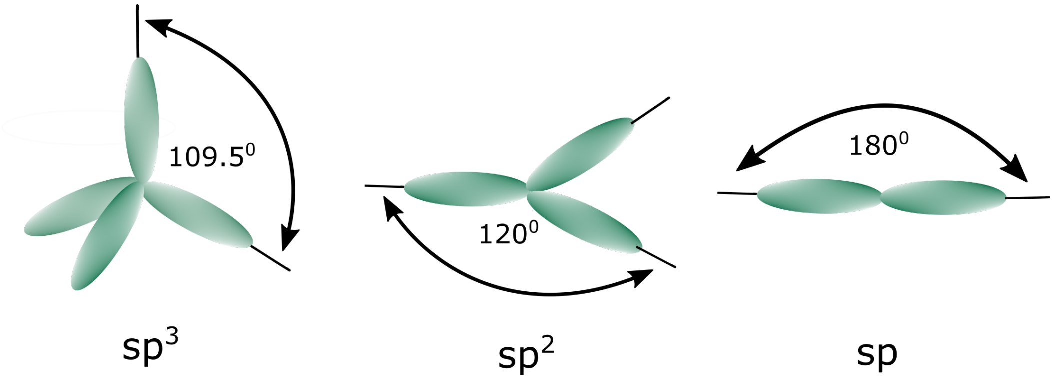

Figure 2.1: Atomic hybrid orbitals :sp^3, sp^2, sp.

On the formation of bonds, the electrons can no longer be described by the atomic orbitals of the parent atoms and the concept of molecular orbital needs to be evoked. Traditionally, molecular orbitals are thought of as the linear combination of atomic orbitals (LCAO). If ϕ_a and ϕ_b represent the atomic orbitals of the bonding partners the resultant molecular orbitals are given as:

$$\psi_+ = c_1\phi_a + c_2\phi_b$$

$$\psi_- = c_1\phi_a - c_2\phi_b$$

where ψ_+ and ψ_- represent the bonding and the anti-bonding orbital, respectively. ψ_+ and ψ_- arise as a result of constructive and destructive interference of the electronic wavefunctions. The energy difference between the bonding and the anti-bonding orbital depends on the resonance integral ($\beta = \int \phi_a H \phi_b d\tau$), where H is the Hamilton operator and $\int d\tau$ denotes the integral over space. Iso-energetic atomic orbitals give rise to the biggest energetic split between the bonding and the anti-bonding orbitals. One of the implications of this is that when considering the energetics of molecular orbitals in a relatively large molecules, the interaction between the atomic orbitals with different energies can be neglected. For example, let us consider the case of the molecule ethene (C_2H_4), and for simplicity, we only consider the carbon-carbon interactions (Figure 2.2). Electrons in the 1s orbital of the carbon atoms interact, leading to the formation of bonding (σ) and anti-bonding (σ^*) orbitals. Since these electrons are closer to the core, resonance interactions are negligible, and it leads to a small splitting between the σ and σ^* orbitals. The 2sp^2 orbitals also interact, leading to the formation of another set of σ and σ^* orbitals. In this case, the splitting between the orbitals is much larger because the orbitals are oriented along the inter-nuclear axis which leads to a much higher resonance interaction. 2p$_z$ orbitals also ‘mix’ leading to the formation of π and π^* orbitals. Splitting between the π and π^* orbitals is smaller as the electron density is located away from the inter-nuclear axis, which implies weaker resonance interactions. Looking at the electronic distribution within these orbitals, σ and σ^* orbitals resulting from 1s interaction are fully occupied, the σ orbital from the 2sp^2 interaction is filled while the higher lying σ^* orbital is empty. Similarly, since the 2p$_z$ orbitals of each

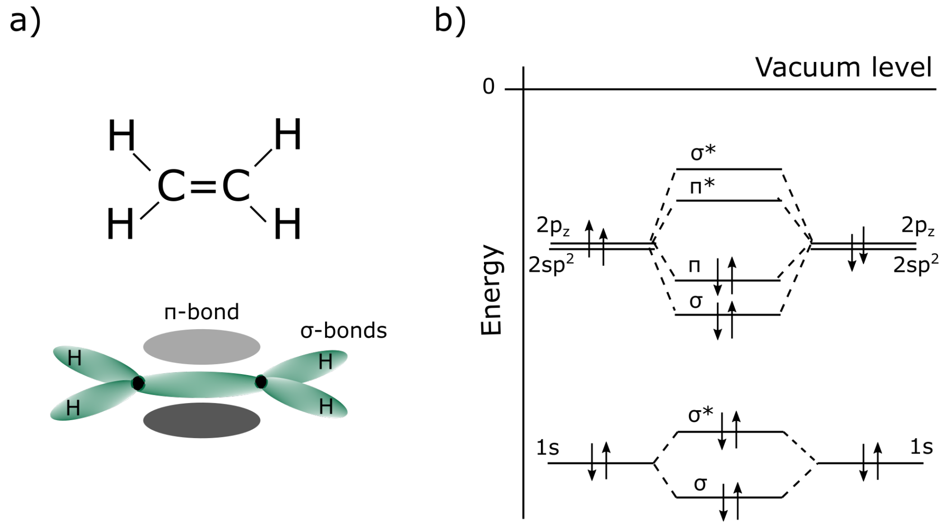

Figure 2.2: (a) Chemical structure of the ethene molecule. Representation of σ and π bonds in the orbital picture. (b) Energy level diagram illustrating the formation of molecular orbitals. For simplicity, only the orbitals involved in the carbon-carbon interaction are shown.

carbon atom contain 1 electron each the corresponding π orbital is filled while the π^* orbital remains empty. Thus we find that the π orbital is the highest occupied molecular orbital (HOMO) while π^* orbital is the lowest unoccupied molecular orbital (LUMO). HOMO and LUMO orbitals are also known as frontier orbitals and play an important role in the optical transitions of a molecule. Usually, the $\sigma - \sigma^*$ transition lies in the UV spectral range while the $\pi - \pi^*$ transitions lie in the visible spectral range. Additionally, the energetics of frontier orbitals is also important when considering the charge injection from the electrodes into the molecular solid film. Ideally, the difference between the work function of the metal electrodes and HOMO/LUMO should be small for efficient charge injection.

From orbitals to states

Considering the orbital picture, once can ask how to visualize the ground state or an excited state of a molecule ? From a quantum chemical perspective, states can be thought of as the superposition of various electronic configurations. This is also known as the configuration interaction (CI) [21]. Here, by configuration we mean how the electrons are distributed in the molecular orbitals. So when all the electrons reside in the lowest energy orbitals, the molecule can be considered to be in the 'electronic' ground state. When an external perturbation (e.g. optical) excites the system the excited state can be thought of as consisting of distribution of various configurations. Very often the dominant exited state configuration consists of one electron in the HOMO and other electron in the LUMO of the system. But other configurations might also exist, for instance, two electrons in the HOMO, one electron in the HOMO-1 and an electron in the LUMO and so on. As one can imagine, numerous configuration of electrons are possible for the same excited state. So it is important to distinguish between the orbitals, configuration, and the so-called state of the system. Since for the description of the optical transitions, the states of the molecule are relevant, and more helpful, we will adhere to the 'state' picture during the course of this thesis.

Singlet and triplet states

Apart from the electronic wavefunction describing the spatial distribution of electrons or orbitals, the spin-wavefunction also needs to be taken into account for describing the state of the system. The total spin of the molecule can be calculated by summing up the spin of all the electrons. But as the filled orbitals consist of electrons with an anti-parallel spin, only the contribution from unpaired excited electrons is relevant. Considering the excited state with an electron in the HOMO and an electron in the LUMO, the two particle system with spin angular momentum has the eigenstates $\hat{S}^2$ and $\hat{S}_z$ with eigenvalues S and M$_s$, where $\hat{S}^2$ is the spin angular momentum operator and $\hat{S}_z$ is its component in the z-direction. The two particle system has four eigenstates. If α and β represent the spin wavefunction of the one-electron state with eigenvalues s=1/2 and m$_s$=1/2 and s=-1/2 and m$_s$=-1/2, the eigenstates of the two particle system are given as :

$$\begin{aligned} \Psi_{spin,T+} &= \alpha_1\alpha_2 && S = 1 \ and \ M_s = 1 \\ \Psi_{spin,T0} &= \tfrac{1}{\sqrt{2}}(\alpha_1\beta_2 + \beta_1\alpha_2) && S = 1 \ and \ M_S = 0 \\ \Psi_{spin,T-} &= \beta_1\beta_2 && S = 1 \ and \ M_s = -1 \end{aligned}$$

$$\Psi_{spin,S} = \frac{1}{\sqrt{2}}(\alpha_1\beta_2 - \beta_1\alpha_2) \qquad S = 0 \ and \ M_s = 0$$

Note that these eigenstates are defined when a magnetic field exists which defines the z-direction. In the absence of the field, $\hat{S}_z$ cannot be defined, which implies that M$_s$ is not a good quantum number. For the more generalized picture of the spin-wavefunction for the two-particle system, the reader is referred to reference [22]. Nevertheless, in the case where M$_s$ is a good quantum number, the first three spin wavefunctions with S=1, differ only in the z-component of the spin with M$_s$=1 ,0, -1 and this arrangement is therefore collectively referred to as the triplet. While the last spin wavefunction has only one value of the z-component (M$_s$=0) and is called a singlet. The spin of the electron in a triplet state is always in phase while the spin is 180°out of phase for the singlet state. The energy of the triplet state is lower than the energy of the singlet state [Figure 2.3]. This difference in energy is due to the repulsion between electrons with parallel spins, which increases the distance between particles and as a result, the coulomb interaction decreases. The energetic difference between the triplet and the singlet states i.e., the exchange energy is given as twice the value of the exchange integral. The exchange integral depends on the degree of overlap between the wavefunctions. With increasing overlap, the exchange energy increases. For π-conjugated polymers the exchange energy typically ranges between 0.5-0.8 eV [23].

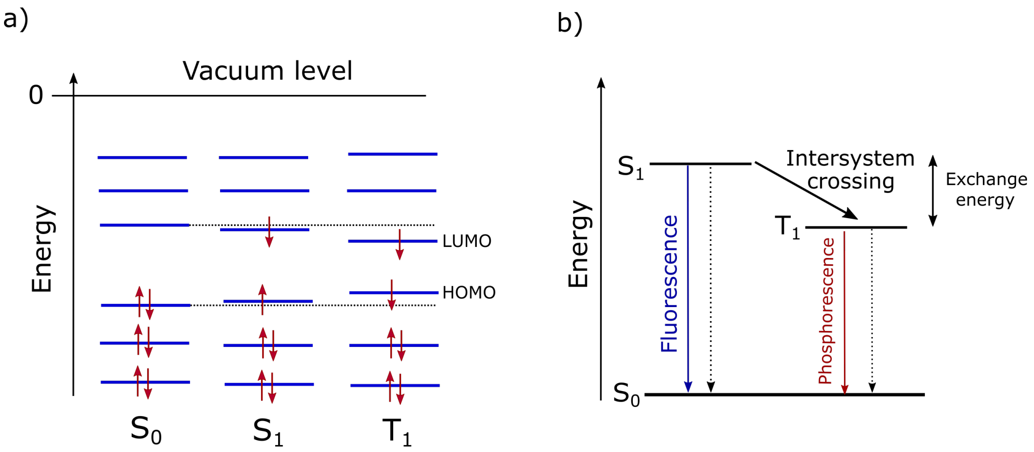

Figure 2.3: (a) Representation of the ground state, singlet and triplet states in the orbital configuration scheme. Red arrows represent the electrons and the direction of the arrow corresponds to the spin.(b) Singlet and triplet states in a state diagram. Solid and dashed arrows represent radiative and non-radiative decay channels respectively. Figure reproduced from [20]

.

2.2 Optical transitions in organic semiconductors

The wavefunction of a molecule primarily consists of three parts: the electronic wavefunction ($\Psi_{elec.}$) which depends on the spatial coordinates of the electrons, the spin wavefunction (Ψ_{spin}) which relates to the spin angular momentum of electrons and the vibrational wavefunction ($\Psi_{vib.}$) which depends on the vibrational modes of the nuclei.

$$\Psi_{molecule} = \Psi_{elec.}\Psi_{spin}\Psi_{vib.} \tag{2.1}$$

Interaction of light with molecules (absorption or emission of photons) changes the wavefunction of the molecule. Quantum mechanically this can be treated using the framework of perturbation theory. The perturbing hamiltonian ($\hat{H}^{'}$) which is the dipole operator ($e\hat{r}$) in case of absorption or emission can be used to calculate the resultant wavefunction. In this framework, the transition rate of going from an initial state (i) to the final state (f) is given according to the Fermi's golden rule [24]:

$$k_{if} = \frac{2\pi}{\hbar}|\langle\Psi_f|\hat{H}^{'}|\Psi_i\rangle|^2\rho \tag{2.2}$$

where Ψ_i and Ψ_f are the initial and the final wavefunctions and ρ is the density of final states.

For absorption and emission where $\hat{H}^{'} = e\hat{r}$ and considering the total wavefunction of the molecule we get :

$$k_{if} = \frac{2\pi}{\hbar}|\langle\Psi_{elec.f}\Psi_{spin,f}\Psi_{vib.,f}|e\hat{r}|\Psi_{elec.,i}\Psi_{spin,i}\Psi_{vib.,i}\rangle|^2\rho \tag{2.3}$$

Physically, only the electrons respond to the electric field of the electromagnetic wave while the nuclei are just too massive to resonantly follow the rapidly oscillating electric field (Born-Oppenheimer approximation). The spin wavefunction remains unaltered in the presence of an electric field, and it is only affected by the changing magnetic field of the electromagnetic wave. But the magnitude of change is minimal in the visible and the IR region and thus can be ignored. Considering these arguments, it follows that only the electronic wavefunction is affected by the dipole operator, and the remaining integrals can be treated as constants. Mathematically this can be represented as :

$$k_{if} = \frac{2\pi}{\hbar}\rho|\langle\Psi_{elec.,f}|e\hat{r}|\Psi_{elec.,i}\rangle|^2|\langle\Psi_{spin,f}|\Psi_{spin,i}\rangle|^2|\langle\Psi_{vib.,f}|\Psi_{vib.,i}\rangle|^2 \tag{2.4}$$

The electronic factor:$|\langle\Psi_{elec.,f}|e\hat{r}|\Psi_{elec.,i}\rangle|^2$

The electronic transition is considered to be dipole allowed if the integral is nonzero; otherwise, it is said to be dipole forbidden. As can be seen from the integral, the transition rate depends on the overlap between the initial and final wavefunctions. The greater the overlap the higher is the transition rate, which leads to higher macroscopic intensity for the transition. Additionally, the transition rate/intensity also depends on the transition dipole moment. With increasing orbital extension, the transition dipole and thus the transition rates increase. For example, it is often found that the absorbance and fluorescence intensities of oligomers increase with the number of repeating units [25].

The vibrational factor:$|\langle\Psi_{vib.,f}|\Psi_{vib.,i}\rangle|^2$

Apart from the electron wavefunction, the intensity of transition also depends on the overlap of initial and final vibrational wavefunctions [Figure 2.4]. The Frank-Condon principle suggests that the intensity of a vibronic transition is proportional to the overlap integral and that the probability of transition follows a Poisson distribution [22]. The intensity of transition from the 0^{th} vibrational level in the ground state to the m^{th} vibrational level in the excited state is given as:

$$I_{0-m} = |\langle \Psi_{vib.,f} | \Psi_{vib.,i} \rangle|^2 = \frac{S^m}{m!} e^{-S} \tag{2.5}$$

$$with \qquad S = \frac{1}{2} k \frac{\Delta Q^2}{\hbar \omega_m} \tag{2.6}$$

where S is the Huang-Rhys parameter, ΔQ is the change in the configuration coordinate as a result of excitation and $\hbar\omega_m$ is the energy of the vibrational quanta. The Huang-Rhys parameters gives an estimate of the amount of quanta involved in vibrational excitation and can be calculated using the ratio :$\frac{I_{0-1}}{I_{0-0}}$.

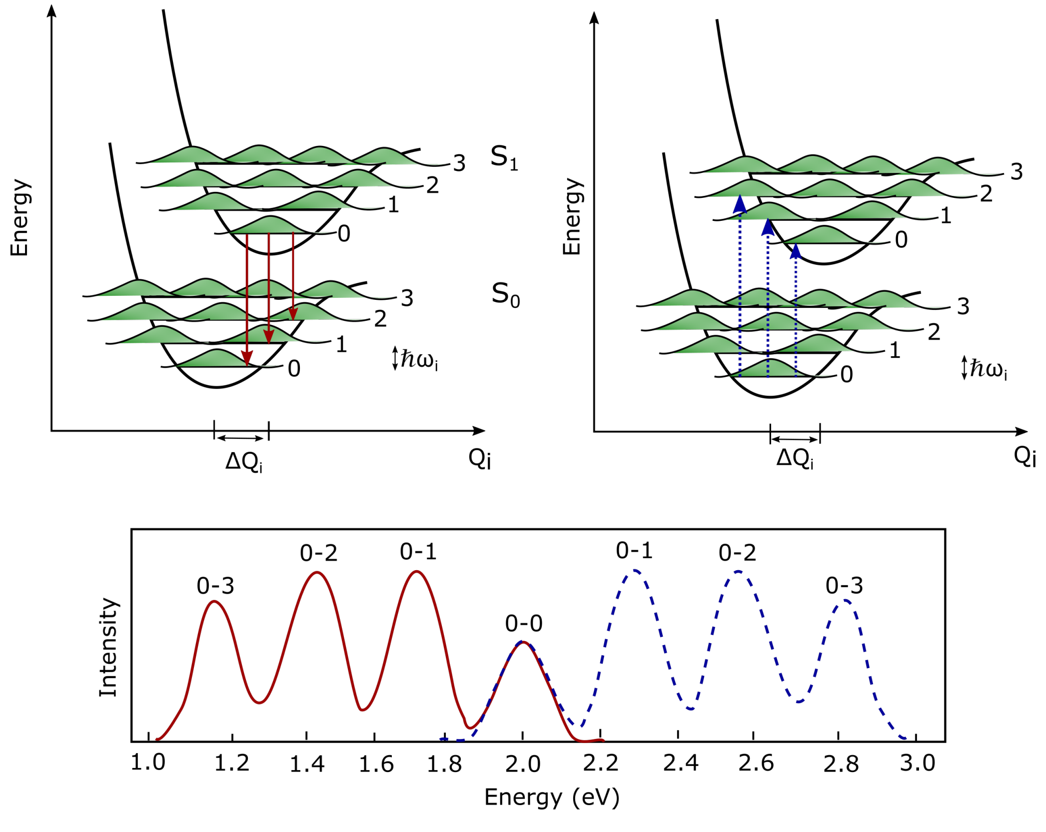

Figure 2.4: Representation of the Frank-Condon principle. The potential energy curves for the ground state and the first excited singlet state are depicted. Vertical arrows represent transitions between the different vibrational levels. The overlap between the initial and the final vibrational wavefunction determines the intensity of transition. The bottom graph illustrates the Stoke-shifted absorbance and luminescence spectra and the corresponding vibronic transitions. Figure reproduced from [20].

The spin factor:$| \langle \Psi_{spin,f} | \Psi_{spin,i} \rangle |^2$

The spin integral assumes only two values, either 0 or 1. If the integral is 0, the transition is said to be spin forbidden, and if the integral's value is 1, it is said to be spin-allowed. Optical transitions between states of the same spin multiplicity ($S_n \leftarrow S_0$,$T_n \leftarrow T_0$) are spin allowed while the transition between the states of different multiplicity ($S_0 \leftarrow T_n$) are usually spin forbidden. One mechanism by which transitions between states of different spin multiplicity can be allowed is known as the 'spin-orbit coupling'. The idea is that as only the total angular momentum needs to be conserved during the transition, the spin and the orbital angular momentum can simultaneously change while compensating each other. The spin-orbit coupling can be treated in terms of a perturbing Hamiltonian which for example adds singlet like character to a triplet wavefunction. The magnitude of spin-orbit coupling is sensitive to the total amount of charge on the molecule, and thus the coupling is usually prevalent in organometallic complexes, which consist of heavy transition metal ions [26, 27].

Non-radiative transitions: Internal conversion and inter-system crossing

Non-radiative transitions are iso-energetic transitions between 0th vibrational level of an initial state to mth vibrational level of another state. If the transition takes place between the states with the same spin ($S_2 \rightarrow S_1$,$T_2 \rightarrow T_1$) it is known as *internal conversion* (IC) and if the transition happens between the states with different spins ($S_1 \rightarrow T_1$,$T_1 \rightarrow S_0$) it is known as *inter-system crossing* (ISC).

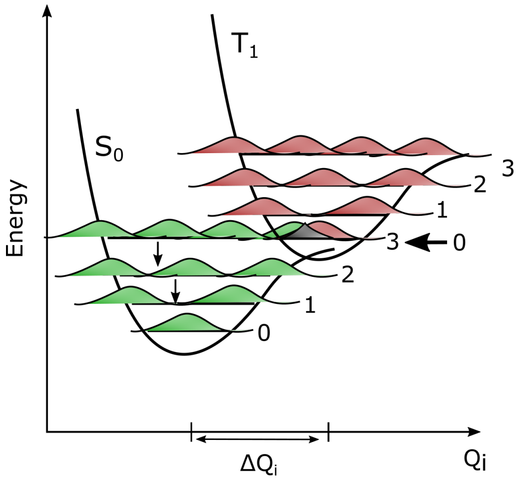

Figure 2.5: Potential energy diagram showcasing the inter-system crossing between the 0th vibrational level of T_1 state to 3rd vibrational level of S_0 state. Shaded region represents the overlap of initial and final vibrational wavefunction. Small arrows indicate the dissipation of excess vibrational energy into the environment.

The rate of transition can be expressed using the form :

$$k_{nr} = \frac{2\pi}{\hbar} \rho J^2 F \tag{2.7}$$

where J is the electronic coupling element and F is the Frank-Condon factor which describes the overlap of the final and initial wavefunction. The Frank-Condon factor and thus the non-radiative transition rate (k$_{nr}$) are found to vary exponentially with the energetic difference between the vibrational levels involved in transition (Δ E):

$$k_{nr} \propto exp(-\gamma\frac{\Delta E}{\hbar\omega_M}) \tag{2.8}$$

where ω_M is the vibrational mode of highest frequency in the final state.
This is the famous energy-gap law [28, 29]. This law has a number of important implications, most important of them being the so called Kasha's rule. It states that emission always takes place from the lowest energy level of the spin-manifold. This makes sense because the energetic difference between the S_2 and S_1 state for instance is much lower than the difference between the S_1 and S_0 states. Thus non-radiative rates between the states of smaller energy differences are much faster than radiative rate between states with a higher energy difference.
Apart from the energy-gap law, the spin-orbit coupling also plays an important role. The rate of inter-system crossing (k_{ISC}) is found to be proportional to the strength of spin-orbit coupling. Typical inter-system crossing rates are around 10^{12} s^{-1} for organo-metallic complexes and around 10^6-10^9 s^{-1} for small molecule semiconductors [30].

2.3 Effects of polarization and disorder

The molecular orbital picture deals with energy levels of isolated single molecules. When considering condensed phases such as liquids or thin films, the energy levels of the molecule change because of the interaction with other molecules. In molecular solids, the inter-molecular interactions are the weak Van der Waals forces which originate from the temporary dipoles of the fluctuating charges. Spectroscopically speaking, a red-shift in absorption and emission is observed when moving from isolated molecules to condensed solids. This red-shift is due to the concomitant reduction in energy of the excited state and the ground state of the molecule. Physically, this can be explained as following, the dipole of the molecule induces a dipole in its adjacent molecules, which results in a dipole-induced dipole interaction (Figure 2.6). The interaction energy between the molecules reduces the overall potential energy of the molecule. The shift in energy is higher in an excited state compared to the energy change in the ground state. As a result, the transition energy for absorption and emission is reduced, causing the red-shift. This change in energy of molecules is known as the electrical polarization effect.

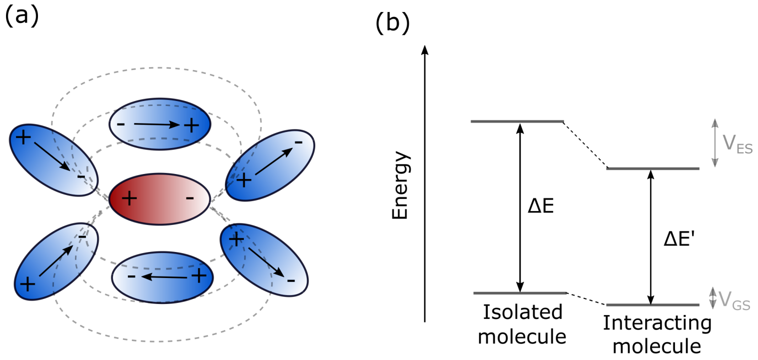

Figure 2.6: (a) Depiction of the electrical polarization effect where the dipole moment of a molecule (red) induces the dipole moment in surrounding molecules (blue).(b) Energy diagram showing the reduction in energy levels for the interacting molecule. V_{ES} and V_{GS} are the interaction energies of the excited state and the ground state respectively. Note that the shift in the energy level is higher for the excited state as compared to the ground state.

The interaction energy for the dipole-induced dipole case is given as [20]:

$$V \propto \frac{1}{(4\pi\epsilon_0)^2}\frac{4p^2\alpha}{r^6} \tag{2.9}$$

where p is the dipole moment of the molecule and α is the polarizability of the surrounding (adjacent molecules). It is important to notice that the dipole-induced dipole interaction varies quadratically with the dipole moment and is also very sensitive to the distance between the molecules ($\propto r^{-6}$). In reality, molecular solids are disordered systems where the spacing between the molecules is not fixed. Additionally, the relative orientation of the dipole moment between molecules is also random. This leads to varying dipole-dipole interactions, which result in a range of energy-shifts. Statistically, for a random arrangement of molecules (polymer chains in our case), one ends up with a 'Gaussian' distribution of energies with some mean energy value (ϵ_0).
Figure 2.7 describes the evolution of energy levels as we progress from isolated molecules to disordered solids in a state picture where the reference level is the vacuum energy. When moving from the isolated molecules to a single crystalline molecular solid, the energy levels shift as a result of the polarization effect, which reduces the HOMO-LUMO gap. In single crystals, wavefunction overlap leads to the formation of the excitonic band-like states similar to the case of inorganic semiconductors, but the width of the bands is much narrower (few hundred meV). On moving to disordered solids, we find a Gaussian distribution of energy sites which arises due to the range of different polarization energies. As very often polymer semiconductors are disordered systems we should have this picture in mind when discussing charge transport properties.

Apart from electronic polarization effects, structural/lattice relaxation effects also induce polarization but on a much slower timescale. An example for this is the polaronic effect, which describes the lattice distortion around a charged molecule

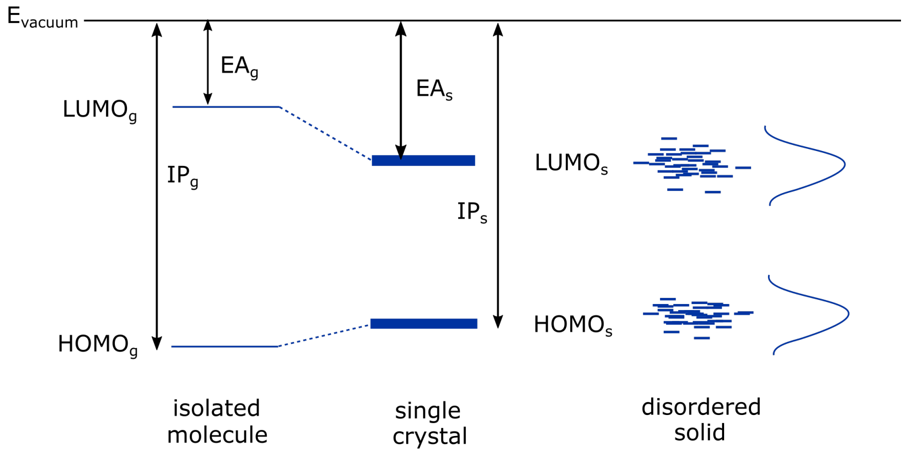

Figure 2.7: Schematic showing the effect of polarization on energy levels of the molecule. Disordered solids give rise to a gaussian distribution of states as result of distribution of polarization energies.

[31, 32]. When placing an electron or hole on a polymer chain, it distorts the environment around the charge and is collectively referred to as negative or positive polaron respectively. The transport of polarons where a charge drags the lattice distortion with it is known as the polaronic transport. We will use the term electron and hole for describing the charge transport, but the reader should remember that the polaronic effects are already entailed in it. Due to the localization of the wavefunction in the disordered system the polaron transport is not facilitated by the formation of the bands but instead, they have to hop from one site to the other. The details of the charge transport mechanism will be discussed in the subsequent section.

2.4 Excitons in organic semiconductors

Besides polarons, excitons are also a type of quasi-particles which are essential for describing the optoelectronic properties of organic semiconductors. In the first approximation, they can be regarded as coulombically bound electron-hole pairs. Based on the coulomb binding energy (E_B) and the interaction radius three different types of excitons can be distinguished: (i) Frenkel exciton (ii) Wannier-Mott exciton and the (iii) charge transfer (CT) exciton.

In organic semiconductors, screening of coulomb forces between charges is negligible due to the low values of the dielectric constant ($\epsilon_r \approx 3.5$). This leads to the formation of highly localized electron-hole pairs, also referred to as Frenkel excitons. Since the bound electron-hole pair is analogous to the hydrogen atom, the binding energy of the Frenkel exciton is given as [20, 33]

$$E_B = -\frac{q^4 m^*}{32\pi^2\hbar^2} \cdot \frac{1}{\epsilon_0\epsilon_r} \cdot \frac{1}{n^2} \tag{2.10}$$

where m^* is the effective mass of electron-hole pair and the n is the electronic quantum number. Assuming ϵ_r=3.5 and n=1 we get E_B values of the order of 1eV.

This binding energy is much higher than the thermal energy at the room temperature ($k_B T \approx 25\text{meV}$). Also, the interaction radius for a Frenkel exciton is of the order of the molecular scale.

In contrast, for inorganic semiconductors, because of their high dielectric constant ($\epsilon_r \approx$ 11-12), the dielectric screening between charges is much larger, and the effective mass of charge carriers is lower due to the band transport, which collectively leads to the formation of loosely bound electron-hole pairs. The binding energy is typically lower than the thermal energy at room temperature, and the interaction radius of the pair of charges is of the order of several lattice sites. This highly delocalized electron-hole pair is referred to as the Wannier-Mott exciton.

When the bound electron-hole pair resides on different molecules, it leads to the formation of charge transfer (CT) excitons. Since the CT-exctions are delocalized spatially, they are loosely bound compared to the Frenkel excitons. In the context of organic solar cells, the CT excitons are formed as a result of an electron transfer event between a donor and an acceptor molecule. Formation and dissociation of CT-excitons controls the photogeneration process in solar cells and ultimately defines its efficiency. More on CT-exciton dissociation will be discussed in the subsequent section. Besides an electron transfer event, the CT-excitons can also directly be excited from the ground state, but the oscillator strength for such a transition is several orders of magnitude lower than for a typical $S_1 \leftarrow S_0$ transition, and thus it is hard to detect.

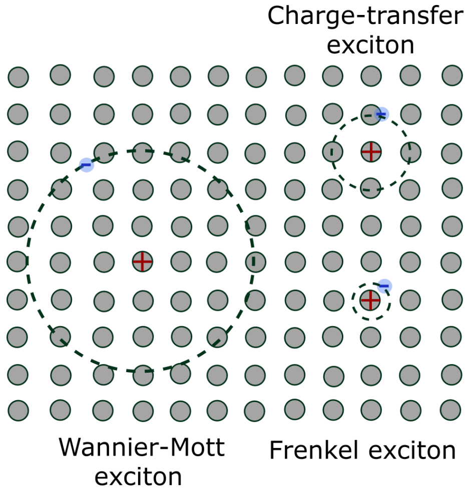

Figure 2.8: Schematic depiction of the different types of excitons. Interaction radius for the Wannier-Mott excitons is much larger than the lattice constant while it is smaller than the lattice constant for the Frenkel exciton. For the charge transfer (CT) exciton the interaction radius is comparable to the lattice constant.

2.5 Transport properties in organic semiconductors

2.5.1 Exciton transport

Excitons are neutral quasi-particles, which implies that they can't be subjected to drift motion in the presence of an electric field. Instead, they undergo diffusive motion in a random-walk manner where the length of diffusion is given as [34]:

$$L_d = \sqrt{D\tau} \tag{2.11}$$

D is the diffusion constant, and τ is the lifetime of the exciton. The excitation energy transfer from one chromophore unit to the next within the finite lifetime of the exciton can take place coherently or incoherently. Coherent energy transfer is limited to perfect molecular crystals where Frenkel excitons move in a wave-like manner. Since polymers semiconductors are far from being ordered, the coherent energy transfer is not a dominant mechanism and will not be discussed further. For a detailed treatment of coherent energy transfer, the reader is referred to [35]. In disordered polymer semiconductors, excitation energy transfer mainly happens incoherently. The dominant mechanisms are non-radiative and depend on the quantum-chemical coupling interaction between the donor and acceptor chromophores of the molecule.

$$\mathrm{D}^* + \mathrm{A} \xrightarrow{\text{coupling interaction}} \mathrm{D} + \mathrm{A}^*$$

If the coupling originates from electromagnetic dipole-dipole interaction the energy transfer process is known as **Förster resonant energy transfer** (FRET) and if the coupling is of the exchange type the energy transfer process is known as **Dexter transfer** [36, 37] [see Figure 2.9]. The energy transfer rate for the Förster type process is directly proportional to the transition dipole moment of the donor (μ_D) and the acceptor (μ_A) and falls off with the sixth power of the donor-acceptor distance [20, 34]:

$$k_{ET} \propto \frac{|\mu_D|^2|\mu_A|^2}{R^6}\kappa^2 \tag{2.12}$$

μ_D and μ_A are the transition dipole moments of the donor and the acceptor respectively, R is the donor-acceptor separation, and κ is a geometric factor related to the relative orientation of the transition dipoles. While for Dexter transfer, the energy transfer rate falls off exponentially with the donor-acceptor separation [37, 38]:

$$k_{ET} \propto e^{\frac{-2R}{L}} J \tag{2.13}$$

where J is the spectral overlap integral. As evident from the energy transfer rates, Dexter transfer is a relatively short-range interaction while Förster transfer is a longer-range interaction. Typically for donor-acceptor distances greater than 1 nm, the Förster mechanism is dominant. Also in FRET, the resonance exchange conserves the spin, and it is mostly observed for singlet states. This is because the ground state of the chromophore is usually of singlet type while Dexter transfer requires wavefunction overlap between the initial and final states and is usually observed for triplet-triplet type transfer.

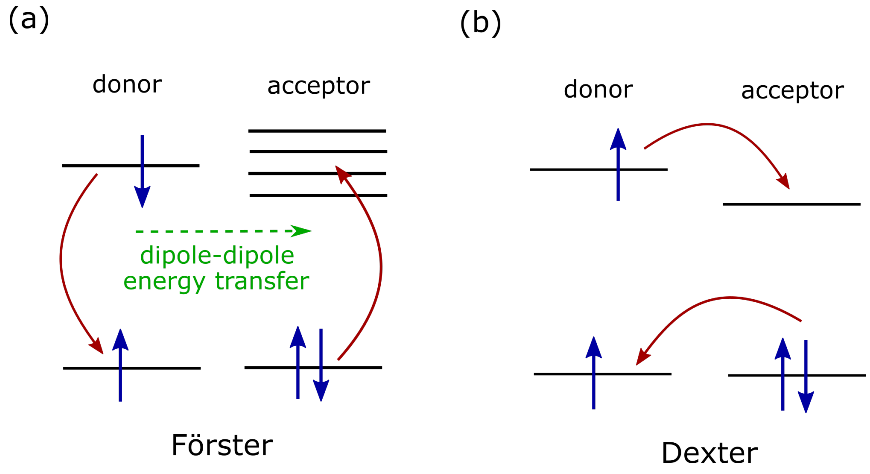

Figure 2.9: Schematic depiction of resonant energy transfer processes.(a)Förster energy transfer mediated by coulombic coupling and (b)Dexter transfer mediated via exchange type of coupling.

2.5.2 Charge Transport in organic semiconductors

The charge transport mechanism in organic semiconductors is primarily dictated by three factors [39]:

- electronic coupling between neighboring chromophores or sites ($\mathbf{J}_{elec.}$) ,
- coupling of electronic motion with intra- and inter-molecular vibrations i.e. the electron-phonon coupling ($\mathbf{J}_{phonon}$)
- static disorder resulting in the distribution of site energies and inter-molecular spacing ($\delta\epsilon$)

where the different J values represent the transfer integral values quantifying overlap of the respective wavefunctions. If the inter-site electronic coupling is much stronger than electron-phonon coupling ($\mathrm{J}_{elec.} \gg \mathrm{J}_{phonon}$) it results in '*band transport*' of charge carriers. For organic semiconductors, band transport is usually only observed in case of single crystals at low temperatures (T $\ll$ 300 K)[40, 41]. In this case, the charge carrier mobility (μ) decreases with temperature and follows an empirical relationship of the form ($\mu \propto T^{-n}$) where 1<n<3. The mobility decreases as the scattering of the coherent charge wave by phonons becomes more probable at higher temperatures. In the case when electron-phonon coupling is strong compared to the electronic coupling between neighboring chromophores ($\mathrm{J}_{phonon} \gg \mathrm{J}_{elec.}$), as for molecular crystals it results in '*polaronic transport*'. The theory of polaron transport was mainly developed by Austin and Mott [31]. Also, a pioneering model describing the hopping transport of polarons was developed by Holstein [42], according to his model the hopping rate of polarons is given as :

$$k_{ET} = \frac{J^2}{\hbar}\sqrt{\frac{\pi}{2E_{pol}k_BT}}exp\left(-\frac{E_{pol}}{2kT}\right) \tag{2.14}$$

where J is the transfer integral and E$_{pol}$ is the polaron binding energy. The key takeway message of the model is that the activation energy for the hopping process is half the polaron binding energy (E$_{pol}$/2). Using the hopping rate, mobility values can be estimated by using the Einstein relation (μ =eD/kT) where D is the diffusivity and k_BT is the thermal energy. The mobility of charge carriers in a polaron hopping model is given as :

$$\mu = \frac{ea^2J^2}{6\hbar(kT)^{\frac{3}{2}}}\sqrt{\frac{\pi}{2E_{pol}}}exp\left(-\frac{E_{pol}}{2k_BT}\right) \tag{2.15}$$

at moderate temperature Arrhenius-type relation is obeyed but at higher temperatures (E$_{pol}$/2kT≪1) the pre-exponential dependence (T$^{-\frac{3}{2}}$) takes over.

Although the band and polaronic transport models describe the charge transport of ordered molecular crystals very well, in reality, most of the organic semiconductors, particularly polymers are intrinsically disordered systems. So the effects of static disorder ($\delta\epsilon$) have to be taken into account when describing the charge transport properties. One of the implications of the static disorder is that the energies of chromophores (sites) and the inter-molecular spacing follow a distribution. The distribution of site energies arises from varying Van der Waals interactions between neighboring molecules as the orientation of molecules and spacing between them varies. Statistically, for an ensemble of chromophores or sites, the varying interactions result in a Gaussian envelope of energies according to the central limit theorem. The theory of charge transport in amorphous systems assuming the Gaussian distribution is known as the Gaussian disorder model (GDM) or the Bässler model as it was pioneered by the physicist Heinz Bässler [43]. The density of energetic states according to the gaussian disorder model is given as :

$$g(\epsilon) = \left(\frac{1}{\sqrt{2\pi}\sigma}\right) exp\left(-\frac{(\epsilon-\epsilon_0)^2}{2\sigma^2}\right) \tag{2.16}$$

where ϵ_0 is the mean energy value, and σ is the standard deviation, also known as the 'disorder parameter'. σ gives an estimate of the spread of the distribution of the density of states (DOS). The gaussian disorder model, neglects the energetic correlation between neighboring sites. In reality, the effects of correlation are important as the polarization of one molecule affects the neighboring molecules. Subsequently, a model named correlated disorder model (CDM) was developed which takes these effects into consideration [44].

As the charges are localized due to the static disorder, they incoherently hop from one site to another in a random walk manner. Hopping between two sites i and j is then described by the evolution of the probabilities of sites i (p$_i$) and j (p$_j$) being occupied [20]:

$$\frac{dp_i}{dt} = \sum_i[-w_{ij}p_i(1-p_j) + w_{ji}p_j(1-p_i)] \tag{2.17}$$

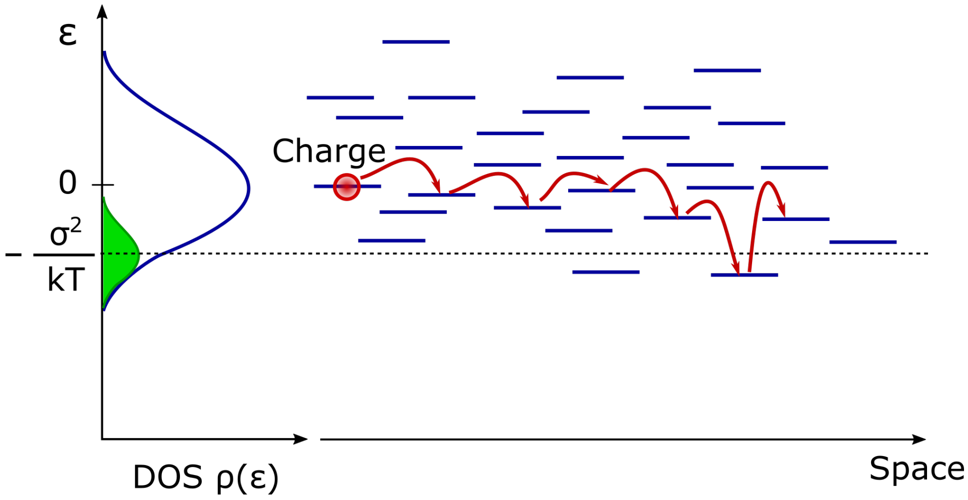

Figure 2.10: Schematic depiction of hopping transport within the gaussian density of states (DOS). The green region represents the occupied DOS and the dashed line is the quasi-equilibrium energy which charge carriers occupy in the long-time limit.

where p$_i$ and p$_j$ are the time-dependent probabilities that the site i or j are occupied. While w$_{ij}$ and the w$_{ji}$ are the hopping rates from a site i to j and site j to i respectively. Within the gaussian disorder model, because of the energetic variation of the sites, the sites i and j will most likely not be iso-energetic and the hopping rate for uphill and downhill transitions will vary. The hopping rates for this asymmetric case is given according to the Miller-Abrahams (MA) model [45] :

$$w_{ij} = \nu_0 exp(-2\gamma r_{ij}) x \begin{cases} exp\left(-\frac{\epsilon_j - \epsilon_i}{kT}\right), & \epsilon_j > \epsilon_i \\ 1, & \epsilon_j \leq \epsilon_i \end{cases} \tag{2.18}$$

where ν_0 is the attempt-to-hop frequency, ϵ_i and ϵ_j are the energies of the site i and j respectively, and γ is the localization radius of the electron wavefunction. According to the above equation for an uphill transition an activation energy is required in the form of the Boltzmann factor while for the downhill hopping rate the Boltzmann factor is unity and the excess energy is dissipated into phonons. It is worth noting that this model does not take into account the reorganization energy of the molecule/chromophore when it acquires a charge. Transition rates derived from Marcus theory can be used to include the effects of molecular reorganization. Considering the charge at a random energetic position it preferentially hops downwards initially but at long times the downhill and the uphill hops create a dynamic equilibrium where the charges rest at the energy ϵ_∞ within the DOS, where ϵ_∞ is given as :

$$\epsilon_\infty = \epsilon_0 - \frac{\sigma^2}{kT} \tag{2.19}$$

Another useful concept in GDM is the *effective transport energy*, which is very similar to the concept of a mobility edge in amorphous inorganic semiconductors. It defines the energy threshold from which multiple hopping events are possible for charge transport and lies between ϵ_0 and ϵ_∞. A peculiar thing of the GDM is that the mobility varies as exp(-1/T^2) instead of the classical thermal activation form: exp(-1/T)[46]. Field dependence of mobility is of the Poole-Frenkel type ($\ln\mu \propto \sqrt{F}$).

2.6 Working principle of organic photovoltaics

The function of every solar cell is based on the conversion of solar photons into electrical charge carriers. Usually, a semiconductor layer is employed in which the energy of the absorbed photon leads to the formation of free electron-hole pairs. In this regard, organic semiconductors are exceptional as the absorption of photons does not lead to the formation of free electron-hole pairs but creates a strongly bound electron-hole pair i.e., the exciton. Due to the low dielectric constant of organic semiconductors the binding energy (E_B) of the exciton is orders of magnitude higher than the thermal energy (k_BT) at room temperature, and additional processes are required to dissociate the exciton. One approach to circumvent this issue is to employ a heterojunction of an electron-donating (D) and an electron-accepting material (A) where excitons can undergo the dissociation process at the interface (see Figure 2.11). Initially, planar heterojunctions were employed, but the efficiencies of devices suffered due to the limited exciton diffusion length [47]. Later the concept of the bulk-heterojunction (BHJ) was evoked where the spatial dimension of donor and acceptor domains is on the order of exciton diffusion lengths [48].

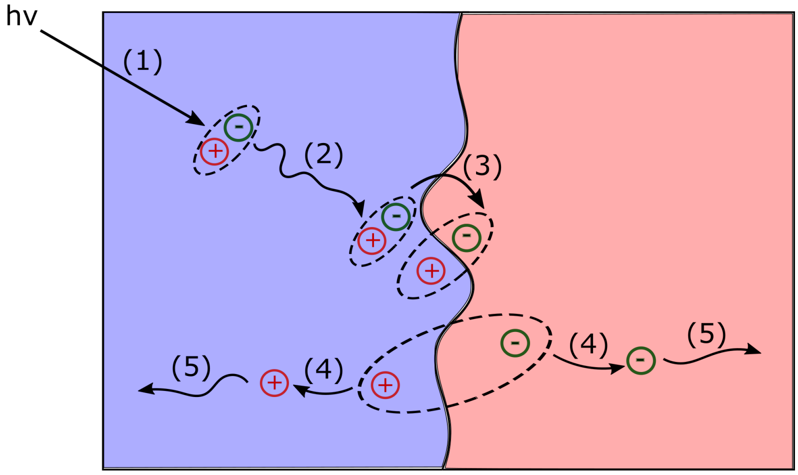

Figure 2.11: Schematic depicting the various processes involved in the generation of charge carriers at the heterojunction interface between donor (blue) and the acceptor (red) phase.

Whether planar or bulk-heterojunction, the charge generation process in the organic photovoltaics can be summed up into the following steps:
Step 1 - Photon absorption: Photons of energy higher than the optical gap are absorbed by the donor and the acceptor molecules, which leads to the formation of tightly bound Frenkel excitons. The absorption strength of the molecules limits this step. Also, as the typical active layer thicknesses are of the order of the wavelength of the sunlight, interference effects are in play. Appropriate placement of the active

layer in the electro-optical field within the stack is essential to enhance the photon absorption process.

$$\mathrm{D} + \mathrm{h}\nu \rightleftharpoons \mathrm{D}^*$$

Step 2 - Exciton Diffusion: The Frenkel exciton undergoes diffusion through incoherent energy transfer processes. As a competing process, the exciton can radiatively or non-radiatively recombine and relax back to the ground state. The diffusion length (L_d) of the excitons depends on the diffusivity (D) and the lifetime (τ) : $L_d = \sqrt{D\tau}$. In polymer semiconductors, the exciton diffusion lengths are typically in the range of 10-15 nm [49, 50]. Higher diffusion lengths are desirable as it increases the chance that the exciton encounters a heterojunction interface.

$$\mathrm{D}_l^* + \mathrm{D}_k \xrightarrow[\text{interaction}]{\text{coupling}} \mathrm{D}_l + \mathrm{D}_k^*$$

Step 3 - Charge transfer step: Once the Frenkel excitons encounter the heterojunction interface, the electron (hole) is transferred to the acceptor (donor) molecule. Conventionally, the difference between the electron affinities (Δ EA) and ionization potential (Δ IP) of the donor and the acceptor is considered to be the driving force for electron and hole transfer respectively. But recent work has pointed out that such driving force might not be necessary for efficient charge transfer [51, 52]. Nevertheless, this photo-induced electron (hole) transfer step is a very efficient process and occurs on ultrafast time scales (45 to several hundred femtoseconds).

$$\mathrm{D}^* + \mathrm{A} \longrightarrow \mathrm{D} + \mathrm{A}^*(\mathrm{D}^+\mathrm{A}^-)$$

Step 4 - Dissociation of charge transfer exciton: Even after the electron transfer process the electron-hole pair remains coulombically bound and leads to the formation of the “charge-transfer” (CT) exciton. CT-excitons are spatially more delocalized and have lower binding energy compared to the Frenkel excitons. Within it’s finite lifetime a CT-exciton either undergoes the dissociation process or recombines. The mechanism of the dissociation step is a topic of debate in the community, and various schools of thought have been developed to explain the dissociation process [53, 54]. This will be discussed in more detail in the subsequent sections. The recombination of the CT-excitons is referred to as *‘geminate’* recombination process.

$$(\mathrm{D}^+\mathrm{A}^-) \rightleftharpoons \mathrm{D}^+ + \mathrm{A}^-$$

Step 5 - Charge transport and collection: Once the CT-excitons dissociate, free electrons and holes are created. The separated electron and holes drift under the influence of the applied electric field and are collected at the electrodes. During charge transport, electron and hole can encounter each other at the interface and recombine nongeminately. The overall charge collection efficiency is determined by the balance between transport and recombination of carriers. Additionally, the selectivity of electrodes is also crucial for efficient charge collection. This can be tuned by manipulating the energetics of the electrodes using electron and hole transport interlayers (ETL/HTL).

2.6.1 j-V characteristics and the power conversion efficiency (PCE)

In darkness, the organic solar cell essentially behaves like a diode and shows a rectifying behavior. The current-voltage relationship can be expressed using the well-known Shockley equation which predicts an exponential dependence of the current density (j) with applied forward bias [55]:

$$j = j_0 \left[exp\left(\frac{qV}{\eta k_B T} \right) - 1 \right] \tag{2.20}$$

where j_0 is the reverse bias saturation current, V is the applied voltage and η is the diode ideality factor. The value of η is representative of the dominant charge recombination mechanism in the device [56].
Under illumination, photocurrent is generated and the entire j-V curves shifts into the fourth quadrant [see Figure 2.12]. The current flowing through the cell under illumination is given as :

$$j_l = j_0 \left[exp\left(\frac{qV}{\eta k_B T} \right) - 1 \right] - j_{ph} \tag{2.21}$$

where j_{ph} is the photo-generated current through the process cycle elaborated in the previous section.

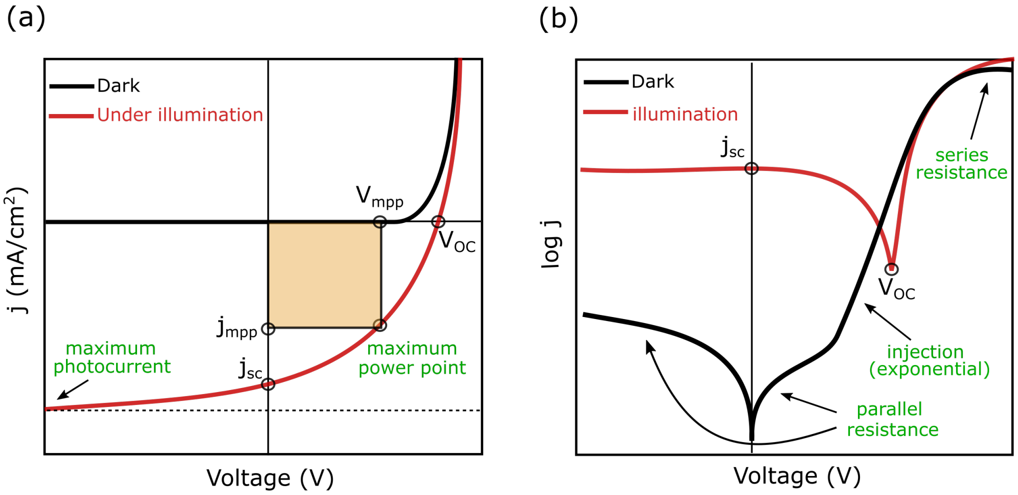

Figure 2.12: (a) Schematic depiction of j-V characteristics for a typical organic solar cell under dark and illuminated conditions.(b) j-V characteristics on a semi-log scale. This representation is helpful as it allows for the analysis of parasitic resistances and inspection of proper injection conditions for the cell.

The efficiency of the solar cell mainly depends on three parameters viz. short-circuit current density (j_{sc}), the open-circuit voltage (V_{OC}) and the fill-factor (FF). j_{sc} is the current flowing through the device under illumination when no voltage is applied. At short-circuit, the photo-generated charge carriers drift under the influence of an internal electric field. V_{OC} is the voltage at which no current flow through this device. Here the recombination current equals the photo-generated current. A more thorough overview of the V_{OC} will be discussed in the following section. The fill-factor of the device is defined as the ratio of the maximum power output to the product of the j_{sc} and the V_{OC} :

$$FF = \frac{j_{mpp}V_{mpp}}{j_{sc}V_{OC}} \tag{2.22}$$

where j_{mpp} and V_{mpp} is the current density and the voltage at the maximum power point (mpp). Intuitively, the FF represents the degree of 'squareness' of the j-V curve. FF is quite an elaborate quantity and depends on the complex interplay between the field-dependence of the photocurrent, charge transport and charge recombination properties.

The power conversion efficiency (PCE) is the most important metric for solar cells and is defined as the ratio of maximum power output (P_{max}) to the incident radiant power (P_{in}).

$$PCE = \frac{P_{max}}{P_{in}} = \frac{j_{mpp}V_{mpp}}{P_{in}} = \frac{j_{sc}V_{OC}FF}{P_{in}} \tag{2.23}$$

As can be seen from the above equation j_{sc}, V_{OC} and FF dictate the PCE of the solar cell. A more comprehensive description of these quantities from the device physics point of view will be discussed in the subsequent sections.

Considering the Shockley model, Equation 2.22 describes the j-V curves for ideal solar cells, but under real operating conditions, parasitic resistances come into play. Namely, the series resistance (R_s), which represents the contact resistance at the interfaces and the bulk 'sheet' resistance of the organic semiconductor film. While parallel resistance (R_p) represents the alternative current pathways i.e., the local shunts in the device. Considering these two parasitic resistances, the above equation modifies to :

$$j_l = j_0\, exp\left(\frac{q(V - jR_s)}{\eta kT} - 1\right) - \frac{V - jR_s}{R_p} - j_{ph} \tag{2.24}$$

The equivalent circuit diagram for the analytical model involving parasitic resistances is shown below:

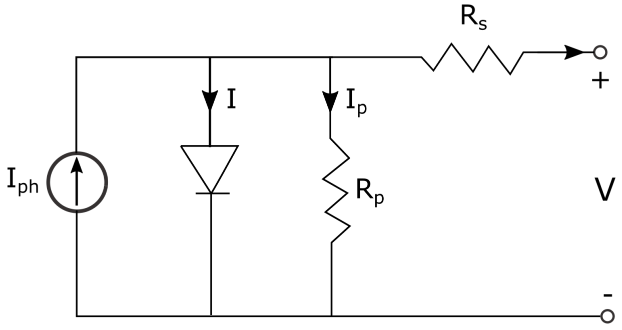

Figure 2.13: Equivalent circuit diagram for the analytical model of a solar cell.

Equation 2.25 is widely used to analytically fit the experimental j-V curves for organic solar cells. But the expression has some underlying assumptions which are particularly not applicable in case of organic photovoltaics. Firstly, it assumes that the photo-generated current is field independent, which is generally not valid in case of organic solar cells [57, 58]. This is mainly because the dissociation of the CT-excitons is a field dependent process as elaborated by the Braun-Onsager formalism [59]. Secondly, the Shockley equation was derived to explain the behavior of pn-junctions of highly conductive inorganic semiconductors while it is well known that the conductivity of the organic semiconductors is orders of magnitude lower than their inorganic counterparts.

Taking these arguments into consideration, recently, two analytical models were developed to explain the j-V curves of organic solar cells. Würfel et al., [60] suggested that due to the poor conductivity of organic semiconductors, there is a significant charge accumulation within the device. As a result, the splitting of the quasi Fermi levels within the active layer varies significantly compared to the externally applied voltage (V_{ext}). They invoke the concept of internal voltage (V_{int}) within the device which is related to the external voltage (V_{ext}) according to:

$$V_{ext} = V_{int} + \frac{d}{\sigma} J \tag{2.25}$$

where d is the active layer thickness, σ is the electrical conductivity and J is the total current density. The value of σ depends on the transport properties and the internal voltage itself and is given by:

$$\sigma = 2q\mu_{eff} n_i exp\left(\frac{qV_{int}}{2k_B T}\right) \tag{2.26}$$

where $\mu_{eff} = \sqrt{\mu_e \mu_h}$ is the effective mobility and n_i is the intrinsic carrier concentration. According to their model, the total current density (J) is related to the internal voltage (V_{int}) according to :

$$J = J_{rec} - J_{ph} = J_0 \left(exp\left(\frac{qV_{int}}{k_B T}\right) - 1\right) - J_{ph} \tag{2.27}$$

Using this formalism, Würfel et al., were able to fit simulated j-V curves obtained from 1-D drift-diffusion simulations over a wide range of charge carrier mobility and illumination intensities. Another model developed by Bartesaghi et al., introduces the dimensionless parameter θ [61]:

$$\theta = \frac{k_2 G d^4}{\mu_e \mu_h (V_i)^2} \propto \frac{J_{rec}}{J_{extr}} \tag{2.28}$$

where k_2 is the second-order recombination coefficient, G is the generation rate, μ_e and μ_h is the electron and hole mobility respectively, J_{rec} is the recombination current and J_{extr} is the extracted current. As can be seen, θ relates to the ratio of recombination and extraction current, which determines the fill factor (FF) of solar cells. In fact, using this figure of merit they could relate θ values to the fill-factor (FF) of a variety of donor-acceptor combinations.

2.7 The concept of the charge transfer (CT) state and the open-circuit voltage (V_{OC}):

The fundamental operating principle of a bulk-heterojunction is based on an interface between electron-donating (D) and an electron-accepting (A) molecule. This interface leads to the creation of an interfacial electronic state which is referred to as the charge transfer (CT) state. Formally speaking, the CT state is coupled to the ground state and is therefore expected to exhibit absorption and emission properties [62]. Indeed, the existence of the charge transfer state has been verified by sensitive external quantum efficiency (EQE_{PV}) measurements to prove its absorbing character [63, 64] or through photo- or electroluminescence to prove its emissive nature [65, 66, 67]. Absorption and emission of these states is theoretically given on the basis of classical Marcus theory:

$$A(E) \propto \frac{1}{E} exp\left(-\frac{(E - E_{CT} - \lambda)^2}{4\lambda k_B T}\right) \tag{2.29}$$

$$N(E) \propto E exp\left(-\frac{(E - E_{CT} + \lambda)^2}{4\lambda k_B T}\right) \tag{2.30}$$

where E is the photon energy, A(E) and N(E) refer to CT state absorption and emission respectively, E_{CT} is the energy of the charge transfer state and λ is the reorganization energy. The energy of the charge transfer state is an important property of a donor-acceptor blend as it determines many parameters of the solar cells, including the V_{OC} as discussed below. Physically, the E_{CT} depends on the dielectric environment around the interface and the coulomb binding energy of the electron-hole pair. It was also found that the aggregation of molecules, for example, clustering of the fullerene molecules also influenced E_{CT} due to the delocalization of charges. Charge transfer (CT) states are important for solar cell because free charge carrier generation and free charge carrier recombination is mediated by them. More on the process of dissociation of the charge transfer state and recombination will be discussed in the subsequent section.

Having introduced the concept of CT states, we can now meaningfully delve into the formalism of open-circuit voltage (V_{OC}). Firstly, Kirchoff's law of radiation states that there is a reciprocity between absorption and emission under thermodynamic equilibrium conditions. This implies that the emission of thermal radiation of a gray body is equal to the emission of thermal radiation from a black-body at a similar temperature T multiplied by the absorptance of the gray body. The emission spectra of the black-body ($\phi_{BB}(E)$) depends on the temperature T and the photon energy (E) as has been derived by Max Planck in 1900

$$\phi_{BB} dE = \frac{2\pi}{c^2 h^3} \frac{E^2}{exp\left(\frac{E}{k_B T}\right) - 1} dE \tag{2.31}$$

where c is the speed of light and h is the Planck's constant. Secondly,Würfel generalized the Kirchoff's law of radiation for non-equilibrium conditions by introducing the concept of the chemical potential μ [68, 69]. Finally in 2007, Rau extended the Würfel's generalized law for photovoltaics and related *total emitted photon flux* (ϕ_{em}) and the *photovoltaic external quantum efficiency* (EQE_{PV}) via the black-body spectrum (ϕ_{BB}) [70]:

$$\phi_{em} = \int EQE_{PV}(E)\phi_{BB}(E)dE \left[exp\left(\frac{qV}{k_BT}\right) - 1\right] \tag{2.32}$$

According to Rau's formalism, the *total emitted photon flux* (ϕ_{em}) is caused by injected current density ($J_{em,0}$) under equilibrium conditions :

$$J_{em,0} = \phi_{em}.q \tag{2.33}$$

In reality not all injected carriers recombine radiatively, the injected carrier density that leads to emission of photons ($J_{em,0}$) is lower than the total injected carrier density (J_{em}). The quantum efficiency of electroluminescence (EQE_{EL}) is defined as the the number of emitted photons per injected charge carriers. EQE_{EL} depends on the number of non-radiative recombination events taking place within the cell. Taking into account the non-radiative recombination equation 2.34 can be expressed as:

$$\begin{aligned} J_{em}(V) &= \frac{1}{EQE_{EL}(V)} J_{em,0}(V) \\ &= \frac{q}{EQE_{EL}(V)} \phi_{em}(V) \\ &= \frac{q}{EQE_{EL}(V)} \int EQE_{PV}(E)\phi_{BB}(E)dE \left[exp\left(\frac{qV}{k_BT}\right) - 1\right] \\ &= J_0(V)\left[exp\left(\frac{qV}{k_BT}\right) - 1\right] \end{aligned} \tag{2.34}$$

where the *dark saturation current density* J_0(V) is equal to :

$$J_0(V) = \frac{q}{EQE_{EL}} \int EQE_{PV}(E)\phi_{BB}(E)dE \tag{2.35}$$

Looking at equation 2.22, an expression for V_{OC} can be derived when the total current flowing through the device is zero :

$$V_{OC} = \frac{k_BT}{q} ln\left(\frac{J_{ph}}{J_0(V)}\right) \tag{2.36}$$

where J_{ph} is the photocurrent generated under illumination. Assuming that there are no non-radiative losses (EQE_{EL}=1), the radiative limit of the open circuit voltage ($V_{OC,Rad-Lim}$) can be derived:

$$V_{OC,Rad-Lim} = \frac{k_BT}{q} ln\left(\frac{J_{ph}}{q\int EQE_{PV}\phi_{BB}dE}\right) \tag{2.37}$$

The black-body radiation exponentially decreases with energy and only the lower energy portion of the EQE_{PV} contributes to the recombination current.

On the other hand in the presence of non-radiative losses ($EQE_{EL} < 1$) the V_{OC} can be expressed as :

$$V_{OC,measu.} = \frac{k_BT}{q} ln\left(\frac{J_{ph}}{q\int EQE_{PV}\phi_{BB}dE}\right) + \frac{k_BT}{q} ln(EQE_{EL}) \tag{2.38}$$

Equation 2.39 suggests that by carefully measuring the external quantum efficiency (EQE_{PV}) and the electroluminescence (EQE_{EL}) of the solar cell, V_{OC} can be determined. However, these equations do not provide a relationship between the effective band gap of donor-acceptor blend and the radiative losses. In 2010 Vandewal et al., derived an expression for the V_{OC} relating the CT-state energy (E_{CT}) and the radiative and non-radiative recombination losses [71]. In the study one of the key ideas was to express the CT-state absorption and emission in terms of Marcus-type Gaussian functions. Since the EQE_{PV} is related to the absorption of the cell, EQE_{PV} was expressed in terms of CT-state absorption as:

$$EQE_{PV}(E) = \frac{f}{E\sqrt{4\pi\lambda k_BT}} exp\left(\frac{-(E_{CT}+\lambda-E)^2}{4\lambda k_BT}\right) \tag{2.39}$$

where f is proportional to the CT state density and the electronic coupling between donor and acceptor units, E_{CT} is the CT state energy and λ is the reorganization energy. It is important to note that the line shape of the EQE_{PV} depends only on the E_{CT} and λ while f acts as a scaling factor when fitting the experimentally obtained EQE_{PV} using the above expression. Similarly, the emission rate of electroluminescence (EL) can be expressed in terms of the CT energy as :

$$EL = \frac{Ef_{EL}}{\sqrt{4\pi\lambda k_BT}} exp\left(\frac{-(E_{CT}-\lambda-E)^2}{4\lambda k_BT}\right) \tag{2.40}$$

where f_{EL} also relates to the electronic coupling between donor and acceptor units. By simultaneously fitting the EQE_{PV} and the EL spectra using equations 2.40 and 2.41, parameters such as f, f_{EL} , E_{CT} and λ can be deduced. Finally, Vandewal derived a formula for $J_0(V)$ by using the equation 2.36 and assuming that the EQE_{PV} for the CT-absorption is given according to the equation 2.40 and by approximating the black-body emission spectra for E $\gg k_BT$. In this way an analytical expression for V_{OC} was determined, directly relating the V_{OC} to radiative and non-radiative recombination losses:

$$V_{OC} = \frac{E_{CT}}{q} + \frac{k_BT}{q} ln\left(\frac{J_{ph}h^3c^2}{fq2\pi(E_{CT}-\lambda)}\right) + \frac{k_BT}{q} ln(EQE_{EL}) \tag{2.41}$$

This formula has some important implications, it not only defines the effective band gap of the donor-acceptor blend to be E_{CT}. But also suggests that the radiative and non-radiative V_{OC} losses can be determined by measuring the EQE_{PV} and the EL of the device.

2.8 Charge carrier recombination

Once the free electron-hole pair is generated, they can drift towards to the electrodes or recombine *'non-geminately'*. The competition between the extraction and the recombination process largely determines the fill-factor of the solar cell. Thus, understanding the underlying mechanism of non-geminate recombination is pivotal in mitigating fill-factor losses. Generally speaking, the non-geminate recombination rate (R) can be expressed in terms of charge carrier concentration(n), recombination coefficient (k) and recombination order (δ):

$$R = -\frac{dn}{dt} = kn^{\delta} \tag{2.42}$$

If the recombination rate varies linearly with the carrier concentration, the process is said to be monomolecular. One of the common examples of the monomolecular recombination is the Shockley-Read-Hall process where trapped carriers assist in the recombination of freely moving carriers [72, 73]. The δ=2 process is referred to as bimolecular recombination. Higher-order recombination processes like Auger recombination ($\delta = 3$) are not commonly observed in organic solar cells as they require very high carrier densities which are unrealistic under normal illumination conditions. It is well established that the major recombination process in organic solar cells is bimolecular in nature [74, 75, 76].If the concentration of electrons and holes is assumed to be equal (n=p), as they arise from a mutual photoexcitation event, the bimolecular recombination rate (BMR) can be expressed as :

$$R_{BMR} = -\frac{dn}{dt} = k_2 n^2 \tag{2.43}$$

A very useful model which explains the bimolecular recombination process is the Langevin recombination model. Originally, Langevin used this model to explain the recombination of ions in gases [77]. The model assumes that every encounter between a hole and an electron leads to a recombination event and hence the process is encounter or transport limited. Thus, the recombination coefficient in Langevin's model is given as the sum of the hole (μ_h) and electron (μ_e) mobility:

$$k_{2,Langevin} = \frac{q}{\epsilon\epsilon_0}(\mu_e + \mu_h) \tag{2.44}$$

where q is the elementary charge and ϵ_0 is the relative permittivity of the medium. Despite its wide acceptance and moderate success, the model usually overpredicts the recombination rates in solar cells. The experimentally obtained recombination rates are three to four orders of magnitude lower than that predicted by the model [78, 79]. This can be due to the fact that the sum of the electron and hole mobility gives a higher encounter probability than in reality or every encounter does not lead to a recombination event. The later of the two hypotheses was taken into account by a model by Burke et.al. where they consider the equilibrium between the population of charge transfer (CT) states and charge separated (CS$_{eq}$) states [80]. According to their model, the CT state can split multiple times before the final recombination event happens. Additionally, they were also able to establish a relationship between the recombination current (J_{rec}) at open-circuit and the CT-state energy, implying that the recombination between electrons and holes is bimolecular in nature and is always mediated via the CT state. According to the model of Burke et al., the recombination current is given as:

$$J_{rec} = \frac{qn_{CT}d}{\tau_{CT}} = \frac{qN_{CT}d}{\tau_{CT}} exp\left(-\frac{E_{CT} - \frac{\sigma^2}{2k_BT} - qV_{OC}}{k_BT}\right) \tag{2.45}$$

where d is the active layer thickness, n_{CT} is the number of populated CT states, N_{CT} is the total number of CT states, τ_{CT} is the average lifetime of the CT states and σ is the width of the energetic distribution of the CT states. It is important to notice that the recombination current does not depend on the total carrier density (n) but only the density of CT state population. Figure 2.14 depicts the schematic showing the equilibrium between the CT and CS_{eq} states and also the recombination of the CT states to the ground state, with the rate k_{ct}. Under equilibrium conditions, the carrier density in the CT states and the free carriers in equilibrium with the CT states is related via k_s: the rate of splitting of the CT states and k_m: the rate coefficient for the formation of CT states, according to:

$$k_s n_{CT} = k_m n_{free} p_{free} = k_m np = k_m n^2 \tag{2.46}$$

In the limit where n$_{free}$ $= p_{free} = n = p$, the recombination coefficient k_m can be replaced by k_2-the bimolecular recombination coefficient. Also, when $k_{ct} \gg k_s$ Langevin model becomes valid and the reduction prefactor approaches unity.

Figure 2.14 (a) depicts two categories of charge-separated (CS) states. Due to the energetic distribution arising from varying morphology, a few CS states lie above the quasi-Fermi level ($E_{F,e}$ for electrons and $E_{F,h}$ for holes) which are in equilibrium with the CT states while some other CS states (CS_{non-eq}) lie below the quasi-Fermi level and can be considered as trapped carriers (electrons). It is important to note that only CS_{eq} states contribute to the recombination current and effect the V_{OC}. When measuring recombination using charge extraction measurements, both free and trapped carriers are extracted. This leads to the overestimation of carrier concentration and thus the underestimation of the recombination coefficient ($k_2(n)$).Here the model invokes the effective recombination coefficient ($k_{2,eff}$) which only takes into account the recombination of free carriers which are in equilibrium with the CT states. An effective way of deducing whether the recombination coefficient (k) is affected by trapped carriers or not, is to measure its carrier concentration dependence. If the value of the recombination coefficient is independent of carrier concentration, then it can be assumed to be free from the effect of trapped carriers.

Figure 2.14 (b) depicts the density of states (DOS) distribution for electron and holes. For simplicity, an exponential DOS is assumed for both the carriers, but it can very well be replaced by the Gaussian DOS. For both electrons and holes, the majority of carriers lie below their respective quasi-Fermi level, explicitly depicting the case of 'trapped' electrons. The green Gaussian distribution is for the CS_{eq} carriers which are in equilibrium with the CT states and have a total concentration of n_{eq}. The schematic depicted here is obviously only one of the many possible configurations which can arise from the complexity of the morphology and molecular orbital interactions. But to first order, it explains the apparently high recombination

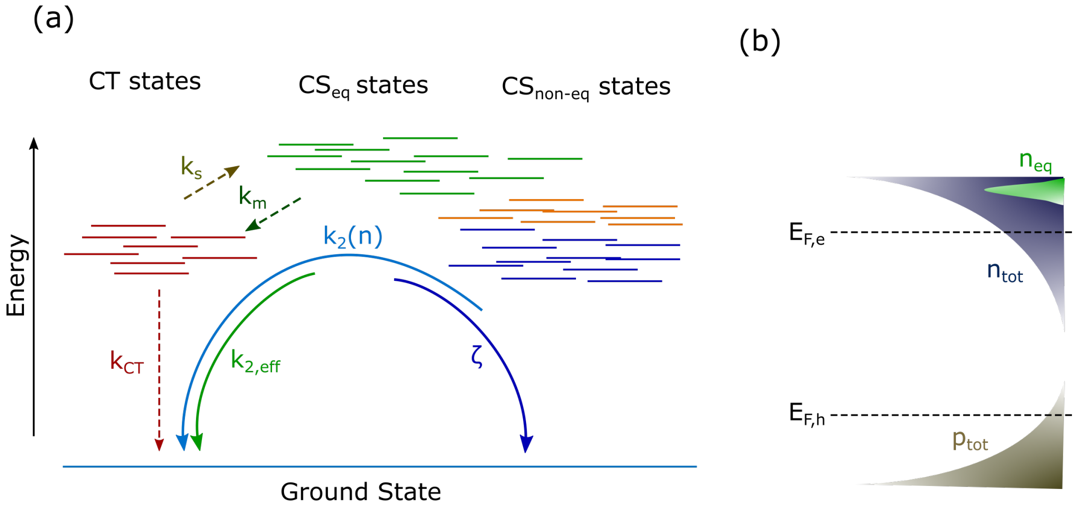

Figure 2.14: (a) Schematic depiction of the recombination model adapted from Burke et al., showing the equilibrium between the CT states and CS_{eq} states with the rates k_s and k_m representing the splitting and formation of the CT states respectively. Also shown is the recombination of CT states to the ground state with the rate coefficient k_{CT}. Charge carriers which are not in equilibrium with the CT states are denoted as the CS_{non-eq} states. Some of these states lie below the quasi-Fermi level (trapped) shown in deep blue while some lie above the quasi-Fermi level shown in orange. The recombination coefficient for free charge carriers is given by $k_{2,eff}$ while the recombination coefficient, which also takes into account the trapped carriers is given as $k_2(n)$. The dark blue arrow represents recombination via higher order processes for instance in presence of traps, represented by coefficient ζ (b) Exponential density of states (DOS) for electrons (top) with total concentration n_{tot} and DOS for holes (bottom) with total hole concentration p_{tot}. The green Gaussian distribution reflects the concentration of the charge carriers in equilibrium with the CT states. This scheme represents the case for trapped electrons but a similar representation for trapped holes or both trapped electrons and holes is valid. Figure adapted from [81].

orders obtained from charge extraction measurements, the origin of which lies in the trapped carriers in the tail of the DOS.

The effect of the trapped carriers in the tail of the DOS can be further elucidated if we consider the recombination current. If measured under open-circuit conditions by, e.g., a charge extraction measurement, the recombination rate and generate rate are equal to satisfy the zero net current condition. Furthermore, the generation rate can be expressed as the generation current divided by the active layer thickness (d) and the elementary charge (q). Considering these arguments, the recombination current at V_{OC} can be given as:

$$J_{rec} = J_G = qdkn^{\delta} \tag{2.47}$$

Also, according to the classical semiconductor theory, the product of electron and hole concentration is given by Fermi-Dirac statistics according to:

$$\begin{aligned} np &= N_e N_h exp\left(-\frac{E_C - E_V}{k_B T}\right) exp\left(\frac{E_{F,e} - E_{F,h}}{k_B T}\right) \\ &= N_e N_h exp\left(-\frac{E_G}{k_B T}\right) exp\left(\frac{E_{F,e} - E_{F,h}}{k_B T}\right) \\ &= n_i^2 exp\left(\frac{E_{F,e} - E_{F,h}}{k_B T}\right) \\ &= n_i^2 exp\left(\frac{qV_{OC}}{k_B T}\right) \end{aligned} \tag{2.48}$$

where $N_{e,h}$ are the effective density of states for electrons and holes, $E_{F,e}$ and $E_{F,h}$ are the quasi-Fermi levels for electrons and holes respectively, E_G is the band gap between conduction band edge (E_C) and the valence band edge (E_V) and n_i is the intrinsic carrier concentration. According to the equation 2.49 the carrier concentration (n) can be expressed as the function of V_{OC} for the condition n=p as:

$$n = n_i exp\left(\frac{qV_{OC}}{2k_B T}\right) \tag{2.49}$$

For exponential distribution of tails states with slope $E_U = k_B T_0$ and with the ratio $m = \frac{T}{T_0}$ the above equation can be written as :

$$\begin{aligned} n &= n_i exp\left(\frac{qV_{OC}}{2mk_B T}\right) \\ &= n_i exp(\zeta V_{OC}) \end{aligned} \tag{2.50}$$

where $\zeta = \frac{q}{2mk_B T}$ as has also been derived by Kirchartz et al. By substituting this expression of charge carrier concentration into equation 2.48 we get a general expression for the recombination current as function of the V_{OC}:

$$\begin{aligned} J_{rec} &= qdkn^{\delta} \\ &= qdkn_i^{\delta} exp\left(\frac{qV_{OC}.\delta}{2mk_B T}\right) \\ &= J_0 exp\left(\frac{qV_{OC}.\delta}{2mk_B T}\right) \\ &= J_0 exp\left(\delta\zeta.V_{OC}\right) \\ &= J_0 exp\left(\frac{qV_{OC}}{n_{id} k_B T}\right) \end{aligned} \tag{2.51}$$

where J_0 is the dark generation current density and n_{id} is the ideality factor. From the above expression it can be concluded that the ideality factor (n_{id}) depends on the recombination order (δ) and the disorder parameter m:

$$n_{id} = \frac{2m}{\delta} = \frac{q}{\delta\zeta k_B T} \tag{2.52}$$

For the bimolecular recombination where the distribution of charges is given according to the Boltzmann approximation (m=1,$\delta = 2$) we get the ideality factor of unity. Alternatively, for electron and holes in an exponential density of states, considering the recombination of charge carriers with the trapped carriers in tail states, the ideality factor is found to be temperature dependent as was reported by Berkel et al. [82]:

$$n_{id} = \left(\frac{1}{2} + \frac{k_B T}{2E_U}\right)^{-1} = \left(\frac{1}{2} + \frac{T}{2T_0}\right)^{-1} \tag{2.53}$$

Thus, measuring the temperature dependence of the ideality factor is one of the ways to discern whether the trapped carriers are involved in the recombination process or not. A report by Tvinstedt [83], however, actually reported temperature independent ideality factor for a range of different organic solar cells and the value of ideality factor for most of the systems was close to 1 hinting at a bimolecular recombination mechanism. The underlying mechanism of the recombination process, higher recombination orders ($\delta > 2$)and the role of trapped charge carriers in the tail of the DOS are still heavily debated topics in the community [84, 85, 86].

Chapter 3

Experimental Methods

This chapter provides the details of the various experimental techniques used in this work. Section 3.1 outlines the device fabrication protocol in a detailed manner. In section 3.2, we discuss the standard device characterization methods viz. the current density-voltage (j-V) and the external quantum efficiency (EQE) measurements. Section 3.3 introduces the transient charge extraction techniques which were used to characterize recombination parameters of the devices.

Secition 3.4 and 3.5 provides the details about the electroluminescence (EL) and photoluminescence (PL) setups respectively. In section 3.6, we discuss the transient absorption (TA) spectroscopy set-up. A brief theoretical introduction about the spectroscopic technique is also provided. Section 3.7 provides details about the electromodulated differential absorption (EDA) spectroscopy. In section 3.8, we discuss the morphological characterization techniques viz. transmission electron microscopy (TEM) and grazing incidence wide angle x-ray scattering (GIWAXS).

3.1 Sample Preparation

Looking at the device architecture, polymer solar cells are essentially a series of vertically stacked layers sandwiched between two conductive contacts i.e. the electrodes. One of the electrodes needs to be optically transparent so that sunlight can penetrate through the stack and be absorbed by the active components of the bulk-heterojunction. Transparent conductive oxides (TCO's) namely indium tin oxide (ITO) or fluorine-doped tin oxide (FTO) are most commonly used. While metal contacts like aluminum (Al) or silver (Ag) are most often used as counter electrodes.

The bulk-heterojunction polymer solar cells can be fabricated in the so called 'conventional' or 'inverted' configuration [87].In conventional stacks, ITO serves as the anode while a low work function aluminum electrode is used for electron collection. On the the other hand, in an inverted configuration ITO is used as the cathode for electron collection and high work function metals like silver (Ag) or gold (Au) are used for hole collection. For most of the the work in this thesis, inverted configuration was used as it results in a more stable device and thus the device performance and other measurements can be performed reliably over an extended period of time.

The entire device fabrication process can be summarized in four steps :

(i) **Substrate cleaning**

Pre-patterned ITO glass slides are used as substrates for device fabrication [Fig 3.2]. The ITO layers are around 90nm thick with a sheet resistance of 30 Ω/sq. As a standard cleaning routine, ITO slides are sequentially ultrasonicated in Hellmanex (cleaning agent) solution, deionized water,acetone and iso-propanol for 7-10 minutes each.Subsequently, the wet ITO slides are dried using nitrogen or compressed air. The dried ITO slides are placed in the UV-ozone chamber for another 20 minutes to get rid of any organic residue.

(ii) **Deposition of electron/hole transport layer (ETL/HTL)**

Immediately after the UV-ozone treatment the electron or hole transport layer is spin-coated onto the cleaned ITO susbtrates. In this work, polyethylenimine ethoxylated (PEIE) or Zinc oxide (ZnO) layers are used as ETL's. PEIE solution is prepared by diluting a viscous PEIE gel (35-40 wt% in H_2O) in iso-propanol. The usual dilution ratio is 1:1000.The diluted PEIE solution is spin-coated onto ITO substrates at 3000rpm for 30 seconds. Then the films are annealed at 80° C for 5 minutes [88].

For ZnO films, a percursor solution is prepared by dissolving zinc acetate dihydrate ($Zn(CH_3COO)_2.2H_2O$,0.5 grams)and ethanolamine ($NH_2CH_2CH_2OH$, 0.14 grams) in 2-methoxyethanol($CH_3OCH_2CH_2OH$,5mL). The solution is stirred vigorously overnight. The ZnO precursor solution is spin-coated at 3000 rpm for 60 seconds. The films are annealed at 150° C for 15 minutes for the hydrolysis reaction in air. Subsequently, the hot plate is switched off and the films are left to cool down slowly to room temperature [89].

When fabricating devices with conventional architecture, PEDOT:PSS is spin-coated onto ITO substrates as the hole transport layer (HTL). Standard formulations for PEDOT:PSS are bought from Heraeus GmbH. The PEDOT:PSS solution is spin-coated at 4000rpm for 30 seconds and the films are annealed at 120° C for 15 minutes [90].

(iii) Spin-coating of the active layer

The active layer consisting of donor:acceptor blends is spin-coated on top of the ETL/HTL (Figure 3.1). The weight ratio of the donor and acceptor components, choice of solvent and the ink temperature is carefully optimized to yield the best device performance. For inks constituting DPP polymers the donor:acceptor ratio is 1:3 and chloroform is used as the solvent. For obtaining the optimum film thickness $\sim$ 200 nm, the films were spin-coated in the range of 2000 to 3000 rpm. For blends constituting the non-fullerene aceptors the donor:acceptor ratio is usually kept around 1:1 and chlorobenzene is used as the solvent. The films were spin-coated in the 1500-3000 rpm range to obtain the optimal thickness for the active layers.

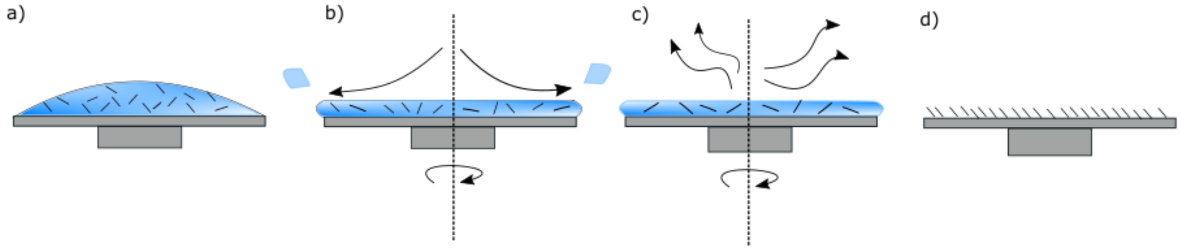

Figure 3.1: Different stages of the spin-coating process. a)Substrates are fully covered with the semiconductor ink. b)Formation of the wet layer soon after the rotation starts.c)Solvent evaporation during the spin-coating process. d)Formation of a completely dried thin film.

(iv) Thermal evaporation of the top electrode

Molybdenum oxide (MoO_3)which is used as the HTL and silver(Ag) contacts are deposited using thermal evaporation in a vacuum chamber. The materials are placed in the crucibles which are electrically heated. Above a certain threshold temperature the material sublimates with a specific evaporation rate. The evaporation rate is measured by a calibrated quartz crystal microbalance (QCM). The deposition rate depends on the temperature of the crucible and the distance between the crucible and the sample holder. For MoO_3 films the evaporation rate was kept between 0.1 to 0.2 $\mathring{A}$/s while for Ag films the evaporation rate was around 1 $\mathring{A}$/s. The pressure in the evaporation chamber is maintained between 10^{-6} and 10^{-7} mbar during the deposition process.

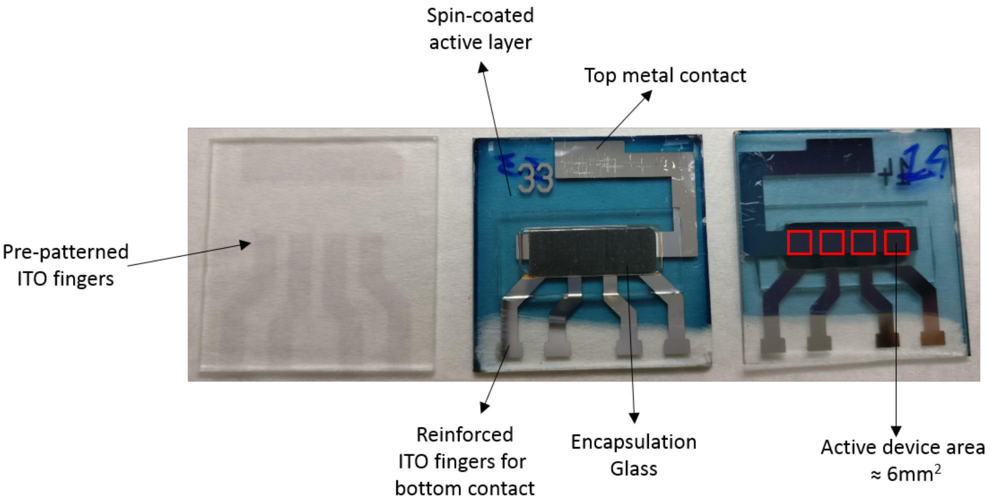

Figure 3.2: From left to right: Picture of the pre-patterned ITO coated glass substrate. Image of the device after complete device fabrication showing spin-coated active layers, electrodes and the encapsulation layer. Lastly, the rear side of the substrate depicting the active device area highlighted by square boxes outlined in the red.

3.2 Device Characterization

3.2.1 Current-Voltage Characteristics

Standard reporting conditions (SRC) as specified by the American society for Testing and Materials (ASTM) state the measurements to determine the power conversion efficiency (PCE) of photovoltaic devices to be conducted under following conditions: 1) standard spectral irradiance:AM1.5g 2) incident intensity of 100mW/cm^2 3)temperature: 25° C. All the j-V measurements were performed under SRC conditions using a fully automated IV-robot. Firstly, planar position of the reference diode (S1337-BQ,Hamamatsu) is optimized by adjusting the x and y position of the diode. This ensures that we obtain the maximum short circuit current density (j_{sc}) out of the diode. Once the diode position is optimized, the intensity of the solar simulator is adjusted according to the spectral mismatch factor (MM) obtained from the EQE measurements, so that we are at the correct j_{sc} value for the reference diode:

$$j_{sc,ref}(E_{AM1.5g}(\lambda)) = MM.j_{sc,ref}(E_{sim}(\lambda)) \tag{3.1}$$

After the intensity of the solar simulator is adjusted, all the measurements parameters (e.g.voltage sweep range,device area,illumination direction) are inserted into the program. On starting the measurement run, the IV-robot first optimizes the position of each pixel on the substrate for obtaining the maximum current. Then the contact head attached to a motorized stage contacts the electrodes to measure j-V characteristics. All the electrical measurements are done using a Keithley 2400 source-measure unit. The j-V characteristics viz. short-circuit current density (j_{sc}), open-circuit voltage(V_{OC}), fill-factor (FF) and power conversion efficiency (PCE) are calculated automatically by the program with the help of input parameters. As the measurements are done in air encapsulation of the samples was necessary to avoid device degradation.

3.2.2 External quantum efficiency (EQE)

The external quantum efficiency (EQE) of a solar cell is defined as the number of extracted electrons per incident photons. In the process upto collection of electrons, a number of physical processes are involved. Thus, the EQE value is the result of different processes, each with their own efficiency. The EQE is the product of all these quantum efficiencies:

$$\eta_{EQE} = \eta_{PA}{\cdot}\eta_{ED}{\cdot}\eta_{CT}{\cdot}\eta_{CD}{\cdot}\eta_{CP}{\cdot}\eta_{CC} \tag{3.2}$$

where the quantum efficiency of photo-absorption(PA), exciton diffusion(ED), charge transfer(CT), charge dissociation(CD), charge percolation(CP) and charge collection(CC) contribute to the overall external quantum efficiency.
In practice, what is measured is the spectral response (SR) of the device which is defined as the extracted current per incident power and is given in Amperes per Watt (A/W). The spectral response can be converted to the EQE value according to the relation [20]:

$$EQE(\lambda) = \frac{hc}{e\lambda} \cdot SR(\lambda) \tag{3.3}$$

The set-up [Figure 3.3] consists of a xenon arc lamp (Oriel Apex Illuminator, Newport, USA) which acts as the source for the white light. The light beam is sent through a monochromator (Cornerstone 260 1/4m,Newport, USA). The monochromatic beam passes through the fiber bundle into an optical chopper which creates a modulated light pulse with an usual chopping frequency of around 220Hz. This beam is then sent through the test device. The photocurrent response of the device is preamplified using a transimpedance amplifier and then measured using a lock-in amplifier (7265 DSP Signal Recovery, UK). The lock-in amplifier improves the signal to noise ratio as it measures the photocurrent at the chopping frequency. Signals and parasitic noise at other frequency or frequency distributions are filtered out.
As a first step, the spectral response of a calibrated reference diode is measured. This enables us to measure the spectral response of the test device using a lamp of unknown spectral irradiance by comparing the photocurrent of the test device with that of the reference diode. From the simple integration of the spectral response (SR) multiplied by the reference solar spectrum, the j_{sc} at AM1.5g can be calculated according to the relation:

$$j_{sc} = \int E_{AM1.5g}(\lambda) SR(\lambda) d\lambda \tag{3.4}$$

where $E_{AM1.5g}$ is the standard reference spectral irradiance given in (W/m^2 nm). j_{sc} values obtained from the EQE measurements can serve as the quality check for the j-V measurements. Ideally, j_{sc} values from j-V and EQE measurements should be within 10% of each other.

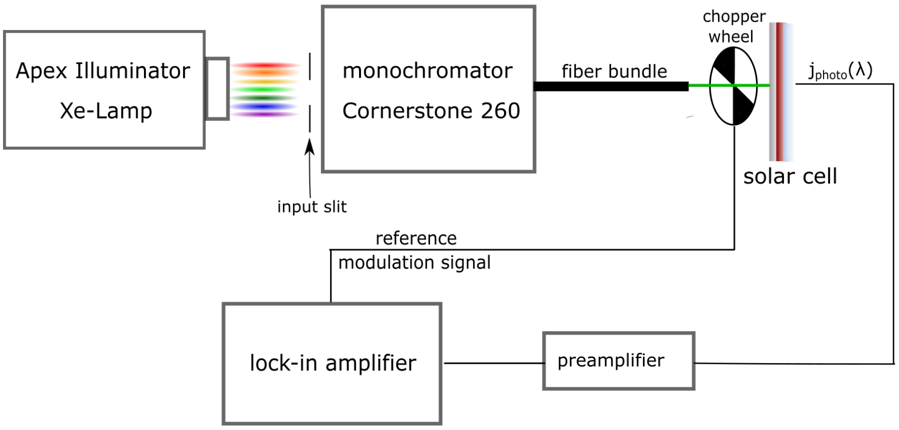

Figure 3.3: Schematic depicting various components of the EQE set-up used for measurements.

3.3 Transient charge extraction techniques

3.3.1 Time delayed collection Field (TDCF)

In recent years, time delayed collection field (TDCF) has been widely employed to study field-dependence of the photogeneration and recombination dynamics in organic solar cells [91, 92, 93]. TDCF is essentially a pump-probe measurement technique using an optical pump and an electrical probe. A pulsed laser system is used to photogenerate carriers in the cell which are then collected using a high reverse bias collection pulse (V_{coll}) after a certain delay time (t_{delay}). An important factor in TDCF is that the delay time needs to be sufficiently small (few tens of ns) so that all the photogenerated carriers are collected before the non-geminate processes can kick in . To study the effect of electric field on photogeneration, a pre-bias voltage (V_{pre}) is applied during the delay time. V_{pre} dictates the internal electric field within the photoactive layer :

$$F_{int} \approx \frac{V_{Bi} - V_{pre}}{L} \tag{3.5}$$

where V_{Bi} is the built-in potential and L is the thickness of the photoactive layer.The magnitude of internal field will affect the polaron-pair dissociation process and can drastically influence the amount of photogenerated carriers. A typical photocurrent transient signal exhibits a dual peak behavior as shown in Figure 3.4. The integral of the first peak of the photocurrent signal corresponds to the amount of total charge carriers collected during the application of the pre-bias voltage (V_{pre}) while the integral of the second peak correlates to the amount the charge carriers collected while application of the extraction pulse V_{coll}. Hence, the total amount of photogenerated carriers (Q_{tot}) can be given as:

$$Q_{tot} = Q_{pre} + Q_{coll} \tag{3.6}$$

where,

$$Q_{pre} = \int_0^{t_{delay}} I_{Ph}(t)dt \quad ; \quad Q_{coll} = \int_{t_{delay}}^{t_{extr}} I_{Ph}(t)dt \tag{3.7}$$

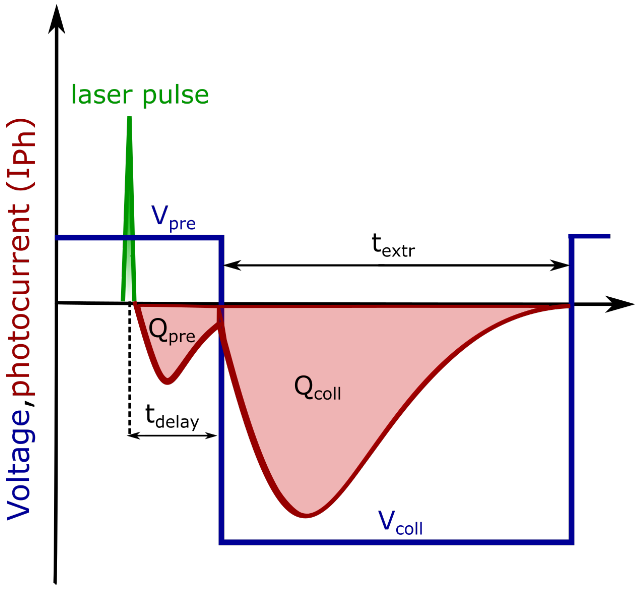

Figure 3.4: Schematic showing the voltage pulse and the photocurrent signal obtained in a typical TDCF experiment. During laser excitation,V_{pre} is applied which modifies the effective electric field within the device during the photogeneration process. After a certain delay time t_{delay} a collection pulseV_{coll} is applied. The first peak of the photocurrrent signal correlates with the photogenerated carriers collected during the delay time whereas the second peak amounts to the carriers collected during the application of V_{coll}.

In our experiments, devices were optically excited using the output of a diode-pumped, Q-switched Nd:YAG laser (NT242, EKSPLA, 500 Hz repetition rate, 3.8 ns pulse duration). To compensate for the internal latency of the pulse generator, the laser pulse was delayed and homogeneously scattered in a 85 m long silica fiber (LEONI). During optical excitation the device is held at a constant ‘pre-bias’ set by an Agilent 81150 A pulse generator through a homebuilt amplifier and then switched to a strong reverse bias ‘collection voltage’ after a delay time of 6 ns. The current through the device is measured via a grounded 10 Ω resistor in series with the sample and recorded with an Agilent DSO9104H oscilloscope. All the TDCF measurements were in Professor Dieter Neher’s lab at the University of Potsdam.

3.3.2 Open circuit corrected charge carrier extraction (OTRACE)

Open circuit corrected charge carrier extraction (OTRACE) is a versatile and state-of-the-art charge extraction technique which enables simultaneous measurement of charge carrier mobility(μ), carrier lifetime (τ_{eff}) and carrier density (n) [94]. As with any transient charge extraction technique the measurement process can be summed up into three steps:(i) photogeneration of charge carriers. In OTRACE, a pulsed LED light source is used for illumination, instead of laser excitation, in order to achieve steady-state conditions (ii) charge carrier recombination during the delay time (t_{delay}) and iii) charge carrier extraction using a triangular voltage pulse in this case. What sets OTRACE apart is that during the delay time (t_{delay}) a time-dependent offset voltage is applied so as to avoid any carrier injection. This adaptive field control limits the RC time of the device to minimal (i.e the pure geometric RC time) by limiting the capacitance of the cell. A small RC time is beneficial as it usually improves the time resolution of charge extraction techniques. If the RC time of the device is greater than the t_{max} (time at which the current transient peaks) the mobility is underestimated as the RC signal starts to interfere with the current transient.

As a first step, the open-circuit voltage (V_{OC}) transient is recorded [Figure 4.11]. For this, the sample is connected to a 1 MΩ resistor of an oscilloscope (Tektronix DPO7354C), to make sure that there is no current flow from the device and that the open-circuit condition is maintained at all times. Upon excitation with a white LED (LUEXEON K2), powered by a 100 ms long, square shaped pulse (Agilent 33600A), the voltage transient is recorded. This V_{OC} transient is applied during the delay time as the time dependent offset voltage to inhibit carrier injection.

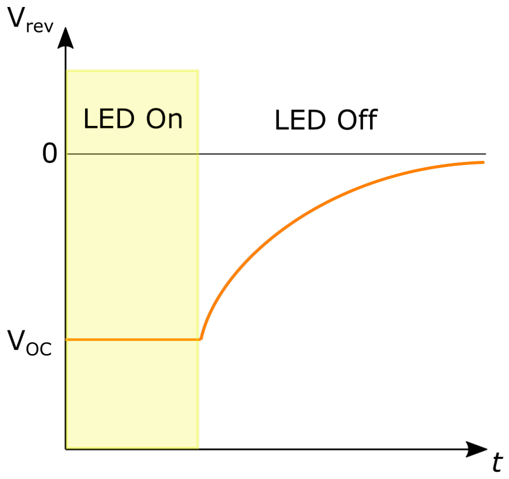

Figure 3.5: Schematic of the V_{OC} transient. When the LED is switched off the V_{OC} value decays to zero due to charge carrier recombination.

For the second step to measure current transients, a linear increasing voltage pulse with an amplitude of 1.5 V and a duration of 80/90 μs is added to the already recorded V(t) function after varied delay times (100 ns to 30 ms). The modified V(t) signal [see Figure 3.6] is applied to the sample, while illuminating the sample with the same pulsed LED as in step one. Up to the delay time, the V(t) just compensates for the field created by the generated charge carriers and keeps them in the device. The characteristic current response is taken with the same oscilloscope and allows to calculate the charge carrier lifetime τ_{eff} and mobility μ. Charge carrier densities (n) are obtained by integrating the difference between the dark and the light current response.

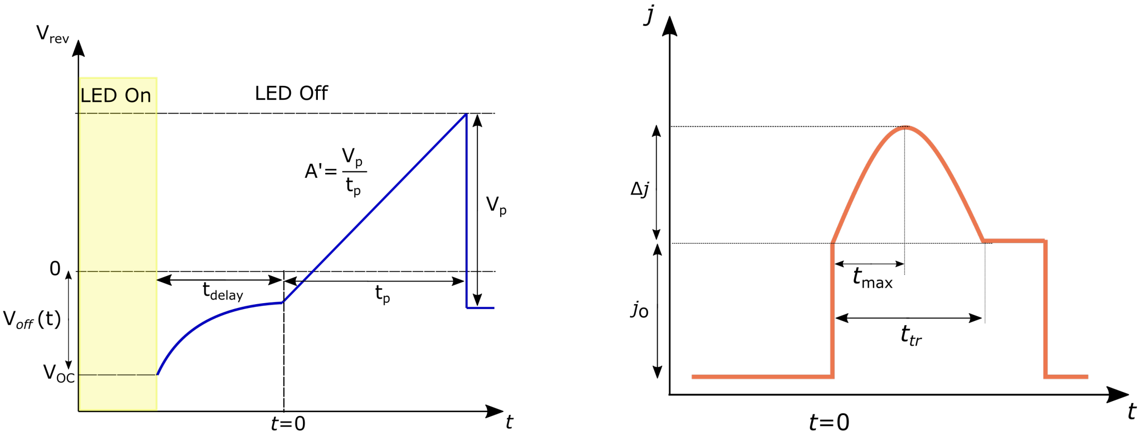

Figure 3.6: Shape of the applied voltage pulse [left]. The measurement process can be summed up into three stages :(i)photogeneration (ii)charge recombination (iii)charge extraction. Time dependent offset voltage is applied during the delay time to inhibit charge carrier injection. The shape of a typical current transient [right]. Using the maxima of the curve, charge carrier mobility(μ) can be calculated. Integration of the transient curve gives the charge carrier density (n). Figure adapted from [94].

3.4 Electroluminescence (EL)

When a solar cell is subjected to forward bias (+V) an electroluminescence (EL) signal can be detected because of the recombination of injected charge carriers. The EL spectra can be used to characterize and measure the energy of CT states and thus is a valuable tool in characterizing the voltage losses of the devices.
To acquire the EL spectra, an Andor SR393i-B spectrometer equipped with a cooled Si and cooled InGaAs detector array (DU420A-BR-DD and DU491A-1.7) was used. As the detectors have different spectral response, the infra-red part and the visible part of the spectra were recorded separately using the InGaAs and the Si detectors respectively. To obtain the broad EL spectra spanning the whole energy range the two individual spectras were scaled accordingly and merged. The spectral response of the set-up was calibrated with a reference lamp (Oriel 63355). Charge injection was achieved using a Keithley 2400 source measure unit. The emission spectrum of the solar cells was recorded at different injection currents with respect to voltages that were higher than or at least similar to the V_{OC} of the device at 1 sun illumination.

3.5 Photoluminescence (PL)-quenching

Exciton recombination gives rise to photoluminescence (PL) in neat polymer semiconductor films. In the donor-acceptor blend films, the degree of quenching of the neat PL signal gives an estimate of what fraction of excitons dissociate at the donor-acceptor interface. The higher the degree of PL quenching is, the more efficient is the exciton dissociation process which enhances the overall photocurrent generation efficiency.

To measure PL quenching of the polymer phase, the PL signal was measured from the neat polymer films and in the polymer-acceptor blend films while selectively exciting the polymer domains. The drop of the PL signal in blend films can be used to measure the quenching efficiency. Similar measurements can also be done for the acceptor molecules to calculate the quenching efficiency of the acceptor phase. In our case, PL samples were prepared by spin-casting either neat or blend films onto a glass substrate. An infrared-LED with peak intensity at 850 nm was used to selectively excite polymer domains. While a laser excitation at 535 nm was used to selectively excite fullerene phase. The PL signal was collected using Andor SR393i-B spectrometer equipped with a cooled Si and cooled InGaAs detector array (DU420A-BR-DD and DU491A-1.7). All the PL quenching measurements were done in Professor Dieter Neher's lab at the Faculty of Physics and Astronomy located in University of Potsdam.

3.6 Transient Absorption (TA) Spectroscopy

Transient absorption spectroscopy (TAS) is an optical pump-probe technique used to measure the dynamics of excited states and photo-chemical reactions (e.g. photoinduced electron transfer)[95, 96]. In this technique, the sample is first excited or perturbed using a monochromatic pump pulse and the change in absorbance $\Delta A(\tau, \lambda)$ of a broadband probe pulse is measured between the excited and the non-excited state of the sample. To trace the dynamics of different species, the time delay (τ) between the pump pulse and probe pulse is controlled using a translational delay stage. The evolution of $\Delta A(\tau, \lambda)$ then gives the characteristic lifetime. The resolution of the technique is limited by the pulse width of pump and the probe pulses. In our experiments, the pulse width was typically around 100 fs and the dynamics with sub-picosecond resolution was probed.

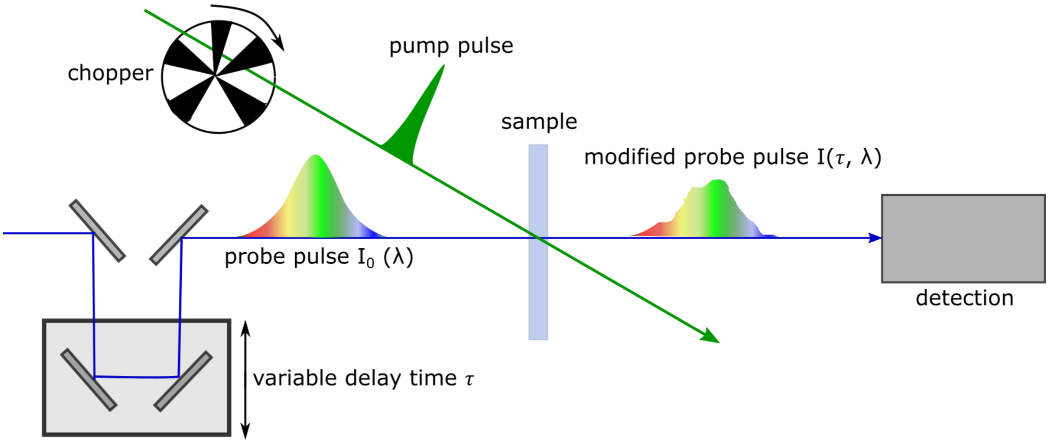

Figure 3.7: Schematic depicting the principle of transient absorption spectroscopy. The pump pulse perturbs the sample and the absorbance of the probe pulse is measured with and without pump excitation. Figure adapted from [97].

.

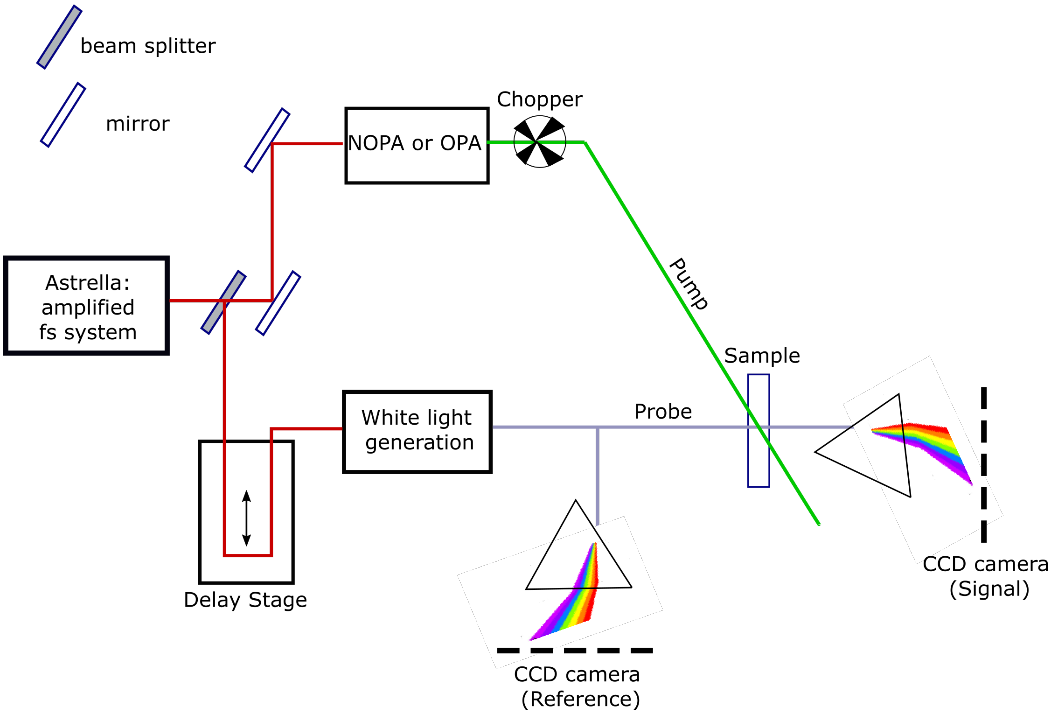

Figure 3.8: Basic sketch depicting the transient absorption setup used for measurements in this thesis. The fundamental frequency of the laser is tuned using an optical parametric amplifier to generate the pump beam. The weaker part of the laser pulse passes through a sapphire crystal to generate white light super continuum probe pulse.

Transient Absorption (TA) setup: In our experiments, a Ti:Sapphire femtosecond pulsed laser system developed by Astrella-Coherent, Inc. is used to generate pump and the probe pulses. Both pump and probe are generated from the same laser output to maintain synchronicity between the pulses. A beam splitter (BS) splits the laser output into two parts with unequal intensities. The stronger portion is used to generate a pump pulse of desired wavelength while the weaker part is modulated to generate a white light continuum which is used as the probe pulse.

As laser pulses of femtosecond timescale possess very high intensity, non-linear optical effects come into picture. We use these non-linear effects, namely, optical parametric generation (OPG) and second harmonic generation (SHG) for tuning the wavelength of the pump pulse. The stronger part of the fundamental laser output is sent through a non-linear optical crystal like BBO ($\beta - BaB_2O_4$) or BIBO (BiB_3O_6) in a non-collinear optical parametric amplifier (NOPA). As a result, of one of the frequency conversion processes, the laser pulse splits into two components namely the signal and the idler. The energy of the signal and idler pulses is controlled by altering the phase-matching conditions. This is done by changing the relative orientation of the crystal with respect to the incoming beam. Additionally, for the generation of the 400nm pulse to excite the sample in the visible region, frequency doubling or second harmonic generation can be used to convert the fundamental wavelength of the amplified laser output ($\lambda = 800nm$).

For the generation of the probe pulse, the weaker part of the laser output is focused

onto sapphire or CaF_2 disk. Here, we use a third order non-linear effect called self phase modulation (SPM). The refractive index of the non-linear crystal changes due to the highly intense laser pulse (also known as the optical-Kerr effect) which leads to a distribution of instantaneous frequencies (ω_{inst}) as the laser beam passes through the medium. This process generates a white light continuum (400nm-1500nm) which is used as the broadband probe pulse. The probe pulse is split into a reference and a signal part which are detected by the CCD cameras after dispersing them through a prism into its spectrum.
The TA spectrum is collected on shot-to-shot basis. Which implies that the intensity of every single transmitted probe pulse is measured separately. The CCD detectors are synchronized to the repetition rate of the amplified laser output (1kHz). While the pump beam is chopped at 500 Hz so that only every second probe pulse experiences the pump pulse. The reference beam allows to correct for shot-to-shot fluctuations.

Absorbance of the probe pulse is given according to the Beer-Lambert law :

$$A(\lambda) = log\frac{I_0(\lambda)}{I(\lambda)} \tag{3.8}$$

where $I_0(\lambda)$ and $I(\lambda)$ are the intensities of the incident and the transmitted probe pulse.
In order to deduce the transient absorption signal $\Delta A(\tau, \lambda)$, the difference between the absorbance of the pumped sample $A_p(\tau, \lambda)$ and the unpumped sample $A_u(\lambda)$ is calculated :

$$\Delta A(\tau, \lambda) = A_p(\tau, \lambda) - A_u(\lambda) = log\frac{I_0(\tau)}{I_p(\tau, \lambda)} - log\frac{I_0^{'}(\lambda)}{I_u(\lambda)} \tag{3.9}$$

Usually the intensity of incident pulse is not measured and is assumed to be constant between the pulses.Using this approximation the above expression simplifies to :

$$\Delta A = log\frac{I_u(\lambda)}{I_p(\tau, \lambda)} \tag{3.10}$$

Contributions to the TA signal: The $\Delta A(\tau, \lambda)$ signal contains a vast amount of information about the dynamics of the physical processes and the nature of photo-induced species generated. In general, a transient absorption signal has four major contributions [95]

1. **Ground state bleaching (GSB)**
   As the pump beam perturbs the system there is a generation of the excited state population. This concomitantly leads to a decrease in population of the ground state. Consequently, as the probe beam arrives after a certain delay time there is a decrease in the absorbance in a certain spectral region as the ground state is depleted. This gives rises to a negative TA signal ($\Delta A < 0$). Usually, the GSB signal correlates very well with the steady state absorption spectrum of the sample [96].

2. **Stimulated emission (SE)**
   The probe can trigger the the relaxation of the already excited species back to the ground state leading to the stimulated emission signal. As the the light is emitted SE also gives rise to a negative contribution ($\Delta A < 0$) to the TA signal.

3. **Excited state absorption (ESA)**
   Certain wavelengths of the probe spectra can excite the already excited species (like singlets,triplet states) to higher lying energetic or vibrational manifold. Absorption of the excited species to higher lying states gives rise to a positive contribution ($\Delta A > 0$) to the TA signal.

4. **Product absorption (PA)**
   Photo-chemical reactions induced by the pump pulse can produce products and/or reactions intermediates which can also absorb the probe pulse and be promote to higher lying states. For example, in solar cells photo-induced electron transfer process creates positive and negative polarons which can subsequently absorb the pump pulse. This gives rise to a positive TA signal($\Delta A >$ 0).

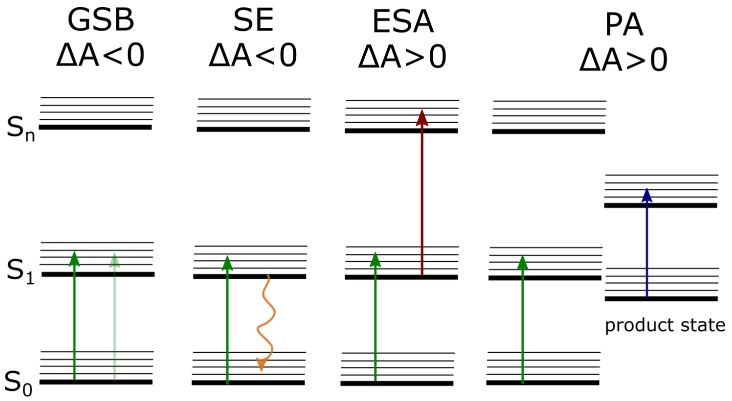

Figure 3.9: Schematic depicting the various contributions to the transient absorption signal. Ground state bleaching and stimulated emission give rise to a negative signal ($\Delta A < 0$) while excited state absorption and product absorption contribute to the rise in the TA signal ($\Delta A > 0$).

Cross-correlation and Chirp correction [98]: To estimate the time resolution of the setup, cross-correlation of the pump and the probe pulse is measured at the sample position using the optical Kerr gating technique. The relative polarization of the pump and the probe pulse is set to 45 deg. Then the pulses are sent through a Kerr medium in our case a microscopic glass slide. A Glan-thompson polarizer is placed in the path of the probe pulse to block it. The pump pulse induces birefringence in the Kerr medium. So, when the pump and the probe pulses temporally overlap, the pump pulse changes the polarization of the probe pulse and it is able to pass through the polarizer and is detected by the CCD camera. Since the probe pulse has a wide spectral range it exhibits large group velocity dispersion. Typically, the longer wavelengths travel faster than the shorter ones. For example, when the blue component arrives at time zero the red component usually already traverses a few picoseconds. The setup used exhibits a cross-correlation of the order of 100 fs. To calculate the correct time delay between the pump and the probe pulses chirp of the white light needs to be considered. A MATLAB routine was used to mathematically correct for the chirp to calculate time zero for each wavelength component of the probe pulse. The corrected data was treated using the Igor Pro software for further analysis.

Data Analysis: To delineate the effects of various physical processes global analyis was performed. The dynamics at different wavelengths (every 5-10 nm) were fitted using a multiexponential function:

$$\Delta A = y_0 + A_1 e^{-\frac{t}{\tau_1}} + A_2 e^{-\frac{t}{\tau_2}} + A_3 e^{-\frac{t}{\tau_3}} \tag{3.11}$$

where A_n is the amplitude and τ_n is the associated time constant. For the fitting routine, time constant was constrained to be similar for the dynamics at different wavelengths, while amplitude of each exponential was allowed to vary freely. Offset y_0 was set to zero. 60 fitting iterations were preformed for 20,000 fit data points for each dynamics.

Usually 3 to 4 time constants were enough to obtain a fit with sufficient accuracy. The corresponding amplitude spectra obtained assigns each spectral region a time constant which is helpful in following each physical process chronologically. For a positive transient absorption signal, a positive amplitude spectra implies decay of the transient species (for example through recombination) while a negative amplitude spectra implies a rise of the transient species. Similarly, for the negative signal if the amplitude is positive the signal is still rising i.e., becoming more negative while if the amplitude is positive the signal is decaying back to zero.

3.7 Electromodulated differential absorption (EDA)

Basics of Electroabsorption

The absorption spectrum of a molecular ensemble can change in the presence of an electric field, commonly known as the Stark effect. In particular, the static electric field (F) acts as the perturbation shifting the energy levels thus directly affecting the electronic transitions.The change in the energy of an electronic transition going from the 0 to n state is given as [99, 98]:

$$\Delta E = E - E(0) = -m_{0n} F - \frac{1}{2} p_{0n} F^2 \tag{3.12}$$

where m_{0n} is the change in the permanent dipole moment and p_{0n} represents the change in polarizability for the transition from the ground state to the n state $(0 \rightarrow n)$.The applied voltage is of the order of 1-100 V which for a 100nm molecular thin film translates to an electric field strength of the order of $10^5 - 10^7 V/cm$.

In presence of the field the absorption spectrum shifts to longer wavelengths and the differential absorption signal $(\Delta\alpha = \alpha(F) - \alpha(0))$ resembles the first derivative

[Figure 3.10].Differential absorption can be expanded using the derivatives according to:

$$\Delta\alpha = \frac{\delta\alpha}{\delta\varepsilon}\Delta\varepsilon + \frac{1}{2}\frac{\delta^2\alpha}{\delta\varepsilon^2}\Delta\varepsilon^2 + ... \tag{3.13}$$

Substituting equation 4.12 into equation 4.13 we get [99, 98]:

$$\Delta\alpha = -\frac{\delta\alpha}{\delta\varepsilon}m_{0n}F - \frac{1}{2}\frac{\delta\alpha}{\delta\varepsilon}p_{0n}F^2 + \frac{1}{2}\frac{\delta^2\alpha}{\delta\varepsilon^2}(m_{0n}F)^2 + ... \tag{3.14}$$

For isotropic samples, the linear term in F averages to zero taking into account all possible orientations of the dipole moment and the first non-zero term is quadratic in F. From the above equation we see that the first derivative of absorption depends on the change in polarizability (quadratic stark effect) and the second derivative depends on the change in permanent dipole moment. Since charge transfer (CT) transitions have typically a large dipole moment the second derivative of the absorption spectrum is usually associated with the CT-states [99].

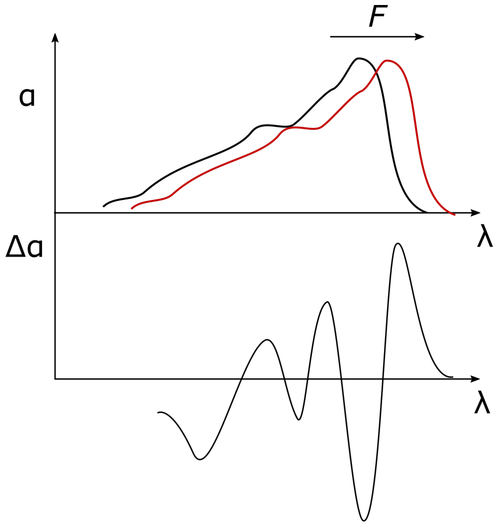

Figure 3.10: Schematic showing the shift in the absorption spectrum.In the presence of the field the spectra shifts to longer wavelengths. The differential absorption signal resembles the first derivative.

Experimental Setup:

EDA is essentially a pump-probe technique combined with an ultra-fast modulation of voltage pulse across the device. The setup used for the EDA measurements was very similar to the one used for transient absorption spectroscopy[see Figure 3.11]. The pump pulse is generated by a non-collinear optical parametric amplifier (NOPA) while the super continuum white light probe is produced using self phase modulation by focusing the weaker part of the laser output onto a 3 mm sapphire disk. The amplified laser output was being generated at a frequency of 1kHz while the frequency of the voltage pulse was kept at 500 Hz. This way only every second pump pulse arrives in the presence of an electric field. Square voltage pulses

(100μs duration) provided by a synchronized function generator (Tektronix AFG 2021) were used to modulate the electric field across the device. To evaluate the dynamics of the EDA signal, the delay time between the pump and the probe pulses was adjusted from 100fs upto 1.2 ns. Samples for EDA measurements consisted of devices with ITO as the front electrode (optically transparent) and silver (Ag) as the back reflective electrode. Because of the Ag electrode all the measurements were carried out in the reflectance mode. The reflected probe beam was dispersed in a grating spectrograph (SpectraPro 2500i, Princeton Instruments or SR163, Andor Technology) and was detected on shot-to-shot basis at a rate of 1kHz with a 512x58 pixel back-thinned charge coupled device(Hamamatsu S07030-0906, assembled by Entwicklungsbüro Stresing). The current response of the device is recorded using a 50 Ω series load with a 400MHz oscilloscope (Tektronix TDS 3044B).

EDA set-up is located in Professor Natalie Banerjie's lab in the department of chemistry and biochemistry at the Univeristy of Bern [100].

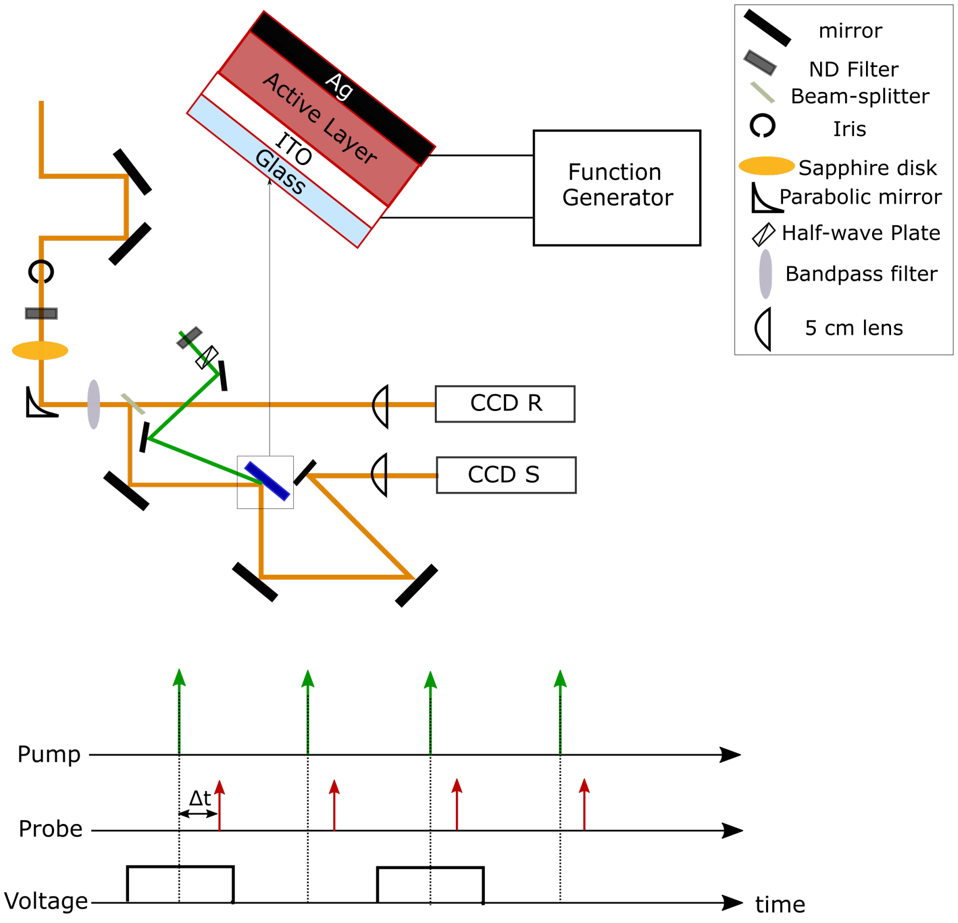

Figure 3.11: Schematic showing the setup used for EDA measurements. The optical path of the pump and the probe pulses is depicted with a ray diagram. The bottom part of the figure depicts the synchronization of the pump, probe and the voltage pulse. The green arrows represent the pump beam while red arrows represent white light continuum probe.

3.8 Morphological Characterization

The morphology of bulk-heterojunctions is fairly complex in nature consisting of a mixture of donor, acceptor and the mixed phases which are intricately interconnected. Resolving the features like average domain size, phase purity, degree of crystallinity (DoC) can provide a detailed quantitative picture of the BHJ morphology and help in correlating these features to the various physical processes leading to charge generation and the overall device performance. In this thesis we have primarily used two techniques, viz. transmission electron microscopy (TEM) and synchrotron based grazing incidence wide angle X-ray scattering (GIWAXS) to investigate the morphological characteristics. TEM probes the structure in real space.It is a powerful technique and can help in resolving structural features on a sub-100 nm length scale.Average domain size and degree of intermixing can be deduced fairly accurately. Whereas, GIWAXS probes the structure in reciprocal space and is helpful in resolving the crystalline features. Quantities like relative degree of crystallinity (rDoC), average π-stacking distance of the polymer chains, lamellar spacing can be estimated. Overall, the combination of these two techniques provides a fairly comprehensive picture of the BHJ morphology which can assist in explaining many features of the device characteristics.

3.8.1 Transmission electron Microscopy

For analysis by electron microscopy, thin films of the neat polymer and the blend films were spin coated on PEDOT:PSS-coated glass slides, floated in the deionized water and picked up on copper TEM grids covered with lacey carbon film. Transmission electron microscopy (TEM) measurements were performed with a Libra200 (Carl Zeiss, Germany) operated at an acceleration voltage of 200 kV. High-angle annular dark field scanning transmission electron microscopy and energy dispersive X-ray mappings (HAADF-STEM and EDX) were conducted with a Talos F200X (Thermo Fischer Scientific / FEI, USA) operated at 200kV and equipped with Super-X-EDX detector.

3.8.2 Grazing incidence wide angle X-ray scattering (GIWAXS)

When the X-ray beam passes through a material it can be scattered by outer shell electrons of the atoms. In case of crystalline materials, reflections from planes of periodically arranged atoms or molecules interfere constructively giving rise to a high intensity diffraction spot. For an X-ray plane wave with wave vector $k_0 = \frac{2\pi}{\lambda}$,the scattering vector is given as [101]:

$$q = k_f - k_i = \frac{4\pi}{\lambda}\sin(\theta) \tag{3.15}$$

where $k_i$and k_f are incident and scattered plane waves, 2θ is the scattering angle and λ is the X-ray wavelength. Following Bragg's condition, q can be related interplanar spacing according to:

$$q = q_B = \frac{2\pi}{d_{hkl}} \tag{3.16}$$

where h,k,l are the miller indices of the scattering plane. While analyzing the scattering data it is often convenient to think in terms of reciprocal space which mathematically is related to real space lattice by an inverse-transpose matrix operation:

$$A_{reciprocal} = [(A_{real})^{-1}]^{T} \tag{3.17}$$

The reciprocal lattice vectors are related to real space lattice vectors according to [102] :

$$a^{*} = 2\pi\frac{b * c}{a.(b * c)}; \quad b^{*} = 2\pi\frac{c * a}{a.(b * c)}; c^{*} = 2\pi\frac{a * b}{a.(b * c)} \tag{3.18}$$

where a,b,c are real space primitive lattice vectors.

Reciprocal lattice is an useful construction because the q values that satisfy the Bragg condition can be re-constrcuted from reciprocal lattice vectors according to:

$$q_{hkl} = (ha^{*} + kb^{*} + lc^{*}) \tag{3.19}$$

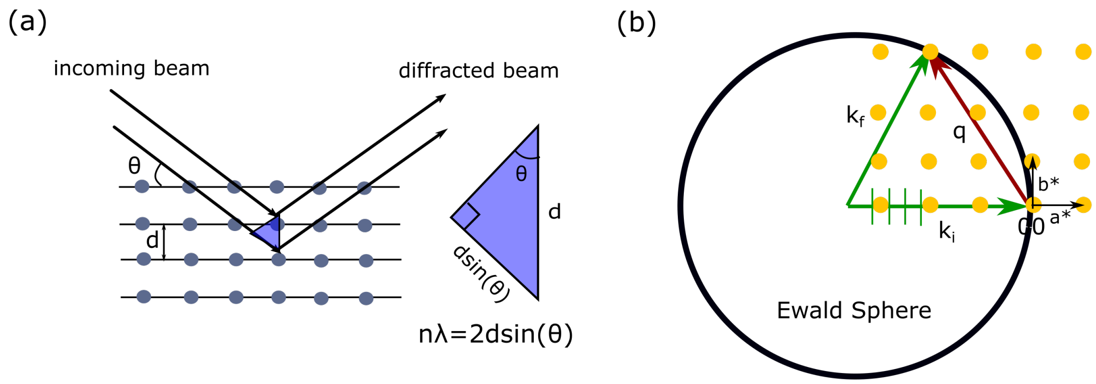

Figure 3.12: (a) Representation of Bragg's law in real space. The condition necessary for constructive interference of diffracted beam from a set of parallel planes consisting the scattering moiety i.e. the atoms and/or molecules. (b) Ewald's construction depicting the condition for elastic scattering of x-rays. 2D reciprocal lattice is superimposed over the Ewald's sphere. To fulfill the conditions for scattering the reciprocal lattice point must intersect with the surface of the sphere.

As organic/polymer semiconductors are commonly cast into thin films for device fabrication it is required that the morphology is probed under similar configuration. Thus,the X-ray scattering measurements are also done for thin films under grazing incidence. Typically the incident angle α_i is very small and is usually around $0.1°$. Depending on the incident angle (α_i) and the critical angle of the substrate (α_c) three conditions are possible:

- $\alpha_i < \alpha_c(sample)$: This is the evanescent regime where the near-surface crystalline features are probed.
- $\alpha_c(sample) < \alpha_i < \alpha_c(substrate)$: In this case the bulk of the thin film is probed.

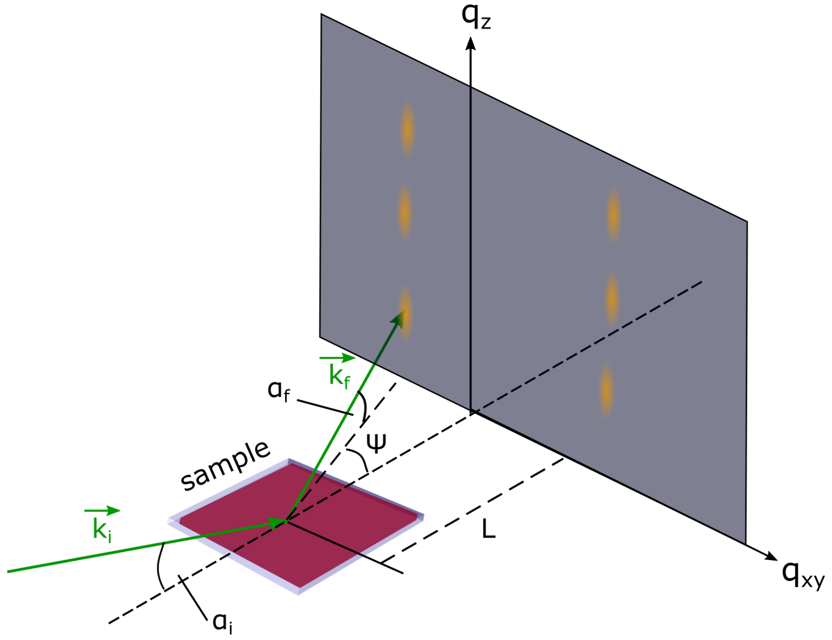

Figure 3.13: Schematic showing the geometry of the GIWAXS setup. k_i and k_f are the incident and the scattered wave vectors. α_i and α_f are the incident angle and the angle of the scattered wave with respect to the substrate plane. Rectangular grey area represents an area detector. L is the sample to detector distance . q_z and q_{xy} are the projections of the scattering vector in the out-of-plane and in-plane direction respectively.

- $\alpha_i > \alpha_c(substrate)$: Broad scattering signal from the substrate contributes to the overall scattering signal.

The scattering signal is detected using either a point detector or an area detector [Fig.3.13]. Using the point detector high resolution data of q-space can be obtained but the method suffers from long data acquisition times. On the other hand, using an area detector scattering data from a large angular range can be measured rather fast.In this case the resolution depends on the pixel size of the detector, sample to detector distance (L) and the energy of the X-ray beam. In our work, both the point-detector and area detectors were used depending on the beamline where the experiments were conducted.

The scattering data obtained is very rich in information and can be used to deduce a variety of features including the unit cell parameters, molecular packing, grain size and the degree of crystallinity. In order to obtain the unit cell, the scattering peaks (q) are indexed where the peaks are assigned miller indices of the plane from which the diffraction spot originates. As a second step, reciprocal lattice vector are obtained using the relation in equation 4.19. Subsequently, using the inverse relation of the equation 4.18 real space lattice vectors are calculated. If a sufficient number of diffraction spots are obtained (typically 20-40) structure refinement can be used to predict the arrangement of molecules within the unit cell [103]. In this case, the theoretically calculated intensity of a diffraction spot is compared to the experimental values to find the molecular arrangement. For calculating the grain size or the coherence length (L_c) along a packing direction, Scherrer's formalism can be used [104]:

$$L_c = \frac{2\pi K}{\Delta q} \tag{3.20}$$

where K is the peak shape factor (0.8-1) and Δq is the full width at half maxima of the scattering peak.
For estimating the degree of crystallinity (DoC), the pole figure of a selected scattering peak needs to be estimated. Pole figure gives the orientation distribution of crystallites with respect to the sample plane while the integrated intensity of the pole figures quantifies the crystalline volume fraction in the films [105, 104] :

$$rDoC \propto \frac{\Delta\beta\Delta\theta}{2\pi}[I_{peak} - I_{baseline}] + \int_0^{\pi/2} sin(\chi)I(\chi)d(\chi) \tag{3.21}$$

where $\Delta\beta$ and $\Delta\theta$ are the horizontal and the vertical acceptance angle respectively. I_{peak} is the maximum intensity of the diffraction peak and $I_{baseline}$ is the baseline intensity. χ represents the polar angle which is the angle between the scattering vector and the substrate normal.
Measuring absolute crystallinity (DoC) of organic thin films is often not possible so relative degree of crystallinity (rDoC) is more commonly reported [106, 107, 108]. For example, using rDoC, crystallinity between the films of the same material which are processed differently can be compared.

Measurement Details

During the course of this thesis, GIWAXS measurements were performed at three different synchrotrons in Europe viz., Elettra lightsource in Treiste, Italy; PETRA III , DESY, Hamburg and European Synchrotron Radiation Faciltiy (ESRF) in Grenoble.The setup used was similar to one described in Fig 3.13. The general measurement routine at all the beamlines consisted of the following steps:

- As a first step, to make sure that sample plane is strictly horizontal the intensity of the primary X-ray beam was tracked by scanning the sample in the vertical direction and rocking-curve pattern, alternatively. In the vertical direction, the sample height was fixed at a value where the maximum intensity of the beam was cut into half (as the intensity of the X-ray beam follows a gaussian distribution in spatial coordinates). During the rocking curve measurements the out-of-plane rotation angle was set to a value where the intensity shows the maximum value. The entire procedure was repeated iteratively until the sample plane was strictly horizontal.

- As a second step, the sample plane was tilted with respect to the primary beam to set the incident angle (α_i). Typically α_i was set in the range of $0.09° - 0.12°$. The critical angle for SiO_2 (susbtrate) at x-ray photon energy of 12keV is around 0.16° . Thus, the incident angle was always lower than the critical angle of the substrate and diffuse scattering signal from SiO_2 was avoided in most cases.

- Next,the sample detector distance is adjusted to cover the relevant q-range. The distance was calibrated by measuring the diffraction signal from a Lanthanum Hexaboride (LaB_6) reference film.
- Finally, the scattering signal from the samples was recorded using area detectors like Piltaus3 1M detector system or 2D MAR300 charge coupled device (CCD) camera. The data acquisition time was adjusted so as to have a good signal to noise ratio while avoiding beam damage of the films.

Chapter 4

Diketopyrrolopyrrole (DPP) Polymers: Effect of alkyl branching on device performance

DPP polymers with different alkyl side chains and conjugation units are introduced. Their UV-Vis-NIR spectra are discussed and the optical gap is determined for each of the polymers. Subsequently the effect of synthesis conditions,molecular weight (M_w) and the choice of solvent on device performance is summarized.

Charge carrier mobility and non-geminate recombination are investigated using OTRACE measurements. The morphology of the neat and bulk-heterojunction blend films is explored using x-ray scattering and transmission electron microscopy. The influence of of these parameters on the fill factor (FF) of the devices is discussed.

PL measurements reveal the origin of the large differences in photocurrent for the various polymers of this series. Finally, both the radiative and the non-radiative voltage losses for the devices are measured. The major conclusion of this work is that the size of fibrillar morphology controls the exciton harvesting efficiency. Also, the structure of alkyl chains should be optimized to limit the solubility of polymers so that fine enough fibrillar morphology can be obtained.

4.1 Introduction

The progress in the field of polymer solar cells majorly relies on the development of new materials for achieving improved device performance. Most important considerations with regards to the development of new polymer semiconductors include tuning of the optical gap (E_{opt}), energy levels of the frontier molecular orbitals (HOMO/LUMO), solubility and aggregation properties. Low E_{opt} polymers are beneficial as they can harvest a larger portion of the solar spectrum thereby improving the current generation in the device. Additionally, these polymers can be used for sub-cells in a tandem device or in a ternary blend heterojunctions as they possess complementary absorption properties in relation to wide band gap materials. In recent years there has been a huge effort in development of low band gap polymer semiconductors [109, 110, 111]. The most common strategy to develop low E_{opt} polymers is to stack electron rich (donor) and electron deficient (acceptor) moieties alternatively to form the so called donor-acceptor (push-pull) co-polymers. In this architecture, the molecular orbitals of the donor and the acceptor groups hybridize which lowers the optical gap by bringing the highest occupied molecular orbital (HOMO) and lowest unoccupied molecular orbital (LUMO) closer to each other [Figure4.1]. These copolymers are also characterized by the intramolecular charge transfer (ICT) transition between the donor and the acceptor groups which leads to the polarization of molecule and results in the formation of molecular dipoles [112].

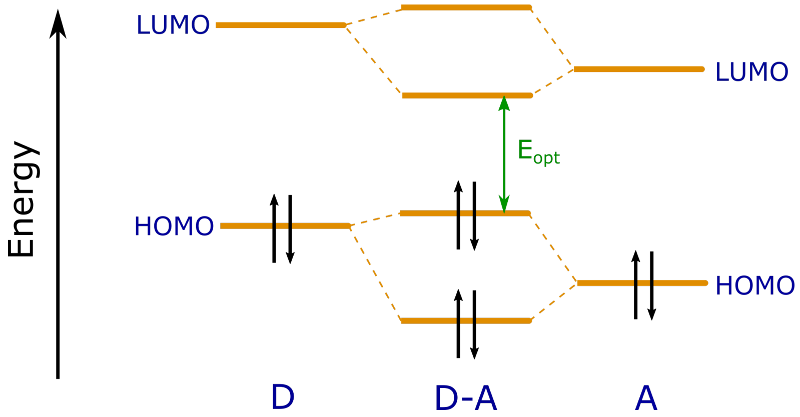

Figure 4.1: Energy level diagram depicting the hybridization of molecular orbitals of the donor and acceptor groups.This interaction lowers the optical gap of the push-pull chromophore segment of the polymer chain.

Within the class of low optical gap polymer semiconductors, the ones with diketopyrrolopyrrole (DPP) electron withdrawing groups have received great attention [113, 114]. Push-Pull structures containing DPP units have yielded optical gaps of 1.1 - 1.5 eV, which is around the optimum for solar cell applications. Small optical gap of these polymers is primarily due to the relatively low lying LUMO levels of the DPP core. Moreover, the polar nature of the DPP unit enhances the polymer's tendancy to crystallize. This has resulted in very high charge carrier mobilities in DPP polymers. There have also been reports of ambipolar charge transport in these polymers with balanced electron and hole mobilities [115].

The chemical structure of the DPP polymers can be broken down into four main components :(i)the DPP unit;(ii)the aromatic substituents;(iii) the π-conjugated segment and (iv) the alkyl side chains. The nature of the aromatic substituents and the π-conjugated segment controls the π-conjugation along the polymer backbone (i.e. the conjugation length and the degree of electron delocalization). The electron donating strength of the aromatic substituents can be also used to tune the optical band gap and the energy of the frontier molecular orbitals by changing it's interaction with the DPP unit. The structure of alkyl side chains dictates the polymer's solubility and aggregation properties. Solubility of the DPP polymers is an important criteria as it controls the morphology of the bulk-heterojunction. More discussion in this regard can be found in section 5.5.1.

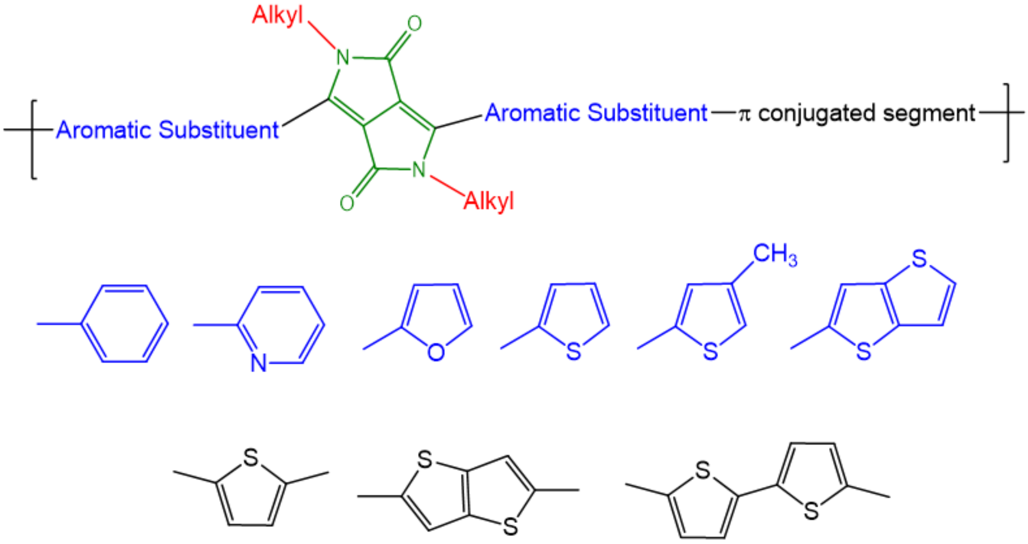

Figure 4.2: Schematic showing the basic structure of diketopyrrolopyrrole (DPP) based donor-acceptor copolymers.Common aromatic substituents are shown in blue while the π-conjugated segment are depicted in black.

For the work in this thesis, a series of DPP based donor-acceptor copolymers were provided by the group of Prof. Dr. Brigitte Voit from Leibniz Institute for Polymer Research Dresden (IPF). Polymers were synthesized by Dr.Tim Erdmann using Stille coupling polycondensation on the basis of previous reports [116, 117, 118]. The DPP core unit was used as an acceptor moiety while thiophene (T) or thieno[3,2-b]thiophene (TT) units flanked by one additional thiophene unit per side were used as donor conjugation segments. Additionally, the chain length and the branching point of the solubilizing alkyl chains was varied. 2-octyldodecyl (2OD) or bulky 6-dodecyloctadecyl (6DO) side chains with branching at 6th carbon position were used. The main design idea was to move the branching point further away from the backbone [P(DPP2ODT2-X) vs. (P(DPP6DOT2-X)] to facilitate stronger intermolecular π-orbital interactions between individual polymer chains and thus to create copolymers with reduced π-stacking distances and enhanced degree of crystallinity. Number average molecular weights (M_n) were derived from high-temperature gel permeation chromatography (HT-GPC) measurements performed in 1,2,4-trichlorobenzene at 150 °C. P(DPP6DOT2-T) and P(DPP2ODT2-T) have a comparable M_n of 19.4 kDa and 16.8 kDa, respectively. Thieno[3,2-b]thiophene-(TT)-substituted DPP copolymers exhibit significantly higher and very similar molecular weights. P(DPP6DOT2-TT) and P(DPP2ODT2-TT) showed a M_n of 92.0 kDa and 91.2 kDa, respectively.

P(DPP2ODT2-T) **P(DPP6DOT2-T)**

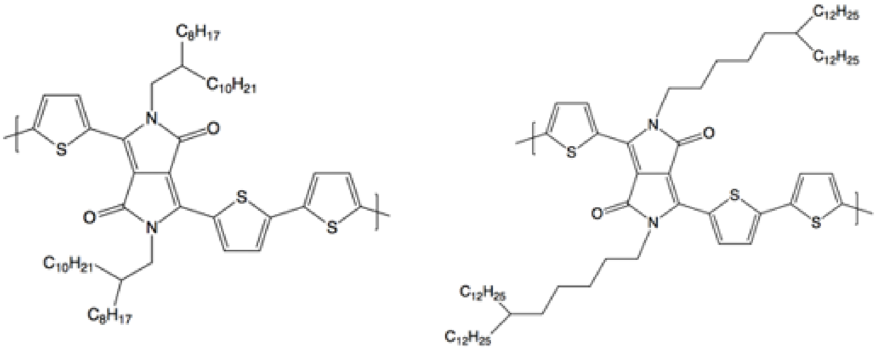

P(DPP2ODT2-TT) **P(DPP6DOT2-TT)**

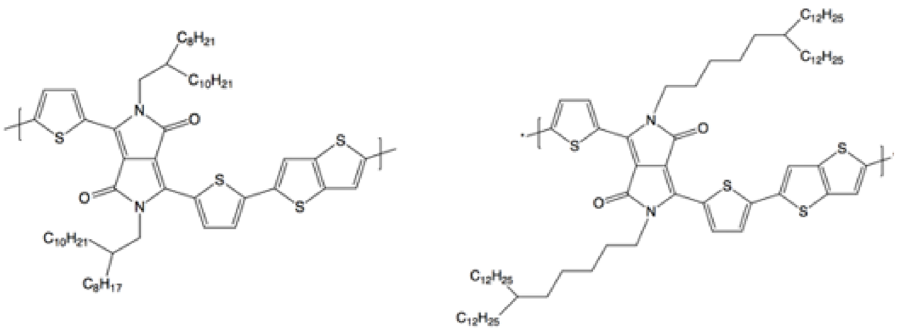

Figure 4.3: The four DPP polymers which were synthesized for this study. The DPP core unit is flanked by thiophene aromatic substituents. Thiophene (-T) or thieno[3,2-b]thiophene (-TT) units are used a π-conjugation segments. Two variations of the side chains include 2-octyldodecyl (-2OD) or 6-dodecyloctadecyl (-6DO) with branching at 2nd or the 6th carbon position respectively.

4.2 Material Characterization

4.2.1 UV-Vis spectroscopy

We measured the UV-Vis absorption spectra for spin coated thin films of the pristine polymer. The absorption spectra for the all the polymer films shows two distinct bands: a higher energy band between 350-520 nm and a wide low energy band from 520-1000 nm. The high energy band (350-520 nm) is associated with a $\pi - \pi^*$ transition delocalised over both the donor and acceptor segments of the polymer chain while the low energy band (520-1000 nm) is mostly associated with the electron redistribution within the DPP unit with a partial $\pi - \pi^*$ character [119]. There is a slight difference in the peak position of the high energy band between the thiophene and thienothiophene substituted DPP's. For the PDPPXXT2-T's the high energy band peaks at 408 nm while for the PDPPXXT2-TT's, peak position is at 425 nm. This might be related to the different π-orbital character for the thiophene and theinothiophene substituted DPP's. In the low energy band (520-1000nm) 0-0 and 0-1 vibronic transitions are visible. PDPP6DOT2-T shows a slight red-shift in the low energy band which can be related to its higher degree of aggregation and better crystallinity (for more details see the section with GIWAXS results).

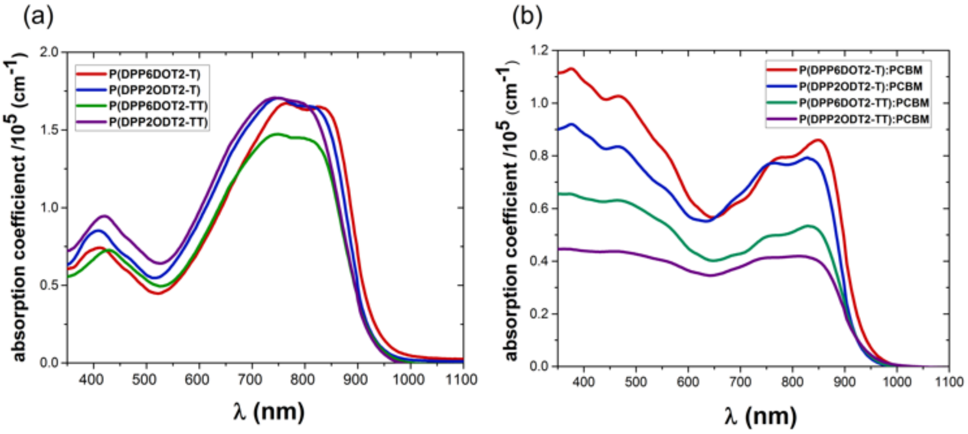

Figure 4.4: (a) UV-Vis absorption spectra for the pristine polymer films (spin cast as thin films). (b) UV-Vis absorption spectra for the polymer:fullerene blend films. PC[70]BM was used as the fullerene derivative and the blending ratio was 1:3 (polymer:fullerene).

In Figure 4.4 (b) we plot the UV-Vis spectra for the polymer:fullerene blend films. The fullrene derivative PC[70]BM was used as an acceptor and the blend ratio was 1:3 (polymer:fullerene). The absorption spectra look like a linear combination of the PCBM and the polymer spectra. One important feature to note is that the vibronic features in the polymer part are more pronounced for the polymers which are substituted with 6-dodecyloctadecyl (6DO) alkyl side chains. This can be related to their relatively higher tendency for aggregation as in these polymers intermolecular π-orbital interaction is much stronger due to reduced π-stacking distance (see section 5.5).

4.2.2 Determination of the optical gap (E_{opt})

In general, absorption spectra for organic semiconductors exhibit a shallow absorption tail which is usually attributed to the static and dynamic disorder [120]. This results in an ambiguity in the determination of the optical gap from the "onset" value of the absorption spectra, since the onset is not well defined. More accurate approach for calculating the optical gap combines the emission and absorption measurements. The optical gap is then determined by the crossing point of the appropriately normalized absorption and emission spectra [120]. It is important to normalize the emission spectra close to the highest energy peak while absorption spectra should be normalized at the lowest energy peak (i.e. close to the 0-0 transition for emission and absorption).

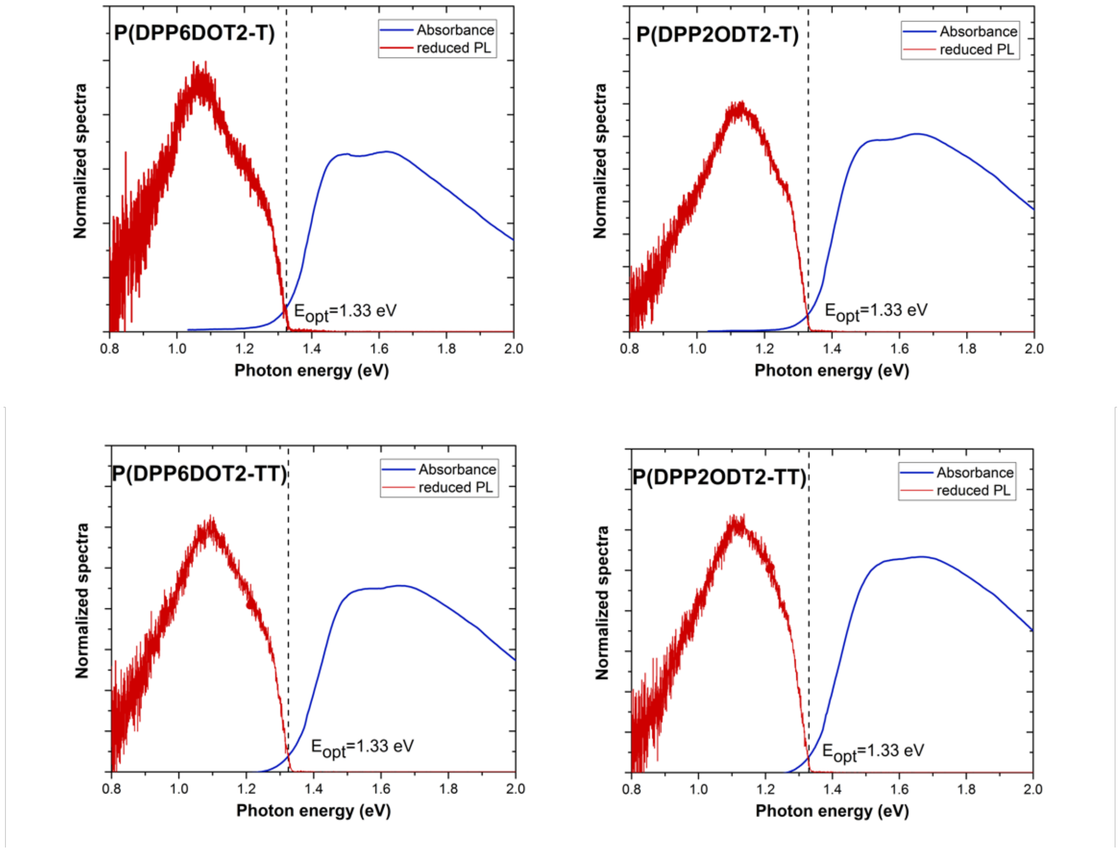

Figure 4.5: Normalized photoluminescence (PL) and absorption spectra for polymer films plotted together.Optical gap for the films is given by the crossing point of the PL and the absorption spectra.

To calculate the optical gap (E_{opt}) for the polymer films we measured the photoluminescence (PL) spectra and combined it with absorption spectra. We find that the optical gap for all four polymers is similar and has value of 1.33 eV. Nearly identical (E_{opt}) values implies that the thiophene(-T) and theinothiophene(-TT) substituted DPP's have a similar electronic structure and as one would expect as the alkyl side chain themselves are electrically neutral and do not significantly interact with the electron density distribution along the conjugated core of the polymer backbone. Thus they do not affect the energy of electronic transitions.

4.3 Device Characteristics

In the following section we discuss the device characteristics for the various DPP polymers :PC[70]BM bulk-heterojunction (BHJ) solar cells. Devices were fabricated in an inverted configuration with a simple stack design: ITO/PEIE/BHJ/MoOx/Ag. Polyethylenimine-ethoxylated (PEIE) was used as an interlayer to modify the work function of ITO. The intrinsic molecular dipole moment of the amine groups present in PEIE leads to a charge-transfer type interaction with the ITO surface thereby reducing the work-function of ITO and rendering it suitable for electron injection and/or collection [121]. An active layer ink consisting of polymer:fullerene blend is spin-coated on top of the PEIE layer. A combination of thin molybdenum oxide (MoO_x) layer (6nm) and silver (Ag, 100nm) is used as the anode for hole collection and/or injection. In what follows, we discuss the effects of polymer synthesis conditions, polymer molecular weight and the choice of solvent. In the end we summarize the optimzed device results for the four DPP polymers.

4.3.1 Effect of choice of Solvent

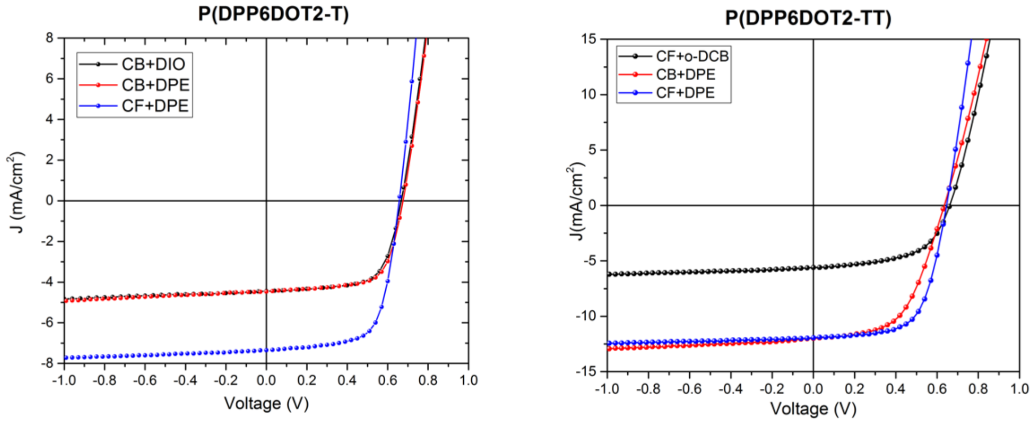

Figure 4.6: j-V curves for the P(DPP6DOT2-T) and P(DPP6DOT2-TT) blends with PC[70]BM when spin-casted using different solvents.

Table 4.1: Device parameters for P(DPP6DOT2-T) and P(DPP6DOT2-TT) for different solvent combinations extracted from the j-V curves.

System	Solvent	V_{OC} [mV]	Jsc[$mAcm^{-2}$]	FF[%]	PCE[%]
P(DPP6DOT2-T):PCBM	CB+DIO	667± 5	4.44± 0.2	67.07± 2	1.99± 0.1
	CB+DPE	676± 6	4.46± 0.1	67.48± 2	2.04± 0.08
	CF+DPE	657± 8	7.35± 0.1	67.61± 1	3.37± 0.1
P(DPP6DOT2-TT):PCBM	CF+o-DCB	662± 10	5.60± 0.5	56.20± 3	2.08± 0.25
	CB+DPE	635± 10	12± 0.3	54.70± 4	4.17± 0.2
	CF+DPE	646± 10	11.94± 0.2	63.96± 3	4.93± 0.15

As a first step towards optimization, we studied the influence of the choice of solvent on device performance. Usually, for DPP polymers a single solvent does not yield the finely mixed morphology which is beneficial for the cell's performance. Hence a combination of solvents are used to tune the morphology of the bulk-heterojunction to yield small enough donor and acceptor domains. In our case we used chlorobenzene (CB) or chloroform (CF) as the primary solvent while ortho-dichlorobenzene(o-DCB), 1,8-diiodooctane(DIO) or diphenylether (DPE) were used as solvent additives. The main idea is to use a solvent additive which has preferentially higher solubility for the fullerene phase. In that way, when the wet spin-cast layer is drying due to solvent evaporation, the fullerene molecules stay in the solution for longer time allowing the polymer chains to crystallize and form ordered domains [122]. We tried a combination of CB+DIO(3 vol%),CB+DPE(3 vol%) and CF+DPE(3 vol%) for P(DPP6DOT2-T):PC[70]BM (1:2 wt/wt) blend films. For CB+DIO and CB+DPE device performance is nearly identical and the cells exhibit a power conversion efficiency (PCE) of around 2%. This finding suggests that the nature of solvent addittive DIO or DPE does not affect the morphology differently in this case. When using DPE as the solvent additive and replacing chlorobenzene with chloroform there is an increase in the j_{sc} from 4.4 mA/cm^2 to around 7.3 mA/cm^2 which improves the PCE to 3.37 %. For P(DPP6DOT2-TT) we also tried three solvent combinations: CF+o-DCB(7.5 vol %) ,CB+DPE(3 vol%) and CF+DPE(3 vol%). For all three solvent combinations the V_{OC} values are nearly similar while the main difference in performance stems from the differences in the j_{sc}. A combination of CF+o-DCB shows the lowest j_{sc} around 5.6 mA/cm^2 while for CB+DPE or CF+DPE there is nearly 100% improvement in j_{sc} values to around 12 mA/cm^2. Between CB+DPE and CF+DPE there is a slight difference in the fill factor with the CF+DPE combination having the higher FF of around 64%. The difference in fill factor is generally attributed to differences in effective mobility of charge carriers. Higher mobility improves the charge collection efficiency which reduces the bias dependence of the photocurrent and improves the fill factor. There might be slight differences in the mobility of charge carriers between blend processed from CB+DPE or CF+FPE which might explain the differences in FF. In general, we find that the solvent combination CF+DPE works the best for both the polymer systems and in the rest of the study we stick to this solvent combination for achieving high device performance.

4.3.2 Effect of Polymer washing step and polymerization time

DPP polymers in this work were synthesized using the Stille coupling reaction. This synthesis routine usually uses palladium based catalysts to enhance the rate of polycondensation reaction of monomers [123]. Later, the polymers are purified using Soxhlet extraction and catalyst washing steps to remove residual palladium based catalyst. In order to optimize the purification routine we tested polymers with no washing step (NW) when they are washed with water (WW) and when they are washed with a Pd scavenging ligand solution (WL). Additionally, we also tested polymers with short (15 minutes) and long (3 days) polymerization times (abbreviated as SP and LP respectively). Surprisingly, we do not find a significant variation in the molecular weight of SP and LP polymers which points to the fact

that the polymerization kinetics are rather fast.
Five different versions of P(DPP2ODT2-T) polymers were tested to see whether there are variations in the device performance depending on the washing steps and/or the polymerization time. Figure 4.7 summarizes the device results. For SP polymers, there is no significant variation in the V_{OC} between the polymers with different washing steps. There are marginal differences in the j_{sc} which can be related to the differences in the EQE values in spectral region where the polymer absorbs. More importantly, we see a very low saturation (in reverse bias) of the photocurrent in the non-washed (NW) version of the polymer. This can be related to the high leakage current in the dark (inset figure) which we believe is associated with local shunts created by palladium nanoparticles. In Figure 4.8 TEM micrographs indeed show that the non-washed (NW) and washed with water (WW) versions of the polymer P(DPP2ODT2-T) contains Palladium nanoparticles. For the LP versions of P(DPP2ODT2-T) observations made were very similar.We observe differences in the j_{sc} and the non-washed variant displays low saturation in the reverse bias. Between the SP an the LP versions, SP P(DPP2ODT2-T) shows a slightly better performance. In the further study, all the polymers were synthesized using short polymerization times and they were purified using a ligand solution to wash off the catalyst nanoparticles.

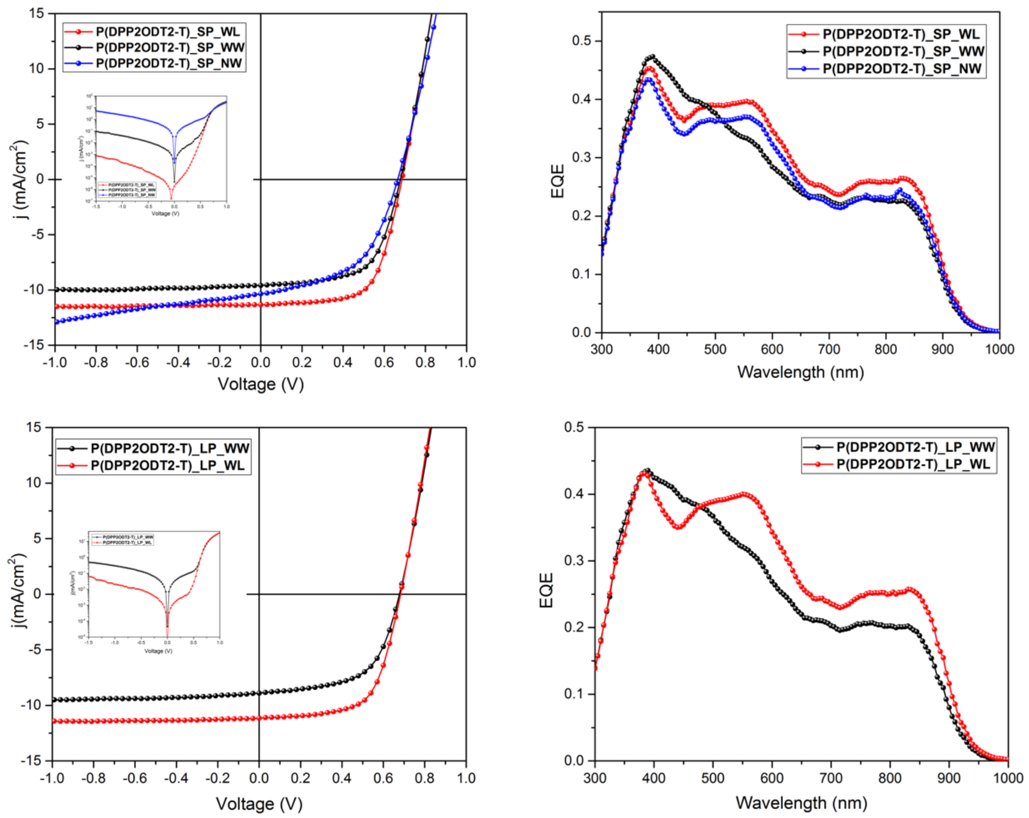

Figure 4.7: j-V curves and EQE spectra for the non-washed (NW),washed with water(WW) and washed with ligand (WL) versions of the SP and LP P(DPP2ODT2-T) polymers.

Table 4.2: Device parameters for SP and LP P(DPP2ODT2-T) for different catalyst washing conditions.

System	Washing Step	V$_{OC}$ [mV]	Jsc[$mAcm^{-2}$]	FF[%]	PCE[%]
P(DPP2ODT2-T)-SP	NW	660± 7	10.34± 0.2	51.30± 3	3.5± 0.3
	WW	680± 6	9.58± 0.1	62± 2	4.08± 0.08
	WL	660± 8	11.3± 0.1	64.80± 1	5± 0.2
P(DPP2ODT2-TT)-LP	WW	680± 10	8.90± 0.5	59± 3	3.56± 0.25
	WL	680± 10	11.15± 0.3	63.80± 4	4.86± 0.1

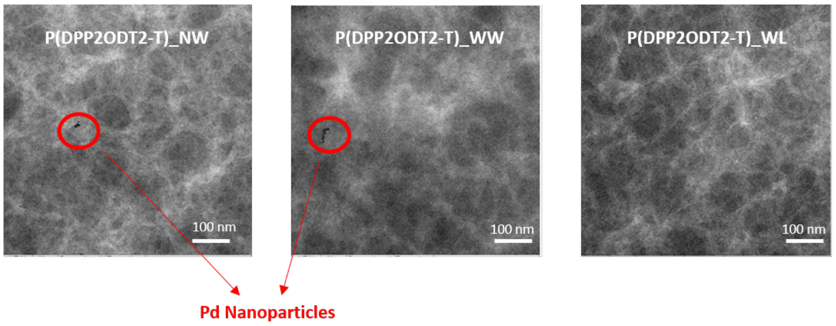

Figure 4.8: TEM micrographs for NW,WW and WL version of P(DPP2ODT2-T). Palladium nanoparticles can be seen in NW and WW version of the polymer.

4.3.3 Effect of Molecular weight(Mw)

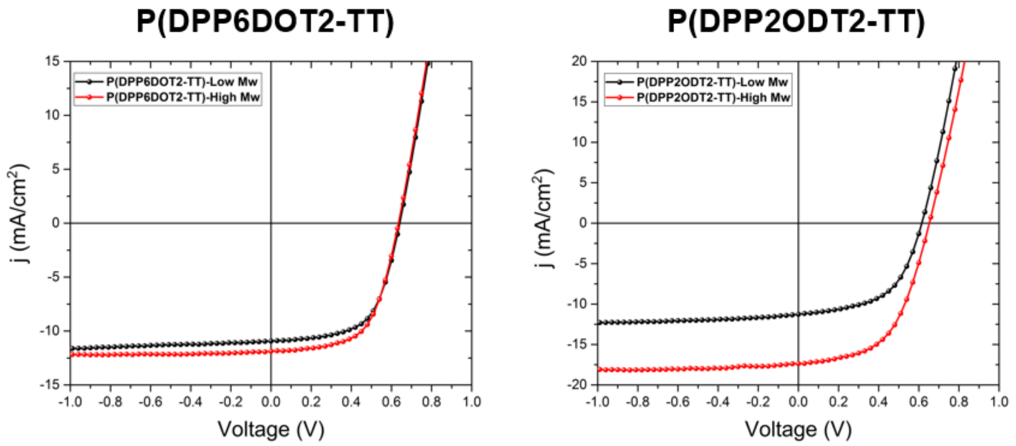

Figure 4.9: j-V characteristics for P(DPP2ODT2-TT) and P(DPP6DOT2-TT) polymers blended with PC[70]BM with low and high molecular weights.

For theinothiophene (-TT) substituted DPP's low and high molecular weight (Mw) polymers were synthesized. The device performance of the polymers was tested to further narrow down the synthesis conditions which can provide polymers for high performance organic solar cells. In general, we find that for both P(DPP2ODT2-TT) and P(DPP6DOT2-TT) polymers their high Mw versions deliver better solar cells.

Once again the main difference in performance stems from the differences in the j_{sc}. High Mw P(DPP6DOT2-TT) has a j_{sc} of 11.98 mA/cm^2 while low Mw version shows a j_{sc} of around 10.97 mA/cm^2. Polymers with a 2-octyldodecyl (-2OD) side chains show a higher j_{sc} values which is due to their finer morphology (directly linked to polymer solubility). Low Mw P(DPP2ODT2-TT) has a j_{sc} around 12 mA/cm^2 while high Mw P(DPP2ODT2-TT) shows the highest j_{sc} of 17.37 mA/cm^2.There is also a considerable difference in the V$_{OC}$ values of high and low Mw P(DPP2ODT2-TT) with values in the range 614±10 mV and 652±10 mV respectively. It appears that -6DO substituted polymers are less sensitive to molecular weight variations compared to the -2OD substituted polymers. To further elucidate the device physics of these polymer solar cells we resort to the high Mw versions.

4.3.4 Optimized Device Characteristics

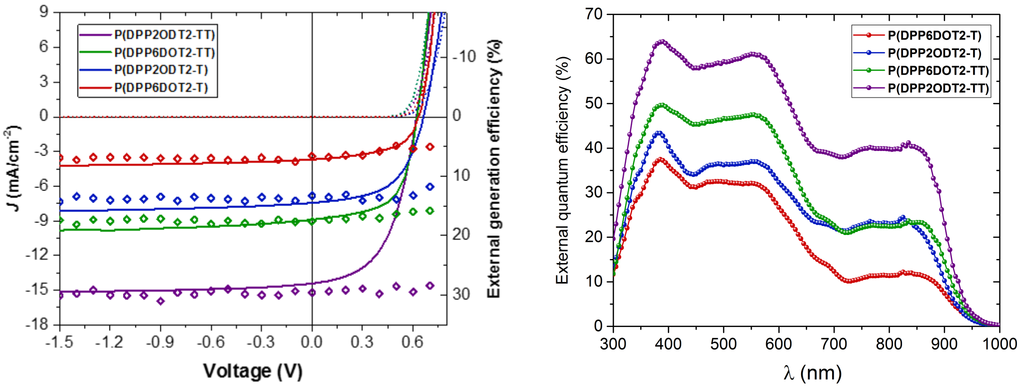

Figure 4.10: j-V curves and the EQE spectra for the four DPP polymers under optimized processing conditions. External generation efficiency (EGE) data measured using TDCF is superimposed over the j-V curves.

Table 4.3: Optimized device paramters for the four DPP polymers: P(DPP6DOT2-T),P(DPP2ODT2-T),P(DPP6DOT2-TT),P(DPP2ODT2-TT).

System	V$_{OC}$ [mV]	Jsc[$mAcm^{-2}$]	FF[%]	PCE[%]	E$_g$-eV$_{OC}$[meV]
P(DPP6DOT2-T)	666± 10	7.32± 0.3	67± 3	3.3± 0.3	664
P(DPP2ODT2-T)	686± 10	11.30± 0.1	64.80± 2	5± 0.1	644
P(DPP6DOT2-TT)	634± 10	11.98± 0.1	59.95± 1	4.52± 0.1	696
P(DPP2ODT2-TT)	652± 10	17.37± 0.2	54± 3	6.12± 0.3	678

Figure 4.10 compares the j-V curves for the four polymers under optimized processing conditions. The main distinguishing factor between the polymers is the j_{sc} value which spans a huge range from 7.3 mA/cm^2 to around 17.4 mA/cm^2.

P(DPP2ODT2-TT) has the highest j_{sc} value while P(DPP6DOT2-T) exhibits the lowest j$_{sc}$. P(DPP2ODT2-T) and P(DPP6DOT2-TT) show an intermediate j_{sc} of around 11.3-12 mA/cm^2. There are also significant differences in the fill factor (FF) of the cells. To exclude the effect of device thickness on the fill factor we make sure to report values for the cells having the same active layer thickness (∼ 250 nm). Interestingly, the P(DPP2ODT2-TT) system with the highest j$_{sc}$ also shows the lowest FF. In general, 6-dodecyloctadecyl (-6DO) substituted DPP's have a higher fill factor value compared to 2-octyldodecyl (-2OD) substituted DPP's. There are minor differences in the V$_{OC}$ values which are spread in the range of 50mV for the four polymers. Also, superimposed on the j-V curves is the external generation efficiency (EGE) data measured using time delayed collection field (TDCF). There is a stark difference in the overall generation efficiency between the polymers and the trend explains the difference in j_{sc} values between the polymers. Another important observation is that the generation efficiency for all the polymers is nearly independent of the applied pre-bias voltage, the filed-independent generation efficiency is indicative of the fact that geminate recombination of CT-excitons is not limiting the photo-generation process in these blends.

Looking at the EQE spectra it is clear that the EQE values are considerably lower in the spectral region where polymer mainly absorbs (NIR). This suggests that the fullerene excitons predominantly contribute to the photocurrent. In the polymer region, EQE values follow the same trend as the j_{sc} with P(DPP2ODT2-TT) having a maximum EQE of 40% , P(DPP2ODT2-T) and P(DPP6DOT2-TT) show an EQE of around 23% while P(DPP6DOT2-T) has the lowest EQE of around 12%. In the subsequent sections of this chapter we investigate the reasons for vastly different performance among the four polymers and understand the underlying device physics in these solar cells.

4.4 Charge transport and non-geminate recombination dynamics

A technique known as open-circuit corrected charge carrier extraction (OTRACE) was used to determine the mobility and effective lifetime of charge carriers under realistic device operating conditions. OTRACE measurements were conducted by Sascha Ullbrich from the Dresden Integrated Center for Applied Physics and Photonic Materials (IAPP).

OTRACE is a modified analogue of photo-CELIV technique which provides better temporal resolution by limiting the RC time of the device (for more information see the experimental section). Figure 4.11 shows the typical photocurrent transient for the four DPP polymers. The charge carrier mobility can extracted from the peak position of the current transient and integration of the transient curve provides the charge charge carrier density (n) [124]:

$$\mu = \frac{d^2}{2A' t_{max}^2}\left[\frac{1}{6.2\left(1+.0002\frac{\Delta j}{j_o}\right)}+\frac{1}{\left(1+0.12\frac{\Delta j}{j_o}\right)}\right]^2 \tag{4.1}$$

where left hand side of the bracket denotes the average extraction time and the term in the bracket is a correction factor to account for redistribution of the electric field within the device during charge extraction. A' is the slope of applied voltage, j_0 is the current response with the capacitive offset, Δj represents the maximum current due to the drift of carriers and t_{max} is the time at which current transient peaks.

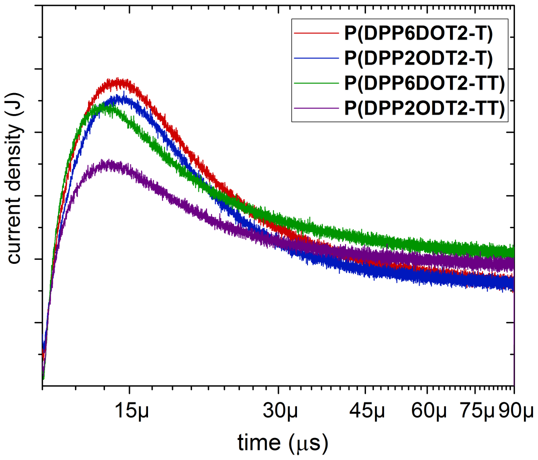

Figure 4.11: Photocurrent transient measured after a delay time (t_d) of 3μs between photogeneration and application of linear extraction pulse.

We estimate the effective charge carrier mobility for the four polymer:fullerene blends as a function of delay time (Figure 4.12). We observe that the charge carrier mobility increases with increasing delay time (t_d) which we attribute to decreasing supersposition of the RC time with the current transient peak.For delay times (t_d) greater than 10^{-5} s the effect of RC time is almost negligible and the mobility value saturates. For all the polymers the effective charge carrier mobility (μ_{eff}) we obtained is on the order of 10^{-3} cm^2 V^{-1} s^{-1}, which is in good agreement with values that have previously been reported for this material class [125]. P(DPP6DOT2-T) has the highest μ_{eff} with an average value around 7 $\cdot 10^{-3}$ cm^2 V^{-1} s^{-1}, while other polymers exhibit marginally lower values with P(DPP2ODT2-TT) having the lowest average mobility of around $2 \cdot 10^{-3}$ cm^2 V^{-1} s^{-1}. DPP's with farther branching point (-6DO) showed higher mobilities compared to the DPPs with closer branching position (-2OD) which can be attributed to their closer π-stacking and a higher degree of crystallinity (see the morphology section).

Apart from the effective charge carrier mobility (μ_{eff}) OTRACE results also give the carrier lifetime (τ_{eff}). In figure 5.12 we plot the mobility-lifetime product ($(\mu\tau)_{eff}$) as function of carrier carrier concentration.$(\mu\tau)_{eff}$ is a useful figure of merit as it depicts the competition between field-dependent charge carrier collection and non-geminate recombination. Both these processes dictate the field (external bias) dependence of the photocurrent in the device and essentially govern the fill-factor of the cell. The $(\mu\tau)_{eff}$ product values obtained for these DPP polymers are amongst the highest reported in polymer:fullerene blends with average values around 10^{-5}-10^{-7} cm^2 V^{-1}. The $(\mu\tau)_{eff}$ product for P(DPP6DOT2-T) was an order of magnitude higher compared to P(DPP2ODT2-TT). This explains higher average fill factor values for P(DPP6DOT2-T) (FF $\approx$ 65-70%) as compared to P(DPP2ODT2-TT) (FF $\approx$ 55-60%) over a wide range of film thicknesses.

Additionally, by tracing the evolution of charge carrier density as a function of delay time (t$_d$) we identify parameters associated with non-geminate recombination

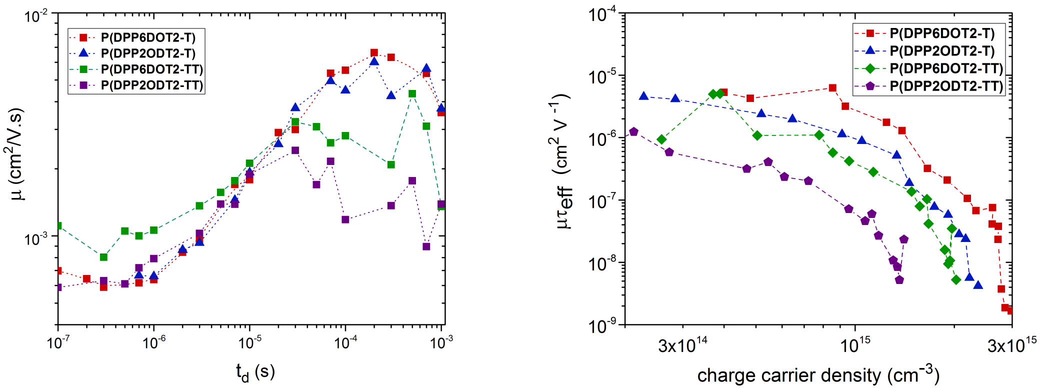

Figure 4.12: Charge carrier mobility as a function of delay time (t_d) for the four polymer:fullerene blends(Left).Mobility-lifetime product plotted as a function of charge carrier concentration (Right).

(Figure 4.13). The non-geminate recombination rate in it's most generic form can be expressed as:

$$R = k \cdot n^{(\alpha+1)} \tag{4.2}$$

where k is the recombination prefactor and $(\alpha + 1)$ denotes the order of recombination. For delay times $< 10^{-5}$ s the carrier concentration (n) nearly stays constant which implies that the non-geminate recombination rate is negligible. For delay times $> 10^{-5}$ we observe a power-law decay (n$\sim$ t$^{-\frac{1}{\alpha}}$) for all the DPP polymers. By fitting this part of the curve we obtain the recombination order (α+1) of 3.56 for 6DO-DPPs and 3.1 for 2OD-DPPs. The difference in recombination cross-section can be related to the varying fibrillar morphology which changes the effective donor-acceptor interfacial area where mobile charge carriers can recombine. Moreover, recombination orders (α+1) > 2 (beyond the classical Langevin case) have previously been associated with disordered density of states (DOS), carrier concentration dependent mobility and recombination in presence of traps [126, 127, 86].A recent model published by Hofacker et al., [128] treats simultaneous thermalization and recombination of charge carriers. Thermal activation of localized carriers in tail states is what contributes to higher (>2) recombination orders (Figure 5.14). Interestingly, decent fill factors were obtained for all the polymers ($\sim$55-70%) which points to the fact that trap-mediated recombination might not be a detrimental loss mechanism in systems with sufficiently high mobility, as far as fill-factor is concerned.

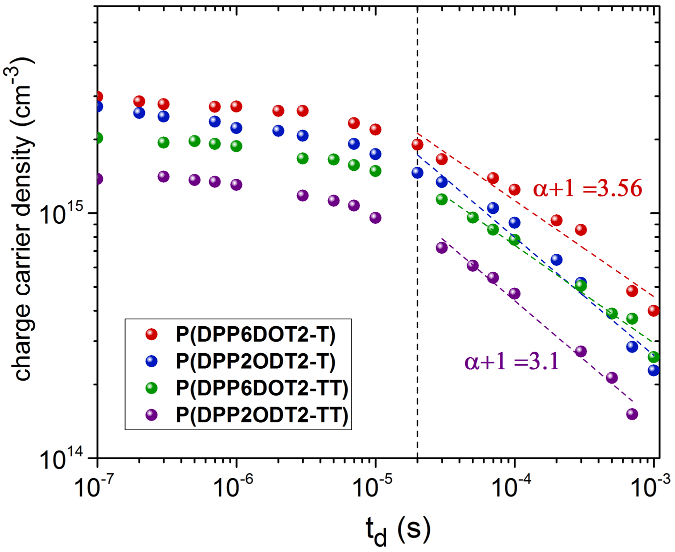

Figure 4.13: Evolution of charge carrier density (n) as a function of delay time (t_d).

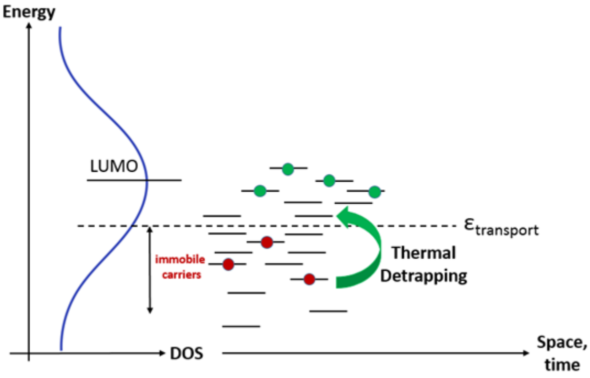

Figure 4.14: Schematic depicting trapped electrons in shallow tail states. Trapped carriers need thermal activation to become mobile and thus be available for recombination. This additional activation step results in higher order $(\alpha + 1) > 2$ recombination.

4.5 Morphological Characterization

4.5.1 GIWAXS and TEM

We used grazing incidence wide angle x-ray scattering (GIWAXS) and transmission electron microscopy (TEM) to investigate the morphology of the neat polymer and polymer:fullerene blend films. Figure 5.15 shows the 2D GIWAXS images for the neat and the blend films. For the neat films we mainly observe three peaks:second (200) and third (300) order reflections related to the lamellar stacking of the alkyl chains and a broad π-stacking peak (010) at relatively higher q-values. In neat films, the π-stacking peak is most intense in the out-of-plane (q$_z$) direction indicating that the majority of the crystallites have a face-on orientation with π-stacking direction being orthogonal to the substrate plane. On close investigation of the position of the π-stacking peak (Figure 4.16) we find that the polymers with bulky -6DO side chains stack closer compared to the polymers with -2OD side chains. Polymers with bulky -6DO side chains have a π-stacking distance around 3.52 Å ($q_{(010)} = 1.79$ Å^{-1}) and lamellar spacing of 28 Å, while polymers with -2OD side chains had a larger π-stacking distance of 3.63 Å ($q_{(010)} = 1.73$ Å^{-1}) and a lamellar spacing around 16 Å.

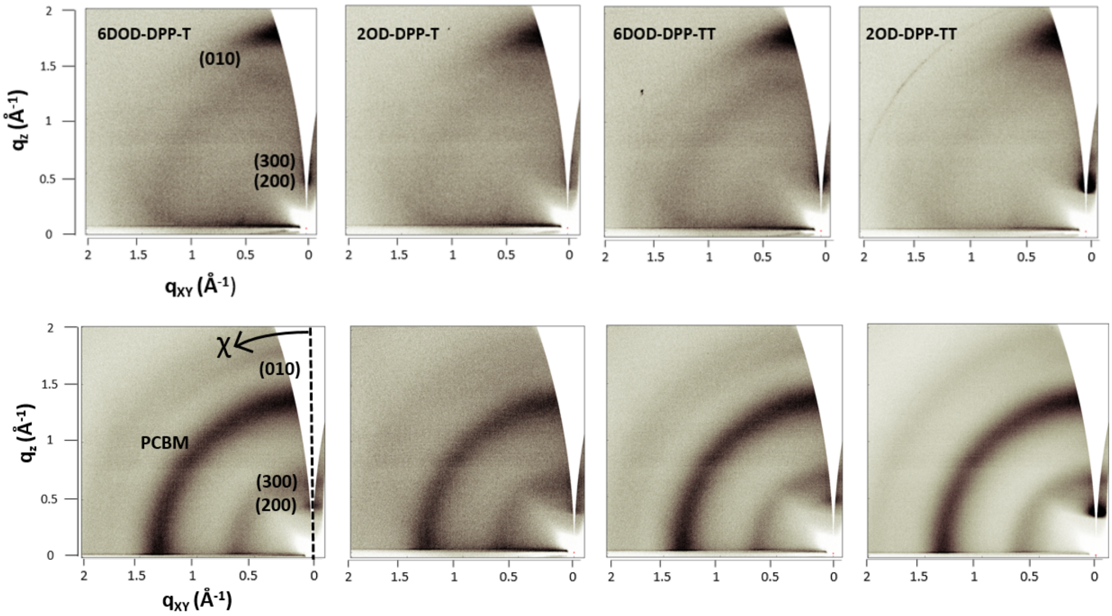

Figure 4.15: 2D GIWAXS images for the neat polymer (top) and polymer:fullerene blend films (bottom).

The fact that the -6DO DPPs stack closer as compared to -2OD DPPs validates our design principle that moving the alkyl branching position further away from the backbone enhances interchain π-orbital interactions and leads to reduced stacking distances. Furthermore, as the π-stacking direction is one of the principal directions for the transport of charge carriers this also supports our finding that the mobility of -6DO DPPs is marginally higher compared to the -2OD DPPs.

In case of polymer semiconductors it is often very difficult to compute the exact crytallite size using GIWAXS peaks because of the defects and the paracrystalline disorder [104]. A coherence length (L_c) can be estimated from the peak widths instead, giving an approximate idea about the crystallite size. We look at the widths of the π-stacking peak and compute the coherence length (L_c) according to the relation :

$$L_c = \frac{2\pi K}{\Delta q} \tag{4.3}$$

where K is the shape factor (0.8-1) and Δq is the full width at half maxima of the peak. We find that the polymer P(DPP6DOT2-T) has the largest coherence length (L_c)of 41 Å while P(DPP2ODT2-TT) has the smallest L_c around 23 Å.P(DPP2ODT2-T) and P(DPP6DOT2-TT) show an intermediate L_c values

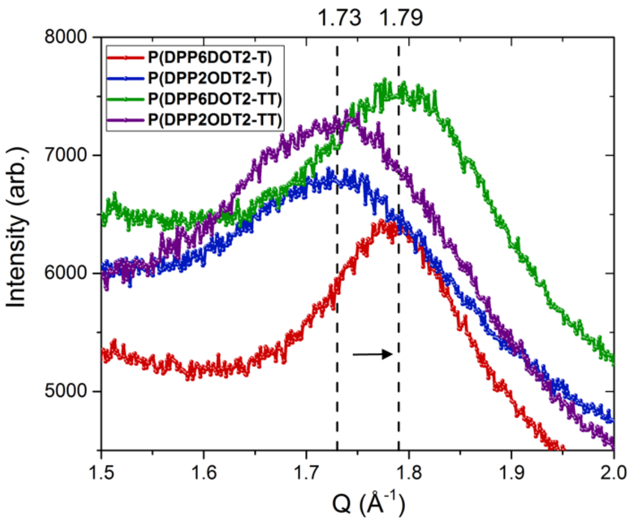

Figure 4.16: Radially integrated π-stacking peak position for the four DPP polymers. The arrow cleary indicates the shift in q-position of the peak for -6DO DPPs, larger q values imply shorter distances in real space.

around 30 Å. Interestingly, the π-stacking coherence length follows the same trend as the polymer fibril diameters as determined from the TEM images. Based on this, one can speculate that the polymer chains are predominantly arranged such that the π-stacking direction roughly coincides with the short fiber axis of the polymers. Similar analysis for the blend films was not possible as the intensity of the π-stacking peak is much weaker. This might be due to disrupted crystallization in the presence of fullerene or due to the intercalation of fullerene molecules within the polymers chains leading to a lack of registry between the polymer backbone planes.

Furthermore, to calculate the orientation distribution of crystallites, we mapped the intensity of the π-stacking peak as a function of polar angle(χ). Here $\chi = 0°$ corresponds to strictly out-of-plane scattering signal resulting from face-on crystallites while $\chi = 90°$ corresponds to in-plane scattering related to edge-on crystallites. For the detailed procedure of the pole figure analysis the reader is referred to earlier reports [129, 130, 108]. For the thienothiophene (-TT)based DPP's, a reliable determination of (010) pole figures was difficult due to the weak scattering signal. However, pole figures of the π-stacking peak were reconstructed for terthiophene (-T) based DPP's.

P(DPP6DOT2-T) and P(DPP2ODT2-T) reveal a bimodal distribution of crystallites with both face-on ($\chi = 0°$) and edge-on crystallites ($\chi = 90°$) contributing to the π-stacking peak. Since the scattering signal mainly arises from the crystalline part of the polymer film, the area under the pole figure curve gives an idea about the relative proportion of crystalline regions between the the films. Figure 4.17 showcases the higher crystallinity for P(DPP6DOT2-T) relative to P(DPP2ODT2-T) corroborating the rationale that moving the alkyl branching point further away from the backbone (-6DO side chains) increases the tendency for aggregation and

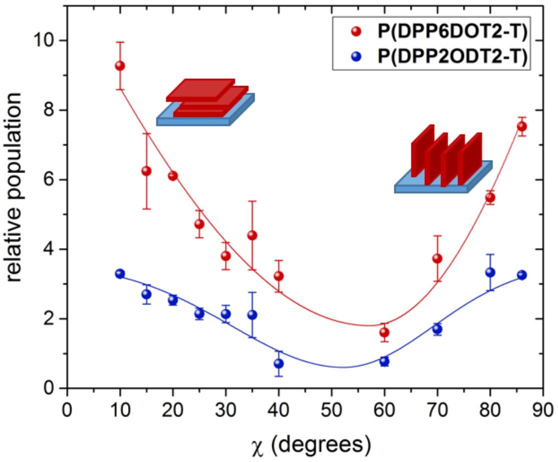

Figure 4.17: (010) pole figures for P(DPP6DOT2-T):PC[70]BM and P(DPP2ODT2-T):PC[70]BM films supplying information on the relative degree of crystallinity(rdoc). For the P(DPP6DOT2-T) and P(DPP2ODT2-T) rdoc value is 44 %.

yields polymer phases with a higher DoC.

To look at the morphology in real space we use transmission electron microscopy (TEM). TEM images reveal a microstructure consisting of semicrystalline polymer fibrils and interspersed fullerene domains (Figure 4.18). To verify that the fibrils indeed constitute the polymer phase we use energy-dispersive x-ray spectroscopy (EDX) to measure the elemental map (see Figure 4.19). In particular we map the distribution of sulphur (S) as it is the only element which is exclusively present in the polymer's DPP unit but is not present in the fullerene molecule. Sulphur distribution re-traces the fibril network which verifies that the fibrils are predominantly composed of polymer phase.

To analytically determine the fibril size TEM micrographs were analyzed using the imageJ software and the plug-in DiameterJ was used to obtain the statistical distribution of fibril widths. Diameter J uses a series of image segmentation algorithms to yield binary images which are then processed using the Euclidean distance transformation algorithm which yields a fiber diameter distribution [131] (see Figure 4.20). Mean Fiber diameters for P(DPP6DOT2-T) and P(DPP6DOT2-TT) were around 25.5 nm and 16.2 nm respectively, whereas for P(DPP2ODT2-T) and P(DPP2ODT2-TT) fiber diameters were 15.2 nm and 13.3 nm. Earlier work by Janssen et. al. [132] suggests a direct correlation between polymer solubility and the fiber diameter of the polymer domains where the fiber width increases with increasing solubility. The family of DPP-polymers investigated in this study also follow this empirical observation where polymers with bulky -6DO side chains (higher solubility) have wider fibers compared to polymers with smaller -2OD side chains.

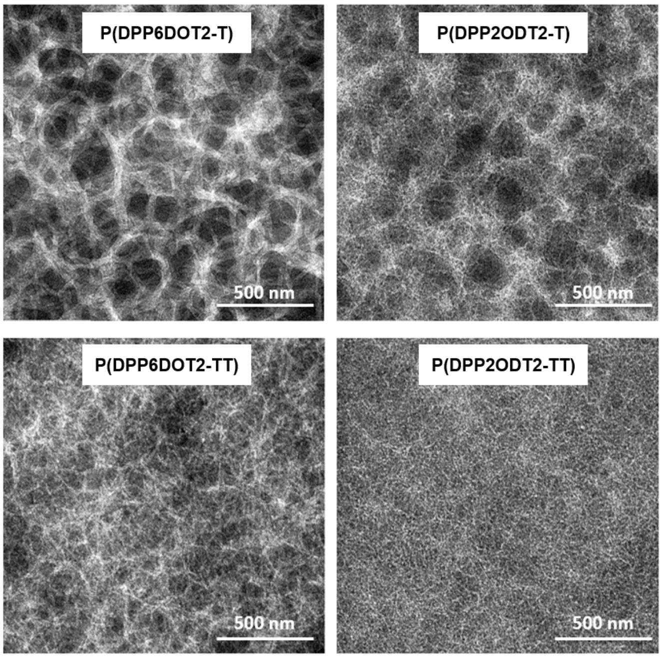

Figure 4.18: TEM mircographs for the polymer:fullerene blend films, clearly revealing polymer fibril formation. The width of the fibrils is directly proportional to the polymer's solubility in the solvent used for spin coating.

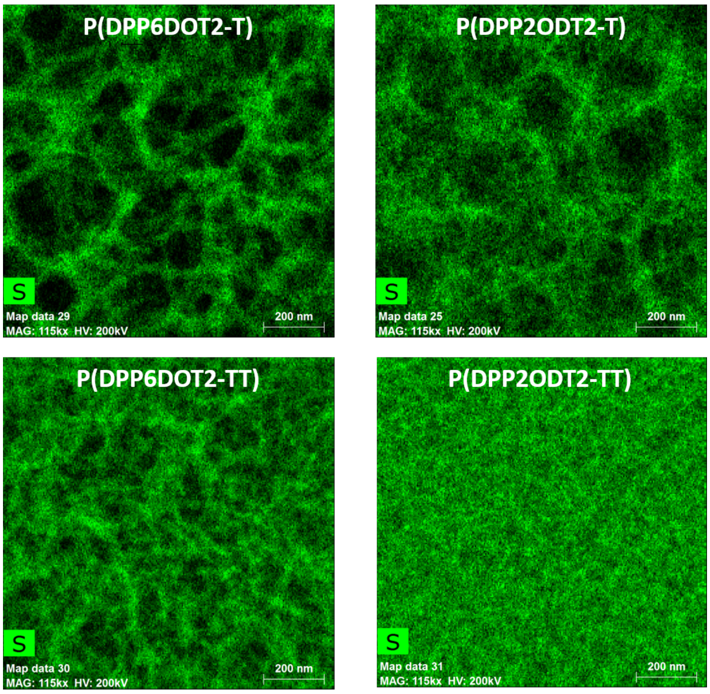

Figure 4.19: Sulphur maps for the polymer:fullerene blend films obtained using energy-dispersive x-ray spectroscopy (EDX).

4.6 Photoluminescence (PL) quenching

To study the effect of the fibrillar morphology and specifically the fiber width and purity on photogeneration PL-quenching measurements were carried out. The PL-

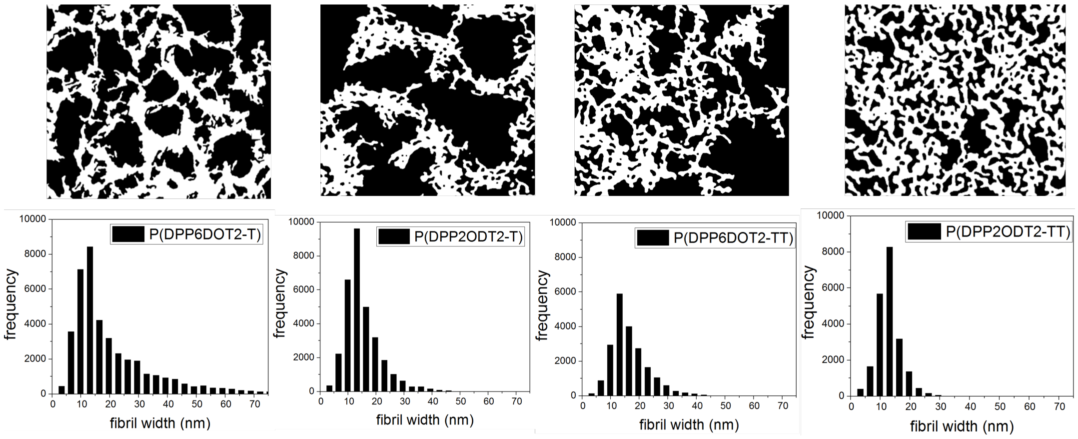

Figure 4.20: Binary TEM images obtained after image segmentation and the subsequent fibril width histograms for the four polymer systems.

setup used for the measurements is located in Prof. Dieter Neher's lab in the University of Potsdam and all the PL-quenching measurements were conducted by Dr. Ulrich Hörmann and Stefan Zeiske.

PL-quenching measurements are quite informative as the degree of PL quenching correlates with the fraction of excitons that dissociate at the donor-acceptor interface. To selectively excite polymer domains, we used an infrared pump LED with peak emission at 850 nm. The PL signal was corrected for absorption over the spectral range of the LED in order to compare the relative PL count of the pure polymer and blend films. All the blend films showed poor luminescence quenching (see Figure 4.21). The PL quenching efficiency of P(DPP6DOT2-T) was surprisingly low, only 15% of the neat polymer signal was quenched. P(DPP2ODT2-T) and P(DPP6DOT2-TT) represent an intermediate case with quenching efficiencies of around 25% and 29% respectively. The best performing system, P(DPP2ODT2-TT), showed a quenching efficiency of about 48%. Although, the PL-quenching efficiency correlates well with the polymer fibril diameter as reported earlier [133], the overall PL quenching is rather low as compared to other high performing polymer:fullerene systems [134, 135].

There are two possible reasons for this poor PL quenching. Firstly, DPP based polymers exhibit rather short exciton lifetimes ($\sim$ 20-50 ps) which allows for a large fraction of polymer excitons to relax back to the ground state before reaching the donor-acceptor interface [136, 137]. In the next chapter of this thesis, we perform transient absorption spectroscopy (TAS) on these polymers and compute the lifetime of excited states). Secondly, in these low band-gap polymers, the energy of the charge transfer state (E_{CT}) lies close to the singlet energy of the donor. This may cause the CT-states to repopulate the donor excited states, thus forming an indirect radiative pathway for CT-states [138]. To verify if this is the case in our system we perform PL measurements on devices at short-circuit (j_{sc}) and open-circuit (V_{OC}) conditions. The idea behind these measurements is that under short-circuit conditions the built-in field acts as an additional driving force and assists in dissociation of the CT states contrary to the CT-dissociation under open-circuit conditions. This field-assisted dissociation of CT-states would translate in lower PL quantum yields

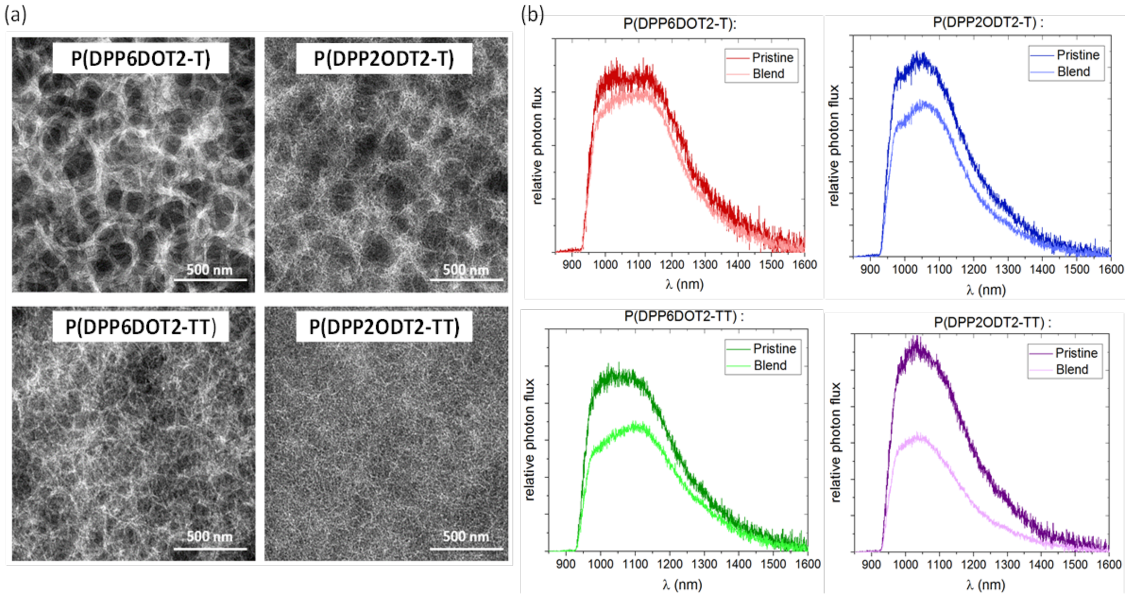

Figure 4.21: (a) TEM micrographs for spin cast polymer:fullerene blend films represented again for the sake of comparison (b) PL-quenching: PL spectra of neat polymer and blend films. Excitation wavelength(λ)=850nm).

as the back transfer to singlet states is avoided. Interestingly, in our measurements we find nearly similar quantum yield for PL under short-circuit (j_{sc}) and open-circuit (V_{OC}) conditions. This implies in our case, the field independent PL yield and field independent charge generation measured via TDCF indicates an efficient dissociation of CT states into free carriers, which makes repopulation of singlets via CT states an unlikely process. Therefore, we conclude short exciton lifetimes to be the predominant cause for the observed poor PL quenching of all tested materials. Overall, even though the DPP polymers absorb a large fraction of the electromagnetic spectrum most of the excitons are not harvested. The situation is aggravated in systems with coarser morphology i.e. bigger polymer fibrils, as shown by the data in Figure 4.21.

4.7 Voltage losses

Power conversion efficiency (PCE) of low band gap polymer solar cells is largely limited by their low V_{OC} values. If the V_{OC} can be improved which then combined with their high photocurrent could yield highly efficient solar cells. Thus understanding the origins of low V_{OC} in these systems is of paramount importance. In this section we quantify the voltage losses (ΔV_{loss}) for the DPP solar cells. According to a recently developed formalism, the analytical expression for the V$_{OC}$ is given as [71] :

$$V_{OC} = \frac{E_{CT}}{q} + \frac{k_B T}{q} ln \frac{J_{Ph} h^3 c^2}{f q 2\pi (E_{CT} - \lambda)} + \frac{k_B T}{q} ln(EQE_{EL}) \tag{4.4}$$

where E_{CT} is the energy of the charge transfer (CT) state, $k_B T$ is the thermal energy, J_{Ph} is the photocurrent, h and c represent the Planck's constant and the

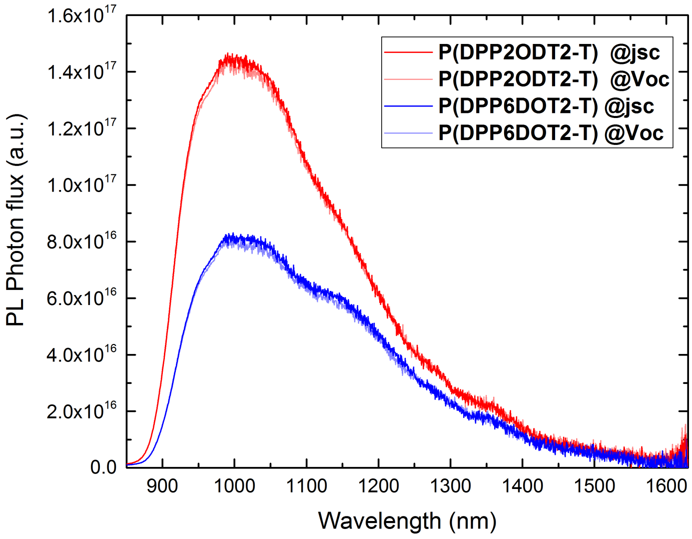

Figure 4.22: Photoluminescence spectra of devices based on P(DPP2ODT2-T) and P(DPP6DOT2-T) under short-circuit and open-circuit conditions.

speed of light in vacuum respectively, f is the donor-acceptor coupling factor and λ is the reorganization energy.

This equation entails some very important implications. First of all, it suggests that the value of the V$_{OC}$ is dictated by the energy of the interfacial charge transfer state (E_{CT}) and that the (E_{CT}) represents the theoretical upper limit for the V$_{OC}$ at T= 0 K. The second part of the left hand side represents the radiative loss (ΔV_{rad}) of charge carriers while the last term represents the non-radiative ($\Delta V_{non-rad}$) loss of carriers which is related to the quantum efficiency of electroluminescence (EQE_{EL}).

As a first step in determining voltage losses, E_{CT} needs to be evaluated. We use sensitive-EQE_{PV} measurements in the sub-bandgap region combined with electroluminescence (EL) spectra of solar cells driven at low forward voltages to determine E_{CT}, which is defined as the crossing point of sensitive-EQE_{PV} and EL spectra according to Rau's reciprocity relations [70].

As is usually the case for low gap polymer:fullerene systems, the singlet energy of the donor (E_{D*}) lies very close to E_{CT} [138]. As a result, broad CT-state transitions are often masked by the absorption and emission tails of the neat films. In our case we observe something similar where the broad CT-state transitions are not visible (see Figure 4.23). Nevertheless, the CT energy (E_{CT}) can be determined from the intersection point of the EQE_{PV} and EL [120]. In our case, all the DPP blends have a nearly identical E_{CT} ~1.33±0.05 eV. Intriguingly, the E_{CT} values for the blend films are marginally higher (≈ 30-50 meV) than the optical gap of the neat polymers which were obtained similarly (see section 5.2.2). This can be attributed to less aggregation of the polymer chains in the blend films, shifting the effective-gap of the blended films to higher energies. More importantly, these findings point to the fact that E_{CT} lies very close to the donor singlet level (E_{D*}), implying nearly zero electron transfer losses (E_{D*} - E$_{CT}$ ≈ 0 eV). From the slope of the absorption

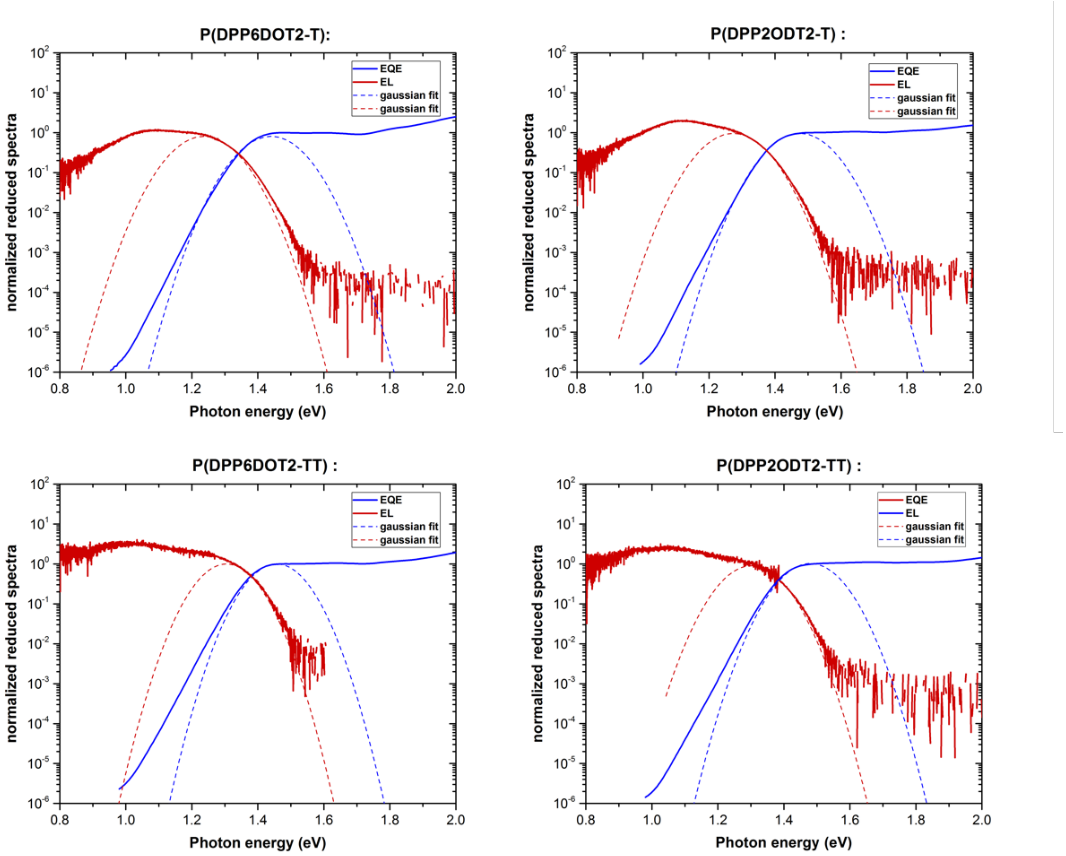

Figure 4.23: Normalized,reduced sensitive-EQE_{PV} and EL spectra for the optimized devices. Dashed lines are the Gaussian fits (fit parameters: f-coupling strength,λ-reorganization energy, and E_{CT}). Additionally, E_{CT} can also be estimated from the crossing point of the sensitive-EQE_{PV} and the EL spectra.

(EQE_{PV}) tails we determine the Urbach energy (E_U) which is around 62-65 meV in these systems.

The second and third term of the equation 5.5 represent radiative (ΔV_{rad}) and non-radiative ($\Delta V_{non-rad}$) voltage losses of free carriers respectively:

$$\Delta V_{rad} = \frac{E_{CT}}{q} - V_{OC,rad} \tag{4.5}$$

$$\Delta V_{non-rad} = V_{OC,rad} - V_{OC} \tag{4.6}$$

$V_{OC,rad}$ is the thermodynamic limit of V_{OC} which would be reached in the absence of non-radiative recombination. $V_{OC,rad}$ can be calculated from the sensitive-EQE_{PV} spectrum by employing the reciprocity relation between absorption and emission.Radiative and non-radiative losses are nearly identical among all tested DPP systems: 255 mV (radiative) and 418 mV (non-radiative). These calculation results suggest that non-radiative recombination pathways dominate the overall voltage losses and are slightly higher than typical values of around 350 mV [139]. According to the energy-gap law [28], high non-radiative decay rates in DPP polymers are related to their low optical band gap which might intrinsically limit the maximum achievable V_{OC} in DPP solar cells.

4.8 Summary and Conclusion

In this study, we investigated a series of DPP polymers with modifications of the alkyl chain length and the branching point of the side chains and studied their suitability for bulk-heterojunction solar cells. The alkyl branching position influences the aggregation tendency and polymers with the branching point farther away from the backbone exhibit a higher degree of crystallinity. The overall alkyl chain structure also influences the polymer's solubility and affects the polymer fibril formation. TEM images reveal polymer fibrils with varying diameters. These structural differences have a strong impact on the photogeneration of charge carriers. By time delayed collection field (TDCF) measurements we were able to show field-independent generation which points to the fact that the geminate recombination of charge-transfer excitons is not a major loss mechanism in the photogeneration process. The crystallinity of the polymer phase has a direct implication on the effective mobility of the blends. 6DO-DPP's show higher effective mobility-lifetime values over a broad range of charge carrier densities. Consequently, 6DO-DPP's also exhibit higher fill factors compared to 2OD-DPP's. Concerning voltage losses, the relative proximity of E_{D*} and E_{CT} points to the fact that there is nearly zero photon energy loss in the electron transfer process. Most of the photon energy loss in DPP polymers can be attributed to radiative and non-radiative decay pathways, especially non-radiative recombination losses are higher than for other donor:acceptor systems, which is related to the small optical gap of DPP polymers (according to the energy-gap law). OTRACE results indicate that non-geminate recombination in these DPP polymers is affected by traps and the overall recombination rate is influenced by the average size of the polymer fibrils. All these factors show that despite improving the crystallinity of the polymer phase and the charge carrier mobility the solar cell performance was intrinsically limited by inefficient exciton harvesting. The solubilizing alkyl side chains in the DPP polymers should be optimized so that the solubility of the polymers is be kept at minimum, this will lead to a finer morphology and improved photo-current generation. It appears there is a 'trade-off' between the ease of solution processability and the overall device performance. This work once again shows the complexity of bulk-heterojunction solar cells and that improving one aspect, in this case the charge transport properties, will not necessarily lead to an overall improvement in device performance, reminding the community that polymer design rules for photovoltaic applications need careful consideration.

Chapter 5

Electron transfer and charge separation dynamics in the near-zero driving force DPP:PCBM blends

This chapter investigates photo-induced electron transfer and charge separation dynamics in the DPP:PCBM system using a combination of transient absorption (TA) spectroscopy and electromodulated differential absorption (EDA) spectroscopy. In section 5.2, TA spectroscopy results are summarized for the neat polymer and polymer:fullerene blend films. Subsequently, a four-state kinetic model is introduced, and the experimental dynamics are modeled.

In section 5.3, we briefly summarize the transfer integrals calculations using the density functional theory (DFT). Finally, the EDA spectroscopy results are discussed in section 5.4, and the summary and conclusions are provided in section 5.5.

We observe ultrafast electron transfer dynamics despite the zero driving force in these blends. DFT calculations reveal large transfer integral values which explain the fast electron transfer process. Using EDA spectroscopy, we find that the early time (10-100 ps) mobility of carriers is quite high in these blends which also assists in the dissociation of bound electron-hole pairs.

5.1 Introduction

In silicon-based and other conventional inorganic solar cells the photoexcitation process leads to the formation of free electrons and holes owing to their high dielectric constant ($\epsilon_r \sim$ 11-12), where the coulombic interaction between the electron-hole pair is small and effectively screened. Organic solar cells fundamentally differ in this respect where the photoexcitation process leads to the formation of bound electron-hole pairs or excitons owing to the low dielectric constant ($\epsilon_r \sim$ 3-4) of organic semiconductors and poor screening of the coulomb forces between the electron-hole pair. As these excitons diffuse towards the donor-acceptor interface, they undergo a charge transfer reaction owing to the differences in the electron affinity (ΔEA) and the ionization potential (ΔIP) between the donor and acceptor materials.

The charge transfer step leads to the formation of the so-called charge transfer (CT) state where the electron resides on the acceptor, and the hole resides on the donor in a donor:acceptor system. A simple estimation using the point charge approximation while assuming the ϵ_r=3 and electron-hole separation distance of 1 nm yields a binding energy of the order of 0.4-0.5 eV for the electron-hole pair or the CT state. This value is considerably higher than the thermal energy (k_BT) at room temperature, and thus the question arises: how does this interfacial electron-hole pair escape the mutual coulomb potential well? This question has eluded the community for the past couple of decades, although there have been a number of studies providing satisfying explanations [140, 141, 142].

The Onsager-Braun formalism [59] which considers equilibrium between field dependent dissociation of the CT state and the relaxation of the CT state back to the ground state was one of the first theories which was used to study the dissociation process. Despite its initial success, the shortcomings of the Onsager-Braun formalism became evident as many polymer:fullerene systems were discovered which exhibited field-independent photogeneration of carriers [143, 144, 54]. In subsequent studies, two major contributions were put forward which possibly lead to the screening of the coulomb potential at the interface: (i) a number of studies reported the formation of interfacial dipoles which can partly screen and lower the coulomb potential at the donor:acceptor interface [145, 146] and (ii) the delocalization of charge carriers was found to be an important parameter [147]. In this regards, Jakowetz et al. [148] reported a direct correlation between the fullerene cluster size and the charge separation rate where the argument is that the fullerene clusters lead to the delocalization of electrons and can provide access to band-like states at early times. The Arkhipov-Baranowskii model extends the Onsager-Braun formalism by taking into account the formation of interfacial dipoles and delocalization of charge carriers and provides a very good correlation with the recent experimental data [147, 149].

Despite the early success of the Arkhipov-Baranowskii model, the theory does not hold well for many polymer:fullerene systems and many questions remain unanswered. In particular, the mechanism of charge transfer and charge separation in systems with near-zero driving force is relatively unexplored. The DPP:PCBM system discussed in the previous chapter provided us with a relevant zero driving force system for electron transfer, and in this chapter, we discuss the study of charge transfer and charge separation dynamics in this system using a combination of transient absorption (TA) spectroscopy and electromodulated differential absorption (EDA) spectroscopy.

5.2 Transient Absorption (TA) Spectroscopy

To study the electron transfer dynamics and other important photophysical processes, transient absorption (TA) spectroscopy measurements were performed on pristine and polymer:fullerene blend films. (Note: The TA set-up used for the measurements is located in Prof. Natalie Banerji's lab and the all the measurements were performed by Gareth Moore.)
To quantify the timescale of the processes, we employed the so-called 'global analysis'. It is essentially a fitting routine where the dynamics at each spectral position are fitted simultaneously using a multi-exponential decay function [150]. The dependence of the amplitude linked to the exponentials with wavelength is referred to as amplitude spectra. For each sample, we will present the transient absorption spectra and the corresponding amplitude spectra obtained through global fitting analysis. Figures 5.1 and 5.2 show the TA and the amplitude spectra for the pristine polymers films respectively.

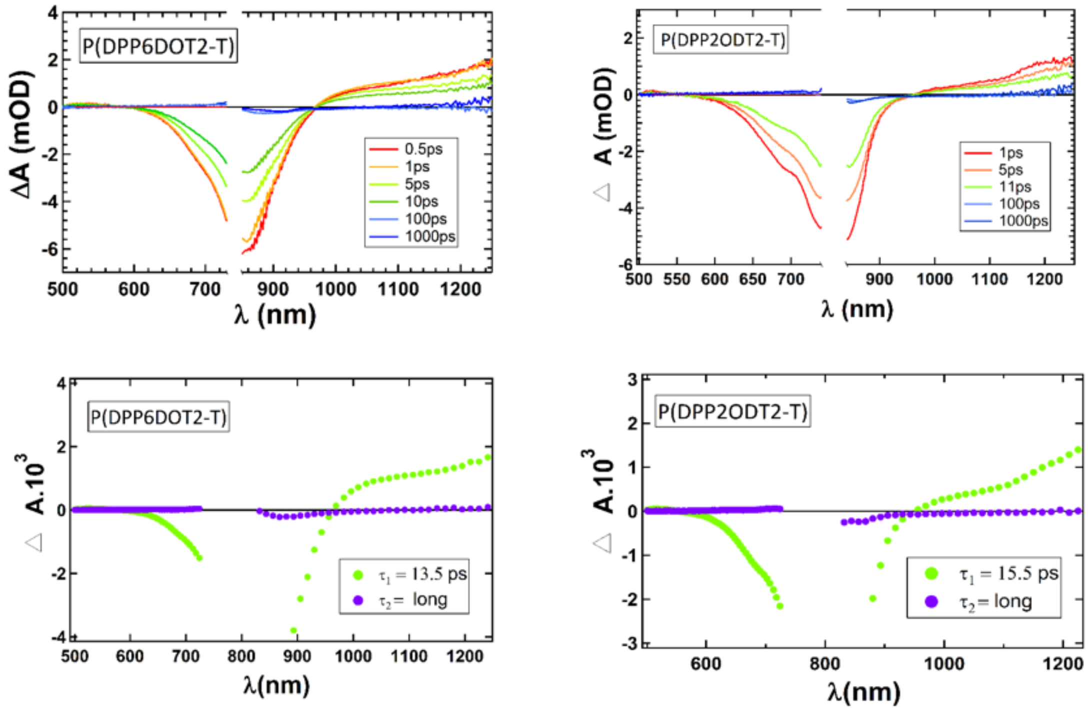

Figure 5.1: Transient absorption (TA) spectra (top) at given pump-probe time delays for the polymers P(DPP6DOT2-T) and P(DPP2ODT2-T) and the corresponding amplitude spectra (bottom) obtained through global fitting analysis.

For the four polymers, the spectra look quite similar wherein for all the cases two main spectral bands are observed. In the 600-950 nm range, a huge negative signal is observed, which corresponds to the ground state bleach (GSB) of the polymers. This is justifiable as this signal lies in the spectral window where these polymers show steady-state absorption. On the other hand, a positive band in the range of 950-1250 nm is also observed and corresponds to the excited state absorption (ESA) signal. This ESA band can be mainly ascribed to the singlet excitons as these are the only photogenerated species following pump excitation. From the decay constant of the ESA signal, the lifetime of the singlet excitons can be estimated. Looking at the amplitude spectra for these polymers, we get a clean decay constant of the ESA band in the range of 13.5 to 20 ps. For the thiophene substituted polymers: P(DPP6DOT2-T) and P(DPP2ODT2-T), the singlet lifetime is of the order of 13.5 and 15.5 ps respectively. Whereas for the thienothiophene substituted DPP's: P(DPP6DOT2-TT) and P(DPP2ODT2-TT), the singlet lifetime is 17.6 and 20 ps respectively. These singlet lifetimes are very short when compared to the singlet lifetimes in other conventional polymer semiconductors where they range between hundreds of picoseconds [34]. In the case of P(DPP2ODT2-T) we see a small indent in the positive signal [see Figure 5.1 (left)], which we believe arises because of the very weak stimulated emission (SE) signal. Due to the low oscillator strength of the SE, it hardly arises as a negative signal in its own but usually appears as the indent in the positive signal.

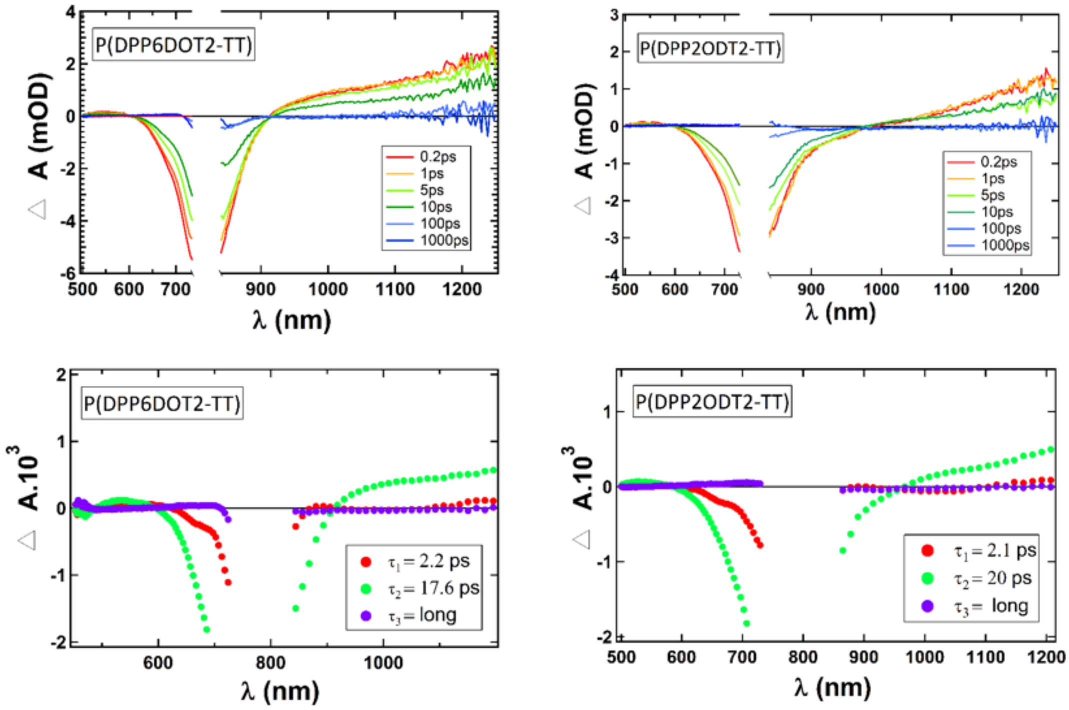

Figure 5.2: Transient absorption (TA) spectra (top) at given pump-probe time delays for the polymers P(DPP6DOT2-TT) and P(DPP2ODT2-TT) and the corresponding amplitude spectra (bottom) obtained through global fitting analysis.

For the polymer:fullerene blends the TA and the amplitude spectra are summarized in Figure 5.3 and 5.4. In the case of P(DPP6DOT2-T):PCBM, we observe two spectral bands: GSB of the polymer in the 600-950 nm range and ESA between 950-1250 nm. The early time (at 0.2 ps) spectra looks substantially different compared to the early time spectra of the neat polymer film. This is indicative of the prompt electron transfer process which happens at a timescale within the instrument resolution time (∼100 fs). Also, the amplitude spectra show the shortest time constant of 2.3 ps, which is related to the delayed electron transfer associated with the excitons which need to diffuse to the donor:acceptor interface. A huge positive amplitude signal with a decay time of 17.6 ps is also seen, which can be ascribed to a recombination process. It can be either the recombination of excitons which could not reach the donor:acceptor interface or it can represent the recombination of the charge-transfer (CT) state. The spectral shape of the amplitude function is quite different when compared to the amplitude function of the neat films, which suggests that the 17.6 ps component represents the decay of the CT-state. Indeed, similar CT-state lifetimes have been reported for DPP polymers using pump-push-probe (PPP) spectroscopy by Dimitrov et al. [151]. Thus, there is a very nice agreement with the values given in the literature.

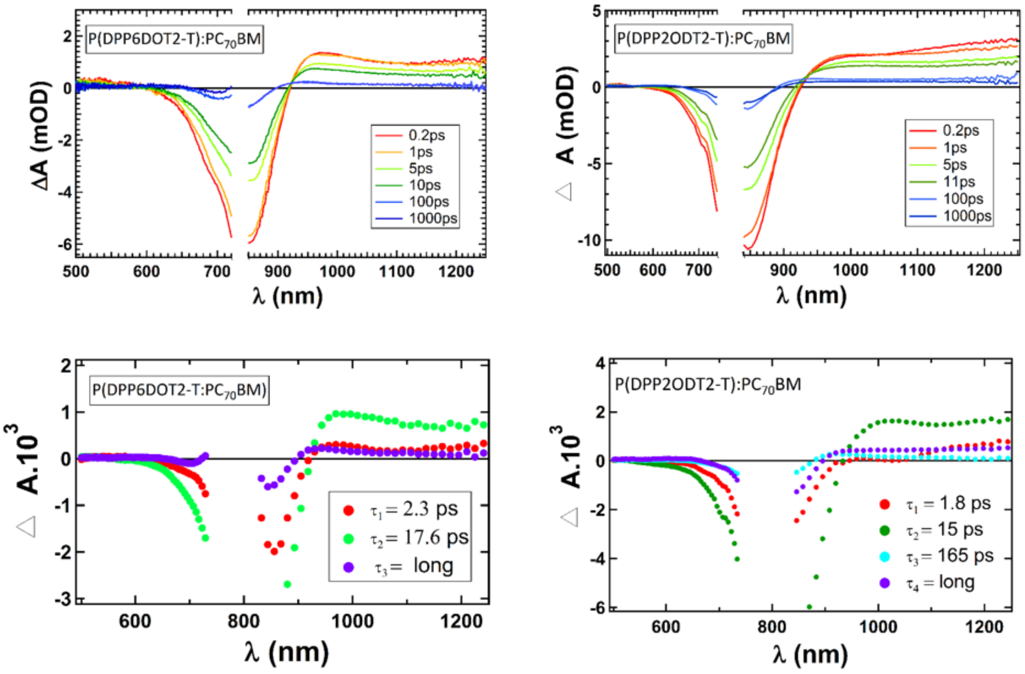

Figure 5.3: Transient absorption (TA) spectra (top) at given pump-probe time delays for the polymer:fullerene blends films- P(DPP6DOT2-T):PCBM and P(DPP2ODT2-T):PCBM and the corresponding amplitude spectra (bottom) obtained through global fitting analysis.

The TA spectra for other polymer:fullerene blend films also show similar features viz. the GSB from the polymer and a relatively flat ESA band in the NIR region. All the blends show a clear difference in the early time spectra compared to the neat films, signaling a prompt electron transfer process. From the amplitude spectra, we get an additional delayed electron transfer component around 2-3 ps and the characteristic CT-recombination decay with a time constant ranging between 15-19 ps. An important finding from this TA data is that the singlet exciton lifetime in the pristine films and the CT-recombination time in the blend films are quite similar. We believe that these two lifetimes are correlated for two specific reasons. Firstly, due to the proximity between the energy of the CT state and the S_1 state, the CT state can back transfer to the S_1 state and then recombine to the ground state. Which would then yield similar decay lifetimes for both the CT states and the singlet states. Secondly, again because of the energetic proximity, the two states can hybridize leading to the formation of the so-called 'LE-CT' complexes [152]. Here, the term 'LE' refers to a locally excited state or a singlet excitonic state. As the two states hybridize, the decay constant of the new states will be indistinguishable which would again yield a similar lifetime in TA measurements.

In the amplitude spectra, the long-time component represents the signature from free charges/polarons. When comparing the long time spectra of the blends we can see a clear difference between the polymers. This difference is also highlighted when we compare the dynamics in the NIR region [Figure 5.5]. The trend in the long-time amplitude signal matches precisely with the trend in the j_{sc} values for the solar cells. This suggests that the yield of carriers extracted at the electrodes is governed by processes happening at early timescale ($\leq$1 ns).

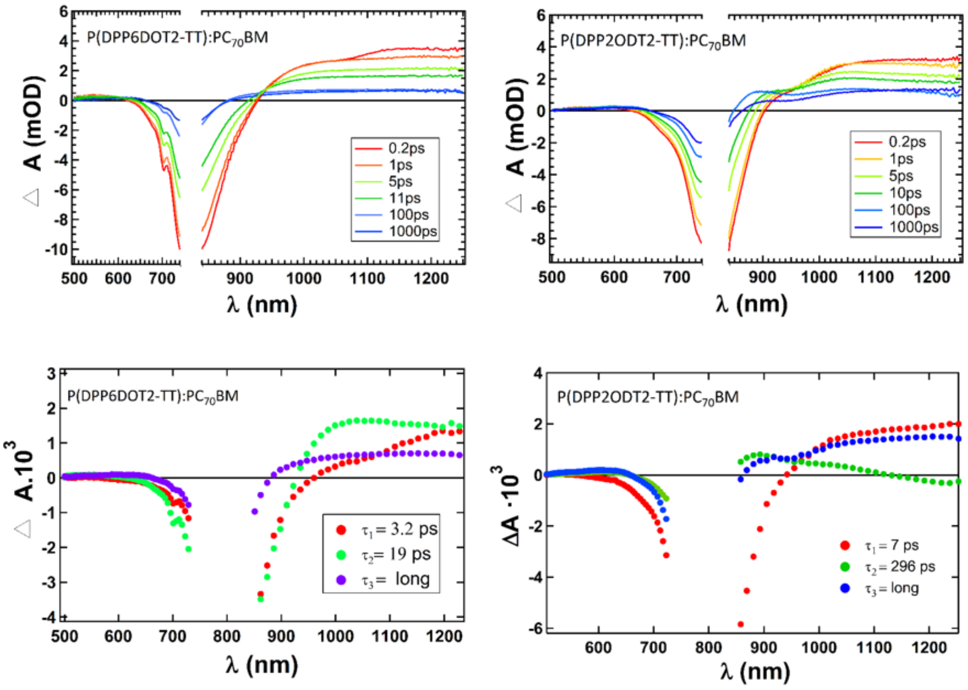

Figure 5.4: Transient absorption (TA) spectra (top) at given pump-probe time delays for the polymer:fullerene blends films- P(DPP6DOT2-TT):PCBM and P(DPP2ODT2-TT):PCBM and the corresponding amplitude spectra (bottom) obtained through global fitting analysis.

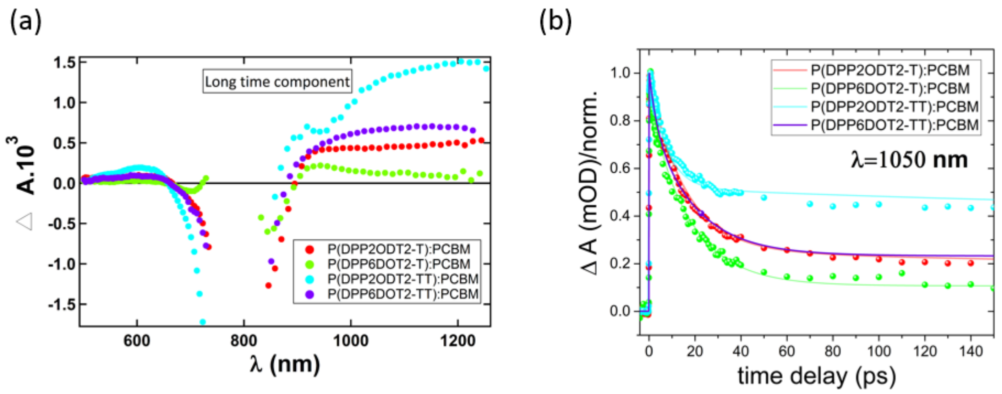

Figure 5.5: (a)Comparison of the long time component amplitude spectra for the four polymer:fullerene blend films (b)Dynamics of the the TA signal (at λ= 1050 nm) as a function of pump-probe delay for the polymer:fullerene blend films.

In order to gain a better understanding of the photophysical processes, a simple kinetic model was developed to simulate the TA spectra and the corresponding dynamics. Simulations for the model were conducted by Andreas Hofacker from the Dresden Integrated Center for Applied Physics and Photonic Materials (IAPP).
It is a four state model consisting of the ground state (GS), the singlet state (S or S_1), the charge transfer state (CT) and the state related to free charges/polarons (F). The transition between each of the states is described using an Arrhenius type rate equation with a certain activation barrier for transitions.

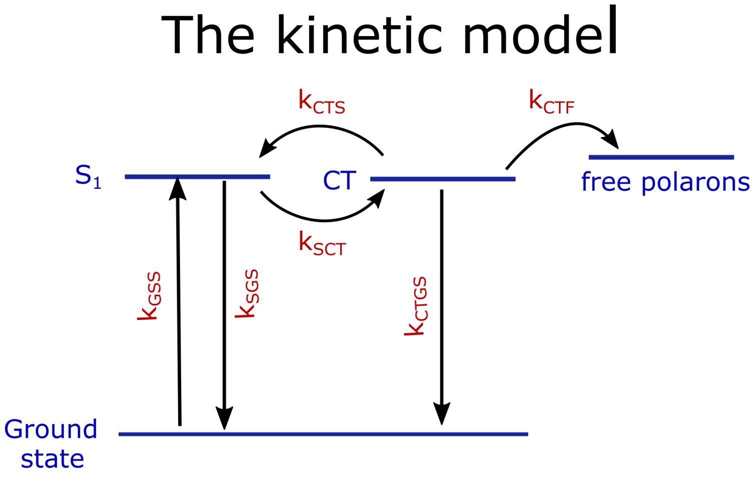

Figure 5.6: (a) A four state kinetic model showing the transitions between the respective states.

The corresponding rate equations are given as follows :

$$k_{GSS} = k^0_{GSS} exp \frac{-\Delta E_{GSS}}{k_B T} \tag{5.1}$$

$$k_{SGS} = k^0_{SGS} \tag{5.2}$$

$$k_{SCT} = k^0_{SCT} \tag{5.3}$$

$$k_{CTS} = k^0_{CTS} \tag{5.4}$$

$$k_{CTGS} = k^0_{CTGS} \tag{5.5}$$

$$k_{CTF} = k^0_{CTF} exp \frac{-\Delta E_{CTF}}{k_B T} \tag{5.6}$$

where the rate k_{XY} refers to the transition from the X state to the Y state. The value of the rate constant prefactors were adopted from the time constants obtained through global analysis. For instance the value for k_{SCT} and K_{CTS} were assumed to be around 2 ps^{-1}. While k_{SGS} was assumed to have a value around 15 ps^{-1} according to the value obtained for singlet lifetimes. The ΔE_{GSS} was assumed to be at 1.33 eV while ΔE_{CTF} was assumed to have a value $\sim k_B T$ according to the recent literature report [93].

Time evolution of the occupation probability can be expressed according to the following relations:

$$\frac{df_{GS}}{dt} = \frac{1}{N_{GS}}[(k_{SGS} f_S N_S + k_{CTGS} f_{CT} N_{CT})(1 - f_{GS}) - k_{GSS} f_{GS} N_{GS}] \tag{5.7}$$

$$\frac{df_S}{dt} = \frac{1}{N_S}[(k_{GSS} f_{GS} N_{GS} + k_{CTS} f_{CT} N_{CT})(1 - f_S) - k_{SGS} f_S N_S (1 - f_{GS}) - k_{SCT} f_S N_S (1 - f_{CT})] \tag{5.8}$$

$$\begin{aligned} \frac{df_{CT}}{dt} = \frac{1}{N_{CT}}[&k_{SCT} f_S N_S (1 - f_{CT}) - kCTS f_{CT} N_{CT} (1 - f_S) \\ &- k_{CTGS} f_{CT} N_{CT} (1 - f_{GS}) - k_{CTF} f_{CT} N_{CT} (1 - f_F)] \end{aligned} \tag{5.9}$$

$$\frac{df_F}{dt} = \frac{1}{N_F}[k_{CTF} f_{CT} N_{CT} (1 - f_F)] \tag{5.10}$$

where N represents the density of states and f is the occupation probability of a respective state. We choose to work with density of states (N) and occupation probabilities (f) but the actual occupation of the state ($N \cdot f$) can be used as a variable itself. As an initial condition (t=0, just after the pump excitation), we assume density of states to be 1 for each of the states, while the occupation probability for the ground state (f_{GS}) was set to 0.7, for the singlet (f_S) and CT-states (f_{CT}) the occupation probability was 0.3 and 0.003 respectively and for the free charge, f_F was set to zero at t=0. The above listed equations form a system of coupled differential equations which were solved using the NumPy package in the python programming language.

This model was able to simulate the experimental dynamics quite accurately. Figure 5.7 shows the experimental and simulated TA dynamics for P(DPP2ODT2-TT):PCBM at three different wavelengths: 720 nm, 1050nm and 1200nm. ESA dynamics in the NIR range (1050,1200 nm) could be reproduced quite closely although there were minor variations in the dynamics of GSB (720 nm). This is mostly due to the overlayed stimulated emission (SE) signal which was not taken into account in the model. The fact that the dynamics could be reproduced quite accurately reaffirms our hypothesis that the CT state has a short lifetime of ∼15 ps, as the rate constants for the model were adopted from the global analysis fitting routine.

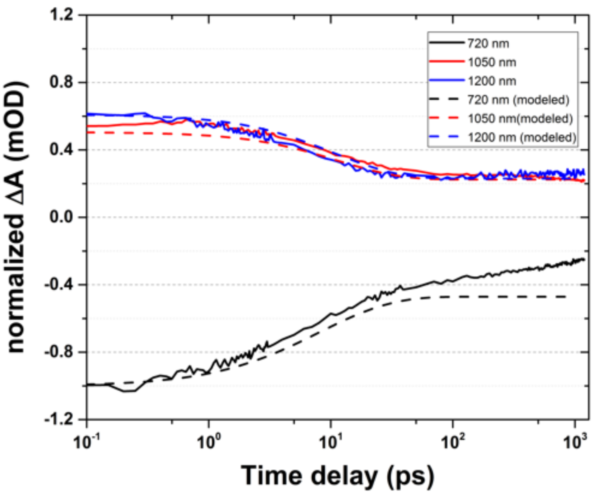

Figure 5.7: Simulated and Experimental TA Dynamics for P(DPP2OD2-TT):PCBM clearly establishing the validity of the four state kinetic model.

We also looked at the occupation number/probability of each of the states and the net transition rates to infer further information about the processes (see Figure 5.8). The occupation number of the ground state (GS) predominantly rises due to the fast relaxation of singlet states (S). While the population of the singlet states (S_1) decreases due to the presence of the two decay channels: either radiative decay back to the ground state or conversion to a charge transfer (CT) state by an electron transfer process. It is interesting to note the similar decay dynamics for the S_1 and the CT state, which can be ascribed to their energetic proximity. Finally, the population of the free charges (F) rises almost at the same rate in the given timescale. For the sake of clarity, we also plot the net transition rates for the CT to F and CT to S_1 transitions. The transition rate for CT to F state is highest at the early times and decreases over time due to the steady decay in the population of the CT states. While for the CT to S_1 transition, the net rate is negative which implies that there is a larger fraction of excitons moving from the S_1 to CT relative to the back transfer process from the CT to S_1. The overall propensity for the formation of CT states (S_1 to CT) is maximum at early times, and at later times it decreases as singlet states are lost because of the relaxation back to the ground state (GS).

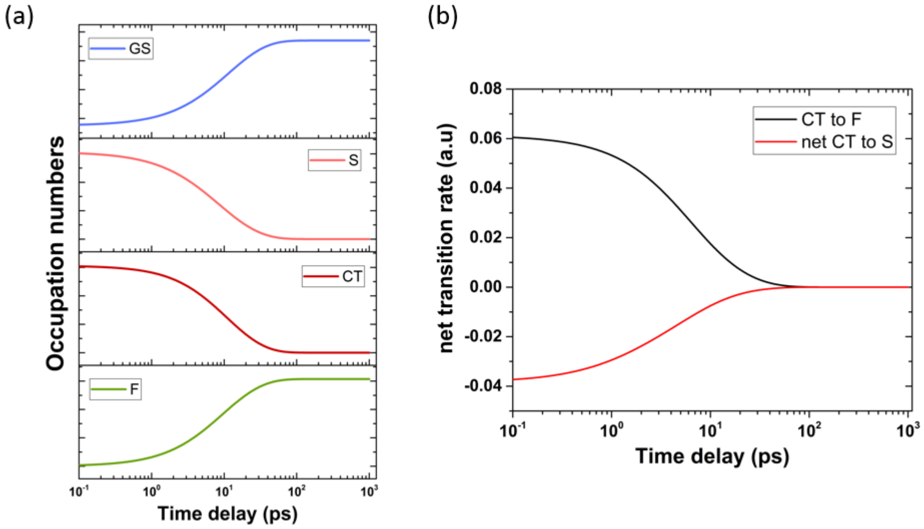

Figure 5.8: (a) Occupation number/probability for each of the states in the four-state kinetic model. (b) The net transition rate for the CT to F and the CT to S_1 transitions.

5.3 Density functional theory (DFT) calculations

To estimate the extent of the electronic coupling between the DPP polymer chains and the fullerene, quantum chemical calculations were carried out. All the DFT calculations related to this work were done by the computational nanoelectronics group of Dr. Frank Ortmann at TU Dresden.

For simplicity of calculations, shortened backbone for the polymer with three repeat units was used, and the alkyl chains were reduced down to the branching point. The starting position of the fullerene along the polymer backbone was screened and the geometry of the dimer was relaxed using the B3LYP/3-21G hybrid functional. The transfer integral (ν_{ij}) between the frontier orbitals was computed for the relaxed geometry of the dimer. Depending on the geometry, we find that the transfer integral values ($\nu_{homo-homo}/\nu_{lumo-lumo}$) for all the polymer:fullerene combinations are distributed in the range of 20-40 meV. These transfer integral values are fairly large and comparable to the values observed for common molecular crystals [153, 154]. According to the classical electron transfer theory such as Marcus formalism [155], the charge transfer rate depends on ν_{ij}^2, the large transfer integral values explain the prompt electron transfer process in the DPP:PCBM system.

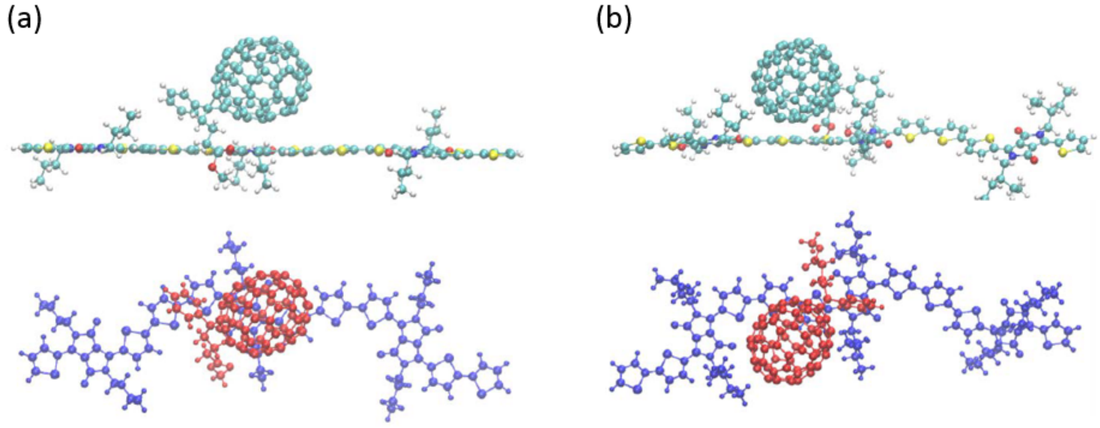

Figure 5.9: Relaxed geometries for the (a) P(DPP6DOT2-T):PCBM and (b) P(DPP2ODT2-T):PCBM obtained using the B3LYP/3-21G hybrid functional.

5.4 Electromodulated differential absorption (EDA) spectroscopy

Apart from conventional TA measurements of thin films on glass, we also carried out TA measurements on a complete device stack under a high reverse bias condition. We use a technique commonly referred to as electromodulated differential absorption (EDA) spectroscopy [156, 157]. Note: The EDA spectrosocpy set-up used here is located in Prof. Natalie Banerjie's lab in the Department of Chemistry and Biochemistry at the University of Bern. The EDA measurements were conducted by Dr.Yufei Zhong and Nikolaos Droseros.

EDA spectroscopy utilizes the quadratic Stark effect, which suggests that the electroabsorption (EA) signal is quadratically related to the magnitude of applied voltage. In EDA spectroscopy, the TA signal is measured on a complete device stack with (E_{on}) and without (E_{off}) the applied electric field. The differential spectra ($\Delta A(E_{on}) - \Delta A(E_{off})$) then yields the electroabsorption (EA) signal originating from the bulk of the film. As the free charges move toward the electrodes, they shield the externally applied electric field, which in turn reduces the EA signal. As mentioned earlier, the amplitude of the EA signal and the applied voltage are quadratically related to each other. Using this relation, the decay of the EA amplitude is converted to the femtosecond resolved voltage drop across the device. For a more detailed description of the technique, the reader is referred to section 3.7 of Chapter 3. Due to EDA being highly time-intensive, we restricted our measurements to the best performing DPP blend of P(DPP2ODT2-TT):PCBM. The time resolved voltage drop is normalized to the total voltage drop (V_{total}) when all the charges are extracted, and the normalized voltage drop is expected to reach the value of -1 when all the charges are extracted. The normalized voltage drop dynamics is presented in Figure 5.10.

Firstly, from the onset of the voltage drop, it is clear that the free charges are generated and begin to be extracted in the 10-20 ps time window which matches

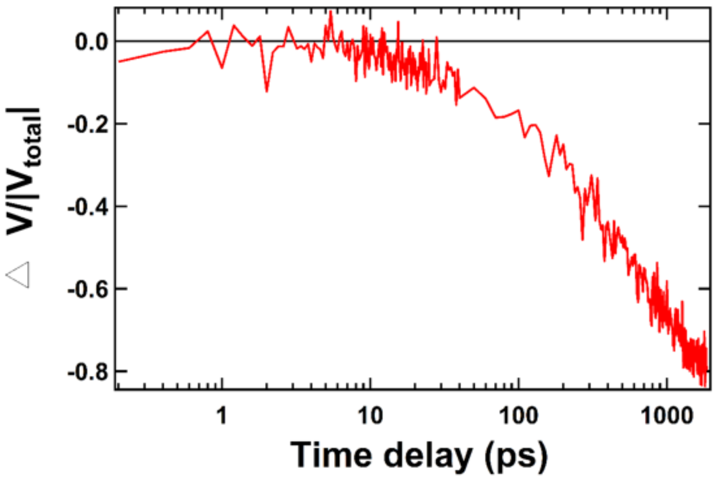

Figure 5.10: Normalized voltage drop dynamics for a P(DPP2ODT2-TT):PCBM device over 1 ns timescale.

quite well with our estimate of the CT-state lifetime (∼15 ps). Also, we can deduce from the spectra that in the 1000ps time scale about 80 % of total generated charges are extracted. The substantial amount of free charges being extracted at such an early timescale points to the fact that the mobility of charge carriers in the blend must be very high at early times (<1 ns). Lastly, we find that the voltage decay is highly multiphasic (consisting of many exponents) which we attribute to the diffusion mediated charge transport in the blend.
Additionally, from the voltage drop dynamics it is possible to estimate average electron-hole separation according to the following relation [158]:

$$< l(t) >= d\left(1 - \sqrt{1 - \frac{\Delta V(t)}{\Delta V_{total}}}\right) \tag{5.11}$$

where l(t) is the average electron-hole separation projected along the device plane, and d is the active layer thickness. It is important to mention that l(t) is representative of the average motion of electron and holes projected along the axis joining the electrodes, and it does not represent the separation of geminate electron-hole pairs. Also, from the obtained average separation, early timescale mobility can be obtained according to [158]:

$$\mu_{EDA} = \frac{d}{U}\frac{\partial}{\partial t}l \tag{5.12}$$

Figure 5.11 shows the average electron-hole separation and the early time mobility values for P(DPP2ODT2-TT):PCBM. The average e-h separation is around 3nm on the 10ps timescale, which increases to around 60nm in 1ns. The mobility values are quite high around 0.1 cm^{2}V^{-1}s^{-1} in the 3nm length scale which gradually reduces by an order magnitude to around 10^{-2}cm^{2}V^{-1}s^{-1} in the 60nm length scale. The gradual decrease in mobility is expected because of the dispersive nature of transport in organic semiconductors where the carriers gradually relax in the broadened density of states [159]. The relaxed carriers need activation to the transport energy level (ϵ_t) to become mobile and contribute to conduction. The macroscopic view of looking at it is that at early times the charge carriers are statistically less likely to encounter traps or grain boundaries and as time passes an increasing fraction of them become trapped in deep energetic states.

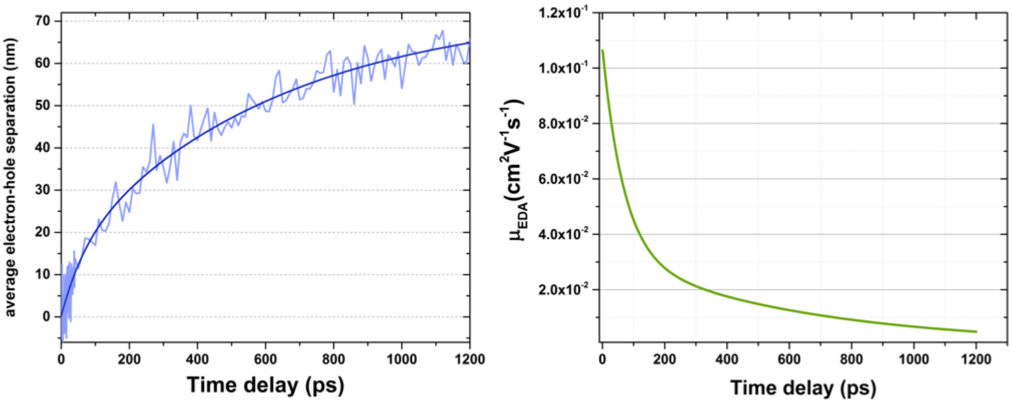

Figure 5.11: Average electron-hole separation distance and early time scale mobility (μ_{EDA}) as a function of pump-probe delay for the P(DPP2ODT2-TT):PCBM blend.

5.5 Summary and Conclusion:

In this chapter, we explore the electron transfer and charge separation dynamics in the DPP:PCBM system using a combination of pump-probe spectroscopy techniques. Transient absorption (TA) spectroscopy on the pristine polymer films reveals extremely short singlet lifetimes of the order of 15-20 ps. The TA spectra of the DPP:PCBM blend films showcase the dominant recombination time constant of the same order as the singlet lifetimes. We hypothesize this time constant to be representative of the CT state lifetime as reported earlier using the pump-push-probe (PPP) spectroscopy technique. The hypothesis is verified using a 4-state kinetic model where the experimental dynamics match very well with the modeled dynamics when CT-state lifetimes of around 15-20 ps are used in the model. The reasons for correlated singlet and CT state lifetimes are twofold:(i) either the back transfer rate from the CT state to the singlet state is reasonably large, where the CT state relaxes back to the ground state via the singlet state forming an indirect radiative decay pathway or, (ii) the correlated lifetimes can arise due to the formation of hybrid singlet-CT states as a result of their energetic proximity.

Moreover, by comparing the early time (0.2 ps) TA spectra of the neat and blend films we can clearly state that the electron transfer is prompt and happens within the instrument resolution of ~100 fs. DFT calculations suggest large transfer integral values between the frontier orbitals of the DPP polymers and the fullerene as a likely reason for the high electron transfer rate despite the zero driving force. Using EDA spectroscopy, we could map the separation of electron-hole pairs along the axis joining the electrodes and compute the early time mobility. The electron-hole pair separate to a distance of 3 nm in 10 ps and to an average distance of 60 nm on the

1ns timescale. The mobility on the 10 ps timescale is of the order 0.1 $\mathrm{cm^2V^{-1}s^{-1}}$ which is rather high for a disordered polymer:fullerene system. The mobility value gradually reduces down to 0.01 $\mathrm{cm^2V^{-1}s^{-1}}$ on the 1ns timescale due to the dispersive nature of charge transport as the carriers relax down in the tail of the density of states (DOS). More importantly, very high mobility explains why the charge carriers could still dissociate despite the near-zero driving force. The study suggests if the mobility of carriers is sufficiently high at early times in the donor and acceptor domains, the material combination with low energetic offset could be chosen which would maximize the V_{OC} and concomitantly give the high yield of photogenerated free charge carriers.

Chapter 6

Fluorinated non-fullerene acceptors (NFAs)

This chapter introduces a novel material class: fluorinated non-fullerene acceptors (NFAs) for organic solar cells. In section 6.1, a brief introduction to the material system, and the chemical structure of the molecules is given. Section 6.2 deals with the energetics of the molecules. The energy of the frontier molecular orbitals is determined using cyclic voltammetry (CV) measurements, and the optical gap (E_{opt}) is deduced by combining absorbance and photoluminescence (PL) spectroscopy.

In section 6.3, the device performance for the blends based on these acceptors is summarized. Also included are the device parameters for ternary solar cells based on P3HT and PTB7-Th polymer donors. Section 6.4 summarizes the sensitive EQE_{PV} and electroluminescence (EL) measurements and a detailed analysis of the voltage losses of the solar cells is performed.

One of the main focuses of this chapter is to elucidate on the charge transfer dynamics and photophysics of blends involving NFAs. In section 6.5, we summarize the transient absorption (TA) spectroscopy results for binary and ternary blends, and the main photophysical processes are outlined. Section 6.6 deals with the morphological investigation. Transmission electron microscopy (TEM), atomic force microscopy (AFM) and grazing incidence wide-angle x-ray scattering (GIWAXS) are used to probe the morphology of the bulk-heterojunctions.

Device results suggests that fluorination of molecules is a beneficial strategy to achieve superior device performance and efficiencies as high as 9.5% were achieved when these acceptors were blended with PTB7-Th.

6.1 Introduction

For almost two and a half decades, organic solar cell research focused on using fullerene derivatives as an electron acceptor in bulk-heterojunctions. Due to their ball-like, isotropic conjugated structure, the charge transfer and charge transport processes were believed to be kinetically enhanced as a result of electron delocalization over fullerene molecules [160, 148]. Thus, the fullerene derivatives remained as a ubiquitous choice to be used as acceptors for the fabrication of efficient solar cells. However, the recent advent of high performing devices based on NFAs has shifted the focus to these new molecules [161, 162, 163]. Intriguingly, the pioneering bilayer devices fabricated by Tang et al. [47] used a non-fullerene molecule as an electron acceptor as well. Since then, a variety of new materials have been developed and tested in devices. As of now, the family of non-fullerene acceptors (NFAs) can be grouped into two categories :

- fused aromatic diimides (rylene-diimides)
- acceptors based on strong intramolecular push-pull effects

Common examples within the rylene-diimides class are the perylene dimiides (PDIs) and the naphthalene diimides (NDIs). The acceptors within this class can be monomers, dimers, trimers or even polymers. For example, multi-linked PDIs (dimers and trimers) are often used to inhibit the strong aggregating tendency of these molecules where the monomers are linked via a ‘twisting’ linking group. Also, another typical example is the polymer N2200 which is probably the most widely used polymer acceptor within the organic solar cell community. As our work does not focus on rylene-diimides, we will limit our discussion on these NFAs. For a more comprehensive description on rylene-diimides, the reader is referred to the following review articles [163, 162, 164].

Acceptors based on the intramolecular push-pull effects mainly consists of the recently developed molecules with an acceptor-donor-acceptor (A-D-A) type architecture. The central electron-rich donor core either consists of the dithiopheneindacenodithiophene (DTIDT) central unit which constitutes the family of NFAs within the 3,9-bis(2-methylene-(3-(1,1-dicyanomethylene)-indanone))-5,5,11,11-tetrakis(4-hexylphenyl)-dithieno[2,3-d:2’,3’-d’]-s-indaceno[1,2-b:5,6-b’]dithiophene (ITIC) category or the central core is made up of indacenodithiophene (IDT) unit which forms the NFA 2,2-((2Z,2Z)-((5,5-(4,4,9,9-tetrakis(4-hexylphenyl)-4,9-dihydro-s-indaceno[1,2-b:5,6-b]dithiophene-2,7-diyl)bis(4-(2-ethylhexyl)thiophene-5,2-diyl))bis(methanyly lidene))-bis(3-oxo-2,3-dihydro-1H-indene-2,1-diylidene))dimalononitrile (IEIC) and its derivatives [165, 166]. Structurally these molecules are very different from fullerenes because of their anisotropic crystal structure. The entire molecular structure can be decomposed into three parts viz., the central electron-rich donor group (DTIDT, IDT), phenyl substituted solvation chains and the electron withdrawing end-capping units [see Figure 6.1]. The solvation chains sterically hinder the delocalization of central electron density. Thus the DIDT/IDT central unit is mainly responsible for intramolecular charge transfer and is not involved in the intermolecular charge transport processes.

On the other hand, the end-capping units are responsible for forming $\pi - \pi$ interactions between adjacent molecules, which creates the pathway for intermolecular charge transport in these molecules. End-capping units of the acceptor also develop $\pi - \pi$ interactions with polymeric donor molecules for the photo-induced charge transfer process. Another important feature of ITIC/IEIC acceptors is the wide tunability of their absorption spectra and the molecular energy levels. By substituting the electron-deficient or electron-rich moieties onto the end-capping units, the frontier energy levels of the molecules can be manipulated over a broad energy range.

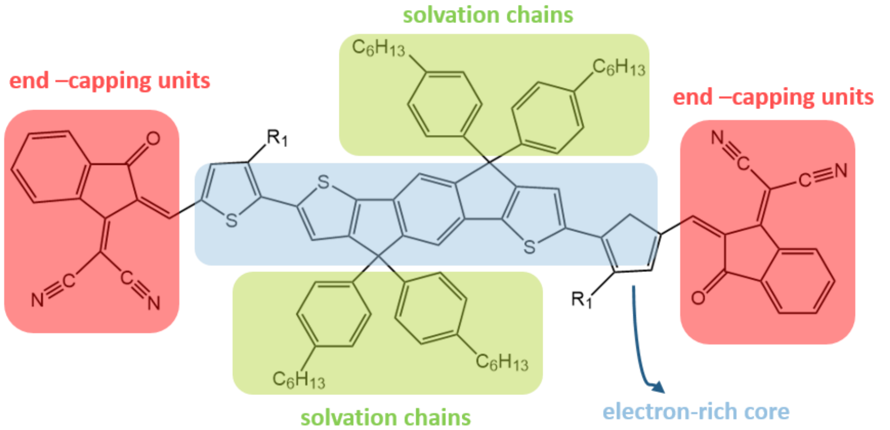

Figure 6.1: Schematic depiction of the chemical structure of the IEIC molecule. Various components of the chemical structure are highlighted in colored boxes viz., the electron rich core, the solvation chains and the electron withdrawing end-capping units.

In this work, we use three different NFAs based on the modification of IEIC's architecture. One of the acceptors (IEICO) is based on the alkoxy substitution onto the electron-rich central core of the IEIC molecule[see Figure 6.2]. This substitution primarily affects the HOMO of the molecule, bringing it up by approximately 0.2 eV while the LUMO remains unchanged relative to IEIC [167]. This design principle is specifically useful for solar cells because it reduces the optical gap of the acceptor without sacrificing the voltage of the device. The voltage (V_{OC}) is not affected as it only depends on the effective gap i.e., the difference between the HOMO of the donor and the LUMO of the acceptor. The other two acceptors used in the study are the fluorinated versions of IEICO with either two (-2F) or four (-4F) fluorine substitutions at the end-capping unit, which from here on are referred to as IEICO-2F and IEICO-4F respectively. The substitution of the highly electronegative fluorine atoms increases the electron withdrawing capability of the end-capping units, which enhances the intramolecular charge transfer (ICT) [168]. This, in turn, shifts the HOMO level up and LUMO level down which results in an ultra-narrow optical gap for the fluorinated acceptors.
We paired these acceptors with poly(3-hexylthiophene) (P3HT) and poly[4,8-bis(5-(2-ethylhexyl)thiophene-2-yl)benzo[1,2-b;4,5-b']dithiophene-2,6-diyl-alt-(4-(2-ethyl hexyl)-3-fluorothieno[3,4-b]thiophene-)-2-carboxylate-2-6-diyl)] (PTB7-Th) polymer

donors to be used as active layers in solar cells. Furthermore, we also fabricated ternary devices using a combination of both P3HT and PTB7-Th as the donors and IEICO-4F as an acceptor. The idea behind using P3HT as the second donor was to extend the absorption range of the binary blend and also introduce an additional energy transfer channel between P3HT and PTB7-Th, as the P3HT luminescence overlaps very well with the absorption spectrum of PTB7-Th. This additional energy transfer channel can facilitate in obtaining a higher yield of free charge carriers. Photophysics of the binary and ternary blends were characterized using transient absorption (TA) spectroscopy, and voltage losses were characterized using electroluminescence (EL) and sensitive EQE_{PV} measurements. Details of the spectroscopic analysis are discussed in the subsequent sections. But as a first step, we start with the energy levels of the materials and estimating the optical gap which is discussed in the next section.

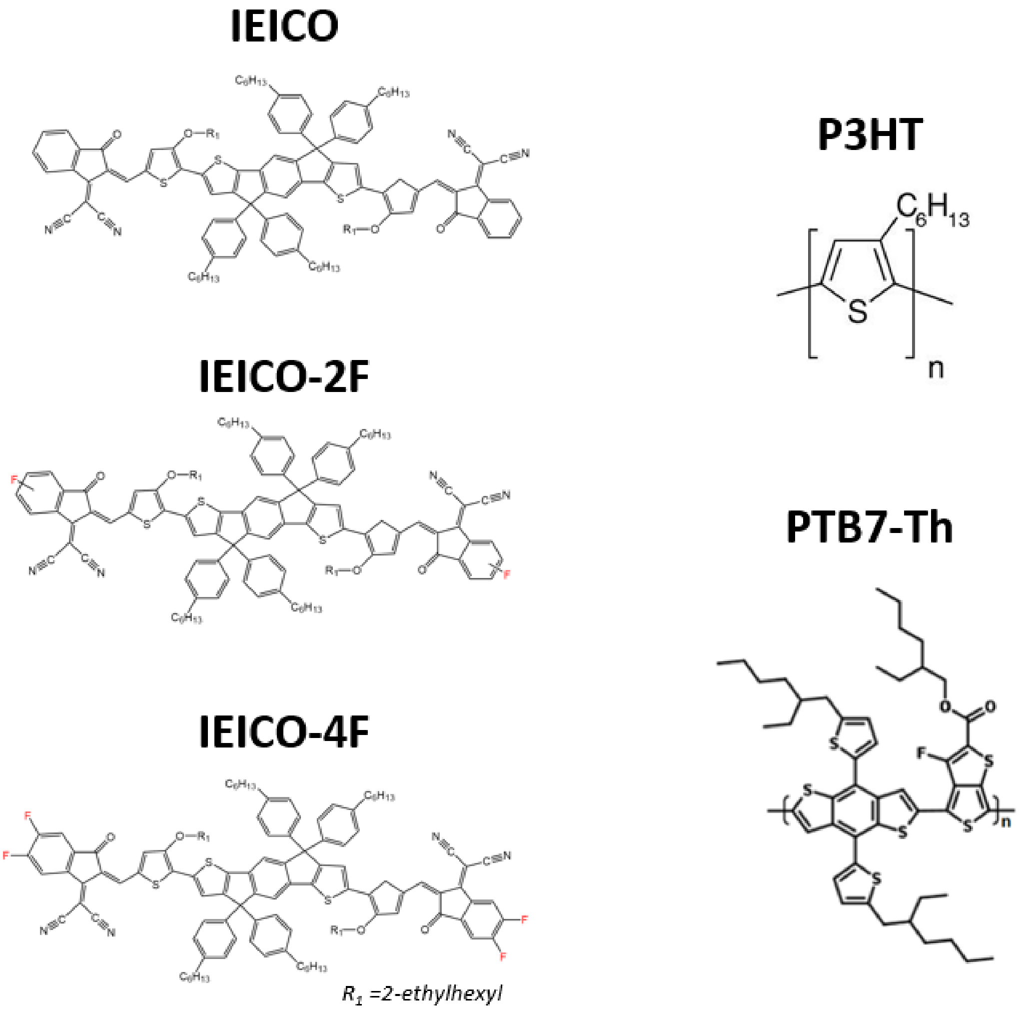

Figure 6.2: Schematic depicting the chemical structure of the NFAs: IEICO, IEICO-2F, IEICO-4F and the polymer donors: P3HT and PTB7-Th.

6.2 Electrochemical and the optical gap

To measure the energy levels of the polymers and the NFAs, cyclic voltammetry (CV) measurements were carried out. All the CV measurements related to this work were carried out by Dr. Tian-yi Li of the Dresden Integrated Center for Applied Physics and Photonic Materials (IAPP).

In CV measurements, the HOMO value of the molecule is given by the onset of its oxidation potential, and the onset of reduction potential characterizes the LUMO value. The absolute values of the HOMO/LUMO can be calculated if the Fermi level of the reference electrode is known. In our measurements, we used ferrocene/ferrocerium (Fc/Fc$^+$) redox couple as the standard reference electrode. For the polymer PTB7-Th, the HOMO value is 5.49 eV and the LUMO is at 3.32 eV (see Figure 6.3). The electrochemical gap given as the difference between the HOMO and the LUMO is around 2.17 eV. Similarly, the HOMO/LUMO values and the electrochemical gap for the NFAs were calculated, and the results are summarized in Table 6.1. HOMO values for all the three NFAs are in a similar range around 5.4-5.6 eV while the LUMO values progressively reduce from 3.74 eV to 4.13 eV with fluorine substitution. This can be attributed to increased electron withdrawing capability of the end-capping units, which enhances the intramolecular charge transfer (ICT).

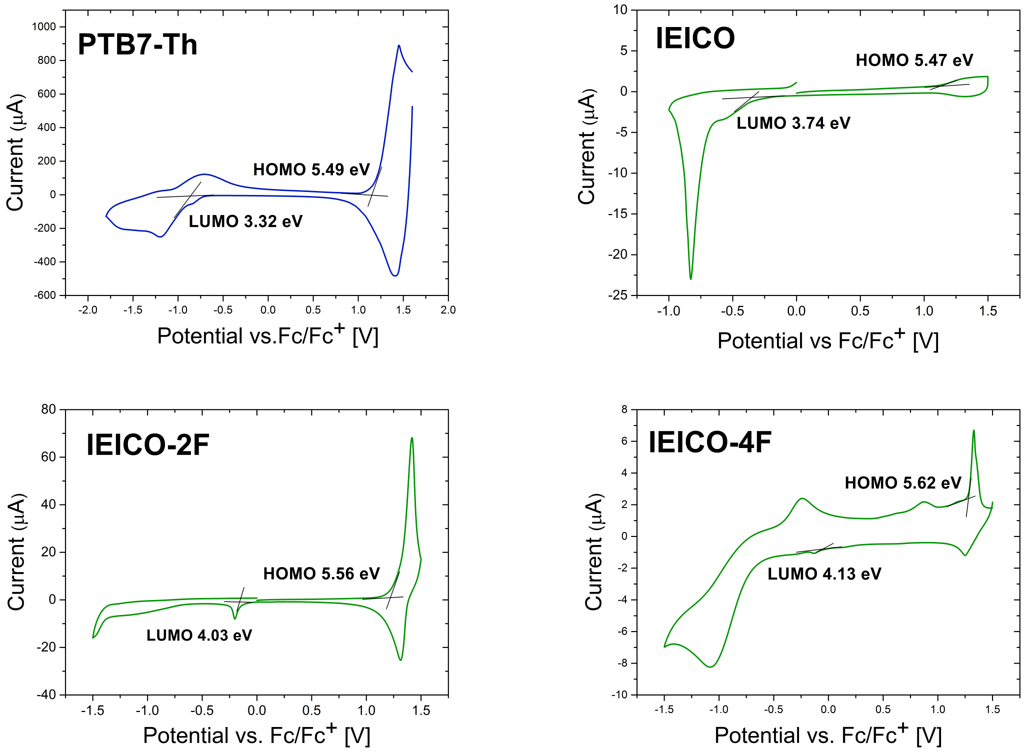

Figure 6.3: Cyclic voltagramms for the polymer PTB7-Th and non-fullerene acceptors: IEICO, IEICO-2F and IEICO-4F measured with respect to ferrocene/ferrocerium (FCO) standard electrode.

Table 6.1: Electrical gap, optical gap and the exciton binding energy for the polymer PTB7-Th and the NFAs: IEICO, IEICO-2F and IEICO-4F.

Material	HOMO [eV]	LUMO [eV]	Electrical gap E_{el} [eV]	Optical gap E_{opt} [eV]	$E_{el} - E_{opt}$
PTB7-Th	5.49	3.32	2.17	1.64	0.53
IEICO	5.47	3.74	1.73	1.4	0.33
IEICO-2F	5.56	4.03	1.53	1.36	0.17
IEICO-4F	5.62	4.13	1.49	1.34	0.15

In addition we also measured the optical gap (E_{opt}) of the materials by combining absorption and photoluminescence (PL) measurements [Figure 6.4]. Due to the reciprocity relation between absorption and emission, the optical gap is given by crossing point of the appropriately normalized absorption and PL spectra [120]. The optical gap for the polymer PTB7-Th is found to be around 1.64 eV while for the NFAs the E_{opt} is much lower. IEICO has an E_{opt} of 1.4 eV which reduces down to 1.34 eV for IEICO-4F. Looking at the values of the electrochemical and the optical gap from Table 6.1, it becomes clear that the electrical gap is much greater than the optical gap. This discrepancy between the electrical and the optical gap comes from electron-hole interactions. Due to the low dielectric constant of organic semiconductors ($\epsilon_r \sim 3 - 5$) the interactions between electrons and holes are not screened, and the coulomb binding energy needs to be taken into account. The difference between the electrochemical and the optical gap gives the first approximation of the exciton binding energy [169]. The exciton binding energy for PTB7-Th is substantially large with a value around 0.53 eV. This value matches well with the literature value of the binding energies for polymer semiconductors [33]. The exciton binding energy for IEICO is lower with value around 0.33 eV and for the fluorinated IEICO's the binding energy further reduces to values around 150-170 meV. The low binding energy of the excitons in IEICO based acceptors is possibly one of the reasons why solar cells based on these acceptors show high EQE values, which is related to the higher yield of exciton dissociation.

To compare the absorption spectra of the various IEICOs, we plot them together in a single graph [Figure 6.5]. Firstly, all the IEICOs have a nice complementary absorption when compared to the absorption spectra of PTB7-Th implying that the PTB7-Th is a spectrally suitable choice to be used as the donor and combined with IEICOs for BHJ devices. Also, when comparing the absorption spectra of the IEICOs, a clear red-shift is visible with fluorination. The absorption maximum for IEICO is at 820 nm, which red-shifts to 850 nm for IEICO-2F and then to 870 nm for IEICO-4F. This red-shift can be attributed to the enhanced intramolecular charge transfer (ICT) which brings the HOMO and LUMO levels closer in energy, thereby reducing the optical gap (E_{opt}).

6.3 j-V characteristics and the EQE

For the donor:acceptor combination of PTB7-Th and the various IEICOs, solar cells were fabricated using the standard architecture :ITO/PEDOT:PSS/BHJ/ETL/Al. For IEICO and IEICO-2F based devices lithium fluoride (LiF) was used as an elec-

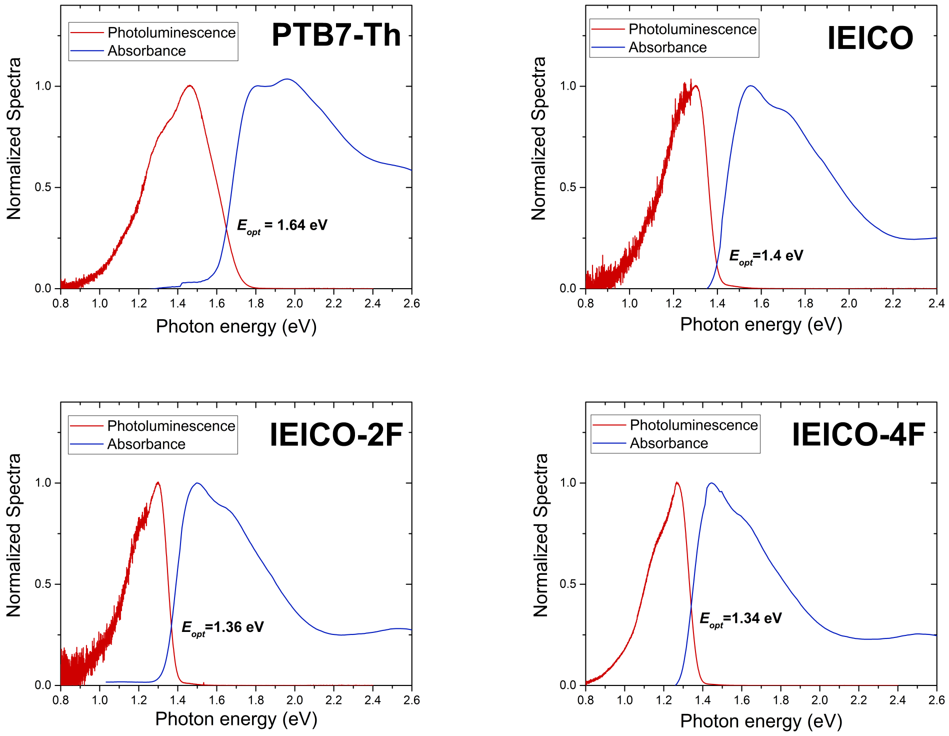

Figure 6.4: Normalized absorbance and photoluminescence (PL) spectra of the polymer PTB7-Th and the NFAs: IEICO, IEICO-2F and IEICO-4F. Optical gap (E_{opt}) is given by the crossing point of the absorbance and the PL spectra.

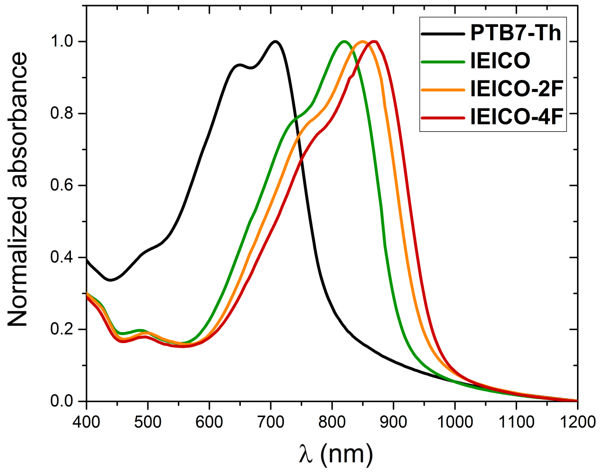

Figure 6.5: UV-Vis-NIR absorption spectra for the polymer PTB7-Th and the NFAs: IEICO, IEICO-2F and IEICO-4F.

tron transport layer, while for IEICO-4F devices with LiF showed a S-kink in the fourth quadrant of the IV curves. A variety of ETLs were tested for IEICO-4F based devices and the best performance was achieved using 2,3,8,9,14,15-hexachloro-

5,6,11,12,17,18-hexaazatrinaphthylene (HATNA-Cl_6) doped with 3wt% tetrakis (1,3,4,6,7,8-hexahydro-2H-pyrimido[1,2-a]pyrimidinato)ditungsten (II), commonly known as tungsten paddlewheel ($W_2(hpp)_4$). j-V characteristics and the EQE spectra for the optimized devices are summarized in Figure 6.6.

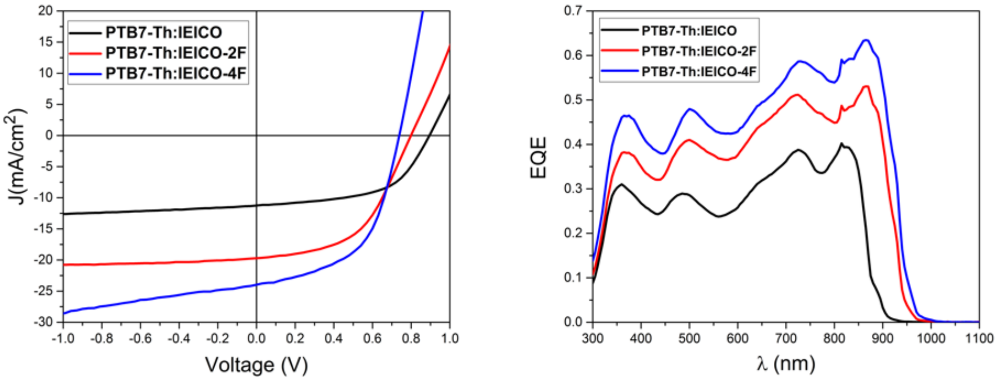

Figure 6.6: j-V charactertics and EQE spectrum for the optimized devices using PTB7-Th as the donor and IEICOs as acceptor.

Table 6.2: Device parameters extracted from j-V curves for PTB7-Th:IEICO based devices.

Material combination	J_{sc} [mA/cm^2]	V_{OC} [mV]	FF (%)	PCE (%)
PTB7-Th+IEICO	11.25	890	56	5.64
PTB7-Th+IEICO-2F	19.71	800	51.5	8.11
PTB7-Th+IEICO-4F	24	740	54	9.5

Looking at the j-V curves, we see a typical trade-off between j_{sc} and V_{OC}. The j_{sc} values for IEICO based devices are around 11 mA/cm^2 which drastically increases to about 20 mA/cm^2 for IEICO-2F, and the highest j_{sc} is obtained for IEICO-4F based solar cells with values around 24 mA/cm^2. Concomitantly, the IEICO-4F based devices exhibit the lowest V_{OC} values around 740 mV, which improves to 800 mV for IEICO-2F and then further increases to 890 mV for IEICO. In general, the V_{OC} values are on the higher side considering the low optical gap of these acceptors, implying that the voltage losses are on the lower side, as will be discussed in the next section. The difference in the j_{sc} values between the IEICOs can be partly explained by the red-shifted absorption of the fluorinated acceptors. The better photon harvesting capability of IEICO-2F and IEICO-4F based devices is evident from the EQE spectra where the EQE spectra are spread over a relatively broader wavelength range (see Figure 6.6). Also, within the common spectral range, the EQE values are highest for IEICO-4F based solar cells followed by IEICO-2F and IEICO. The fill factor values (50-56%) are fairly low in comparison to other bulk-heterojunction systems. As suggested in the literature, this is most likely due to the poor electron mobility within the acceptor domains. For IDT based NFAs like the IEICOs, electron mobility values of around 10^{-4} cm^{2}V^{-1}s^{-1} are reported which is much lower than their fullerene counterpart [170]. Nevertheless, because of achieving good j_{sc} and V_{OC} values simultaneously, solar cells exhibit decent power conversion efficiency (PCE). The IEICO based system showed the lowest PCE of 5.64% which improved to 8.11% for IEICO-2F and for IEICO-4F based devices we achieved a PCE around 9.5% , which is rather on the higher side for single-junction organic solar cells.

When P3HT was used as the donor instead of PTB7-Th, the device performance was sub-optimal (see Figure 6.7). The j_{sc} for P3HT:IEICO was around 8.4 mA/cm^2 which improved to 12.7 mA/cm^2 when IEICO-2F was used instead. Surprisingly, the j_{sc} value reduced down to 9.7 mA/cm^2 when using IEICO-4F as an acceptor. The V_{OC} values showed an expected trend with the highest V_{OC} of 560 mV for IEICO which reduces to a value of 500 mV for IEICO-2F which further decreases down to 400 mV for IEICO-4F. Compared to PTB7-Th based solar cells, the V_{OC} values for P3HT based devices are much lower. This can be attributed to the much higher-lying HOMO level for P3HT (5eV vs. 5.49eV) which implies that the effective gap of the blend is at least 500 meV lower for P3HT:IEICOs than for PTB7-Th:IEICOs. Also compared to PTB7-Th devices, the fill-factor values are much smaller (45-48%). IEICO based devices show a PCE of 2.2%, IEICO-2F exhibit the highest PCE values of around 2.8% while for IEICO-4F based devices, PCE is reduced down to 1.75%. Overall, the performance of the devices drastically decreases when P3HT is used as the donor with IEICO acceptors.

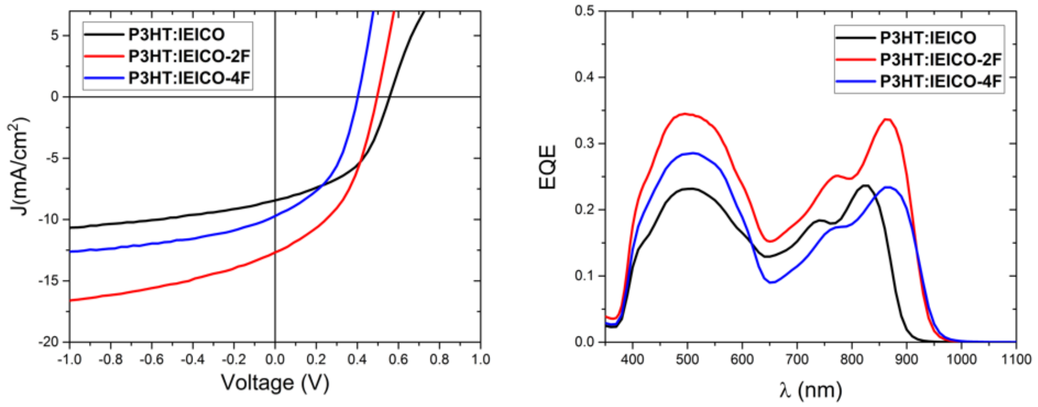

Figure 6.7: j-V charactertics and EQE spectrum for the optimized devices using P3HT as the donor and IEICOs as acceptor.

Table 6.3: Device parameters extracted from j-V curves for P3HT:IEICO based devices.

Material combination	J_{sc} [mA/cm^2]	V_{OC} [mV]	FF (%)	PCE (%)
P3HT+IEICO	8.4	560	47.5	2.23
P3HT+IEICO-2F	12.7	500	44	2.8
P3HT+IEICO-4F	9.7	400	44.5	1.75

EQE spectra show two dominant spectral ranges where charge generation takes place. Firstly, between the 400-600 nm interval, where mainly P3HT absorbs,

IEICO-2F devices show the highest EQE values. Secondly, in the spectral range 700-1000nm where predominantly IEICOs absorb the trend is similar. For IEICO-2F and IEICO-4F a clear red-shift can be seen in the EQE spectra analogous to the absorption spectra. But between the IEICO-2F and IEICO-4F, the difference is very marginal, implying that the effective-gap of the blends is almost the same. Also worth noticing is that in the spectral range of IEICOs, vibronic features of the absorption spectra are clearly retained. This might be due to the formation of large aggregates of acceptor domains, which also explains the overall low EQE values compared to PTB7-Th based devices. Morphology of the pristine and bulk-heterojunction layers will be discussed in a subsequent section.
To see whether we can further improve the device performance of PTB7-Th:IEICOs, we used a ternary blend approach. P3HT was chosen as the third component as it has complementary absorption properties when compared to PTB7-Th and IEICOs. This complementary absorption property can lead to a better harvesting solar spectrum which increases the chance of achieving higher j_{sc} values in the ternary blend. Another reason to make ternary devices with P3HT was because the luminescence spectra of P3HT overlaps very well with the absorption spectra of PBT7-Th, and this overlap can lead to a possible energy-transfer channel between the polymers.
Ternary solar cells (TSCs) were fabricated based using both P3HT and PTB7-Th as donors and IEICO-4F as an acceptor (D_1:D_2:A system). Donor:acceptor ratio was 1:1, and the ratio between the donors was varied between 25 to 75 %. Usually, in the case of ternary devices, the variation of the V_{OC} with blend composition is used as a probe to find out the active operational mode of the TSC and the type of nanomorphology formed [171, 172]. We find that the V_{OC} of the ternary blend ranged between the V_{OC} of the two binary blends and varied continuously with the composition of the donors. This type of behavior is usually reported when the two donor components are miscible and form a single homogeneous phase, which can explain the trend in the V_{OC} of our ternary blends [172]. We also find that the J_{sc} and the FF of the ternary devices is comparatively lower than the better performing binary blend (PTB7-Th:IEICO-4F). This can be ascribed to the mixed-phase morphology of the donor polymers which have poor charge transport channels and poor charge recombination properties. The best performing ternary device had a PCE of 4.4% where the PTB7-Th to P3HT ratio was 3:1. While for the ternary blend where P3HT was the dominant donor component, the PCE values reduced down to 3%. This happened because of the simultaneous decrease in all three parameters namely the j_{sc},V_{OC} and the FF. The detailed device parameters are summarized in table 6.4. Overall, the addition of P3HT to PTB7-TH:IEICO-4F blend was detrimental to its performance and there is a need to look for other compatible, panchromatic donor polymers which absorb in the high energy visible spectral region.

6.4 Voltage losses

To characterize the voltage losses of the devices, the energy of the charge transfer state (E_{CT}) needs to be determined first. We combine sensitive external quantum efficiency (EQE_{PV})and electroluminescence (EL) measurements where the E_{CT} is

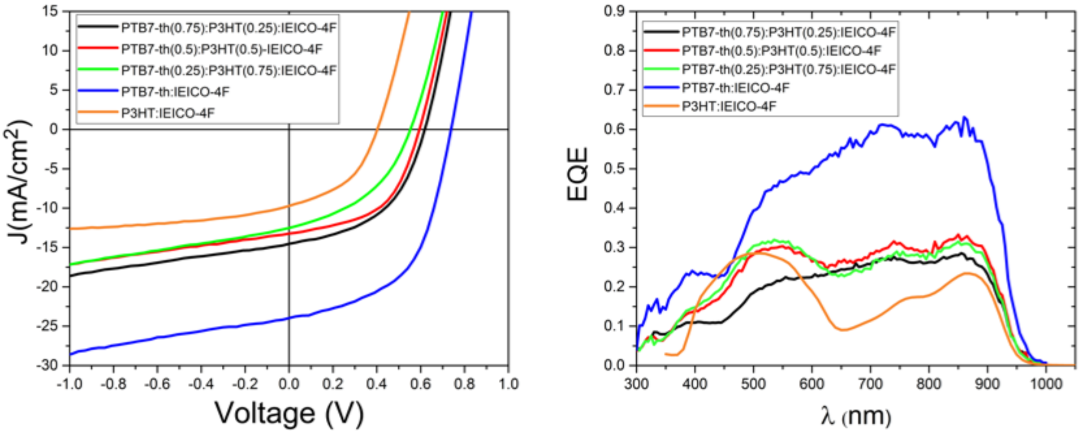

Figure 6.8: j-V characteristics and the EQE spectra for the ternary solar cells based on P3HT,PTB7-th and IEICO-4F.

Table 6.4: Solar cell parameters for binary and ternary blends based on P3HT,PTB7-Th and IEICO-4F.

System	Blend ratio	V_{OC} [mV]	Jsc[$mAcm^{-2}$]	FF[%]	PCE[%]
PTB7-Th:IEICO-4F	1:1	740	24	54	9.5
PTB7-Th:P3HT:IEICO-4F	0.75:0.25:1	620	14.5	48.8	4.4
PTB7-Th:P3HT:IEICO-4F	0.5:0.5:1	590	13.2	52.3	4.1
PTB7-Th:P3HT:IEICO-4F	0.25:0.75:1	550	12.5	42.3	3
P3HT:IEICO-4F	1:1	400	9.7	44.5	1.75

given by the crossing point of the two spectra. Figure 6.9 shows the EQE_{PV} and the EL spectra for PTB7-Th:IEICOs.

From the crossing point, it is clear that the E_{CT} is nearly identical to the optical gap (E_{opt}) of the acceptor. In fact, E_{CT} values are marginally higher ($\sim$ 10-40 meV) than the E_{opt}. This can be explained through the different aggregation tendency of the acceptor in the neat and the blend film. In the blend film, due to the presence of the other component (donor phase), crystallization of the acceptor domains is disrupted while in neat films uninterrupted crystallization leads to the formation of large aggregates. That is the reason why E_{CT} is slightly blue-shifted with respect to the E_{opt} of the neat material. The same aggregation argument also explains why the EL of the blends is blue-shifted with respect to the PL of the neat acceptor film. Also worth noticing is that for IEICO and IEICO-4F devices, EQE_{PV} nearly matches with the absorbance of the acceptor. While for IEICO-2F device, EQE_{PV} is red-shifted compared to the absorbance of the neat material which is usually expected.

Since the absolute EL measurements were conducted, we also extracted the external quantum efficiency of electroluminescence (EQE_{EL}).The EQE_{EL} for PTB7-Th:IEICO is 8.84 x 10^{-6}, for PTB7-Th:IEICO-2F it is around 2.87 x 10^{-5} and for PTB7-Th:IEICO-4 the value is around 1.64 x 10^{-6}. EQE_{EL} is a useful quantity because it enables the estimation of non-radiative voltage losses ($\Delta V_{non-rad}$) according to the following relation:

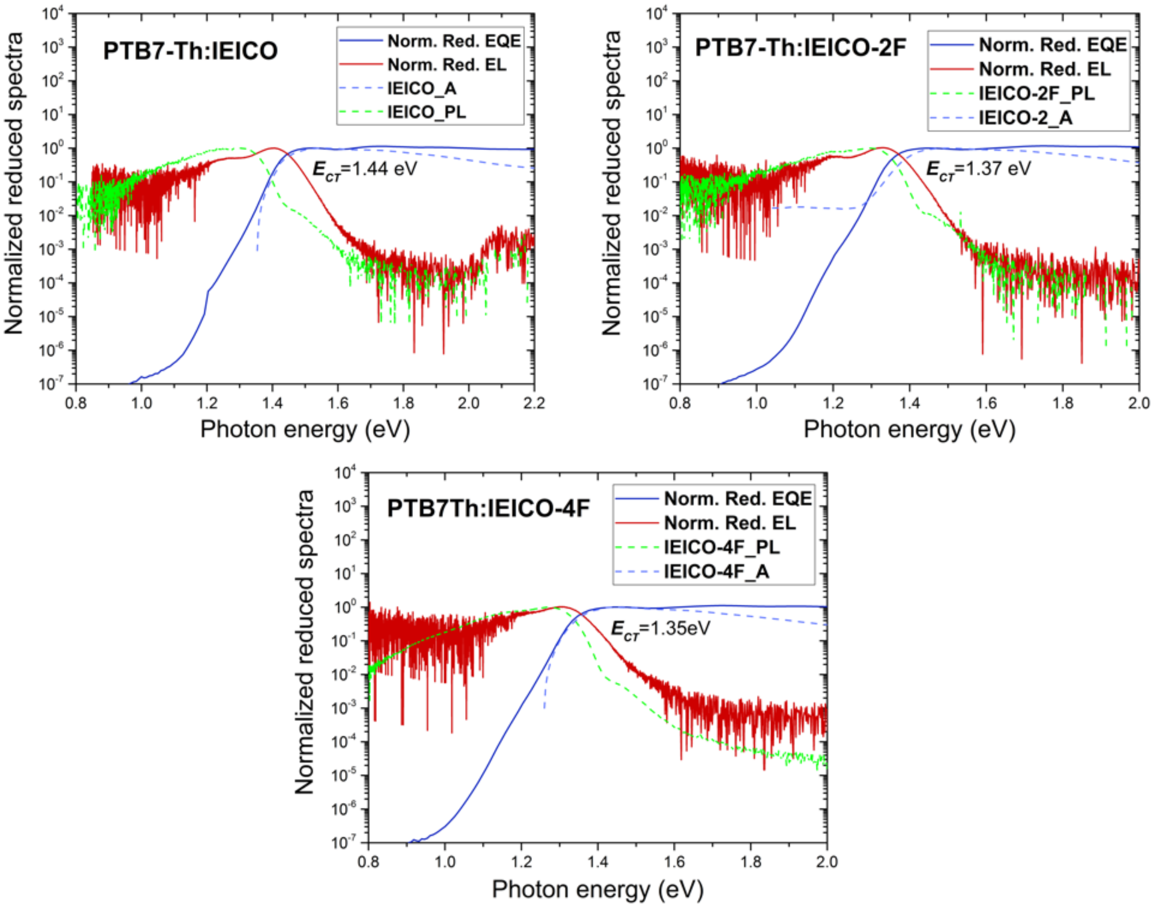

Figure 6.9: Sensitive EQE_{PV} and EL spectra for PTB7-Th:IEICOs based devices.Also shown in the same graph is the absorbance and the photoluminescence (PL) of the respective acceptor in the blend.

$$\Delta V_{non-rad} = \frac{k_B T}{q} ln(EQE_{El}) \tag{6.1}$$

Furthermore, the radiative voltage losses (ΔV_{rad}) can then be simply extracted by substracting the non-radiative voltage loss ($\Delta V_{non-rad}$) from the total voltage losses ($E_{CT} - V_{OC}$). The summary of the total voltage losses for PTB7-Th:IEICO based devices is given in table 6.5. It is worth mentioning that non-radiative voltage losses ($\Delta V_{non-rad}$) for these blends are quite low (typical value for OPVs is of the order of 350 mV). One of the explanations which has been put forward recently relates this to the hybridization of the CT and the singlet state [173]. As the states hybridize because of the energetic proximity, the oscillator strength of the CT-state increases in magnitude due to the intensity borrowing mechanism. This increases the radiative decay rate of the CT-state and prevents loss of energy through vibrational modes or non-radiatively. This argument also explains why the EQE_{EL} is relatively higher for these blends when compared to other donor:acceptor systems.

Lastly, from the slope of the sub-optical gap absorption (EQE_{PV}) we extracted the Urbach energy (E_U) for the blends. For PTB7-Th:IEICO, E_U is close to 24 meV

Table 6.5: CT-state energetics and voltage losses for devices with PTB7-Th as the donor and IEICOs as the acceptor.

System	E_{CT}/q [mV]	V_{OC} [mV]	ΔV_{total} [mV]	$\Delta V_{non-rad}$ [mV]	ΔV_{rad}[mV]
PTB7-Th:IEICO	1440	890	550	294	256
PTB7-Th:IEICO-2F	1370	800	570	264	306
PTB7-Th:IEICO-4F	1350	740	610	336	274

while for PTB7-Th:IEICO-2F and PTB7-Th:IEICO-4F blends the E_U is around 22 meV. These values are very small compared to the values usually obtained for polymer:fullerene blends and signifies a very low interfacial energetic disorder. The low energetic disorder at the interface can explain why the charge transfer in these blends is efficient despite near-zero driving force, as will be discussed in the next section. A recent report by Menke et al., [174] suggests that the Urbach energy for zero driving force blends should be lower than 30meV for efficient charge transfer, a condition very well met by these blends. Low E_U values also add to the reasoning why voltage losses in these devices are so low.

For P3HT based devices, no measurable EL signal was detected even at high injection current densities. Thus the E_{CT} was calculated by fitting the expression for CT-state absorption in the sub-band gap region of the EQE. As discussed in the introduction chapter, the CT-state absorption is given by the Marcus-type Gaussian equation of the form:

$$EQE_{PV}(E) = \frac{f}{E\sqrt{4\pi\lambda k_B T}} exp\left(\frac{-(E_{CT} + \lambda - E)^2}{4\lambda k_B T}\right) \tag{6.2}$$

where f, E_{CT} and λ are the fitting parameters. From the fitting results for P3HT:IEICO we get the E_{CT} value around 1.34 eV while for P3HT:IEICO-2F and P3HT:IEICO-4F the values are 1.27 and 1.25 eV respectively. When moving to the fluorinated acceptors, the E_{CT} value decreases slightly, which might be related to the lower-lying LUMO levels for IEICO-2F and IEICO-4F. Overall, the CT-state energies are slightly lower than for PTB7-Th devices, which explains the lower V_{OC} for P3HT based devices. Additionally, a second set of Gaussian's were fitted to obtain the effective optical gap of the blend layers. E_{opt} for P3HT:IEICO obtained from the fit is 1.43 eV while for P3HT:IEICO-2F and P3HT:IEICO-4F it is 1.36 and 1.35 eV respectively. The values obtained are very close to the E_{opt} value for neat IEICO films.

Similar to the case of PTB7-Th, we also extracted E_U values from the slope of sub-optical gap EQE. The value for all three P3HT based blends lies in the range of 25-33 meV, which is again on the lower side and signifies low interfacial energetic disorder.

Table 6.6: EQE_{PV} fitting results for P3HT:IEICOs.

System	E_{opt} [meV]	λ_{opt} [meV]	f_{opt} [meV^2]	E_{CT} [meV]	λ_{CT} [meV]	f_{CT} [meV^2]
P3HT:IEICO	1433	39.4	16.9	1346	126.6	0.83
P3HT:IEICO-2F	1367	32.3	21.8	1269	92.1	0.5
P3HT:IEICO-4F	1352	38.9	17.45	1256	220.3	3

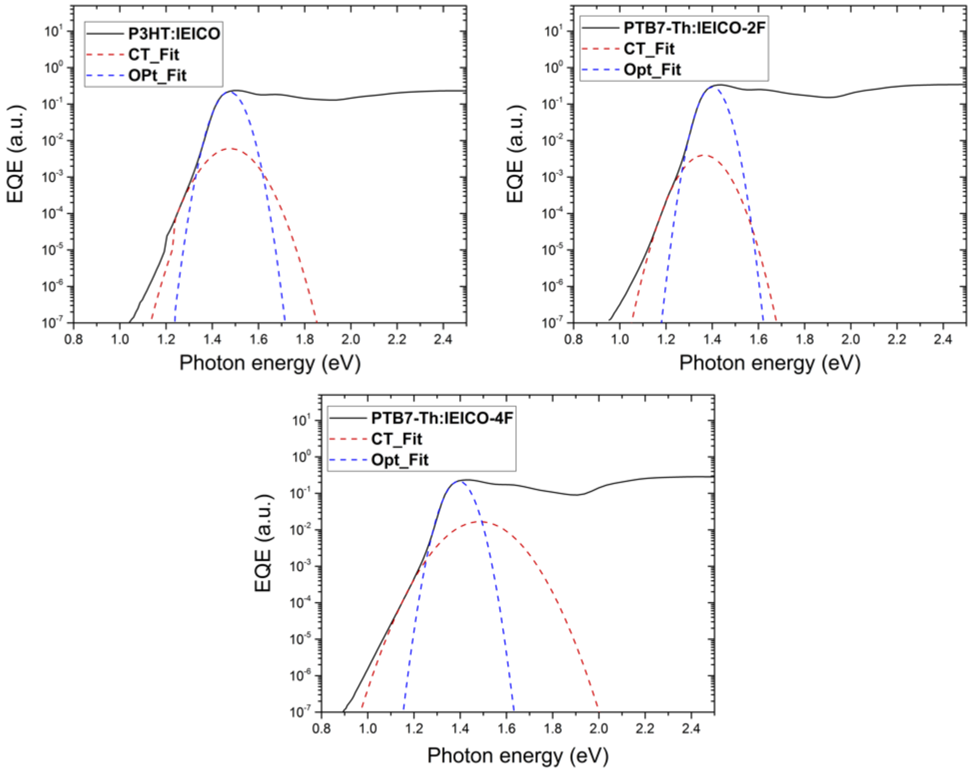

Figure 6.10: Sensitive EQE_{PV} spectra for P3HT:IEICO, P3HT:IEICO-2F and P3HT:IEICO-4F. The gaussian curves are the fits to determine CT-state energy and the effective optical gap of the blend.

6.5 Transient absorption (TA) spectroscopy

To determine the charge transfer dynamics and explore early timescale ($\leq$ 1 ns) photophysics, we measured the transient absorption spectra for the neat and blend films. (Note: All the TA measurements were conducted by Gareth Moore and the set-up used in located in Prof. Natalie Banerji's lab at the University of Bern, Switzerland). Due to the measurements being time-intensive, we focus only on IEICO-4F as the acceptor while using P3HT or PTB7-Th as the donor material. Additionally, TA spectroscopy measurements were also conducted on a ternary blend consisting of both P3HT and PTB7-Th as donors. Here we summarize the TA spectroscopy results and discuss the spectra and dynamics with important features. For a better understanding of the data, the reader is referred to section 3.6 of chapter 3 where the methodology and the basic principles of the measurements are discussed. For each sample, we will present the transient absorption (TA) spectra at 5-6 different pump-probe delay times, and the corresponding amplitude spectra obtained through global analysis. In global analysis, the dynamics at each spectral position are simultaneously fitted using a multi-exponential decay function. In this context, the amplitude spectra refer to the amplitude or the *'weight'* of each of the exponentials plotted as a function of wavelength. These spectra help in delineating different processes and as a first approximation also give the characteristic timescales associated with the main photophysical processes. As a starting point, we measured the TA spectra for the pristine films to identify particular spectral bands associated with each component.

6.5.1 TA spectra for the pristine films

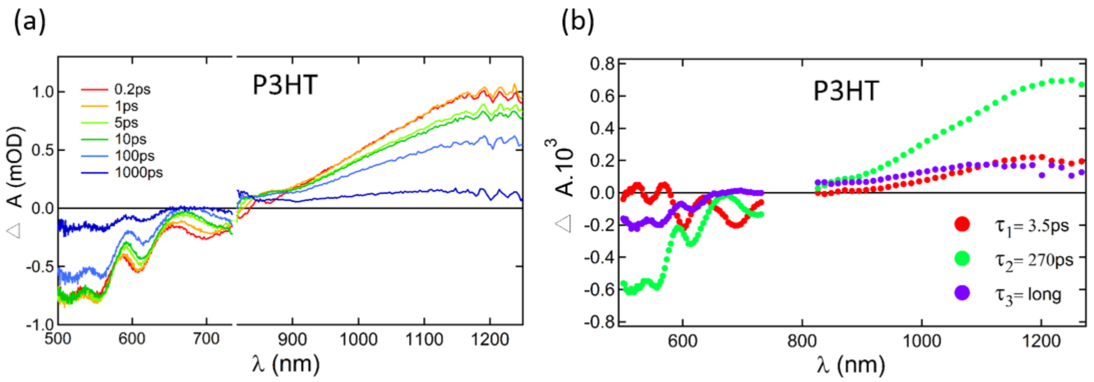

Figure 6.11: (a)Transient absorption (TA) spectra at different pump-probe delays for the neat P3HT film (b) Amplitude spectrum obtained through global fitting of dynamics of the TA signal. The characteristic time constant of 270 ps denotes the singlet exciton lifetime.

Figure 6.11 shows the TA spectra (left) and the amplitude spectra (right) obtained from the multi-exponential fit at each wavelength (global analysis). The wavelength of the pump pulse was set to 480 nm to excite the P3HT sample. In the TA spectra, three distinct bands can be distinguished: ground state bleach (GSB) between ∼500-650 nm, stimulated emission (SE) between 650-800 nm and the excited state absorption (ESA) in the range 800-1250 nm. Other important features include a slight temporal red-shift in the SE band and that all the three bands persist at long delay times (∼1000 ps). The amplitude spectra depict the collective dynamics at each spectral position. Additionally, it can be seen that the ESA signal predominantly decays with a timescale of around 270 ps. As in the pristine films the ESA mainly arises from the promotion of the first singlet excited state to higher excited states ($S_1 \rightarrow S_n$), this decay time constant denotes the lifetime of singlet excitons in pristine P3HT films. The value of the exciton lifetime matches very well with the literature reports [175, 176] although there are slight variations which can arise due to varying aggregation tendencies and different molecular weights for different batches of P3HT used in the different studies.

Figure 6.12 depicts the TA spectra for the pristine PTB7-Th film. The excitation wavelength in this case was 625 nm. Here two different bands, namely GSB and ESA, can be identified. The GSB spans within 500-750 nm range while the ESA band extends from 800 to 1250 nm. The figure on the right depicts the amplitude spectrum with a dominant decay time of 322 ps, representing the singlet lifetime. Again the values obtained from the fit are in good correlation with the earlier reported values [136, 177].

Similarly, the TA spectra for the IEICO-4F film (Figure 6.13) also show two dominant spectral bands. GSB lies in the range of 780-1050 nm while the ESA band is

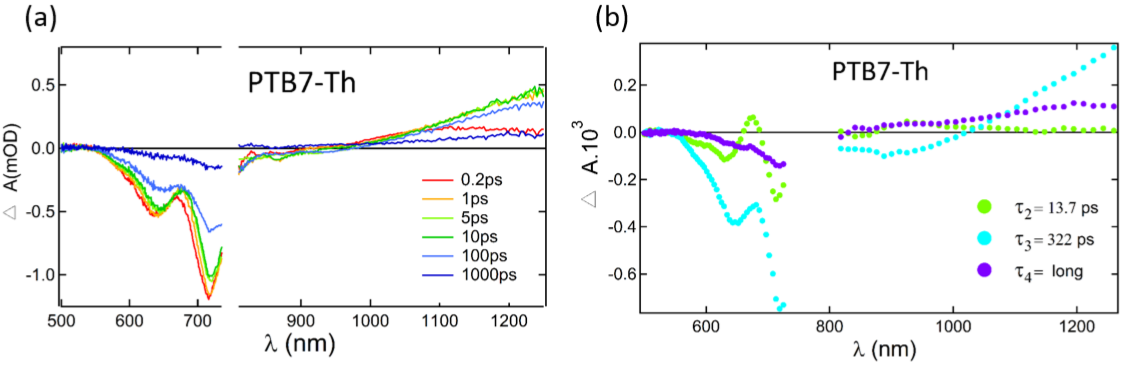

Figure 6.12: (a)Transient absorption (TA) spectra for the neat PTB7-Th film and (b)amplitude spectra depicting the characteristic time constants.

centered around 1150 nm. From the amplitude spectra, we get the singlet lifetime of 48 ps for IEICO-4F. The exciton lifetime for the acceptor is considerably shorter than for the donor polymers. This implies a stringent restriction on the size of the acceptor domains if the excitons are to be harvested efficiently. The excitons might recombine radiatively before they can diffuse to the donor:acceptor interface.

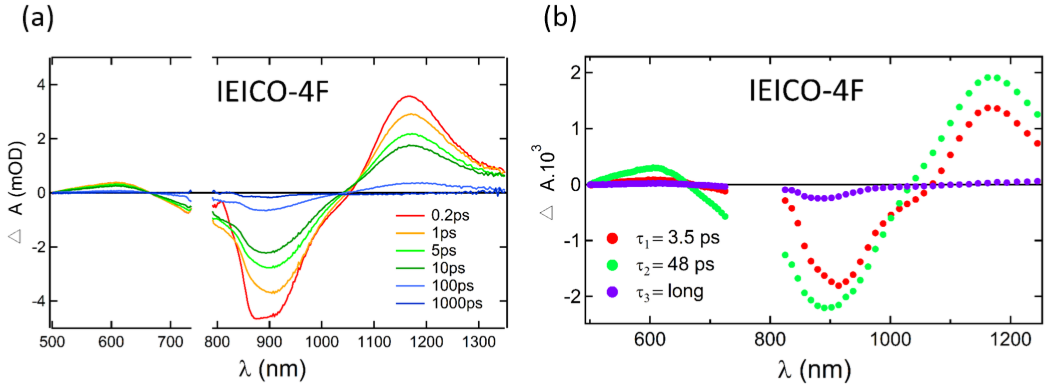

Figure 6.13: (a)Transient absorption (TA) spectra for the neat IEICO-4F film (b)Amplitude spectrum depicting the characteristic time constants.

6.5.2 TA spectra for the blend films

Next, we measured the TA spectra for the polymer:NFA and the polymer:polymer (P3HT:PTB7-Th) blend films. For the selective excitation of each component, we used a wavelength where only one of the components absorbs to avoid any contributions from the other materials. For P3HT excitation we use λ =480 nm while for PTB7-Th and IEICO-4F, the excitation wavelength is 625 and 900 nm respectively. Figure 6.14 shows the transient absorption and the amplitude spectra for the P3HT:IEICO-4F blend. For the P3HT excitation (λ =480 nm), the TA spectra show the GSB signal of P3HT and IEICO in the spectral range where the respective components absorb. Just next to the GSB (500-620 nm) of P3HT we observe a positive signal centered at ∼650 nm, we attribute this to the local electroabsorption (EA) signal resulting from P3HT chains surrounding the electron-hole pairs/CT-excitons. A prompt (t∼0.2 ps) rise of the electroabsorption (EA) signal implies a fast electron transfer process. Indeed, through the amplitude spectra, we obtain a time constant of 0.45 ps, which we assign to the very fast electron transfer from P3HT to IEICO-4F.

Additionally, the larger time constant of 6.3 ps can be assigned to the delayed electron transfer process. A delayed electron transfer component arises from the excitons created way from the interface which need the diffusion process for dissociation. Also, a third time constant of 43 ps is important. On close inspection of the TA spectra, we find that the GSB of P3HT decreases rapidly in 10-100 ps interval while the GSB of IEICO-4F remains constant. This can be attributed to an energy-transfer channel from P3HT to IEICO-4F. Also, the ESA band between 1000-1300 nm resembles very closely with the ESA features in the pristine IEICO-4F film, which means the excitation of IEICO-4F could not be completely avoided. Thus, there is also a hole transfer from IEICO-4F to P3HT involved in the spectra as well. Overall, this TA spectra represents a complicated scenario with a variety of parallel processes. Namely, prompt and delayed electron transfer from P3HT to IEICO-4F, energy transfer from P3HT to IEICO-4F and a slight contribution to the spectra from hole transfer from IEICO-4F to P3HT.

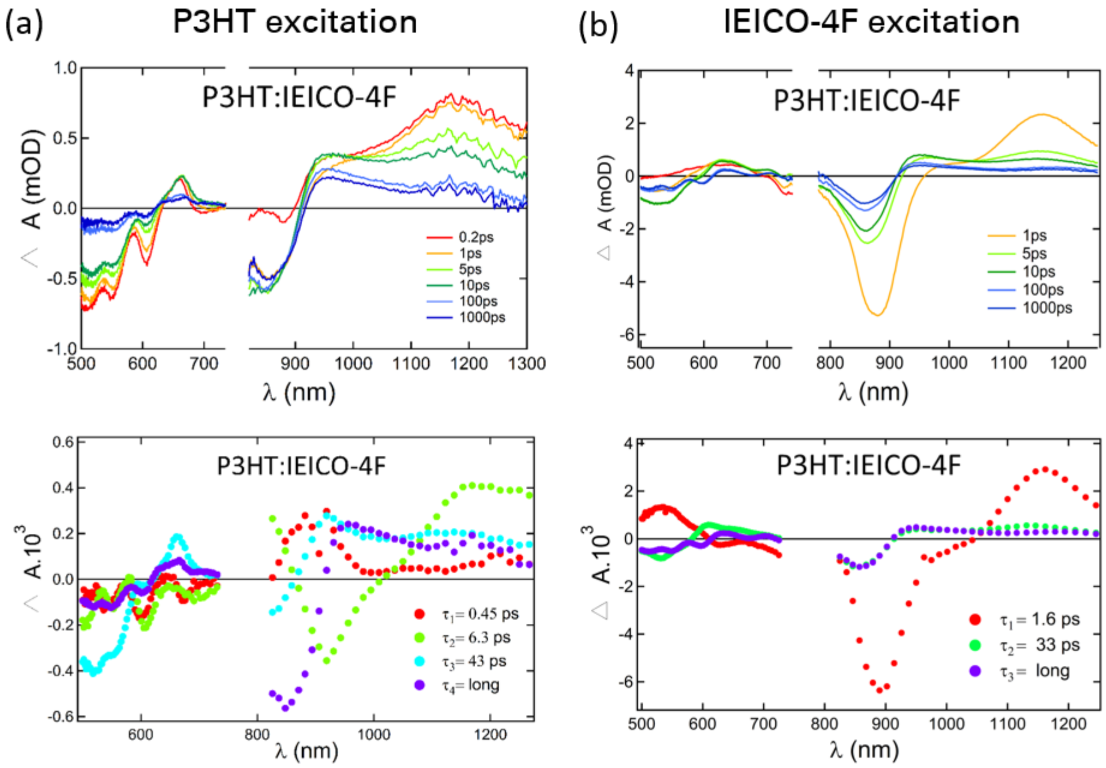

Figure 6.14: (a)Transient absorption and amplitude spectra for P3HT:IEICO-4F blend film with selective excitation of P3HT (λ =480 nm). (b)Transient absorption and amplitude spectra for P3HT:IEICO-4F with selective excitation of IEICO-4F (λ =900 nm).

In the case of IEICO excitation (λ =900 nm), we predominantly observe the GSB signal of the IEICO-4F and the ESA from IEICO-4F excitons and free polarons. Characteristic time constant for the hole-transfer process is 1.6 ps. A relatively slower hole-transfer compared to electron transfer can be related to a near-zero energetic offset between the HOMO levels of P3HT and IEICO-4F, which implies a negligible driving force. The schematic depicting all the important photophysical processes in the P3HT:IEICO-4F blend is presented as Figure 6.15.

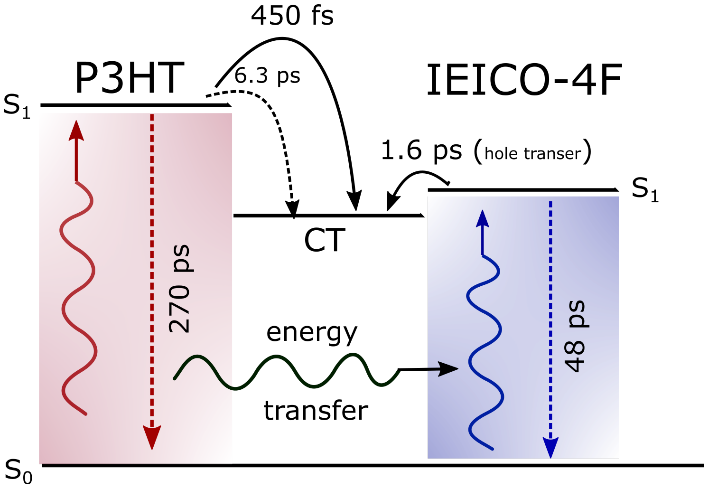

Figure 6.15: Schematic depicting all the important photophysical processes in P3HT:IEICO-4F blend. The delayed electron transfer component is shown using the dashed arrow.

We also looked at the PTB7-Th:IEICO-4F blend with excitation wavelengths for the donor and the acceptor at 625 and 900 nm respectively. Figure 6.16 (a) shows the TA spectra with predominant excitation of PTB7-Th at 625 nm. At early time scales, the GSB signal from PTB7-Th and IEICO can be identified. Also, the characteristic peak associated with the IEICO excitation is present at an early time scale. The presence of the IEICO GSB signal and ESA peak at 1200 nm implies that the IEICO is also partly excited at this wavelength. Looking at the amplitude spectrum, we get the fastest time constant of 0.4 ps, which can be ascribed to the prompt electron transfer from PTB7-Th to IEICO-4F. The second time constant of 27.2 ps is associated with delayed hole transfer from IEICO-4F to PTB7-Th. This is because in this time scale (10-100 ps) the GSB signal of the polymer rises again, which hints at the charge accepting process from the polymer. Also during the same time window (10-100 ps), the GSB of IEICO-4F decreases. One argument which can explain this behavior is that the GSB signal of IEICO-4F is overlayed over its weak stimulated emission (SE) signal, which quenches as a result of the hole transfer process. Quenching of the SE signal causes the apparent decrease in the GSB signal of IEICO-4F. Also worth noticing is the peak centered around 1200 nm persists at long delay times (>1000 ps), this might be due to the additional overlayed signal from free polarons which lies in the same spectral region as the IEICO-4F exciton features.

For the case of the IEICO-4F excitation (λ =900 nm), the spectra are straight forward to interpret. At early time scales, we see the GSB and the ESA signal due to the IEICO-4F excitons. The GSB signal of the polymer gradually rises with increasing delay times as a result of the hole transfer process. From the amplitude spectra, it can be concluded that the hole transfer is delayed and occurs with an average time constant of 5 ps. Also worth noticing is the shape of the GSB signal of the polymer, which attains a more vibronic character at longer delay times. This is usually the case when free polarons are moving from an amorphous region to a crystalline region in the film.

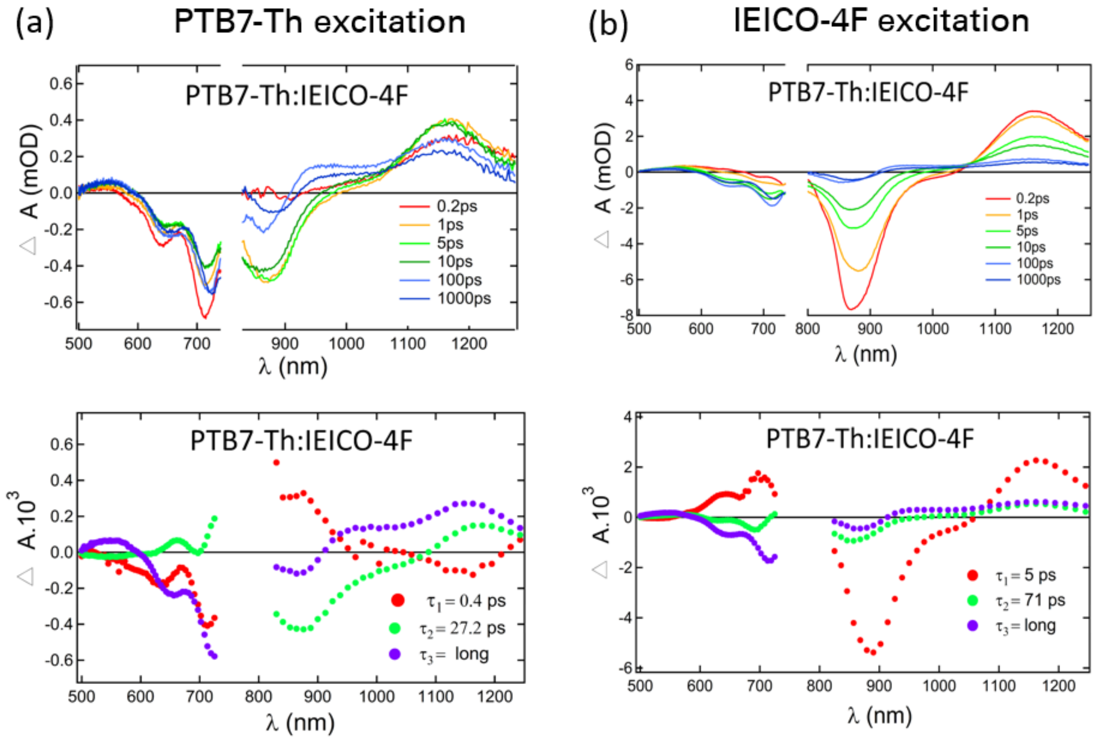

Figure 6.16: (a)Transient absorption and amplitude spectra for PTB7-Th:IEICO-4F blend film with selective excitation of PTB7-Th (λ =625 nm). (b)Transient absorption and amplitude spectra for PTB7-Th:IEICO-4F with selective excitation of IEICO-4F (λ =900 nm).

As a precursor to investigating the charge transfer dynamics in a ternary blend, we first examined the polymer blend of P3HT and PTB7-Th. Figure 6.18 represents the respective TA and the amplitude spectra for selective P3HT excitation (λ =480 nm) and the selective PTB7-Th excitation (λ =625 nm). At both the wavelengths, the TA spectra look quite similar, which is indicative of the fact that the wavelengths are not highly selective and that both the polymers are excited at the two wavelengths. In the spectra, the GSB signal for both the polymers appears at early times and persists until longer delay times (~1 ns). Since there is no selective decrease of the GSB signal of one polymer and the concomitant rise of another one, an energy transfer process between the polymers can be ruled out. This is quite surprising as the luminescence spectra of P3HT overlaps very well with the absorption spectra of PTB7-Th where one would expect Förster type energy transfer.

Other possibility is that there is some charge transfer between the polymers. From the amplitude spectra, we get the time constant of 1.4 ps for the electron transfer

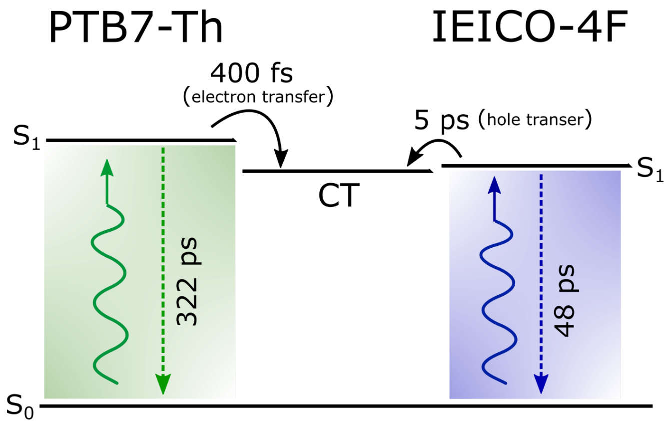

Figure 6.17: Schematic depicting the important photophysical processes in PTB7-Th:IEICO-4F blend.

from P3HT to PTB7-Th and a time constant of 3 ps for the hole transfer from PTB7-Th to P3HT. The longer time constants of 563 and 990 ps can be assigned to recombination of polarons as the ESA signal reduces sharply between the 100-1000 ps time window.

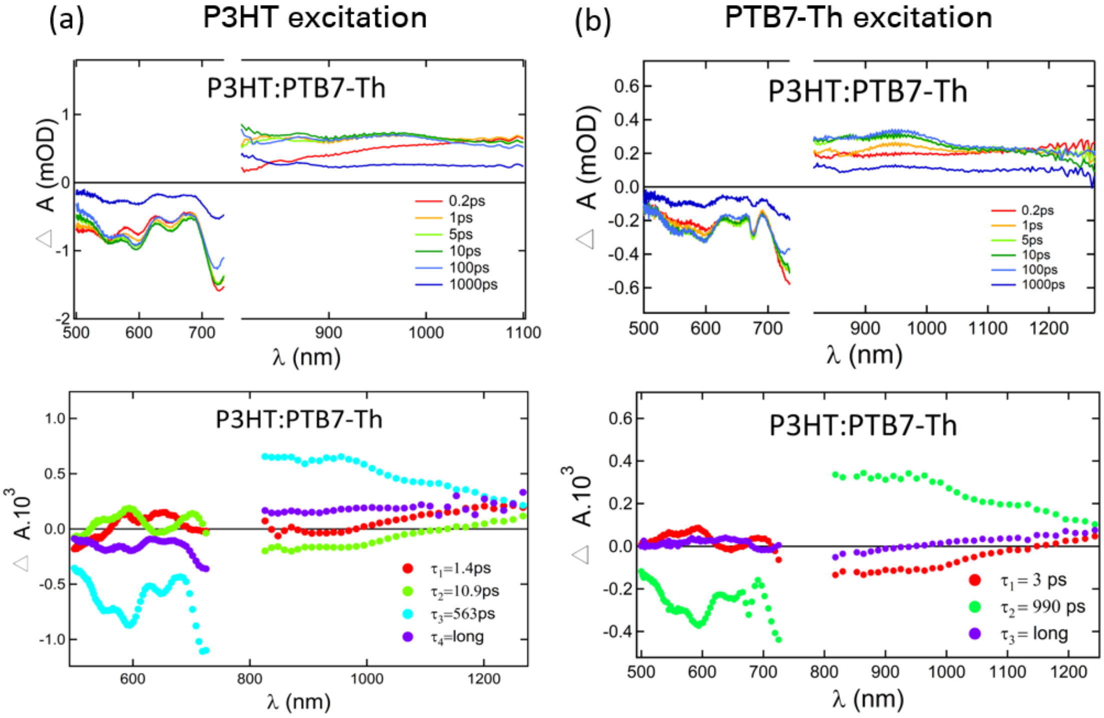

Figure 6.18: (a)Transient absorption and amplitude spectra for P3HT:PTB7-Th blend film with selective excitation of P3HT (λ =480 nm). (b)Transient absorption and amplitude spectra for P3HT:PTB7-Th with selective excitation of PTB7-Th (λ =625 nm).

Now we explore the photophysics of the ternary blend - P3HT:PTB7-Th:IEICO-4F (0.5:0.5:1). We first discuss the spectra with selective IEICO-4F excitation (λ =900 nm), as at this wavelength we are sure that none of the polymers is excited, which eliminates the possibility of several processes happening simultaneously. Looking at Figure 6.19 (a), the early time TA spectra shows the GSB and ESA of IEICO-4F. At longer pump-probe delays, the GSB signal of P3HT rises sharply. This is indicative of the hole transfer process from IEICO-4F to P3HT. There is also a slight rise in the PTB7-Th GSB indicative of hole transfer to the PTB7-Th. In the amplitude spectra, the 3.5 ps component is representative of the hole transfer to both the polymers. But as the amplitude is much higher in the spectral region of P3HT's GSB, it implies that the hole transfer process is more favorable to P3HT rather than to PTB7-Th. This can be related to the higher driving force (ΔHOMO) for the hole transfer from IEICO-4F to P3HT. The 28.2 ps component has the same spectral shape as the 3.5 ps component and is indicative of the delayed hole transfer process. Also, as the GSB of both the polymers persists at long delay times, it implies that the free polarons mainly reside in the polymer domains. Overall, the key takeaway message is that the hole transfer is more favorable to P3HT and happens on a time scale of around 3.5 ps.

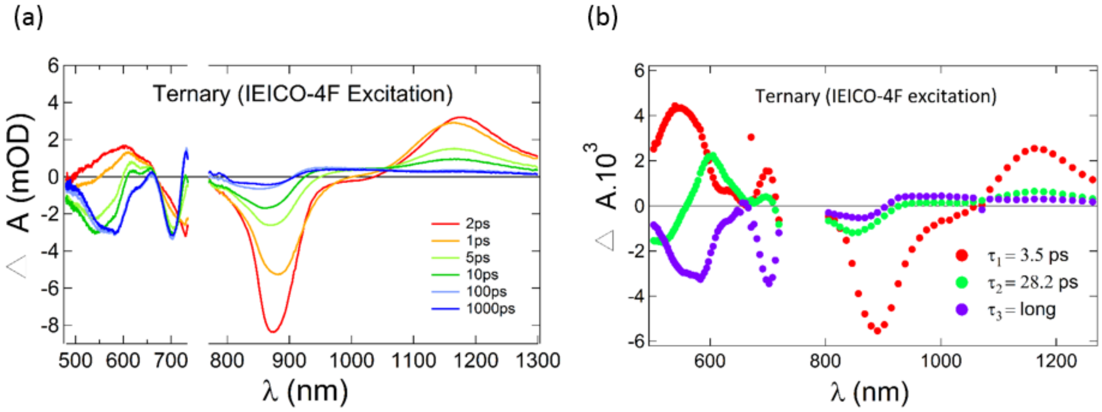

Figure 6.19: (a)Transient absorption spectra for the ternary blend film with selective excitation of IEICO-4F (λ =900 nm). (b) Amplitude spectra for the ternary blend showing representative timescale of the hole transfer process.

Looking at the case of P3HT (λ =480 nm) and PTB7-Th (λ =625 nm) excitation of the ternary blend (see Figure 6.20), in both cases we observe a GSB signal from all three components at early times. This means that all the three components, i.e., the two polymers and the IEICO-4F are excited at both the wavelengths, hence the scenario is again quite complicated. Nevertheless, the main photophysical processes can be deduced from the spectra. One of the main features at both wavelengths is the sharp decrease in the GSB signal of PTB7-Th while a concomitant rise in the GSB signal of IEICO-4F can be seen at early times. This indicates an energy transfer channel from PTB7-Th to IEICO-4F, and from the amplitude spectra, it can be deduced that this process occurs on a 0.5-0.6 ps timescale. Also evident from the amplitude spectra is the subsequent hole transfer from IEICO-4F to P3HT which occurs in a time window of 7-10 ps (the green spectra where the GSB signal of P3HT rises and that of IEICO-4F reduces simultaneously). Also worth mentioning is the spectral shape of the P3HT GSB. No vibronic character is visible like in the case of binary blends, which suggests the morphology of P3HT domains is drastically different in the ternary blend and mostly consists of amorphous fractions. At long delay times, the GSB of P3HT persists while that of PTB7-Th is diminished. This implies that most of the holes are present in the P3HT domains which can be explained by the more favorable hole transfer process from IEICO-4F to P3HT rather than to PTB7-Th (as discussed in the previous paragraph). The 89 and 134 ps component can be related to the recombination of charges/polarons as it mainly indicates the reduction of the ESA signal. The overall important photophysical processes happening in the ternary blend is presented in form of a schematic in Figure 6.21.

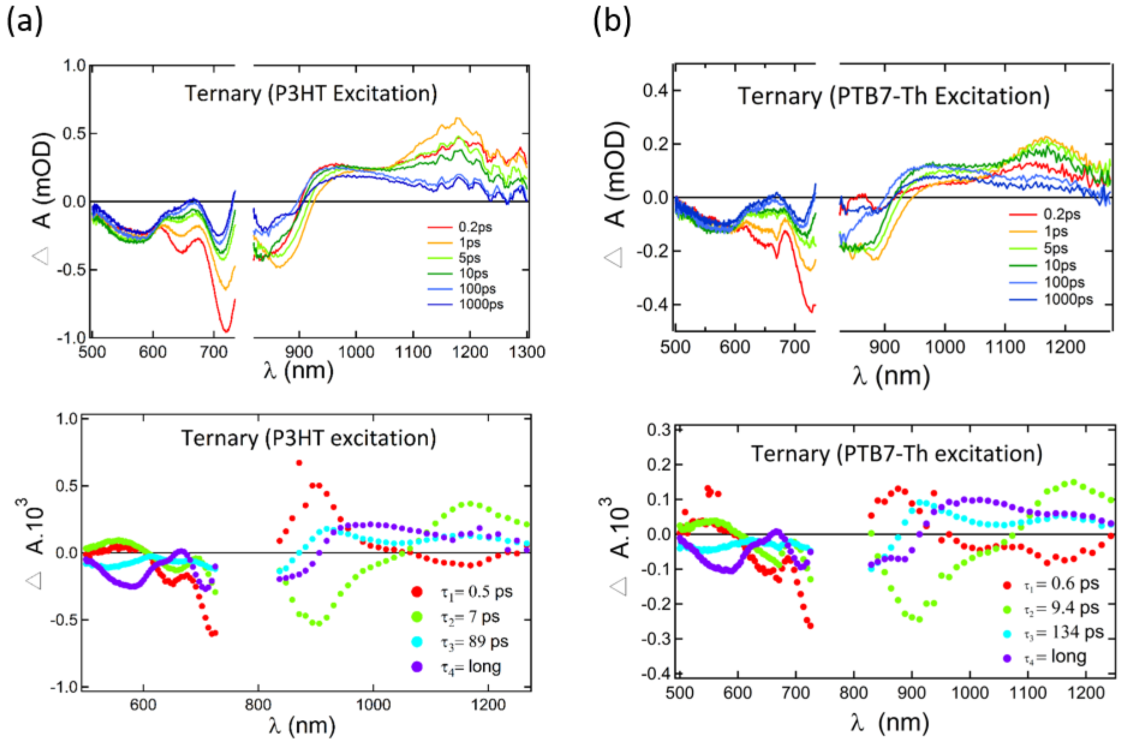

Figure 6.20: (a)Transient absorption and amplitude spectra for a ternary blend film with selective excitation of P3HT (λ =480 nm). (b)Transient absorption and amplitude spectra for the ternary blend with selective excitation of PTB7-Th (λ =625 nm).

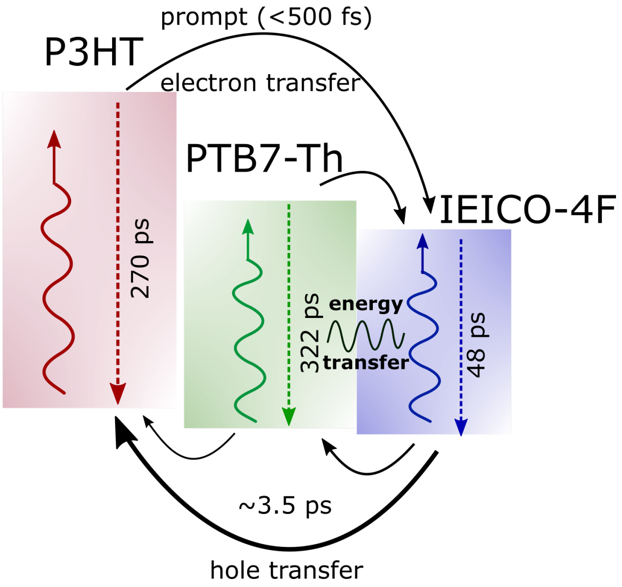

Figure 6.21: Schematic depicting the most important photophysical processes in the ternary blend of P3HT,PTB7-Th and IEICO-4F.

6.6 Morphology

We investigated the morphology of the blends using transmission electron microscopy (TEM), atomic force microscopy (AFM) and grazing incidence x-ray scattering (GIWAXS). Figure 6.22 and 6.23 show the TEM and AFM micrographs for the blend films. For P3HT based blends, we observe needle-like flaky structures in the TEM images. While the surface morphology measured using AFM shows some domain like features and moderately high surface roughness values. On the other hand, for PTB7-Th based blends, a fibrillar morphology can be seen clearly in the TEM images. While the surface structure measured using AFM shows a granular structure. We measured the grain size with 2D-fast Fourier transform (FFT), and the average values range between 30-40 nm for the three PTB7-Th blends. Also, the surface roughness for these films is considerably lower than that for P3HT based films. Overall, using the real-space imaging techniques, it can be concluded that P3HT and PTB7-Th interact differently with IEICO based acceptors, which leads to a marked difference in morphology between the blends.

For the GIWAXS analysis, we first measured the scattering signal from the pristine films to identify the peak positions of each component. For the polymers P3HT and PTB7-Th, we see the typical GIWAXS signal with lamellar and π-stacking peaks being clearly visible. For P3HT, the π-stacking peak and the lamellar stacking peak are at q=1.66 $\mathring{A}^{-1}$ (d= 3.78 $\mathring{A}$) and q=0.37 $\mathring{A}^{-1}$ (d= 17 $\mathring{A}$) respectively. While for PTB7-Th the π-stacking distance is slightly larger, d = 3.92 $\mathring{A}$ (q_z=1.60$\mathring{A}^{-1}$) and it has a lamellar stacking distance of 25 $\mathring{A}$ (q=0.25 $\mathring{A}^{-1}$). For the IEICOs, we observe a π-stacking distance of around 3.4 $\mathring{A}$. The π-stacking in these molecules arises from the interactions between end-capping units of the adjacent molecules, and this interaction also forms the intermolecular charge transport channel in these molecules. Between the IEICO's we did not observe a change in peak position, which

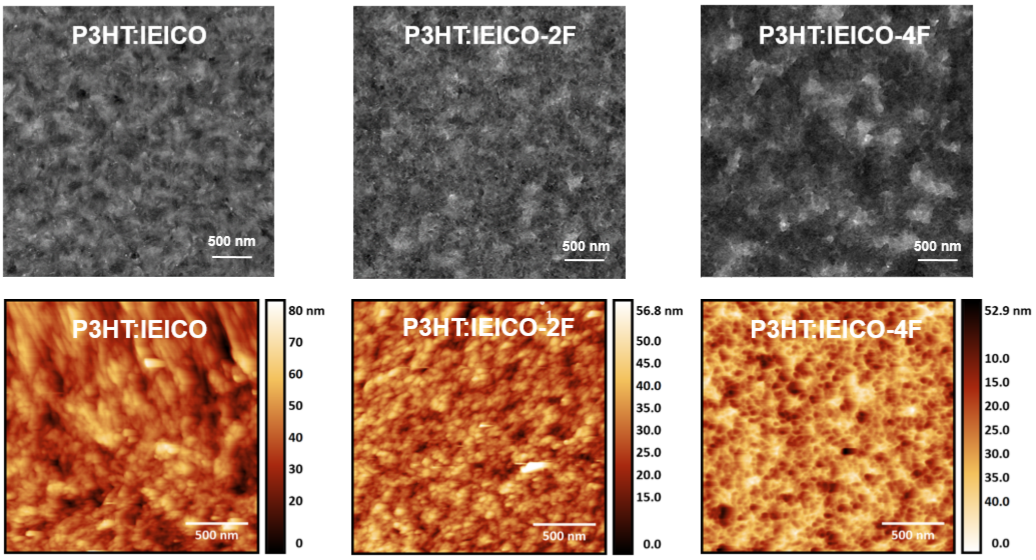

Figure 6.22: TEM (top) and AFM (bottom) micrographs for the P3HT:IEICOs blend films.

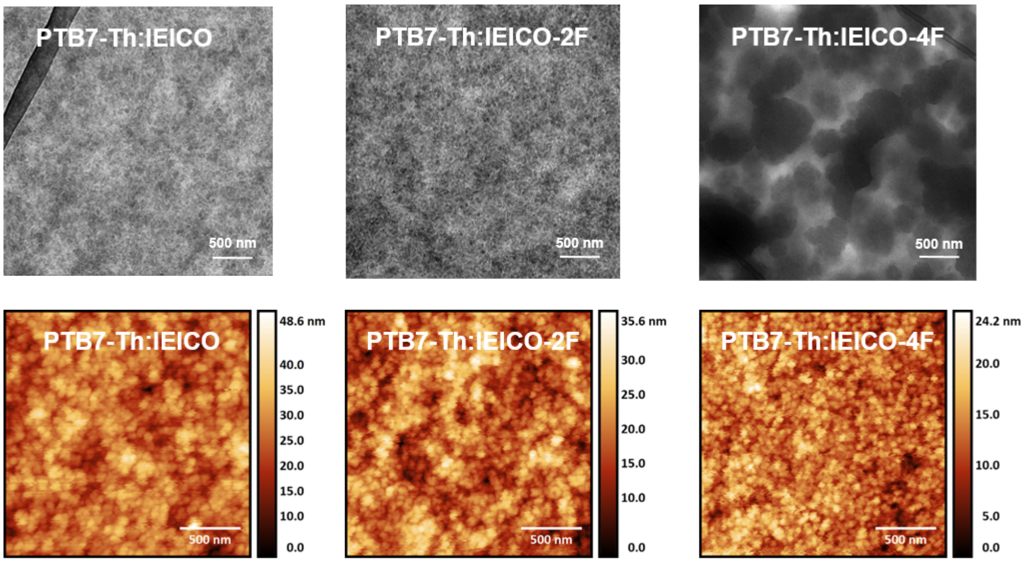

Figure 6.23: TEM (top) and AFM (bottom) micrographs for the PTB7-Th:IEICOs blend films.

implies that the fluorine substitution (-2F,-4F) does not have a significant influence on the molecular packing.

Now looking at the PTB7-Th based blend films (Figure 6.26) there is a marked difference in the GIWAXS signal compared to the neat films. We can clearly identify multiple peaks from the IEICOs and PTB7-Th, which indicates a high degree of crystallinity in these films. High crystallinity of donor and acceptor domains for

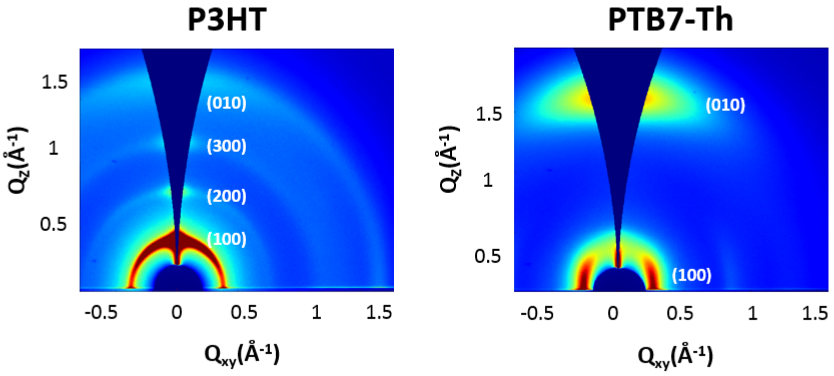

Figure 6.24: GIWAXS images for the pristine polymer films: P3HT and PTB7-Th.

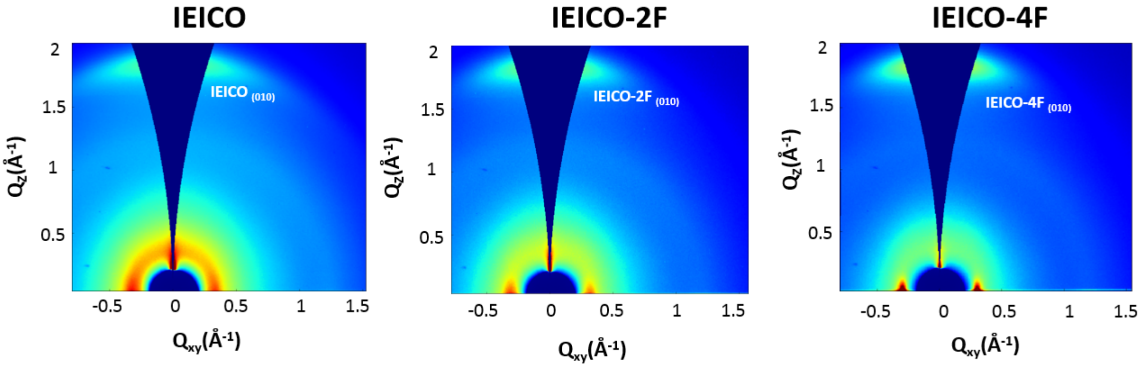

Figure 6.25: GIWAXS images for the pristine acceptor films: IEICO,IEICO-2F and IEICO-4F.

these blends partly justify the high performance in solar cells. This is because the high crystallinity improves the average charge carrier mobility of the blend, which increases the overall charge collection efficiency and enhances the fill factor of the device.

On the contrary, the GIWAXS image of the P3HT:IEICO-4F blend shows only IEICO-4F peaks and no P3HT peaks (Figure 6.27). This points to the fact that the blend film mostly consist of amorphous polymer domains, which also explains the poor performance of these blends. We also measured the GIWAXS signal from the ternary blends, and the outcome was very similar. Again, we just observe the peaks of the IEICO-4F and no polymer peaks were observed, suggesting that the crystallization of the polymers is greatly restricted and they mainly contribute to the amorphous fraction in the film. Thus, the relatively poor performance of the P3HT and PTB7-Th based ternary blend can be ascribed to the highly amorphous morphology, which can be the result of the hindered crystallization in the presence of other components or co-crystallization of the polymers forming a single homogeneous donor phase which mainly remains amorphous due to entangled polymer chains.

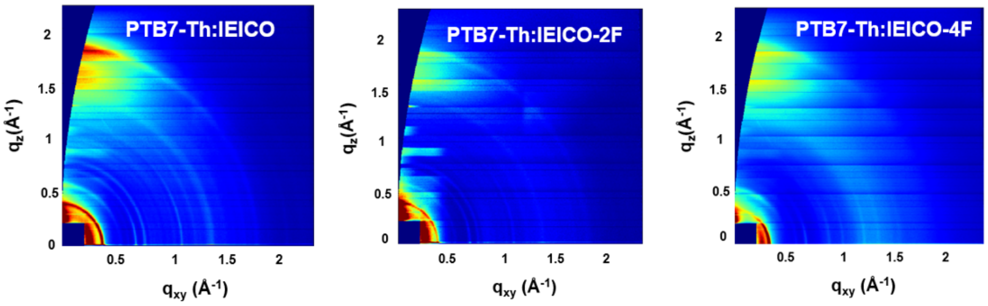

Figure 6.26: GIWAXS images for the PTB7-Th based blend films :PTB7-Th:IEICO,PTB7-Th:IEICO-2F and PTB7-Th:IEICO-4F

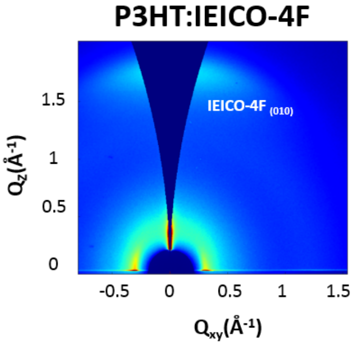

Figure 6.27: GIWAXS image for the P3HT:IEICO-4F blend film.

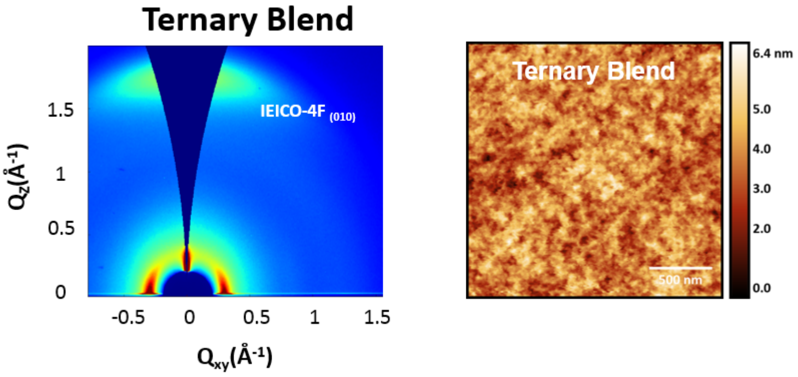

Figure 6.28: GIWAXS image for the ternary blend (left) and an AFM micrograph of the ternary blend.

6.7 Summary and Conclusion

The work in this chapter focuses on the investigation of fluorinated non-fullerene acceptors (NFAs) involving indacenodithiophene (IDT) based IEICO molecules. The main idea behind the fluorination of the NFAs was to increase the electron withdrawing capability of the end-capping units, which enhances the intramolecular charge transfer (ICT) effect. Enhanced ICT shifts the energy of the frontier molecular orbitals, bringing the HOMO and LUMO closer to each other, which results in a pronounced red-shift in the absorption spectra of the fluorinated molecules. These acceptors were blended with P3HT and PTB7-Th donor polymers and the device performance was tested for binary and ternary solar cells. Devices based on PTB7-Th performed the best, and the blend of PTB7-Th:IEICO-4F shows an impressive PCE of 9.5%.

On the other hand, the devices based on P3HT as the donor and the ternary blends show low device performance. Morphological investigations suggest that the good performance of the PTB7-Th based devices is based on the high crystallinity of the blends, while for P3HT based devices and the ternary blend, the reduced performance partly results from a poor morphology and the formation of predominantly amorphous domains. In addition, sensitive EQE_{PV} and EL measurements were used to compute the energy of the charge transfer state (E_{CT}) and quantify the voltage losses. Voltage losses in PTB7-Th blends are of the order of 500 mV, which are quite low compared to the reported values for other bulk-heterojunction solar cells. The low voltage losses and the relatively narrow optical gap of these acceptors allow the devices to achieve high V_{OC} and high j_{sc} simultaneously which results in the superior device performance for PTB7-Th based devices. Additionally, we also find that the E_{CT} values in these blends lie exceptionally close to the measured E_{opt} value of the NFAs implying that these blends form a near-zero driving force system for the hole transfer process.

The other main focus of this chapter is on the investigation of the charge transfer dynamics and photophysics in these blends using transient absorption spectroscopy. From the investigation of pristine films, we find that the singlet lifetime in IEICO-4F is relatively short (around 50 ps) and much lower than in the polymers where the singlet lifetimes are of the order of few hundred picoseconds. In the case of binary blends, both the P3HT and PBT7-Th based blends exhibit a prompt electron transfer process while the hole transfer from IEICO-4F to the polymer is much slower. This can be attributed to the near-zero driving force for the hole transfer process in both the blends. Also, in these blends, we identify an energy transfer channel from the polymer to the acceptor IEICO-4F. In the ternary blends we could detect an energy transfer channel from PTB7-Th to IEICO-4F as well followed by a preferable hole transfer to P3HT. As a result, in the ternary blends most of the holes accumulate in the P3HT domains, where their transport is hindered due to the formation of an amorphous morphology. The anticipated energy transfer from P3HT to PTB7-Th was not observed which can be explained by the formation of larger polymer domains of both the polymers in comparison to the Förster radius. These factors lead to a reduced performance for the ternary blends despite P3HT having a complementary absorption spectra and suitable energy levels. These findings point out once again the complexity of ternary blends and suggest that careful consideration is needed when choosing the third component in a ternary blend. Despite these results, we believe there is still room to improve the efficiency of NFA based solar cells using a ternary blend approach provided compatible, panchromatic donor polymers can be identified which form improved morphology and yield better charge transport properties. All in all, the fluorination of the IEICO molecules is a promising strategy to obtain improved acceptor molecules which yield a superior device performance. These materials show a great promise to be used in high efficiency binary and ternary solar cells.

Chapter 7

Conclusions and Outlook

The work in this thesis focuses on the investigation of low optical gap donor and acceptor materials for organic solar cells. The study of low optical gap materials is becoming increasingly important as the research community moves towards tandem device architectures and/or ternary blend junctions to achieve superior device performance. In this body of work, we primarily study the effect of the molecular structure of donor/acceptor materials with the aim of identifying key design principles which could, in turn, help synthetic chemists design better organic semiconductors for the application in organic solar cells.

In the first part of the thesis, we investigated a series of low optical gap diketopyrrolopyrrole (DPP) polymers. The emphasis was placed on altering the central conjugated core and the solubilizing alkyl side chains to see how it affects the blend morphology and the device performance. Usually, linear side chains are not enough to make these polymer semiconductors soluble in common organic solvents and the need for branched side chains arises. We altered the branching point of the alkyl side chains and found that there is a direct correlation between the position of the branching point and the polymer's tendency to crystallize. The further out the branching position of the side chains, the closer the central conjugated core can π-stack. Closer π-stacking was seen to directly influence the carrier mobility as the intermolecular charge hopping process primarily depends on the π-stacking distance. Apart from the crystallization and the pi-stacking effect, the side chains had a far-reaching consequence on the morphology of the blend films. We observed a direct correlation between the length of the side chains and the width of the polymer fibrils, which in turn affects the photogeneration yield of carriers. In general, we could identify the requirements on the structure of the alkyl side chains to synthesize optimal polymers for their improved device performance in organic solar cells. For DPP polymers, side chains should be designed so that the polymers are at a solubility threshhold in a given solvent. Although this might introduce difficulties in the processing of the films but it is a necessary condition to obtain fine morphology. In this regards, short side chains will be beneficial. Also, to enhance crystallization of the polymers, branching position of the side chains should be far away from the conjugated backbone.

Using sensitive spectroscopy measurements, we found that the DPP:PCBM blends form a near-zero driving force system for the electron transfer process. Thus, in the second part of the thesis, we focused on investigating the electron and charge transfer dynamics in the DPP blends. Transient absorption (TA) spectroscopy measurements revealed ultra-short singlet lifetimes (15-20 ps) in DPP polymers, which puts a huge constraint on the domain size of the polymers for efficient exciton harvesting. In fact, in the first part of the thesis, we found a direct correlation between the photogeneration yield and the width of the polymer fibrils and the short singlet lifetimes validate this finding. In the blends films, we observed an ultrafast electron transfer within the instrument resolution (100 fs). DFT calculations of the donor:acceptor complex reveal a very high coupling strength of the order of 30-50 meV between the DPP and PCBM frontier orbitals which results in a high charge transfer rate and consequently the ultrafast electron transfer times. Another important finding from the transient absorption (TA) measurements was that we found similar recombination time constants in the blend films as compared to the singlet lifetimes in the neat polymer films. We ascribe this dominant recombination component in the DPP blends to be the CT-state lifetime. The reason for the correlated singlet and CT state lifetimes are two-fold: either a significant back transfer of the CT to the singlet sate forming an indirect radiative decay pathway for the CT states or because of the hybridization of the singlet and the CT states due to their energetic proximity. Electromodulated differential absorption (EDA) spectroscopy revealed high early time ($<$ 1 ns) mobilities in the blend, which also facilitates the dissociation and extraction process of charge carriers.

In the last part of the thesis, we move our attention to the low optical gap non-fullerene acceptors (NFAs). We investigated a series of indacenodithiophene (IDT) based IEICO molecules with a varying degree of fluorination at their end groups. Fluorination in these molecules tends to enhance the intramolecular charge transfer (ICT) effect, which has a pronounced impact on the energetics of the frontier orbitals and the corresponding absorption spectra. The acceptor molecules are paired with PTB7-Th and P3HT donor polymers. In combination with PTB7-Th, the fluorinated IEICO acceptors demonstrated impressive power conversion efficiencies around 10%, while with P3HT as the donor and in ternary blends, the device performance was sub-optimal. The reasons for the reduced device performance can be in part attributed to the formation of a predominantly amorphous morphology as revealed by GIWAXS measurements. For the PTB7-Th:IEICO blends a number of IEICO diffraction peaks were observed signaling a relatively high crystallinity of these blends which explains their superior device performance. Additionally, we used transient absorption (TA) spectroscopy to investigate the photophysics of the binary and ternary blends. We observed prompt/ultrafast electron transfer processes while the hole transfer was found to be relatively slower because of the near-zero driving force (similar energy for the HOMO levels). In the binary as well as the ternary blend we could identify signatures of energy transfer from the donor polymer to the acceptor while the expected energy transfer between the two polymers in the ternary blend was not observed. In the ternary blend, it was found that the accumulation of charge carriers is very selective depending on the energetics of the components. For our systems, we observed a predominant accumulation of holes in the P3HT domains. Overall, the fluorination seems to have a positive effect on device performance, and in the future IEICO/ITIC based molecules should be synthesized while involving fluorination of the acceptor/donor end units as an active design strategy. Also concerning the ternary blend approach, the low optical gap of these acceptors enables a lot of suitable combinations with medium to large optical gap polymers. The compatibly of different donor polymers with IEICO/ITIC based acceptors needs to be tested to identify potential high performing ternary blends.

In present times, it is safe to say that a lot of the underlying physical and chemical processes in organic solar cells have been studied extensively and are relatively well understood. Owing to this fact, the research direction in the organic solar cells field has been changing its course and these days a lot of emphasis is given on the applied device engineering and the material development. With regards to the efficient/swift material development process, the role of a device physicist has changed from primarily investigating the fundamental properties to relating device physics with the molecular structure of the semiconductors. In this thesis, we followed this direction by investigating new materials systems and relating findings from the physical measurements to their molecular structure.

We believe that in the future, an even closer collaboration between device physicists and chemists will be needed to identify key design rules for polymers and small molecule acceptors. Given the seemingly infinite possibilities of tuning the properties of organic semiconductors, narrowing down of design rules becomes a crucial step in the designing of optimal materials for high device performance. Also, given the intrinsic limits on the efficiency of single-junction devices, the emphasis will shift towards ternary blends and tandem device architectures. With regards to this, the investigation of low optical gap polymers and small molecule acceptors is important as they exhibit complementary absorption and energetic properties in relation to the widely developed medium to large optical gap organic semiconductors. Additionally, a specific issue to be addressed in the future will be the investigation of non-radiative voltage losses in non-fullerene systems. In particular, identifying the molecular features for example, specific functional groups or chemical bonds which are detrimental and thus lead to a higher degree of non-radiative loss. Cutting down the non-radiative losses whilst simultaneously reducing the optical gap of the materials could potentially circumvent the fundamental trade-off between the j_{sc} and the V_{OC} and yield superior organic solar cells which are on par with other 3rd and 4th generation photovoltaic technologies.

Bibliography

[1] `https://yearbook.enerdata.net/total-energy/world-consumption-statistics.html`. Accessed: 2019-07-10.

[2] `https://www.globalenergyinstitute.org/look-iea%E2%80%99s-new-global-energy-forecast`. Accessed: 2019-07-10.

[3] `https://oilprice.com/Energy/Energy-General/BPs-Latest-Estimate-Says-Worlds-Oil-Will-Last-53.3-Years.html`. Accessed: 2019-07-10.

[4] `https://www.worldcoal.org/coal/where-coal-found`. Accessed: 2019-07-10.

[5] `https://climate.nasa.gov/scientific-consensus/`. Accessed: 2019-07-10.

[6] `https://climate.nasa.gov/evidence/`. Accessed: 2019-07-10.

[7] `https://www.iea.org/publications/freepublications/publication/TechnologyRoadmapSolarPhotovoltaicEnergy_2014edition.pdf`. Accessed: 2019-07-10.

[8] `https://www.oxfordpv.com/perovskite-silicon-tandem`. Accessed: 2019-07-10.

[9] X. Xu, K. Feng, Z. Bi, W. Ma, G. Zhang, and Q. Peng, "Single-junction polymer solar cells with 16.35% efficiency enabled by a platinum (ii) complexation strategy," *Advanced Materials*, p. 1901872, 2019.

[10] L. Meng, Y. Zhang, X. Wan, C. Li, X. Zhang, Y. Wang, X. Ke, Z. Xiao, L. Ding, R. Xia, *et al.*, "Organic and solution-processed tandem solar cells with 17.3% efficiency," *Science*, vol. 361, no. 6407, pp. 1094–1098, 2018.

[11] L. Nian, Y. Kan, H. Wang, K. Gao, B. Xu, Q. Rong, R. Wang, J. Wang, F. Liu, J. Chen, *et al.*, "Ternary non-fullerene polymer solar cells with 13.51% efficiency and a record-high fill factor of 78.13%," *Energy & Environmental Science*, vol. 11, no. 12, pp. 3392–3399, 2018.

[12] Y.-J. Cheng, S.-H. Yang, and C.-S. Hsu, "Synthesis of conjugated polymers for organic solar cell applications," *Chemical reviews*, vol. 109, no. 11, pp. 5868–5923, 2009.

[13] H. Zhou, L. Yang, and W. You, "Rational design of high performance conjugated polymers for organic solar cells," *Macromolecules*, vol. 45, no. 2, pp. 607–632, 2012.

[14] `https://www.bbc.com/news/science-environment-45132427`. Accessed: 2019-07-10.

[15] `https://www.heliatek.com/product/`. Accessed: 2019-07-10.

[16] `https://infinitypv.com/technology/opv`. Accessed: 2019-07-10.

[17] `https://www.bbc.com/news/science-environment-45132427`. Accessed: 2019-07-10.

[18] J. L. Bredas and G. B. Street, "Polarons, bipolarons, and solitons in conducting polymers," *Accounts of Chemical Research*, vol. 18, no. 10, pp. 309–315, 1985.

[19] V. Coropceanu, J. Cornil, D. A. da Silva Filho, Y. Olivier, R. Silbey, and J.-L. Brédas, "Charge transport in organic semiconductors," *Chemical reviews*, vol. 107, no. 4, pp. 926–952, 2007.

[20] A. Köhler and H. Bässler, *Electronic processes in organic semiconductors: An introduction.* John Wiley & Sons, 2015.

[21] P. Atkins, J. De Paula, and J. Keeler, *Atkins' physical chemistry.* Oxford university press, 2018.

[22] P. W. Atkins and R. S. Friedman, *Molecular quantum mechanics.* Oxford university press, 2011.

[23] A. Köhler and D. Beljonne, "The singlet–triplet exchange energy in conjugated polymers," *Advanced Functional Materials*, vol. 14, no. 1, pp. 11–18, 2004.

[24] J. J. Sakurai and E. D. Commins, "Modern quantum mechanics, revised edition," 1995.

[25] A. J. Sandee, C. K. Williams, N. R. Evans, J. E. Davies, C. E. Boothby, A. Köhler, R. H. Friend, and A. B. Holmes, "Solution-processible conjugated electrophosphorescent polymers," *Journal of the American Chemical Society*, vol. 126, no. 22, pp. 7041–7048, 2004.

[26] A. J. Lees, *Photophysics of organometallics*, vol. 29. Springer Science & Business Media, 2010.

[27] A. F. Rausch, H. H. Homeier, and H. Yersin, "Organometallic pt (ii) and ir (iii) triplet emitters for oled applications and the role of spin–orbit coupling: A study based on high-resolution optical spectroscopy," in *Photophysics of Organometallics*, pp. 193–235, Springer, 2010.

[28] R. Englman and J. Jortner, "The energy gap law for radiationless transitions in large molecules," *Molecular Physics*, vol. 18, no. 2, pp. 145–164, 1970.

[29] J. V. Caspar and T. J. Meyer, "Application of the energy gap law to nonradiative, excited-state decay," *The Journal of Physical Chemistry*, vol. 87, no. 6, pp. 952–957, 1983.

[30] D. Beljonne, Z. Shuai, G. Pourtois, and J. Bredas, "Spin- orbit coupling and intersystem crossing in conjugated polymers: a configuration interaction description," *The Journal of Physical Chemistry A*, vol. 105, no. 15, pp. 3899–3907, 2001.

[31] I. Austin and N. F. Mott, "Polarons in crystalline and non-crystalline materials," *Advances in physics*, vol. 18, no. 71, pp. 41–102, 1969.

[32] S. Brazovskii and N. Kirova, "Excitons, polarons, and bipolarons in conducting polymers," *JETP lett*, vol. 33, no. 4, 1981.

[33] M. Knupfer, "Exciton binding energies in organic semiconductors," *Applied Physics A*, vol. 77, no. 5, pp. 623–626, 2003.

[34] O. V. Mikhnenko, P. W. Blom, and T.-Q. Nguyen, "Exciton diffusion in organic semiconductors," *Energy & Environmental Science*, vol. 8, no. 7, pp. 1867–1888, 2015.

[35] C. Harris and D. Zwemer, "Coherent energy transfer in solids," *Annual Review of Physical Chemistry*, vol. 29, no. 1, pp. 473–495, 1978.

[36] I. L. Medintz and N. Hildebrandt, *FRET-Förster resonance energy transfer: from theory to applications.* John Wiley & Sons, 2013.

[37] S.-H. Lin, W. Xiao, and W. Dietz, "Generalized förster-dexter theory of photoinduced intramolecular energy transfer," *Physical Review E*, vol. 47, no. 5, p. 3698, 1993.

[38] A. Köhler and H. Bässler, "What controls triplet exciton transfer in organic semiconductors?," *Journal of Materials Chemistry*, vol. 21, no. 12, pp. 4003–4011, 2011.

[39] M. Pope and C. E. Swenberg, "Electronic processes in organic solids," *Annual Review of Physical Chemistry*, vol. 35, no. 1, pp. 613–655, 1984.

[40] W. Warta and N. Karl, "Hot holes in naphthalene: High, electric-field-dependent mobilities," *Physical Review B*, vol. 32, no. 2, p. 1172, 1985.

[41] N. Koch, A. Vollmer, I. Salzmann, B. Nickel, H. Weiss, and J. Rabe, "Evidence for temperature-dependent electron band dispersion in pentacene," *Physical review letters*, vol. 96, no. 15, p. 156803, 2006.

[42] T. Holstein, "Studies of polaron motion: Part ii. the "small" polaron," *Annals of physics*, vol. 8, no. 3, pp. 343–389, 1959.

[43] H. Bässler, "Charge transport in disordered organic photoconductors a monte carlo simulation study," *physica status solidi (b)*, vol. 175, no. 1, pp. 15–56, 1993.

[44] L. Schein and A. Tyutnev, "The contribution of energetic disorder to charge transport in molecularly doped polymers," *The Journal of Physical Chemistry C*, vol. 112, no. 19, pp. 7295–7308, 2008.

[45] A. Miller and E. Abrahams, “Impurity conduction at low concentrations,” *Physical Review*, vol. 120, no. 3, p. 745, 1960.

[46] S. Heun and P. Borsenberger, “A comparative study of hole transport in vapor-deposited molecular glasses of n, n, n , n-tetrakis (4-methylphenyl)-(1, 1-biphenyl)-4, 4-diamine and n, n-diphenyl-n, n-bis (3-methylphenyl)-(1, 1-biphenyl)-4, 4-diamine,” *Chemical physics*, vol. 200, no. 1-2, pp. 245–255, 1995.

[47] C. W. Tang, “Two-layer organic photovoltaic cell,” *Applied physics letters*, vol. 48, no. 2, pp. 183–185, 1986.

[48] G. Yu, J. Gao, J. C. Hummelen, F. Wudl, and A. J. Heeger, “Polymer photovoltaic cells: enhanced efficiencies via a network of internal donor-acceptor heterojunctions,” *Science*, vol. 270, no. 5243, pp. 1789–1791, 1995.

[49] O. V. Mikhnenko, H. Azimi, M. Scharber, M. Morana, P. W. Blom, and M. A. Loi, “Exciton diffusion length in narrow bandgap polymers,” *Energy & Environmental Science*, vol. 5, no. 5, pp. 6960–6965, 2012.

[50] O. V. Mikhnenko, M. Kuik, J. Lin, N. van der Kaap, T.-Q. Nguyen, and P. W. Blom, “Trap-limited exciton diffusion in organic semiconductors,” *Advanced Materials*, vol. 26, no. 12, pp. 1912–1917, 2014.

[51] A. J. Ward, A. Ruseckas, M. M. Kareem, B. Ebenhoch, L. A. Serrano, M. Al-Eid, B. Fitzpatrick, V. M. Rotello, G. Cooke, and I. D. Samuel, “The impact of driving force on electron transfer rates in photovoltaic donor–acceptor blends,” *Advanced Materials*, vol. 27, no. 15, pp. 2496–2500, 2015.

[52] G. Ren, C. W. Schlenker, E. Ahmed, S. Subramaniyan, S. Olthof, A. Kahn, D. S. Ginger, and S. A. Jenekhe, “Photoinduced hole transfer becomes suppressed with diminished driving force in polymer-fullerene solar cells while electron transfer remains active,” *Advanced Functional Materials*, vol. 23, no. 10, pp. 1238–1249, 2013.

[53] A. A. Bakulin, A. Rao, V. G. Pavelyev, P. H. van Loosdrecht, M. S. Pshenichnikov, D. Niedzialek, J. Cornil, D. Beljonne, and R. H. Friend, “The role of driving energy and delocalized states for charge separation in organic semiconductors,” *Science*, vol. 335, no. 6074, pp. 1340–1344, 2012.

[54] K. Vandewal, S. Albrecht, E. T. Hoke, K. R. Graham, J. Widmer, J. D. Douglas, M. Schubert, W. R. Mateker, J. T. Bloking, G. F. Burkhard, *et al.*, “Efficient charge generation by relaxed charge-transfer states at organic interfaces,” *Nature materials*, vol. 13, no. 1, p. 63, 2014.

[55] W. Shockley, “The theory of p-n junctions in semiconductors and p-n junction transistors,” *Bell System Technical Journal*, vol. 28, no. 3, pp. 435–489, 1949.

[56] G. Wetzelaer, M. Kuik, M. Lenes, and P. Blom, “Origin of the dark-current ideality factor in polymer: fullerene bulk heterojunction solar cells,” *Applied physics letters*, vol. 99, no. 15, p. 153506, 2011.

[57] V. Mihailetchi, L. Koster, J. Hummelen, and P. Blom, “Photocurrent generation in polymer-fullerene bulk heterojunctions,” *Physical review letters*, vol. 93, no. 21, p. 216601, 2004.

[58] H. Gommans, M. Kemerink, J. Kramer, and R. Janssen, “Field and temperature dependence of the photocurrent in polymer/fullerene bulk heterojunction solar cells,” *Applied Physics Letters*, vol. 87, no. 12, p. 122104, 2005.

[59] C. L. Braun, “Electric field assisted dissociation of charge transfer states as a mechanism of photocarrier production,” *The Journal of chemical physics*, vol. 80, no. 9, pp. 4157–4161, 1984.

[60] U. Würfel, D. Neher, A. Spies, and S. Albrecht, “Impact of charge transport on current–voltage characteristics and power-conversion efficiency of organic solar cells,” *Nature communications*, vol. 6, p. 6951, 2015.

[61] D. Bartesaghi, I. del Carmen Pérez, J. Kniepert, S. Roland, M. Turbiez, D. Neher, and L. J. A. Koster, “Competition between recombination and extraction of free charges determines the fill factor of organic solar cells,” *Nature communications*, vol. 6, p. 7083, 2015.

[62] K. Vandewal, “Interfacial charge transfer states in condensed phase systems,” *Annual review of physical chemistry*, vol. 67, pp. 113–133, 2016.

[63] K. Vandewal, A. Gadisa, W. D. Oosterbaan, S. Bertho, F. Banishoeib, I. Van Severen, L. Lutsen, T. J. Cleij, D. Vanderzande, and J. V. Manca, “The relation between open-circuit voltage and the onset of photocurrent generation by charge-transfer absorption in polymer: fullerene bulk heterojunction solar cells,” *Advanced Functional Materials*, vol. 18, no. 14, pp. 2064–2070, 2008.

[64] K. Vandewal, K. Tvingstedt, A. Gadisa, O. Inganäs, and J. V. Manca, “On the origin of the open-circuit voltage of polymer–fullerene solar cells,” *Nature materials*, vol. 8, no. 11, p. 904, 2009.

[65] M. A. Loi, S. Toffanin, M. Muccini, M. Forster, U. Scherf, and M. Scharber, “Charge transfer excitons in bulk heterojunctions of a polyfluorene copolymer and a fullerene derivative,” *Advanced Functional Materials*, vol. 17, no. 13, pp. 2111–2116, 2007.

[66] H. Kim, J. Y. Kim, S. H. Park, K. Lee, Y. Jin, J. Kim, and H. Suh, “Electroluminescence in polymer-fullerene photovoltaic cells,” *Applied Physics Letters*, vol. 86, no. 18, p. 183502, 2005.

[67] K. Tvingstedt, K. Vandewal, A. Gadisa, F. Zhang, J. Manca, and O. Inganas, “Electroluminescence from charge transfer states in polymer solar cells,” *Journal of the American Chemical Society*, vol. 131, no. 33, pp. 11819–11824, 2009.

[68] P. Würfel and U. Würfel, *Physics of solar cells: from basic principles to advanced concepts*. John Wiley & Sons, 2016.

[69] P. Wurfel, “The chemical potential of radiation,” *Journal of Physics C: Solid State Physics*, vol. 15, no. 18, p. 3967, 1982.

[70] U. Rau, “Reciprocity relation between photovoltaic quantum efficiency and electroluminescent emission of solar cells,” *Physical Review B*, vol. 76, no. 8, p. 085303, 2007.

[71] K. Vandewal, K. Tvingstedt, A. Gadisa, O. Inganäs, and J. V. Manca, “Relating the open-circuit voltage to interface molecular properties of donor: acceptor bulk heterojunction solar cells,” *Physical Review B*, vol. 81, no. 12, p. 125204, 2010.

[72] W. Shockley and W. Read Jr, “Statistics of the recombinations of holes and electrons,” *Physical review*, vol. 87, no. 5, p. 835, 1952.

[73] R. N. Hall, “Electron-hole recombination in germanium,” *Physical review*, vol. 87, no. 2, p. 387, 1952.

[74] L. Koster, V. Mihailetchi, and P. Blom, “Bimolecular recombination in polymer/fullerene bulk heterojunction solar cells,” *Applied physics letters*, vol. 88, no. 5, p. 052104, 2006.

[75] C. Deibel, A. Baumann, and V. Dyakonov, “Polaron recombination in pristine and annealed bulk heterojunction solar cells,” *Applied Physics Letters*, vol. 93, no. 16, p. 386, 2008.

[76] C. M. Proctor, M. Kuik, and T.-Q. Nguyen, “Charge carrier recombination in organic solar cells,” *Progress in Polymer Science*, vol. 38, no. 12, pp. 1941–1960, 2013.

[77] P. Langevin, “Recombinaison et mobilites des ions dans les gaz,” *Ann. Chim. Phys*, vol. 28, no. 433, p. 122, 1903.

[78] J. Kniepert, I. Lange, N. J. Van Der Kaap, L. J. A. Koster, and D. Neher, “A conclusive view on charge generation, recombination, and extraction in as-prepared and annealed p3ht: Pcbm blends: Combined experimental and simulation work,” *Advanced Energy Materials*, vol. 4, no. 7, p. 1301401, 2014.

[79] C. Deibel, A. Wagenpfahl, and V. Dyakonov, “Origin of reduced polaron recombination in organic semiconductor devices,” *Physical Review B*, vol. 80, no. 7, p. 075203, 2009.

[80] T. M. Burke, S. Sweetnam, K. Vandewal, and M. D. McGehee, “Beyond langevin recombination: How equilibrium between free carriers and charge transfer states determines the open-circuit voltage of organic solar cells,” *Advanced Energy Materials*, vol. 5, no. 11, p. 1500123, 2015.

[81] S. Roland, “Charge carrier recombination and open circuit voltage in organic solar cells,” 2017.

[82] C. Van Berkel, M. Powell, A. Franklin, and I. French, "Quality factor in a-si: H nip and pin diodes," *Journal of applied physics*, vol. 73, no. 10, pp. 5264–5268, 1993.

[83] K. Tvingstedt and C. Deibel, "Temperature dependence of ideality factors in organic solar cells and the relation to radiative efficiency," *Advanced Energy Materials*, vol. 6, no. 9, p. 1502230, 2016.

[84] R. A. Street, A. Krakaris, and S. R. Cowan, "Recombination through different types of localized states in organic solar cells," *Advanced Functional Materials*, vol. 22, no. 21, pp. 4608–4619, 2012.

[85] G.-J. A. Wetzelaer, M. Kuik, and P. W. Blom, "Identifying the nature of charge recombination in organic solar cells from charge-transfer state electroluminescence," *Advanced Energy Materials*, vol. 2, no. 10, pp. 1232–1237, 2012.

[86] C. Göhler, A. Wagenpfahl, and C. Deibel, "Nongeminate recombination in organic solar cells," *Advanced Electronic Materials*, vol. 4, no. 10, p. 1700505, 2018.

[87] L.-M. Chen, Z. Hong, G. Li, and Y. Yang, "Recent progress in polymer solar cells: manipulation of polymer: fullerene morphology and the formation of efficient inverted polymer solar cells," *Advanced Materials*, vol. 21, no. 14-15, pp. 1434–1449, 2009.

[88] P. Li, G. Wang, L. Cai, B. Ding, D. Zhou, Y. Hu, Y. Zhang, J. Xiang, K. Wan, L. Chen, *et al.*, "High-efficiency inverted polymer solar cells controlled by the thickness of polyethylenimine ethoxylated (peie) interfacial layers," *Physical Chemistry Chemical Physics*, vol. 16, no. 43, pp. 23792–23799, 2014.

[89] T. Yang, W. Cai, D. Qin, E. Wang, L. Lan, X. Gong, J. Peng, and Y. Cao, "Solution-processed zinc oxide thin film as a buffer layer for polymer solar cells with an inverted device structure," *The Journal of Physical Chemistry C*, vol. 114, no. 14, pp. 6849–6853, 2010.

[90] J. Y. Kim, K. Lee, N. E. Coates, D. Moses, T.-Q. Nguyen, M. Dante, and A. J. Heeger, "Efficient tandem polymer solar cells fabricated by all-solution processing," *Science*, vol. 317, no. 5835, pp. 222–225, 2007.

[91] J. Kniepert, M. Schubert, J. C. Blakesley, and D. Neher, "Photogeneration and recombination in p3ht/pcbm solar cells probed by time-delayed collection field experiments," *The Journal of Physical Chemistry Letters*, vol. 2, no. 7, pp. 700–705, 2011.

[92] E. Collado-Fregoso, S. N. Hood, S. Shoaee, B. C. Schroeder, I. McCulloch, I. Kassal, D. Neher, and J. R. Durrant, "Intercalated vs nonintercalated morphologies in donor–acceptor bulk heterojunction solar cells: Pbttt: Fullerene charge generation and recombination revisited," *The Journal of Physical Chemistry Letters*, vol. 8, no. 17, pp. 4061–4068, 2017.

[93] J. Kurpiers, T. Ferron, S. Roland, M. Jakoby, T. Thiede, F. Jaiser, S. Albrecht, S. Janietz, B. A. Collins, I. A. Howard, *et al.*, "Probing the pathways of free charge generation in organic bulk heterojunction solar cells," *Nature communications*, vol. 9, no. 1, p. 2038, 2018.

[94] A. Baumann, J. Lorrmann, D. Rauh, C. Deibel, and V. Dyakonov, "A new approach for probing the mobility and lifetime of photogenerated charge carriers in organic solar cells under real operating conditions," *Advanced materials*, vol. 24, no. 32, pp. 4381–4386, 2012.

[95] R. Berera, R. van Grondelle, and J. T. Kennis, "Ultrafast transient absorption spectroscopy: principles and application to photosynthetic systems," *Photosynthesis research*, vol. 101, no. 2-3, pp. 105–118, 2009.

[96] J. Cabanillas-Gonzalez, G. Grancini, and G. Lanzani, "Pump-probe spectroscopy in organic semiconductors: Monitoring fundamental processes of relevance in optoelectronics," *Advanced Materials*, vol. 23, no. 46, pp. 5468–5485, 2011.

[97] F. Kanal, "Femtosecond transient absorption spectroscopy–technical improvements and applications on ultrafast molecular phenomena," 2015.

[98] J. RISSE, *Ultrafast dynamics of photoinduced charge separation in cyanine- and polymer-based organic photovoltaic systems.* PhD thesis, ÉCOLE POLYTECHNIQUE FÉDÉRALE DE LAUSANNE, 2015.

[99] G. Lanzani, *The photophysics behind photovoltaics and photonics.* John Wiley & Sons, 2012.

[100] `https://banerji.dcb.unibe.ch/natalie-banerji/`. Accessed: 2019-07-19.

[101] B. D. Cullity, "Elements of x-ray diffraction, addison," *Wesley Mass*, 1978.

[102] B. E. Warren, *X-ray Diffraction.* Courier Corporation, 1990.

[103] S. C. Mannsfeld, M. L. Tang, and Z. Bao, "Thin film structure of triisopropylsilylethynyl-functionalized pentacene and tetraceno [2, 3-b] thiophene from grazing incidence x-ray diffraction," *Advanced Materials*, vol. 23, no. 1, pp. 127–131, 2011.

[104] J. Rivnay, S. C. Mannsfeld, C. E. Miller, A. Salleo, and M. F. Toney, "Quantitative determination of organic semiconductor microstructure from the molecular to device scale," *Chemical reviews*, vol. 112, no. 10, pp. 5488–5519, 2012.

[105] L. H. Jimison, *Understanding microstructure and charge transport in semicrystalline polythiophenes.* Stanford University, 2011.

[106] B. W. Boudouris, V. Ho, L. H. Jimison, M. F. Toney, A. Salleo, and R. A. Segalman, "Real-time observation of poly (3-alkylthiophene) crystallization and correlation with transient optoelectronic properties," *Macromolecules*, vol. 44, no. 17, pp. 6653–6658, 2011.

[107] K. L. Gu, Y. Zhou, X. Gu, H. Yan, Y. Diao, T. Kurosawa, B. Ganapathysubramanian, M. F. Toney, and Z. Bao, "Tuning domain size and crystallinity in isoindigo/pcbm organic solar cells via solution shearing," *Organic Electronics*, vol. 40, pp. 79–87, 2017.

[108] Y. Diao, Y. Zhou, T. Kurosawa, L. Shaw, C. Wang, S. Park, Y. Guo, J. A. Reinspach, K. Gu, X. Gu, *et al.*, "Flow-enhanced solution printing of all-polymer solar cells," *Nature communications*, vol. 6, p. 7955, 2015.

[109] T. Lei, J.-Y. Wang, and J. Pei, "Design, synthesis, and structure–property relationships of isoindigo-based conjugated polymers," *Accounts of chemical research*, vol. 47, no. 4, pp. 1117–1126, 2014.

[110] L. Dou, Y. Liu, Z. Hong, G. Li, and Y. Yang, "Low-bandgap near-ir conjugated polymers/molecules for organic electronics," *Chemical reviews*, vol. 115, no. 23, pp. 12633–12665, 2015.

[111] K. Kawabata, M. Saito, I. Osaka, and K. Takimiya, "Very small bandgap π-conjugated polymers with extended thienoquinoids," *Journal of the American Chemical Society*, vol. 138, no. 24, pp. 7725–7732, 2016.

[112] C. Duan, F. Huang, and Y. Cao, "Recent development of push–pull conjugated polymers for bulk-heterojunction photovoltaics: rational design and fine tailoring of molecular structures," *Journal of Materials Chemistry*, vol. 22, no. 21, pp. 10416–10434, 2012.

[113] Y. Li, P. Sonar, L. Murphy, and W. Hong, "High mobility diketopyrrolopyrrole (dpp)-based organic semiconductor materials for organic thin film transistors and photovoltaics," *Energy & Environmental Science*, vol. 6, no. 6, pp. 1684–1710, 2013.

[114] W. Li, K. H. Hendriks, M. M. Wienk, and R. A. Janssen, "Diketopyrrolopyrrole polymers for organic solar cells," *Accounts of chemical research*, vol. 49, no. 1, pp. 78–85, 2015.

[115] J. C. Bijleveld, A. P. Zoombelt, S. G. Mathijssen, M. M. Wienk, M. Turbiez, D. M. de Leeuw, and R. A. Janssen, "Poly (diketopyrrolopyrrole- terthiophene) for ambipolar logic and photovoltaics," *Journal of the American Chemical Society*, vol. 131, no. 46, pp. 16616–16617, 2009.

[116] Y. Karpov, T. Erdmann, I. Raguzin, M. Al-Hussein, M. Binner, U. Lappan, M. Stamm, K. L. Gerasimov, T. Beryozkina, V. Bakulev, *et al.*, "High conductivity in molecularly p-doped diketopyrrolopyrrole-based polymer: The impact of a high dopant strength and good structural order," *Advanced Materials*, vol. 28, no. 28, pp. 6003–6010, 2016.

[117] R. Di Pietro, T. Erdmann, N. Wang, X. Liu, D. Gräfe, J. Lenz, J. Brandt, D. Kasemann, K. Leo, M. Al-Hussein, *et al.*, "The impact of molecular weight, air exposure and molecular doping on the charge transport properties and electronic defects in dithienyl-diketopyrrolopyrrole-thieno [3, 2-b] thiophene

copolymers," *Journal of Materials Chemistry C*, vol. 4, no. 46, pp. 10827–10838, 2016.

[118] R. Di Pietro, T. Erdmann, J. H. Carpenter, N. Wang, R. R. Shivhare, P. Formanek, C. Heintze, B. Voit, D. Neher, H. Ade, *et al.*, "Synthesis of high-crystallinity dpp polymers with balanced electron and hole mobility," *Chemistry of Materials*, vol. 29, no. 23, pp. 10220–10232, 2017.

[119] S. Wood, J. Wade, M. Shahid, E. Collado-Fregoso, D. D. Bradley, J. R. Durrant, M. Heeney, and J.-S. Kim, "Natures of optical absorption transitions and excitation energy dependent photostability of diketopyrrolopyrrole (dpp)-based photovoltaic copolymers," *Energy & Environmental Science*, vol. 8, no. 11, pp. 3222–3232, 2015.

[120] K. Vandewal, J. Benduhn, and V. Nikolis, "How to determine optical gaps and voltage losses in organic photovoltaic materials," *Sustainable Energy & Fuels*, vol. 2, no. 3, pp. 538–544, 2018.

[121] Y. Zhou, C. Fuentes-Hernandez, J. Shim, J. Meyer, A. J. Giordano, H. Li, P. Winget, T. Papadopoulos, H. Cheun, J. Kim, *et al.*, "A universal method to produce low–work function electrodes for organic electronics," *Science*, vol. 336, no. 6079, pp. 327–332, 2012.

[122] C. McDowell, M. Abdelsamie, M. F. Toney, and G. C. Bazan, "Solvent additives: Key morphology-directing agents for solution-processed organic solar cells," *Advanced Materials*, vol. 30, no. 33, p. 1707114, 2018.

[123] B. Carsten, F. He, H. J. Son, T. Xu, and L. Yu, "Stille polycondensation for synthesis of functional materials," *Chemical reviews*, vol. 111, no. 3, pp. 1493–1528, 2011.

[124] J. Lorrmann, B. H. Badada, O. Inganäs, V. Dyakonov, and C. Deibel, "Charge carrier extraction by linearly increasing voltage: Analytic framework and ambipolar transients," *Journal of Applied Physics*, vol. 108, no. 11, p. 113705, 2010.

[125] A. Armin, M. Hambsch, P. Wolfer, H. Jin, J. Li, Z. Shi, P. L. Burn, and P. Meredith, "Efficient, large area, and thick junction polymer solar cells with balanced mobilities and low defect densities," *Advanced Energy Materials*, vol. 5, no. 3, p. 1401221, 2015.

[126] C. G. Shuttle, R. Hamilton, J. Nelson, B. C. O'Regan, and J. R. Durrant, "Measurement of charge-density dependence of carrier mobility in an organic semiconductor blend," *Advanced Functional Materials*, vol. 20, no. 5, pp. 698–702, 2010.

[127] M. Kuik, L. Koster, G. Wetzelaer, and P. Blom, "Trap-assisted recombination in disordered organic semiconductors," *Physical review letters*, vol. 107, no. 25, p. 256805, 2011.

[128] A. Hofacker and D. Neher, “Dispersive and steady-state recombination in organic disordered semiconductors,” *Physical Review B*, vol. 96, no. 24, p. 245204, 2017.

[129] J. L. Baker, L. H. Jimison, S. Mannsfeld, S. Volkman, S. Yin, V. Subramanian, A. Salleo, A. P. Alivisatos, and M. F. Toney, “Quantification of thin film crystallographic orientation using x-ray diffraction with an area detector,” *Langmuir*, vol. 26, no. 11, pp. 9146–9151, 2010.

[130] M. R. Hammond, R. J. Kline, A. A. Herzing, L. J. Richter, D. S. Germack, H.-W. Ro, C. L. Soles, D. A. Fischer, T. Xu, L. Yu, *et al.*, “Molecular order in high-efficiency polymer/fullerene bulk heterojunction solar cells,” *ACS nano*, vol. 5, no. 10, pp. 8248–8257, 2011.

[131] N. A. Hotaling, K. Bharti, H. Kriel, and C. G. Simon Jr, “Validated open source nanofiber diameter measurement tool— nist,” tech. rep., 2015.

[132] J. J. van Franeker, G. H. Heintges, C. Schaefer, G. Portale, W. Li, M. M. Wienk, P. van der Schoot, and R. A. Janssen, “Polymer solar cells: solubility controls fiber network formation,” *Journal of the American Chemical Society*, vol. 137, no. 36, pp. 11783–11794, 2015.

[133] W. Li, K. H. Hendriks, A. Furlan, W. Roelofs, S. C. Meskers, M. M. Wienk, and R. A. Janssen, “Effect of the fibrillar microstructure on the efficiency of high molecular weight diketopyrrolopyrrole-based polymer solar cells,” *Advanced Materials*, vol. 26, no. 10, pp. 1565–1570, 2014.

[134] Y. Liu, J. Zhao, Z. Li, C. Mu, W. Ma, H. Hu, K. Jiang, H. Lin, H. Ade, and H. Yan, “Aggregation and morphology control enables multiple cases of high-efficiency polymer solar cells,” *Nature communications*, vol. 5, p. 5293, 2014.

[135] C. Lee, H. Kang, W. Lee, T. Kim, K.-H. Kim, H. Y. Woo, C. Wang, and B. J. Kim, “High-performance all-polymer solar cells via side-chain engineering of the polymer acceptor: The importance of the polymer packing structure and the nanoscale blend morphology,” *Advanced Materials*, vol. 27, no. 15, pp. 2466–2471, 2015.

[136] S. Dimitrov, B. Schroeder, C. Nielsen, H. Bronstein, Z. Fei, I. McCulloch, M. Heeney, and J. Durrant, “Singlet exciton lifetimes in conjugated polymer films for organic solar cells,” *Polymers*, vol. 8, no. 1, p. 14, 2016.

[137] E. Collado-Fregoso, F. Deledalle, H. Utzat, P. S. Tuladhar, S. D. Dimitrov, A. Gillett, C.-H. Tan, W. Zhang, I. McCulloch, and J. R. Durrant, “Photophysical study of dpptt-t/pc70bm blends and solar devices as a function of fullerene loading: An insight into eqe limitations of dpp-based polymers,” *Advanced Functional Materials*, vol. 27, no. 6, p. 1604426, 2017.

[138] K. Vandewal, Z. Ma, J. Bergqvist, Z. Tang, E. Wang, P. Henriksson, K. Tvingstedt, M. R. Andersson, F. Zhang, and O. Inganäs, "Quantification of quantum efficiency and energy losses in low bandgap polymer: Fullerene solar cells with high open-circuit voltage," *Advanced Functional Materials*, vol. 22, no. 16, pp. 3480–3490, 2012.

[139] J. Benduhn, K. Tvingstedt, F. Piersimoni, S. Ullbrich, Y. Fan, M. Tropiano, K. A. McGarry, O. Zeika, M. K. Riede, C. J. Douglas, *et al.*, "Intrinsic non-radiative voltage losses in fullerene-based organic solar cells," *Nature Energy*, vol. 2, no. 6, p. 17053, 2017.

[140] T. M. Clarke and J. R. Durrant, "Charge photogeneration in organic solar cells," *Chemical reviews*, vol. 110, no. 11, pp. 6736–6767, 2010.

[141] B. A. Gregg, "Entropy of charge separation in organic photovoltaic cells: the benefit of higher dimensionality," *The Journal of Physical Chemistry Letters*, vol. 2, no. 24, pp. 3013–3015, 2011.

[142] H. Bässler and A. Köhler, ""hot or cold": how do charge transfer states at the donor–acceptor interface of an organic solar cell dissociate?," *Physical Chemistry Chemical Physics*, vol. 17, no. 43, pp. 28451–28462, 2015.

[143] F. C. Jamieson, T. Agostinelli, H. Azimi, J. Nelson, and J. R. Durrant, "Field-independent charge photogeneration in pcpdtbt/pc70bm solar cells," *The Journal of Physical Chemistry Letters*, vol. 1, no. 23, pp. 3306–3310, 2010.

[144] T. M. Burke and M. D. McGehee, "How high local charge carrier mobility and an energy cascade in a three-phase bulk heterojunction enable¿ 90% quantum efficiency," *Advanced Materials*, vol. 26, no. 12, pp. 1923–1928, 2014.

[145] I. Avilov, V. Geskin, and J. Cornil, "Quantum-chemical characterization of the origin of dipole formation at molecular organic/organic interfaces," *Advanced Functional Materials*, vol. 19, no. 4, pp. 624–633, 2009.

[146] C. Schwarz, S. Tscheuschner, J. Frisch, S. Winkler, N. Koch, H. Bässler, and A. Köhler, "Role of the effective mass and interfacial dipoles on exciton dissociation in organic donor-acceptor solar cells," *Physical Review B*, vol. 87, no. 15, p. 155205, 2013.

[147] V. Arkhipov, P. Heremans, and H. Bässler, "Why is exciton dissociation so efficient at the interface between a conjugated polymer and an electron acceptor?," *Applied Physics Letters*, vol. 82, no. 25, pp. 4605–4607, 2003.

[148] A. C. Jakowetz, M. L. Bohm, J. Zhang, A. Sadhanala, S. Huettner, A. A. Bakulin, A. Rao, and R. H. Friend, "What controls the rate of ultrafast charge transfer and charge separation efficiency in organic photovoltaic blends," *Journal of the American Chemical Society*, vol. 138, no. 36, pp. 11672–11679, 2016.

[149] A. Nenashev, S. Baranovskii, M. Wiemer, F. Jansson, R. Österbacka, A. Dvurechenskii, and F. Gebhard, “Theory of exciton dissociation at the interface between a conjugated polymer and an electron acceptor,” *Physical Review B*, vol. 84, no. 3, p. 035210, 2011.

[150] M. Scarongella, J. De Jonghe-Risse, E. Buchaca-Domingo, M. Causa’, Z. Fei, M. Heeney, J.-E. Moser, N. Stingelin, and N. Banerji, “A close look at charge generation in polymer: fullerene blends with microstructure control,” *Journal of the American chemical society*, vol. 137, no. 8, pp. 2908–2918, 2015.

[151] S. D. Dimitrov, A. A. Bakulin, C. B. Nielsen, B. C. Schroeder, J. Du, H. Bronstein, I. McCulloch, R. H. Friend, and J. R. Durrant, “On the energetic dependence of charge separation in low-band-gap polymer/fullerene blends,” *Journal of the American Chemical Society*, vol. 134, no. 44, pp. 18189–18192, 2012.

[152] X.-K. Chen, V. Coropceanu, and J.-L. Bredas, “Assessing the nature of the charge-transfer electronic states in organic solar cells,” *Nature communications*, vol. 9, no. 1, p. 5295, 2018.

[153] J.-L. Brédas, J. P. Calbert, D. da Silva Filho, and J. Cornil, “Organic semiconductors: A theoretical characterization of the basic parameters governing charge transport,” *Proceedings of the National Academy of Sciences*, vol. 99, no. 9, pp. 5804–5809, 2002.

[154] K. Hannewald, V. Stojanović, J. Schellekens, P. Bobbert, G. Kresse, and J. Hafner, “Theory of polaron bandwidth narrowing in organic molecular crystals,” *Physical Review B*, vol. 69, no. 7, p. 075211, 2004.

[155] R. A. Marcus, “On the theory of oxidation-reduction reactions involving electron transfer. i,” *The Journal of Chemical Physics*, vol. 24, no. 5, pp. 966–978, 1956.

[156] J. De Jonghe-Risse, M. Scarongella, J. C. Brauer, E. Buchaca-Domingo, J.-E. Moser, N. Stingelin, N. Banerji, *et al.*, “The fate of electron–hole pairs in polymer: fullerene blends for organic photovoltaics,” *Nature communications*, vol. 7, p. 12556, 2016.

[157] P. Krauspe, D. Tsokkou, E. Buchaca-Domingo, Z. Fei, M. Heeney, N. Stingelin, N. Banerji, *et al.*, “Terahertz short-range mobilities in neat and intermixed regions of polymer: fullerene blends with controlled phase morphology,” *Journal of Materials Chemistry A*, vol. 6, no. 44, pp. 22301–22309, 2018.

[158] V. Pranculis, Y. Infahsaeng, Z. Tang, A. Devizis, D. A. Vithanage, C. S. Ponseca Jr, O. Inganas, A. P. Yartsev, V. Gulbinas, and V. Sundstrom, “Charge carrier generation and transport in different stoichiometry apfo3: Pc61bm solar cells,” *Journal of the American Chemical Society*, vol. 136, no. 32, pp. 11331–11338, 2014.

[159] T. Tiedje and A. Rose, “A physical interpretation of dispersive transport in disordered semiconductors,” *Solid State Communications*, vol. 37, no. 1, pp. 49–52, 1981.

[160] S. Gélinas, A. Rao, A. Kumar, S. L. Smith, A. W. Chin, J. Clark, T. S. van der Poll, G. C. Bazan, and R. H. Friend, “Ultrafast long-range charge separation in organic semiconductor photovoltaic diodes,” *Science*, vol. 343, no. 6170, pp. 512–516, 2014.

[161] J. Hou, O. Inganäs, R. H. Friend, and F. Gao, “Organic solar cells based on non-fullerene acceptors,” *Nature materials*, vol. 17, no. 2, p. 119, 2018.

[162] Y. Lin and X. Zhan, “Non-fullerene acceptors for organic photovoltaics: an emerging horizon,” *Materials Horizons*, vol. 1, no. 5, pp. 470–488, 2014.

[163] C. Yan, S. Barlow, Z. Wang, H. Yan, A. K.-Y. Jen, S. R. Marder, and X. Zhan, “Non-fullerene acceptors for organic solar cells,” *Nature Reviews Materials*, vol. 3, p. 18003, 2018.

[164] N. Zhou and A. Facchetti, “Naphthalenediimide (ndi) polymers for all-polymer photovoltaics,” *Materials Today*, vol. 21, no. 4, pp. 377–390, 2018.

[165] P. Cheng, G. Li, X. Zhan, and Y. Yang, “Next-generation organic photovoltaics based on non-fullerene acceptors,” *Nature Photonics*, vol. 12, no. 3, p. 131, 2018.

[166] A. Wadsworth, M. Moser, A. Marks, M. S. Little, N. Gasparini, C. J. Brabec, D. Baran, and I. McCulloch, “Critical review of the molecular design progress in non-fullerene electron acceptors towards commercially viable organic solar cells,” *Chemical Society Reviews*, vol. 48, no. 6, pp. 1596–1625, 2019.

[167] H. Yao, Y. Chen, Y. Qin, R. Yu, Y. Cui, B. Yang, S. Li, K. Zhang, and J. Hou, “Design and synthesis of a low bandgap small molecule acceptor for efficient polymer solar cells,” *Advanced Materials*, vol. 28, no. 37, pp. 8283–8287, 2016.

[168] H. Yao, Y. Cui, R. Yu, B. Gao, H. Zhang, and J. Hou, “Design, synthesis, and photovoltaic characterization of a small molecular acceptor with an ultra-narrow band gap,” *Angewandte Chemie International Edition*, vol. 56, no. 11, pp. 3045–3049, 2017.

[169] C. Deibel, D. Mack, J. Gorenflot, A. Schöll, S. Krause, F. Reinert, D. Rauh, and V. Dyakonov, “Energetics of excited states in the conjugated polymer poly (3-hexylthiophene),” *Physical Review B*, vol. 81, no. 8, p. 085202, 2010.

[170] L. Zhang, B. Lin, Z. Ke, J. Chen, W. Li, M. Zhang, and W. Ma, “A universal approach to improve electron mobility without significant enlarging phase separation in idt-based non-fullerene acceptor organic solar cells,” *Nano Energy*, vol. 41, pp. 609–617, 2017.

[171] Q. An, F. Zhang, J. Zhang, W. Tang, Z. Deng, and B. Hu, "Versatile ternary organic solar cells: a critical review," *Energy & Environmental Science*, vol. 9, no. 2, pp. 281–322, 2016.

[172] N. Gasparini, A. Salleo, I. McCulloch, and D. Baran, "The role of the third component in ternary organic solar cells," *Nature Reviews Materials*, p. 1, 2019.

[173] F. D. Eisner, M. Azzouzi, Z. Fei, X. Hou, T. D. Anthopoulos, T. J. S. Dennis, M. Heeney, and J. Nelson, "Hybridization of local exciton and charge-transfer states reduces nonradiative voltage losses in organic solar cells," *Journal of the American Chemical Society*, vol. 141, no. 15, pp. 6362–6374, 2019.

[174] S. M. Menke, A. Cheminal, P. Conaghan, N. A. Ran, N. C. Greehnam, G. C. Bazan, T.-Q. Nguyen, A. Rao, and R. H. Friend, "Order enables efficient electron-hole separation at an organic heterojunction with a small energy loss," *Nature communications*, vol. 9, no. 1, p. 277, 2018.

[175] P. E. Shaw, A. Ruseckas, and I. D. Samuel, "Exciton diffusion measurements in poly (3-hexylthiophene)," *Advanced Materials*, vol. 20, no. 18, pp. 3516–3520, 2008.

[176] J. Piris, T. E. Dykstra, A. A. Bakulin, P. H. v. Loosdrecht, W. Knulst, M. T. Trinh, J. M. Schins, and L. D. Siebbeles, "Photogeneration and ultrafast dynamics of excitons and charges in p3ht/pcbm blends," *The Journal of Physical Chemistry C*, vol. 113, no. 32, pp. 14500–14506, 2009.

[177] Y. Tamai, Y. Fan, V. O. Kim, K. Ziabrev, A. Rao, S. Barlow, S. R. Marder, R. H. Friend, and S. M. Menke, "Ultrafast long-range charge separation in nonfullerene organic solar cells," *ACS nano*, vol. 11, no. 12, pp. 12473–12481, 2017.

List of Figures

List of Tables

List of Abbreviations

A	electron accepting
AFM	atomic force microscope
BMR	bimolecular recombination rate
CCD	charge coupled device
CDM	correlated disorder model
CT	charge transfer
D	electron donating
DFT	density functional theory
DOS	density of states
DPP	diketopyrrolopyrrole
EA	electroabsorption
EDA	electromodulated differential absorption
EL	electroluminescence
ESA	excited state absoprtion
ETL	electron transport layer
EQE/EQE_{PV}	photovoltaic external quantum efficiency
FF	fill factor
FRET	Förster resonance energy transfer
GDM	gaussian disorder model
GIWAXS	grazing incidence wide angle x-ray scattering
GS	ground state
GSB	ground state bleaching
GW	giga-watt
HOMO	highest occupied molecular orbital
HTL	hole transport layer
IEC	International Energy Agency
ITO	indium tin oxide
LCAO	linear combination of atomic orbitals

LUMO	lowest unoccupied molecular orbital
MM	mismatch factor
Mtoe	million tonnes
NOPA	non-collinear optical parametric amplifier
OPV	organic photovoltaic
PA	product absorption
PCE	power conversion efficiency
PL	photoluminescence
PV	photovoltaic
QCM	quartz crystal microbalance
S_1/S	singlet state
SE	stimulated emission
SHG	second harmonic generation
SPM	self phase modulation
T	thiophene
TT	thienothiophene
TA	transient absorption
TCO	transparent conductive oxide
TDCF	time delayed collection field

Acknowledgements

First and foremost, I would like to express my sincere gratitude to Professor Stefan Mannsfeld for giving me this fantastic opportunity of doing research in his lab. I also sincerely thank him for his immense support throughout these years and the kind of flexibility he allowed with the research projects. Professor Mannsfeld is a wonderful teacher, and I love his enthusiasm for teaching and doing research. I was lucky to learn GIWAXS analysis from him, and I thank him for sharing his knowledge and invaluable experiences. Next, I would like to thank Professor Koen Vandewal for helping me with the research projects. Discussions with him always provided clarity, and this thesis would not have been possible without his support. A big thanks to Mike for always being there and for helping me with research in general. He has been a huge support throughout. I will remember our initial synchrotron experiences.

I would like to sincerely thank Professor Natalie Banerji from the University of Bern. She was kind enough to offer me the possibility of doing some very interesting measurements in her lab. I want to thank Gareth for helping me with transient absorption measurements. Also, sincere regards to Kaila, Martina, Nikos, Lisa, Yufei, Philipp, and Gonzague for making my stay in Bern memorable.

I would like to thank a few guys from the IAPP institute. My sincere regards to Johannes for doing sensitive-EQE measurements and for all the valuable discussions. He has been a great person to work and spend time with. I will also remember our cooking stint with Indian food. I also thank Sascha for the OTRACE measurements and for the interesting scientific discussions. Sincere regards to Vasilis, Jonas, Donato, Martin, Bernhard, Sven, Tobias, Christian, Karla and all the wonderful people of the IAPP institute. A big thank you to all the guys in the lab in Dresden: Cecilia, Felix, Jakob, Jonathan, Katherina, Nara, Tianyu, Yichu, and Zhe. Thanks for all the support throughout these years and you guys are wonderful people to work with.

My stay in Dresden would not have been possible without support of the Friends and Family. My sincere thanks to Anne for always being there and for the help with all kinds of things imaginable. You made my stay in Dresden a very memorable one. Heartiest regards to Andreas for his support and wonderful company. Thanks for the countless evenings we spent together discussing science, philosophy, and everything else. A big thank you to my roommate Philipp for all his support and time. Thanks for making Easter a very special festival. Also, sincere regards to Katha, Nikki, Johannes, and Astrid. Lastly, I would like to express my deepest gratitude to my family. I thank my mother and sister for their immeasurable support throughout this journey. I dedicate this work to you guys. Sincere thanks to my father for his support during these years. I would also like to thank and remember my late grandfather for always motivating me and encouraging me to pursue my dreams.

Erklärung

Hiermit versichere ich, dass ich die vorliegende Arbeit ohne unzulässige Hilfe Dritter und ohne Benutzung anderer als der angegebenen Hilfsmittel angefertigt habe. Die aus fremden Quellen direkt oder indirekt übernommenen Gedanken sind als solche kenntlich gemacht. Die Arbeit wurde bisher weder im Inland noch im Ausland in gleicher oder ähnlicher Form einer anderen Prüfungsbehörde vorgelegt.

Rishi Ramdas Shivhare
Dresden, den 12.08.2019